molecules

Special Issue Reprint

Novel Electrode Materials for Rechargeable Batteries, 2nd Edition

Edited by
Jian Peng, Wei Zhang and Shiyue Cao

mdpi.com/journal/molecules

MDPI

Novel Electrode Materials for Rechargeable Batteries, 2nd Edition

Novel Electrode Materials for Rechargeable Batteries, 2nd Edition

Guest Editors

Jian Peng
Wei Zhang
Shiyue Cao

MDPI

Basel • Beijing • Wuhan • Barcelona • Belgrade • Novi Sad • Cluj • Manchester

Guest Editors

Jian Peng	Wei Zhang	Shiyue Cao
Eastern Institute for Advanced Study	School of Materials and Energy	Eastern Institute for Advanced Study
Eastern institute of Technology	Guangdong University of Technology	Eastern Institute of Technology
Ningbo	Guangzhou	Ningbo
China	China	China

Editorial Office
MDPI AG
Grosspeteranlage 5
4052 Basel, Switzerland

This is a reprint of the Special Issue, published open access by the journal *Molecules* (ISSN 1420-3049), freely accessible at: https://www.mdpi.com/journal/molecules/special_issues/3M79MKDJR0.

For citation purposes, cite each article independently as indicated on the article page online and as indicated below:

Lastname, A.A.; Lastname, B.B. Article Title. *Journal Name* **Year**, *Volume Number*, Page Range.

ISBN 978-3-7258-6420-1 (Hbk)
ISBN 978-3-7258-6421-8 (PDF)
https://doi.org/10.3390/books978-3-7258-6421-8

© 2026 by the authors. Articles in this book are Open Access and distributed under the Creative Commons Attribution (CC BY) license. The book as a whole is distributed by MDPI under the terms and conditions of the Creative Commons Attribution-NonCommercial-NoDerivs (CC BY-NC-ND) license (https://creativecommons.org/licenses/by-nc-nd/4.0/).

Contents

molecules

Article

Morphology-Engineered NiMo Alloy on Nickel Foam for Enhanced Hydrogen Evolution Reaction Performance

Yanhong Ding, Yong Cao, Zhichao Gao, Hanzhou Ding, Haifeng Xu, Bin Liu, Fusheng Liu and Yirong Zhu *

School of Materials Science and Engineering, Hunan University of Technology, Zhuzhou 412007, China; dyh2004@126.com (Y.D.); qq04261998@163.com (Y.C.); gzc20201222@126.com (Z.G.); 18974956112@163.com (H.D.); 19174423169@163.com (H.X.); 15170898688@163.com (B.L.); liucsu@gmail.com (F.L.)

* Correspondence: zhuyirong2004@163.com or zhuyirong@hut.edu.cn

Abstract: A nanoflower-like nickel-molybdenum alloy was synthesized by hydrothermal in situ growth of $NiMoO_4$ nanorod arrays on nickel foam (NF) followed by gas-phase re-reduction at 600 °C. The resulting structure has a uniform porosity and high specific surface area, which improves the availability of active sites and facilitates efficient electron and mass transport. SEM and XPS analyses confirm that the formed $NiMoO_4$ nanorods are uniformly distributed, which leads to significant optimization of their electronic structure. The electrochemical measurements revealed that the sample exhibited excellent hydrogen evolution reaction (HER) performance, with an overpotential as low as 127 mV at 100 mA cm^{-2} and a Tafel slope of 124 mV dec^{-1}. CV and EIS showed that the sample had the largest electrochemically active surface area (121.3 mF cm^{-2}) among the samples treated at different temperatures, with the smallest charge transfer resistance. In addition, the catalyst maintained high stability after 45 h of continuous operation. These results highlight the potential of NiMo/NF as a highly efficient and durable HER catalyst to help advance hydrogen energy technology.

Keywords: NiMo alloy; water electrolysis; electrocatalysis; hydrogen evolution performance

1. Introduction

The escalating severity of global climate challenges, coupled with the progressive depletion of fossil fuel reserves, has rendered energy transition an urgent global imperative. This critical juncture positions clean energy technologies as a pivotal strategy for concurrently addressing climate change mitigation and sustainable energy security [1–6]. Among various clean energy technologies, water electrolysis is regarded as a promising approach for producing green hydrogen, as it enables the clean conversion of water into hydrogen and oxygen using electricity, yielding a high energy-density, emission-free fuel [7,8]. Coupling water electrolysis with renewable energy sources such as wind and solar mitigates their intermittency, reduces carbon emissions, and enhances energy efficiency and sustainability [9–12]. As a result, water electrolysis for hydrogen production is gaining increasing attention as a key component of future clean energy systems [13].

Although water electrolysis offers high theoretical efficiency, its practical performance is hindered by the sluggish kinetics of the hydrogen evolution reaction (HER), which demands a high overpotential to overcome energy barriers, resulting in elevated energy consumption and production costs [14–17]. Precious metal-based electrocatalysts, such as platinum and its alloys, are regarded as the most effective HER catalysts due to their superior activity and low overpotential. However, their high cost and limited availability present major obstacles to large-scale deployment [18–20]. Therefore, the development of

https://doi.org/10.3390/molecules30112396

non-precious metal-based HER catalysts with high catalytic performance and low cost has become the key to solving this problem. In recent years, transition metals have become a hot spot in electrocatalyst research due to their abundant resources, low cost and excellent electrochemical performance, among which nickel–molybdenum (NiMo) alloys have attracted much attention due to their unique electronic structure and excellent HER catalytic performance [21–23]. It has been shown that the catalytic activity of NiMo alloys can be significantly enhanced by modulating the component ratio, optimizing its surface structure and compounding with other functional materials [24,25]. However, the traditional NiMo alloy catalysts still face the problems of insufficient exposure of active sites, limited mass transfer, and poor electrical conductivity in practical applications, and these bottlenecks seriously limit their industrial promotion [26–29]. Consequently, optimizing the structure and performance of NiMo alloys while preserving their intrinsic advantages has become a key focus of current research [30–35].

To address the aforementioned limitations, this study presents a structural engineering strategy for NiMo alloy catalysts supported on nickel foam, aiming to enhance HER performance through material optimization. NiMo alloys were synthesized on a high-surface-area, three-dimensional porous nickel foam via a combined hydrothermal and gas-phase reduction method. The nickel foam not only ensured excellent electrical conductivity but also increased the exposure of active sites, thereby improving catalytic activity. Additionally, the NiMo alloy's electronic structure was tailored by controlling crystal growth orientation and surface morphology, effectively reducing the overpotential for HER. The gas-phase reduction further promoted alloy uniformity and stability, contributing to long-term electrochemical durability. The catalyst's performance was systematically evaluated, demonstrating its potential as a cost-effective and efficient material for hydrogen production via water electrolysis.

2. Results and Discussion

2.1. Structural Topography Analysis

Figure 1 illustrates the X-ray diffraction (XRD) spectra of four NiMo/NF electrode samples prepared at different reduction temperatures (the 'heart' and 'diamond' symbols in the figure represent Ni and NiMo, respectively). It can be observed that diffraction peaks corresponding to the (111), (200) and (220) crystal planes appear at 44.50°, 51.85°, and 76.38°, respectively, which are in agreement with the standard data for NF (PDF#04-0850). Under the reduction conditions at 600 °C, 800 °C, and 950 °C (Figure 1b–d), the diffraction peaks of the (200) and (220) crystal planes were shifted to the left, indicating an increase in the crystal plane spacing, which may be due to the doping of Mo ions, which have a larger radius than that of Ni ions. In addition, diffraction peaks corresponding to the (011), (041), (331) and (242) crystal planes appeared at 44.34°, 41°, 43°, and 49.18°, respectively, which were consistent with the standard data for NiMo alloys (PDF#48-1745) [36]. In Figure 1a, the diffraction peaks of NiMo alloy were not observed, which may be due to the low reduction temperature (400 °C), which did not allow a sufficient reduction reaction to take place. The differences in atomic radii and electronegativity of Ni and Mo resulted in lattice distortion, which led to the formation of diverse structures on some of the crystalline surfaces, which manifested as new NiMo alloy diffraction peaks, such as (041) and (331) crystalline peaks (Figure 1b) and (242) crystalline peaks (Figure 1c). The relatively weak intensity and broadening of these diffraction peaks [37] indicate the presence of defects in the crystal structure, leading to an increase in surface energy [37]. These structural changes contribute to the enhancement of the hydrogen evolution reaction (HER) activity, which significantly increases the hydrogen precipitation rate. When the reduction temperature was raised to 950 °C, the diffusion rates of Ni and Mo ions increased, facilitating the formation of Ni-Mo alloys. Consequently, the intensity of the diffraction peaks corresponding to the (011) crystal plane of NiMo was significantly enhanced (see Figure 1d), indicating an improvement in the integrity of the crystal structure [38–40]. In addition, by comparing with the standard data of Ni (PDF#48-1745), no obvious $NiMoO_4$ diffraction peaks were found, which indicates that $NiMoO_4$ has amorphous structural properties.

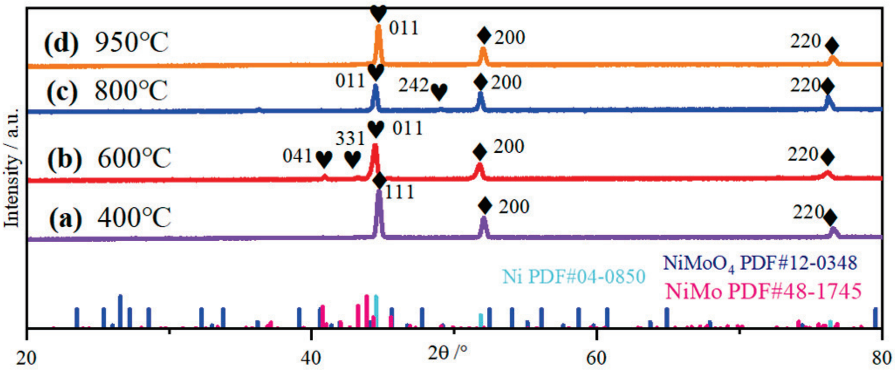

Figure 1. XRD images of NiMo/NF at different reduction temperatures.

2.2. SEM Analysis

The microscopic morphological features of the electrodes were systematically investigated through scanning electron microscopy (SEM) characterization, as presented in Figure 2. Energy-dispersive spectroscopic analysis confirmed the substantial deposition of active materials onto the three-dimensional nickel foam substrate with an interconnected porous architecture. High-magnification images (inset in Figure 2a) revealed the presence of rod-shaped nanostructures with amorphous characteristics, which were subsequently identified as $NiMoO_4$ through comparative XRD pattern analysis (Figure 1). Notably, these nanorods demonstrated heterogeneous spatial distribution (Figure 2b) with longitudinal dimensions varying between 2 and 8 μm. Thermal reduction treatment induced significant morphological evolution, where the elevated temperatures facilitated the enhancement of the diffusion kinetics of Ni and Mo species. This phenomenon promoted the heterogeneous nucleation processes, ultimately resulting in the surface decoration of nanorods with spherical NiMo alloy particulates (inset in Figure 2c). The formation of metallic NiMo phases was further corroborated by the emergence of characteristic (111) and (200) diffraction peaks in corresponding XRD patterns (Figure 1), confirming the successful phase transformation under reductive thermal conditions [41].These spherical particles have a diameter of about 1 μm and a uniform particle size distribution (Figure 2d). From the inset of Figure 2d, it can be clearly observed that these spherical particles exhibit a flower-spherical shape, whose surface is not smooth but consists of a uniform nanosheet structure. This flower-spherical structure not only significantly increases the specific surface area, but also exposes more catalytically active sites, which in turn shortens the diffusion paths of electrons and ions and reduces the transport resistance, thus accelerating the rate of the hydrogen evolution reaction (HER) and enhancing the electrocatalytic performance. Moreover, the flower-spherical structures synthesized at a high temperature of 600 °C show significant morphological advantages and excellent performance, which is mainly attributed to the following key factors: firstly, the high-temperature environment provides sufficient energy for the self-assembly process of the nanosheets, which promotes the orderly arrangement and directional growth of the nanosheets, resulting in the formation of a regular flower-spherical structure. This unique morphological feature not only endows the material with rich pore structure, but also significantly increases the specific surface area, providing more active sites for electrochemical reactions. Secondly, the high-temperature treatment helps to improve the crystallinity of the material and enhance its structural stability. In addition, the multilevel pore network of the flower-spherical structure facilitates the penetration of the electrolyte and the diffusion of the reaction products, further enhancing the electrochemical performance of the material. The synergistic effect of these structural advantages enabled the samples synthesized at 600 °C to exhibit significantly better catalytic activity in the electrochemical hydrogenolysis reaction (HER) than those prepared at other temperature conditions. The synthesis temperature of 600 °C induces three critical enhancements in material properties: (1) The hierarchical structure with abundant nanorod arrays creates substantial adsorption sites for reactive species (H_2O, H^+, OH^-, etc.), significantly improving interfacial contact efficiency while establishing a stable microstructural framework. This ordered architecture not only reinforces mechanical stability but also establishes favorable preconditions for catalytic processes. (2) Elevated crystallinity accompanied by reduced lattice defects facilitates efficient charge carrier migration through two mechanisms: the minimized crystal imperfections reduce the probability of electron scattering, while the intimate interrod contact within the spherical-flower morphology effectively diminishes interfacial charge-transfer resistance, thereby optimizing electrochemical reaction kinetics. (3) Thermally optimized elemental distribution enables electronic synergy between Ni and Mo components—the d-electron-enriched Ni sites preferentially adsorb and reduce H^+ species, while high-valent Mo centers promote O_2 evolution through oxidative pathways. This bimetal synergy, combined with their homogeneous dispersion in the spherical-flower matrix, generates maximized interfacial active sites that significantly boost hydrogen evolution reaction (HER) efficiency. Collectively, the structural advantages of the temperature of 600 °C, including enhanced specific surface area, optimized electronic configuration, and improved charge transfer capability, synergistically contribute to the superior electrocatalytic performance, positioning these materials as promising candidates for high-efficiency hydrogen evolution applications [42–45]. Elevating the reduction temperature beyond optimal levels induced two sequential morphological transitions: (1) At intermediate temperatures, the density of spherical particles increased with concomitant size polydispersity (inset in Figure 2e), while the lamellar architectures progressively evolved into smooth-surfaced spherical superstructures composed of subunit assemblies (inset in Figure 2f), which is attributed to thermally accelerated Ni-Mo alloying dynamics. (2) Upon reaching the critical threshold of 950 °C, complete structural reorganization occurred, marked by nanorod dissolution (inset in Figure 2g) and replacement of spherical morphologies with linear configurations featuring multi-nodal strand assemblies (inset in Figure 2h). This terminal transition confirms exhaustive alloying of the rod-like $NiMoO_4$ precursor and full oxygen reduction, which is consistent with the emergence of dominant NiMo intermetallic phases in XRD analysis (Figure 2d) [46]. In summary, SEM analyses showed that the specimens with lamellar flower ball structure exhibited better electrocatalytic properties at the reduction temperature of 600 °C.

To systematically investigate the surface elemental distribution of NiMo-600 °C/NF composites, energy-dispersive spectroscopy (EDS) mapping was conducted within a representative 5 μm microregion (Figure 3). The EDS spectra exhibit prominent characteristic peaks of Ni and Mo, confirming their dominance in the surface composition. Corresponding elemental mapping reveals spatially consistent distributions of both metallic components across the nickel foam (NF) substrate, demonstrating successful homogeneous loading of NiMo species onto the three-dimensional NF framework. This uniform dispersion is further evidenced by high-intensity superposition in the composite elemental mapping, indicative of a well-controlled synthesis process. Quantitative analysis of the atomic ratio highlights the predominant contribution of Ni and Mo, aligning with the designed stoichiometry of the NiMo alloy. The observed microstructural homogeneity not only validates the structural integrity of the NiMo/NF hybrid system but also suggests long-range ordering at the atomic level, a critical factor for stabilizing active sites during the electrocatalytic processes. These findings collectively establish a direct correlation between the synthesis-controlled elemental distribution and the enhanced functional performance of the composite material.

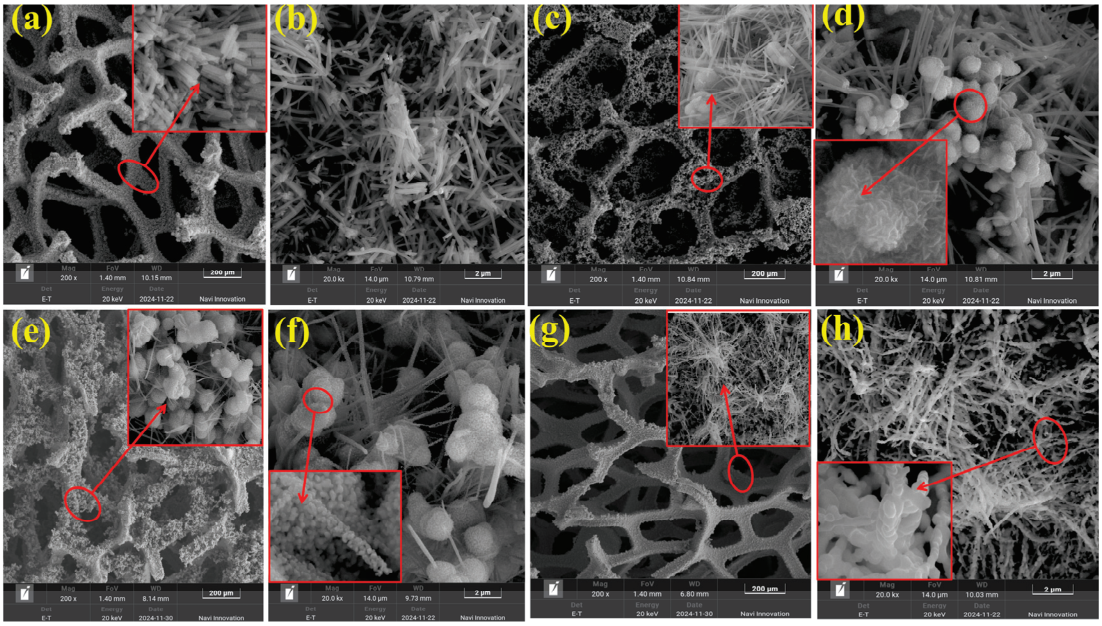

Figure 2. (**a**,**b**) SEM images of NiMo/NF at 400 °C; (**c**,**d**) SEM images of NiMo/NF at 600 °C; (**e**,**f**) SEM images of NiMo/NF at 800 °C; (**g**,**h**) SEM images of NiMo/NF at 950 °C.

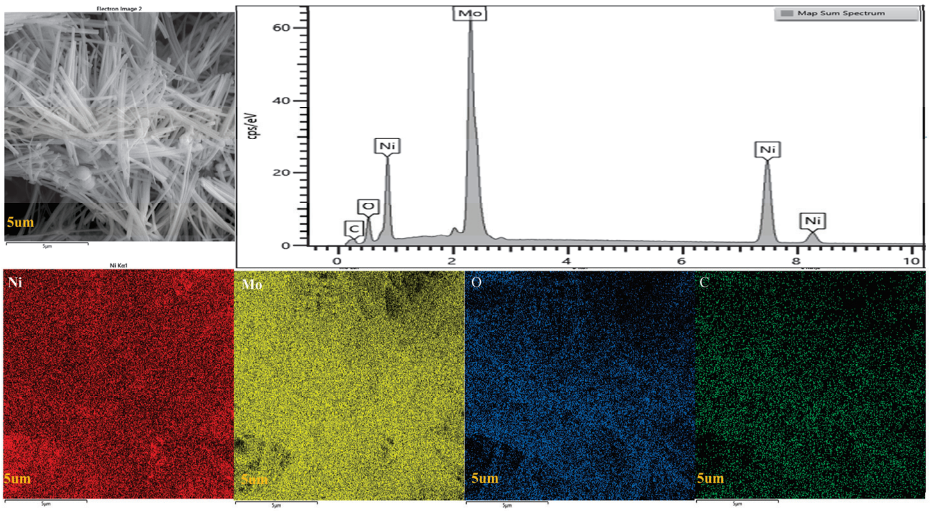

Figure 3. EDS scan of a NiMo-600 °C/NF sample.

Combining the application of scanning electron microscopy (SEM) and EDS analysis, the relationship between the microstructure and the electrocatalytic performance of NiMo/NF materials can be more clearly understood. The systematic analysis of the elemental distribution can reveal the catalytic mechanism of NiMo composites, which provides an important theoretical basis and practical guidance for their potential practical application in electrocatalytic reactions. Further studies can focus on optimizing the loading and distribution of NiMo to enhance its catalytic activity and stability and to promote the wide application of this material in the field of energy conversion and storage.

2.3. XPS Analysis

The valence states of the elements Ni and Mo in NiMo/NF and Ni/NF were analyzed by X-ray photoelectron spectroscopy (XPS). The full XPS spectra of NiMo/NF and Ni/NF (Figure 4a) show that the elemental compositions of NiMo/NF are Ni and Mo, whereas that of Ni/NF is Ni. The Ni 2p spectra of NiMo/NF are illustrated in Figure 4b. The peaks with binding energies of 870.2 eV and 852.6 eV are attributed to Ni^{2+}, while satellite peaks are also observed at 876.4 eV and 857.4 eV. The presence of Ni^{2+} is attributed to the formation of oxides on the surface of NiMo/NF after exposure to air, a phenomenon that has been reported in previous studies. Ni^{2+} is able to accelerate the electron transfer to water molecules and promote the decomposition of water molecules, thus enhancing the HER performance. In addition, the peaks at 859.5 eV and 849 eV correspond to Ni^0, indicating that $NiMoO_4$ was successfully reduced during the annealing process. For the Ni 2p spectrum of Ni/NF (Figure 4b), the two main peaks with binding energies of 869.4 eV and 851.9 eV are likewise attributed to Ni^{2+}, which is related to the formation of oxides from Ni/NF in air. Figure 4c presents the results of Mo 3d X-ray photoelectron spectroscopy (XPS) analysis conducted on NiMo/NF. The characteristic peaks observed at binding energies of 232.6 eV and 230 eV align with the metallic state of Mo^0 (zero-valent molybdenum), providing further evidence that the $NiMoO_4$ precursor was successfully reduced to a NiMo alloy during the annealing process. Additionally, four distinct peaks corresponding to Mo^{4+} (231.7 eV and 225.5 eV) and Mo^{6+} (228.8 eV and 224.5 eV) were identified in the spectra. The presence of these higher valence molybdenum species (Mo^{4+} and Mo^{6+}) can be attributed to the formation of oxide layers on the surfaces of nickel–molybdenum alloys upon exposure to air. Importantly, the electron redistribution between nickel and molybdenum significantly optimizes the electronic structure of the material, which in turn enhances its catalytic activity. Specifically, the synergistic effect of Ni and Mo in NiMo alloys not only stabilizes reaction intermediates (such as H*, O*, etc.) but also promotes catalytic reaction kinetics by lowering the energy barriers associated with the reactions. In summary, the NiMo alloy produced through the annealing reduction method exhibits an optimized valence distribution and electronic structure, effectively enhancing catalytic reactions. This provides a crucial structural basis for its application in electrochemical hydrogenation reactions (HERs) and other fields [47,48].

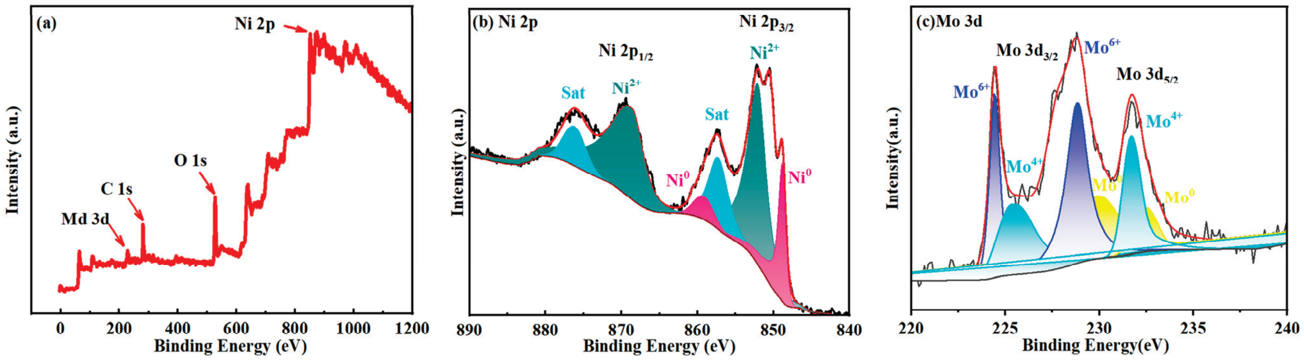

Figure 4. XPS spectra of NiMo-600 °C/NF sample: (**a**) full spectrum, (**b**) Ni 2p; (**c**) Mo 3d.

2.4. Electrochemical Performance Analysis

By comparative analysis of the polarization curves of NiMo alloy catalysts prepared at different calcined reduction temperatures (Figure 5, with a scan rate of 5 mV/s), it can be clearly observed that the curves in Figure 5a indicate that the activity of the catalysts calcined and reduced at 600 °C is significantly better than that of the samples under other temperature conditions. Specifically, the 600 °C-treated Ni-Mo alloy catalyst exhibited excellent hydrogen evolution reaction (HER) performance with an overpotential η_{100} only 127 mV [49–52], which was significantly lower than that of the catalysts prepared under the other temperature conditions, suggesting that 600 °C is the optimal temperature for the preparation of high-performance Ni-Mo alloy catalysts. Figure 5b demonstrates the Tafel slope data of catalysts at different calcined reduction temperatures. Among them, the lowest Tafel slope was observed for NiMo 600 °C, followed by NiMo 800 °C, NiMo 950 °C and NiMo 400 °C in that order. This trend clearly indicates that 600 °C is the optimum temperature for the calcined reduction of the catalyst. At this temperature, the Tafel slope of the NiMo catalyst was 124 mV dec^{-1} [53,54]. The diminished Tafel slope demonstrates accelerated hydrogen evolution reaction (HER) kinetics through reduced activation energy barriers, manifesting as lower overpotential requirements at equivalent current densities that synergistically enhance interfacial charge transfer efficiency and current density escalation rates, thereby conclusively validating the superior electrochemical performance of 600 °C-synthesized NiMo/NF catalysts in facilitating energy-efficient hydrogen production. Through this optimized calcined–reduction protocol, the critical structure–activity correlation was established, providing mechanistic insights into Ni-Mo synergism while offering practical design principles for developing scalable electrocatalysts toward industrial hydrogen generation systems.

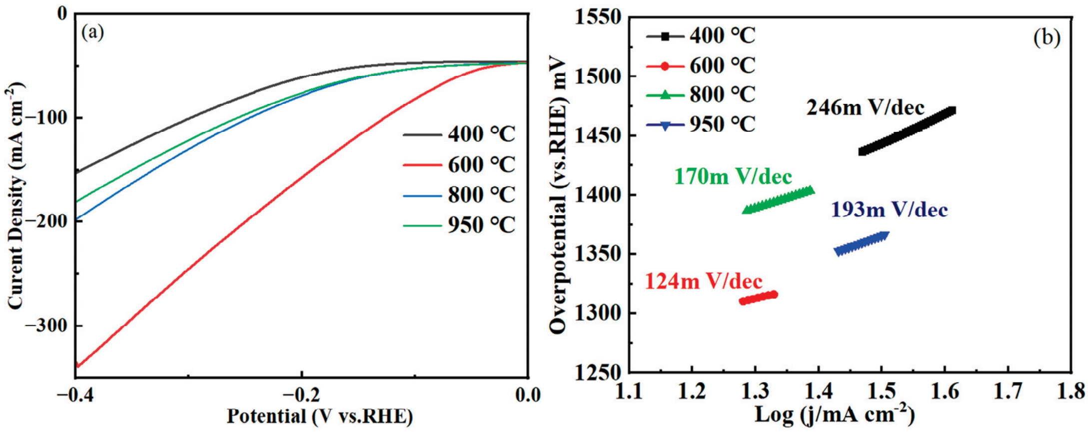

Figure 5. (**a**) Polarization curves of nickel–molybdenum alloy catalysts at different reduction temperatures; (**b**) Tafel plot.

In order to investigate the effect of different calcination temperatures on the catalytic hydrogen precipitation performance of Ni-Mo alloys, in this study, cyclic voltammetry (CV) was used to perform multi-scan rate tests (20–100 mV/s) in the non-Faraday region (−0.8 ~ −0.7 V vs. RHE), and the electrochemically active surface area (ECSA) of the catalysts was evaluated by calculating the electrochemical double layer capacitance (C_{dl}). According to the equation $C_{dl} = 1/2$ Slope, the C_{dl} value was calculated using the slope of the CV curve. Figure 6a–d demonstrate the CV curves of NiMo alloy at 400 °C, 600 °C, 800 °C and 950 °C calcination temperatures, which shows that the oxidation peaks and reduction peaks are symmetrically distributed, and the peak heights are consistent with the peak spacing, which indicates that the redox reaction is easily reversible. Further analysis showed that the NiMo alloy catalyst reduced by calcination at 600 °C exhibited the highest ECSA (121.3 mF/cm^{-2}, Figure 6e), which was significantly better than the samples at other temperature conditions [55]. This is due to the fact that in NiMo alloys, the electron density distributions of Ni and Mo are realigned. The difference between the higher electron density of Ni and the lower electron density of Mo promotes the transfer of electrons from Ni to Mo. This causes the 3d electron orbitals of Ni to interact with the 4d electron orbitals of Mo, resulting in a redistribution of the electron density. The addition of Ni modulates the electron density of Mo and lowers the d-band center of Mo, thus optimizing the hydrogen adsorption free energy (ΔGH). Moreover, in NiMo alloys, there is a charge transfer phenomenon between Ni and Mo. Ni tends to provide electrons while Mo tends to accept electrons, and this charge transfer enhances the catalytic activity of the alloys. The electron density of Ni decreases and the electron density of Mo increases due to its electron transfer. This redistribution of electron density modulates the local electronic environment at the catalytically active sites. For the HER, the electron density of the catalytic active site needs to be moderate: too high an electron density may lead to too strong adsorption of hydrogen, making it difficult to desorb, while too low an electron density may lead to too weak adsorption of hydrogen, making it difficult to form the reaction intermediate. The electron transfer of Ni and Mo brings the electron density to an equilibrium state, thus optimizing the HER. This resulted in a significant increase in the density of active sites on the surface of the catalyst after treatment at 600 °C, and its multi-interfacial structure provided abundant catalytically active sites for the hydrogen evolution reaction (HER), and consequently enhanced the catalytic performance substantially. The electrochemical impedance spectroscopy (EIS) test results (Figure 6f) showed that the nickel–molybdenum alloy (NiMo) catalyst treated at 600 °C exhibited the smallest charge transfer resistance (R_{ct}) [56,57]. In the Nyquist plot, the arc radius of the EIS spectral line is directly correlated with R_{ct}, while the NiMo catalyst treated at 600 °C has the smallest arc radius of the EIS spectral line, indicating that its R_{ct} value is significantly lower than that of the samples treated at other temperatures. This result confirms that the catalyst treated at 600 °C has the least charge transfer resistance at the electrochemical interface and a more efficient electron transfer path. This excellent charge transfer property is mainly attributed to the following mechanisms: firstly, during the 600 °C treatment, the electron density of the 3d orbitals of Ni decreases while the number of holes increases. This change in electronic structure makes it easier for the Ni sites to adsorb H^+ (protons), thus facilitating the Volmer step ($H^+ + e^- \rightarrow H^*$) of the reduction of H^+ to H^* (adsorbed hydrogen atoms). Secondly, NiMo alloys form a more homogeneous crystal structure and tighter metal–metal bonding under high-temperature treatment, which significantly reduces the electron transport resistance within the material. In addition, the surface defects (e.g., oxygen vacancies) induced by the high-temperature treatment can act as 'highways' for electron transport, further accelerating the charge transfer process. At the same time, Mo sites are more prone to promote H desorption and H_2; formation due to the increase in electron density and 4d-orbital electron density, thus optimizing the Tafel step ($2H \rightarrow H_2$) or Heyrovsky step ($H^* + H^+ + e^- \rightarrow H_2$) [58,59]. Therefore, the NiMo catalysts treated at 600 °C significantly enhanced the kinetic performance of the key steps of the HER (hydrogen adsorption and hydrogen desorption) by synergistically optimizing the electronic structures and surface defects of the Ni and Mo sites, providing an important theoretical basis for the design of high-efficiency non-precious metal catalysts. Since Ni has a stronger adsorption capacity for hydrogen but a weaker desorption capacity for Mo, the synergistic effect of Ni and Mo can regulate the free energy of hydrogen adsorption (ΔGH^*) to be close to the thermodynamic optimum ($\Delta GH^* \approx 0$), thus improving the reaction efficiency. The synergistic effect of nickel and molybdenum also improves the stability of the reaction intermediate (H), which further accelerates the reaction and provides efficient kinetic support for HER. During the long-term stability test, the NiMo catalyst treated at 600 °C demonstrated remarkable stability. As illustrated in Figure 6g, after 45 h of continuous operation using the constant current method at a high current density of 100 mA/cm^2, the performance parameters showed no significant decline. This indicates that the structure of the active sites remained stable and no deactivation occurred [60]. These findings robustly confirm that the Ni-Mo alloy catalyst produced through calcination at 600 °C exhibits a combination of high activity, excellent stability, and efficient charge transfer capabilities. As such, it represents an ideal catalytic material for hydrogen evolution reactions (HERs) and serves as a crucial reference for advancing aquatic energy technologies.

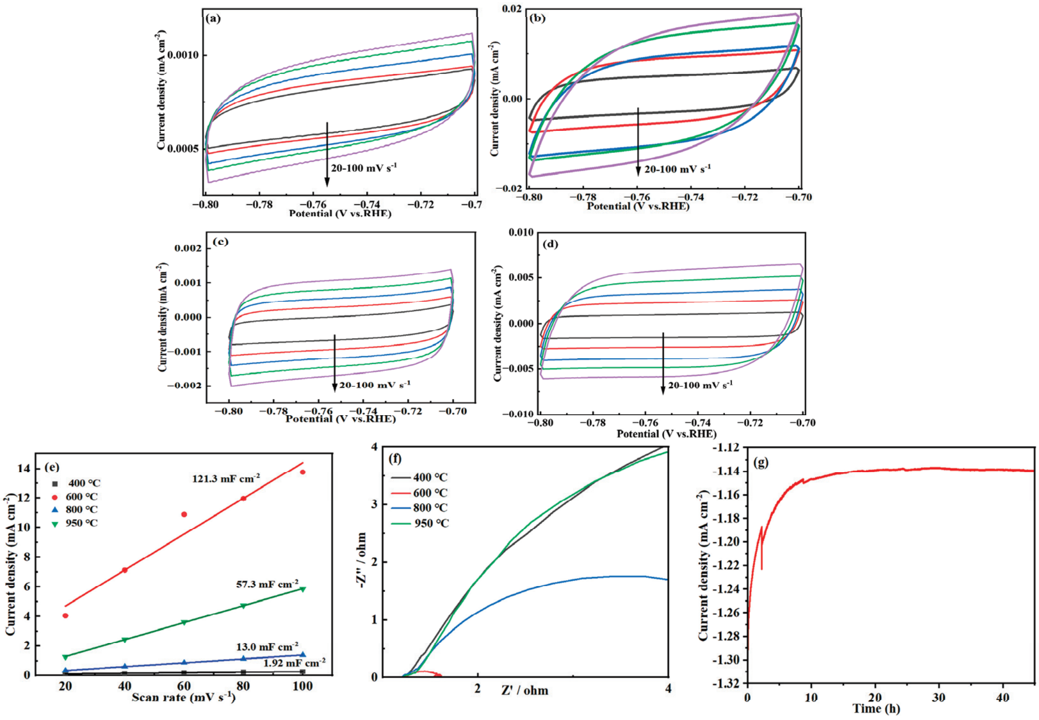

Figure 6. Cyclic voltammograms of nickel–molybdenum alloys in a 1.0 M NaOH solution at different scan rates in the non-Faradaic region under different calcination–reduction temperatures: (**a**) 400 °C, (**b**) 600 °C, (**c**) 800 °C, and (**d**) 950 °C. The scan range is from −0.8 V to −0.7 V vs. RHE, where the scan rates range from 20 mV/s to 100 mV/s, and the temperature is 25 °C. (**e**) The curve of the electrochemically active surface area of nickel–molybdenum alloy catalysts under different calcination–reduction temperatures. (**f**) Electrochemical impedance spectra of nickel–molybdenum alloy catalysts under different calcination–reduction temperatures. (**g**) Stability diagram of the nickel–molybdenum alloy catalyst at 600 °C measured by chronopotentiometry (CP).

3. Materials and Methods

In this study, NiMo/NF materials were successfully synthesized using nickel foam (NF) as a substrate by weighing 0.475 g of nickel chloride ($NiCl_2$) and 0.484 g of sodium molybdate (Na_2MoO_4) using the hydrothermal method and gas phase reduction method. Its preparation process and micro-morphology were analyzed by SEM characterization (shown in Figure 7). Figure 7a demonstrates the porous network structure of NF with a smooth skeleton surface, which provides an ideal support platform for the subsequent growth of nanomaterials. The $NiMoO_4$/NF precursor was synthesized by the hydrothermal method according to the chemical reaction equation $Na_2MoO_4 + NiCl_2 \rightarrow NiMoO_4 + 2NaCl$ (Figure 7b). The SEM image (Figure 7c) shows that the NF backbone is uniformly grown with a large number of $NiMoO_4$ nanorods, indicating that the hydrothermal method has significant advantages in controlling the morphology of nanostructures. Subsequently, four NiMo/NF materials at different temperatures were prepared by gas-phase reduction reaction at 400 °C, 600 °C, 800 °C and 950 °C, according to the reaction equation $NiMoO_4 + 4H_2 \rightarrow NiMo + 4H_2O$, respectively. (Chemicals were purchased from McLean's Reagent and NF was purchased from China Xing Zhenghong Technology Enterprise Store).

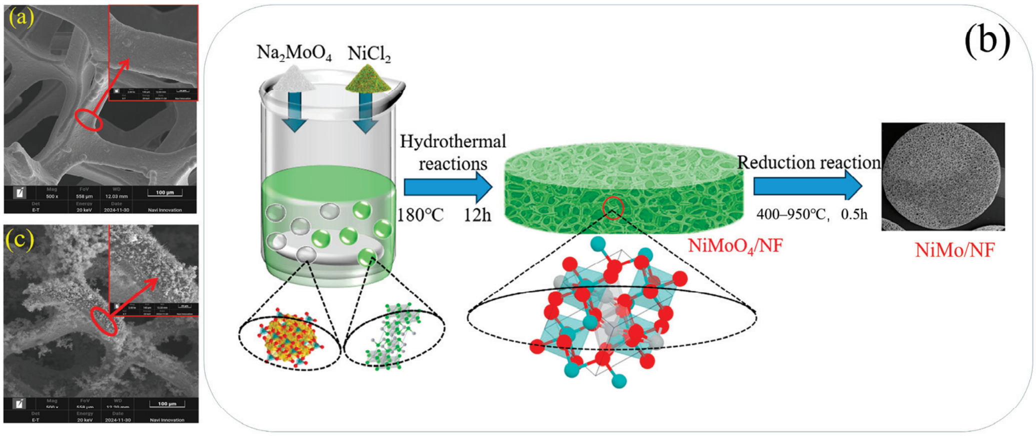

Figure 7. Preparation process and SEM images of NiMo/NF: (**a**) SEM image of NF; (**b**) process flow chart for the preparation of NiMo/NF; (**c**) SEM image of $NiMoO_4$/NF.

Nickel foam was selected as an ideal substrate due to its excellent electrical conductivity and high specific surface area. Nickel chloride and sodium molybdate served as metal precursors, offering the potential for high catalytic efficiency. Uniformly distributed $NiMoO_4$ nanorods were synthesized under mild conditions via a hydrothermal method, followed by gas-phase reduction at various temperatures to form metallic NiMo. This combined approach ensures both the controllability and reproducibility of the synthesis process, providing a practical and scalable strategy for fabricating NiMo/NF materials with promising catalytic applications.

For the electrochemical test, a three-electrode system was tested using an electrochemical workstation (Model CHI-760E Shanghai Chenhua Instrument Co., Ltd. is from Shanghai, China.). The three-electrode system consists of four catalyst samples (working electrode), a platinum sheet (counter electrode), and a Hg/HgO electrode (reference electrode). As for the washing of nickel foam, the cut nickel foam (1 cm × 1 cm) was washed thoroughly with acetone, 3 mol/L hydrochloric acid, anhydrous ethanol, and deionized water. The electrolyte solution is usually 1 mol/L NaOH. Test conditions were as follows: the electrocatalytic hydrogen polarization curve (scan speed of 5 mV/s) and impedance were tested using 1 mol/L NaOH electrolytes, and the electrode stability was tested using the constant current method.

4. Conclusions

In this study, $NiMoO_4$ nanofiber precursors were successfully synthesized on nickel foam (NF) via a hydrothermal method, followed by gas-phase reduction to obtain NiMo alloys. This controllable and straightforward synthesis significantly enhances the electrochemical performance of the resulting electrodes. The synergistic interaction between Ni and Mo, combined with the 3D porous nanostructure, increases the electrochemically active surface area (ECSA) and active site density, thereby improving HER kinetics. The porous structure also enlarges the contact area, reducing contact resistance and ensuring uniform current distribution, which minimizes localized heating and enhances overall conductivity. In alkaline media, the NiMo/NF electrode exhibits outstanding HER performance, achieving 100 mA cm^{-2} at an overpotential of 127 mV and a high double-layer capacitance of 121.3 mF cm^{-2}. Stability testing over 45 h at high current density confirmed excellent durability without noticeable degradation. These results underscore the benefits of combining the favorable electrochemical properties of NiMo alloys with the high surface area and conductivity of nickel foam, offering a promising strategy for the development of efficient, durable HER catalysts in clean energy applications.

Author Contributions: Conceptualization, Y.D. and Y.C.; methodology, Y.C.; software, Z.G.; validation, H.D.; formal analysis, Y.C.; investigation, H.X.; resources, Y.Z.; data curation, B.L.; writing—original draft preparation, Y.C.; writing—review and editing, Y.D. and Y.Z.; visualization, H.D.; supervision, F.L.; project administration, Y.D.; funding acquisition, Y.D. All authors have read and agreed to the published version of the manuscript.

Funding: This work is financially supported by Hunan Provincial Natural Science Foundation of China (2022JJ50068).

Institutional Review Board Statement: Not applicable.

Informed Consent Statement: Not applicable.

Data Availability Statement: Data are contained within the article.

Conflicts of Interest: The authors declare no conflicts of interest.

References

1. Sebbahi, S.; Assila, A.; Alaoui Belghiti, A.; Laasri, S.; Kaya, S.; Hlil, E.K.; Rachidi, S.; Hajjaji, A. A comprehensive review of recent advances in alkaline water electrolysis for hydrogen production. *Int. J. Hydrogen Energy* **2024**, *82*, 583–599. [CrossRef]
2. Shaya, N.; Glöser-Chahoud, S.J.E. A Review of Life Cycle Assessment (LCA) Studies for Hydrogen Production Technologies through Water Electrolysis: Recent Advances. *Energies* **2024**, *17*, 3968. [CrossRef]
3. Dash, S.; Singh, A.; Jose, S.; Elangovan, D.; Surapraraju, S.K.; Natarajan, S.K. Advances in green hydrogen production through alkaline water electrolysis: A comprehensive review. *Int. J. Hydrogen Energy* **2024**, *83*, 614–629. [CrossRef]
4. Zhu, Y.; Zhao, R.; Xu, Y.; Chen, W.; Hu, Z.; Xi, L.; Xie, Y.; Hou, H.; Liu, T.; Amine, K.; et al. Anion vacancies coupling with heterostructures enable advanced aerogel cathode for ultrafast aqueous zinc-ion storage. *Adv. Mater.* **2025**, *37*, 2419582. [CrossRef]
5. Sun, H.; Xu, X.; Kim, H.; Shao, Z.; Jung, W. Advanced electrocatalysts with unusual active sites for electrochemical water splitting. *InfoMat* **2024**, *6*, e12494. [CrossRef]
6. Zhong, W.; Zhao, R.; Zhu, Y.; Xu, Y.; Chen, W.; Peng, C. Vacancy engineering on MnSe cathode enables high-rate and stable zinc-ion storage. *Adv. Funct. Mater.* **2025**, *35*, 2419720. [CrossRef]
7. Tüysüz, H. Alkaline Water Electrolysis for Green Hydrogen Production. *Acc. Chem. Res.* **2024**, *57*, 558–567. [CrossRef]
8. Shiva Kumar, S.; Lim, H. An overview of water electrolysis technologies for green hydrogen production. *Energy Rep.* **2022**, *8*, 13793–13813. [CrossRef]
9. Yang, Y.; Wang, G.; Lin, L.; Zhang, S. Analysis of Hydrogen Production Potential Based on Resources Situation in China. *E3S Web Conf.* **2019**, *118*, 03021. [CrossRef]
10. Ham, K.; Bae, S.; Lee, J. Classification and technical target of water electrolysis for hydrogen production. *J. Energy Chem.* **2024**, *95*, 554–576. [CrossRef]
11. Guo, Y.; Li, G.; Zhou, J.; Liu, Y. Comparison between hydrogen production by alkaline water electrolysis and hydrogen production by PEM electrolysis. *IOP Conf. Ser. Earth Environ. Sci.* **2019**, *371*, 042022. [CrossRef]
12. Zeng, K.; Zhang, D. Recent progress in alkaline water electrolysis for hydrogen production and applications. *Prog. Energy Combust. Sci.* **2010**, *36*, 307–326. [CrossRef]
13. Hui, Y.; Wang, M.; Guo, S.; Akhtar, S.; Bhattacharya, S.; Dai, B.; Yu, J. Comprehensive review of development and applications of hydrogen energy technologies in China for carbon neutrality: Technology advances and challenges. *Energy Convers. Manag.* **2024**, *315*, 118776. [CrossRef]
14. Yu, J.; Le, T.A.; Tran, N.Q.; Lee, H. Frontispiece: Earth-Abundant Transition-Metal-Based Bifunctional Electrocatalysts for Overall Water Splitting in Alkaline Media. *Chem. A Eur. J.* **2020**, *26*, 6423–6436. [CrossRef]
15. Kempler, P.A.; Coridan, R.H.; Luo, L. Gas Evolution in Water Electrolysis. *Chem. Rev.* **2024**, *124*, 10964–11007. [CrossRef]
16. Lei, Q.; Wang, B.; Wang, P.; Liu, S. Hydrogen generation with acid/alkaline amphoteric water electrolysis. *J. Energy Chem.* **2019**, *38*, 162–169. [CrossRef]
17. Bayro-Kaiser, V.; Nelson, N. Microalgal hydrogen production: Prospects of an essential technology for a clean and sustainable energy economy. *Photosynth. Res.* **2017**, *133*, 49–62. [CrossRef]
18. Ju, H.; Badwal, S.; Giddey, S. A comprehensive review of carbon and hydrocarbon assisted water electrolysis for hydrogen production. *Appl. Energy* **2018**, *231*, 502–533. [CrossRef]
19. Chi, J.; Yu, H. Water electrolysis based on renewable energy for hydrogen production. *Chin. J. Catal.* **2018**, *39*, 390–394. [CrossRef]
20. Miller, E.L.; Randolph, K.; Peterson, D.; Rustagi, N.; Vickers, J.W.; Lyubovsky, M.; Cierpik-Gold, K.; Byham, S. (Invited) Addressing Fundamental Materials Challenges in Electrochemical Water Splitting Technologies for Sustainable Hydrogen Production. *ECS Meet. Abstr.* **2018**, *MA2018-02*, 1595. [CrossRef]

21. Bonifacio, R.M.; Mena, M.G. Activity of electrodeposited rhodium in acidic and basic water electrolysis. *Int. J. Hydrogen Energy* **2024**, *52*, 364–377. [CrossRef]
22. Ahn, S.H.; Choi, I.; Park, H.-Y.; Hwang, S.J.; Yoo, S.J.; Cho, E.; Kim, H.-J.; Henkensmeier, D.; Nam, S.W.; Kim, S.-K.; et al. Effect of morphology of electrodeposited Ni catalysts on the behavior of bubbles generated during the oxygen evolution reaction in alkaline water electrolysis. *Chem. Commun.* **2013**, *49*, 9323–9325. [CrossRef]
23. Hu, B.; Xu, L.; Li, Y.; Sun, F.; Wang, Z.; Yang, M.; Zhang, Y.; Kong, W.; Shen, B.; Wang, X.; et al. Biochar and Fe^{2+} mediation in hydrogen production by water electrolysis: Effects of physicochemical properties of biochars. *Energy* **2024**, *297*, 131275. [CrossRef]
24. Yadav, V.; Dileep, N.P.; Nair, N.; Kumar Behura, P.; Shaijumon, M.M. Hydrogen production via alkaline seawater electrolysis using iron-doped nickel diselenide as an efficient bifunctional electrocatalyst. *Mater. Today Chem.* **2024**, *40*, 102276. [CrossRef]
25. Wu, W.; Wu, X.-Y.; Wang, S.-S.; Lu, C.-Z. Highly efficient hydrogen evolution from water electrolysis using nanocrystalline transition metal phosphide catalysts. *RSC Adv.* **2018**, *8*, 39291–39295. [CrossRef]
26. Pein, M.; Neumann, N.C.; Venstrom, L.J.; Vieten, J.; Roeb, M.; Sattler, C. Two-step thermochemical electrolysis: An approach for green hydrogen production. *Int. J. Hydrogen Energy* **2021**, *46*, 24909–24918. [CrossRef]
27. Shah, A.M.; Modi, K.H.; Pataniya, P.M.; Joseph, K.S.; Dabhi, S.; Bhadu, G.R.; Sumesh, C.K. Self-Supported Mn-Ni_3Se_2 Electrocatalysts for Water and Urea Electrolysis for Energy-Saving Hydrogen Production. *ACS Appl. Mater. Interfaces* **2024**, *16*, 11440–11452. [CrossRef]
28. Wang, N.; Otor, H.O.; Rivera-Castro, G.; Hicks, J.C. Plasma Catalysis for Hydrogen Production: A Bright Future for Decarbonization. *ACS Catal.* **2024**, *14*, 6749–6798. [CrossRef] [PubMed]
29. Di Franco, F.; Zaffora, A.; Pupillo, D.; Seminara, B.; Pärnamäe, R.; Tedesco, M.; Santamaria, M. Optimized base metals electrodeposition on Ni perforated plate type electrodes for high-performance alkaline water electrolysis. *Int. J. Hydrogen Energy* **2024**, *70*, 548–556. [CrossRef]
30. Yao, H.; Wang, S.; Cao, Y.; Chen, R.; Lu, Z.; Hu, J.; Xie, J.; Hao, A. High-performance bifunctional electrocatalysts of CoFe-LDH/$NiCo_2O_4$ heterostructure supported on nickel foam for effective overall water splitting. *J. Alloys Compd.* **2022**, *926*, 166846. [CrossRef]
31. Deng, B.; Zhou, L.; Jiang, Z.; Jiang, Z.-J. High catalytic performance of nickel foam supported Co_2P-Ni_2P for overall water splitting and its structural evolutions during hydrogen/oxygen evolution reactions in alkaline solutions. *J. Catal.* **2019**, *373*, 81–92. [CrossRef]
32. Chen, M.-T.; Duan, J.-J.; Feng, J.-J.; Mei, L.-P.; Jiao, Y.; Zhang, L.; Wang, A.-J. Iron, rhodium-codoped Ni_2P nanosheets arrays supported on nickel foam as an efficient bifunctional electrocatalyst for overall water splitting. *J. Colloid Interface Sci.* **2022**, *605*, 888–896. [CrossRef] [PubMed]
33. Zhou, Y.; Lin, T.; Luo, X.; Yan, Z.; Wu, J.; Wang, J.; Shen, Y. Mechanistic study on nickel-molybdenum based electrocatalysts for the hydrogen evolution reaction. *J. Catal.* **2020**, *388*, 122–129. [CrossRef]
34. Sivanantham, A.; Shanmugam, S. Nickel selenide supported on nickel foam as an efficient and durable non-precious electrocatalyst for the alkaline water electrolysis. *Appl. Catal. B Environ.* **2017**, *203*, 485–493. [CrossRef]
35. Deng, B.L.; Guo, L.P.; Lu, Y.; Rong, H.B.; Chen, D.C. Sulfur–nitrogen co-doped graphene supported cobalt–nickel sulfide rGO@SN-$CoNi_2S_4$ as highly efficient bifunctional catalysts for hydrogen/oxygen evolution reactions. *Rare Met.* **2022**, *41*, 911–920. [CrossRef]
36. Zhao, X.; Che, M.; Gong, Y. Synthesis and performance study of Fe_2WO_6@Ni_3S_2-WS_2/NF for efficient electrolytic water to hydrogen. *Sustain. Mater. Technol.* **2025**, *43*, e01302. [CrossRef]
37. Nady, H.; El-Rabiei, M.M.; Samy, M.; Deyab, M.A.; Abd El-Hafez, G.M. Novel Ni–Cr-based alloys as hydrogen fuel sources through alkaline water electrolytes. *Int. J. Hydrogen Energy* **2021**, *46*, 34749–34766. [CrossRef]
38. Ren, T.; Chen, Q.; Tang, C.; Chen, J.; Huang, X.; Feng, G.; Xie, H.; Bao, F.; Guo, W. Facile electrodeposition of Iron-doped NiMo alloys as bifunctional electrocatalysts for alkaline overall water splitting. *Fuel* **2025**, *381*, 133302. [CrossRef]
39. Wang, Y.; He, F.; Ren, Y.; Lin, Y.; Zhong, M.; Su, B.; Lei, Z. Straightforward preparation of nickel selenide nanosheets supported on nickel foam as a highly efficient electrocatalyst for oxygen evolution reaction. *Int. J. Hydrogen Energy* **2022**, *47*, 25631–25637. [CrossRef]
40. Xiao, R.; Wang, F.; Luo, L.; Yao, X.; Huang, Y.; Wang, Z.; Balogun, M.S. Efficient Self-Powered Overall Water Splitting by Ni_4Mo/MoO_2 Heterogeneous Nanorods Trifunctional Electrocatalysts. *Small Methods* **2023**, *7*, 2201659. [CrossRef]
41. Calle-Vallejo, F.; Martínez, J.I.; García-Lastra, J.M.; Abad, E.; Koper, M.T.M. Oxygen reduction and evolution at single-metal active sites: Comparison between functionalized graphitic materials and protoporphyrins. *Surf. Sci.* **2013**, *607*, 47–53. [CrossRef]
42. Gao, Z.-W.; Liu, J.-Y.; Chen, X.-M.; Zheng, X.-L.; Mao, J.; Liu, H.; Ma, T.; Li, L.; Wang, W.-C.; Du, X.-W. Engineering NiO/NiFe LDH Intersection to Bypass Scaling Relationship for Oxygen Evolution Reaction via Dynamic Tridimensional Adsorption of Intermediates. *Adv. Mater.* **2019**, *31*, 1804769. [CrossRef]
43. Wang, Y.; Wang, Y.; Bai, J.; Lau, W.-M. Efficient Self-Supported Bifunctional NiMo Alloy Electrocatalysts for Water Splitting in Alkaline Environment. *ChemistrySelect* **2022**, *7*, e202200468. [CrossRef]

44. Du, W.; Shi, Y.; Zhou, W.; Yu, Y.; Zhang, B. Unveiling the In Situ Dissolution and Polymerization of Mo in Ni_4Mo Alloy for Promoting the Hydrogen Evolution Reaction. *Angew. Chem. Int. Ed.* **2021**, *60*, 7051–7055. [CrossRef]
45. Sun, S.; Diao, P.; Feng, C.; Ungureanu, E.-M.; Tang, Y.; Hu, B.; Hu, Q. Nickel-foam-supported β-$Ni(OH)_2$ as a green anodic catalyst for energy efficient electrooxidative degradation of azo-dye wastewater. *RSC Adv.* **2018**, *8*, 19776–19785. [CrossRef]
46. Chen, N.; Mo, Q.; He, L.; Huang, X.; Yang, L.; Zeng, J.; Gao, Q. Heterostructured MoC-MoP/N-doped carbon nanofibers as efficient electrocatalysts for hydrogen evolution reaction. *Electrochim. Acta* **2019**, *299*, 708–716. [CrossRef]
47. Tang, J.; Guan, D.; Xu, H.; Zhao, L.; Arshad, U.; Fang, Z.; Zhu, T.; Kim, M.; Pao, C.-W.; Hu, Z.; et al. Undoped ruthenium oxide as a stable catalyst for the acidic oxygen evolution reaction. *Nat. Commun.* **2025**, *16*, 801. [CrossRef] [PubMed]
48. Xu, X.; Pan, Y.; Zhong, Y.; Ge, L.; Jiang, S.P.; Shao, Z. From scheelite $BaMoO_4$ to perovskite $BaMoO_3$: Enhanced electrocatalysis toward the hydrogen evolution in alkaline media. *Compos. Part B Eng.* **2020**, *198*, 108214. [CrossRef]
49. McKone, J.R.; Sadtler, B.F.; Werlang, C.A.; Lewis, N.S.; Gray, H.B. Ni–Mo Nanopowders for Efficient Electrochemical Hydrogen Evolution. *ACS Catal.* **2013**, *3*, 166–169. [CrossRef]
50. Zhang, Y.; Ouyang, B.; Xu, K.; Xia, X.; Zhang, Z.; Rawat, R.S.; Fan, H.J. Prereduction of Metal Oxides via Carbon Plasma Treatment for Efficient and Stable Electrocatalytic Hydrogen Evolution. *Small* **2018**, *14*, 1800340. [CrossRef]
51. Fang, M.; Gao, W.; Dong, G.; Xia, Z.; Yip, S.; Qin, Y.; Qu, Y.; Ho, J.C. Hierarchical NiMo-based 3D electrocatalysts for highly-efficient hydrogen evolution in alkaline conditions. *Nano Energy* **2016**, *27*, 247–254. [CrossRef]
52. He, Y.; Zhang, M.; Shi, J.-J.; Cen, Y.-L.; Wu, M. Improvement of Visible-Light Photocatalytic Efficiency in a Novel InSe/Zr_2CO_2 Heterostructure for Overall Water Splitting. *J. Phys. Chem. C* **2019**, *123*, 12781–12790. [CrossRef]
53. Chen, G.-F.; Ma, T.Y.; Liu, Z.-Q.; Li, N.; Su, Y.-Z.; Davey, K.; Qiao, S.-Z. Efficient and Stable Bifunctional Electrocatalysts Ni/NiM (M = P, S) for Overall Water Splitting. *Adv. Funct. Mater.* **2016**, *26*, 3314–3323. [CrossRef]
54. Xing, Z.; Liu, Q.; Asiri, A.M.; Sun, X. Closely Interconnected Network of Molybdenum Phosphide Nanoparticles: A Highly Efficient Electrocatalyst for Generating Hydrogen from Water. *Adv. Mater.* **2014**, *26*, 5702–5707. [CrossRef] [PubMed]
55. Allam, M.; Benaicha, M.; Dakhouche, A. Electrodeposition and characterization of NiMoW alloy as electrode material for hydrogen evolution in alkaline water electrolysis. *Int. J. Hydrogen Energy* **2018**, *43*, 3394–3405. [CrossRef]
56. Dharmaraj, K.; Hanna, R.; Lauermann, I.; Bagacki, R.; Xi, F.; Kemppainen, E.; Schlatmann, R.; Calnan, S. Electrodeposited Porous Nickel–Copper as a Non-Noble Metal Catalyst for Urea-Assisted Anion Exchange Membrane Electrolysis for Hydrogen Production. *ACS Sustain. Chem. Eng.* **2024**, *12*, 9908–9921. [CrossRef]
57. Zhao, Y.; Tian, C.; Chen, H.; Zhai, Y.; Li, X.; Li, J.; Zhang, R.; Mao, Y.; Shan, T.; Zheng, K.; et al. Carbon-supported nickel–molybdenum alloy/tungsten carbide nanoparticles as efficient bifunctional catalysts for hydrogen evolution and oxidation reactions in alkaline media. *Int. J. Hydrogen Energy* **2025**, *114*, 229–238. [CrossRef]
58. Guo, C.; Jiao, Y.; Zheng, Y.; Luo, J.; Davey, K.; Qiao, S.-Z. Intermediate Modulation on Noble Metal Hybridized to 2D Metal-Organic Framework for Accelerated Water Electrocatalysis. *Chem* **2019**, *5*, 2429–2441. [CrossRef]
59. Liang, Z.; Ahn, H.; Bard, A. A Study of the Mechanism of the Hydrogen Evolution Reaction on Nickel by Surface Interrogation Scanning Electrochemical Microscopy. *J. Am. Chem. Soc.* **2017**, *139*, 4854–4858. [CrossRef]
60. Jiang, L.; Pan, Y.; Zhang, J.; Chen, X.; Ye, X.; Li, Z.; Li, C.; Sun, Q. Mo propellant boosting the activity of Ni-P for efficient urea-assisted water electrolysis of hydrogen evolution. *J. Colloid Interface Sci.* **2022**, *622*, 192–201. [CrossRef]

Disclaimer/Publisher's Note: The statements, opinions and data contained in all publications are solely those of the individual author(s) and contributor(s) and not of MDPI and/or the editor(s). MDPI and/or the editor(s) disclaim responsibility for any injury to people or property resulting from any ideas, methods, instructions or products referred to in the content.

molecules

Article

Supercooling Behavior of 2-Amino-2-methyl-1,3-propanediol for Thermal Energy Storage

Xuelian Wang [1], Jin Bai [2,*], Xian Zhang [1,*], Xiaobo Shen [1], Zhengrong Xia [1] and Haijun Yu [1]

[1] School of Electronic Engineering, Huainan Normal University, Huainan 232038, China; wangxuelian@mail.ustc.edu.cn (X.W.); shenxb@hnnu.edu.cn (X.S.); zhengrongxia@hnnu.edu.cn (Z.X.); haijun20030@163.com (H.Y.)
[2] Key Laboratory of Materials Physics, Institute of Solid State Physics, The Hefei Institutes of Physical Science (HFIPS), Chinese Academy of Sciences, Hefei 230031, China
* Correspondence: jbai@issp.ac.cn (J.B.); zhangxian035@163.com (X.Z.)

Abstract: With the increasing demand for thermal management in electronic devices, highly efficient and controllable phase change materials have attracted significant attention. The compound 2-amino-2-methyl-1,3-propanediol (AMPD), as a solid–solid phase change material, exhibits remarkable supercooling behavior and a high latent heat storage (ΔH_{endo} = 247.9 J/g). However, its phase transition kinetics and mechanically triggered properties have not been systematically investigated. In this study, the phase transition behavior of AMPD under different cooling rates and thermal cycling conditions was systematically analyzed using differential scanning calorimetry (DSC). Furthermore, the mechanical triggering characteristic of AMPD under a supercooled state was also studied. The results demonstrated that AMPD can maintain a supercooled state for an extended period, and the exothermic enthalpy change (ΔH_{exo}) increased by 17.8% (from 154.1 to 181.6 J/g) during thermal cycling. Additionally, mechanical triggering could induce rapid heat release from AMPD, enabling the on-demand regulation of heat utilization. This study revealed that AMPD enables stable supercooling and controllable heat release via thermal or mechanical triggers, offering a novel strategy for tunable solid–solid phase change materials.

Keywords: AMPD; phase change material; supercooling state; mechanically triggered; thermal management

1. Introduction

The increasing global energy demand and urgent pursuit for carbon neutrality have underlined thermal energy storage technologies as the critical enablers of sustainable energy transitions [1,2]. Phase change materials (PCMs), renowned for their high latent heat capacity and reversible energy storage capabilities, have become indispensable in applications spanning industrial waste heat recovery to advanced microelectronic thermal management systems [3,4]. Among PCMs, solid–solid PCMs stand out for their leakage-free operation and exceptional volumetric stability, making them ideal for precision-critical fields such as aerospace thermal regulation and flexible wearable devices [5,6]. However, the limited availability of high-performance solid–solid PCMs and insufficient understanding about their phase transition kinetics still impede progress toward next-generation thermal management solutions [7].

The compound 2-amino-2-methyl-1,3-propanediol (AMPD) is a multifunctional polyol containing both hydroxyl and amino groups, widely utilized in pharmaceutical synthesis

https://doi.org/10.3390/molecules30102206

and asymmetric catalysis [8]. Its structural analog, 2-amino-2-methyl-1-propanol (AMP, ΔH_{exo} = 134 J/g), corresponding to a glassy-to-ordered crystal transition, has been extensively studied as a solid–solid phase change material due to its supercooling behavior, while the thermal energy storage potential of AMPD remains unexplored despite its superior molecular architecture [9]. The additional hydroxyl group in AMPD strengthens hydrogen-bonding interactions, enhancing structural stability during phase transitions and theoretically optimizing the energy storage capacity [10]. Compared to AMP, AMPD exhibits a 35.5% higher exothermic enthalpy (ΔH_{exo} = 181.6 J/g) and enables pressure-independent energy release through mechanical triggering, eliminating the need for the 6.7 MPa external pressure required in plastic crystal systems [11–13]. The decoupling from pressure-driven energy release significantly enhances both the safety and operational feasibility. However, the critical issues remain in exploring the thermal storage performance of AMPD. Fundamental thermodynamic parameters, including latent heat, supercooling behavior, and cycling stability, have still not been fully quantified, and its mechanically triggered energy release mechanism requires systematic evaluation to determine its scalability. Addressing these key issues is crucial for realizing AMPD as a potential next-generation PCM for thermal management applications [14,15].

Herein, we present the first comprehensive investigation into the phase transition behavior of AMPD, demonstrating its exceptional supercooling stability, tunable crystallization kinetics, and mechanically triggered heat release. These findings highlight the potential of AMPD as a solid–solid phase change material for thermal energy storage, with the ability to achieve an exothermic enthalpy increase of 17.8% through thermal cycling, and the release of stored energy on demand via mechanical activation. Additionally, the successful design and implementation of AMPD-based waste heat recovery modules further illustrate its practical application in electronic thermal management and off-grid heating scenarios. This work demonstrated that AMPD exhibits dual-controllable supercooling and latent heat release behavior, providing a new model for on-demand solid–solid thermal energy storage.

2. Results and Discussion

The commercially obtained AMPD exists as a white crystalline solid (α-phase) at room temperature. Thermal pretreatment at 360 K induced its transformation into a colorless plastic crystalline state (β-phase), enabling the subsequent phase transition process [16]. A sealed aluminum crucible containing 11.42 mg of AMPD was subjected to DSC analysis under controlled cooling and heating rates of 2 K/min. As shown by the yellow curve in Figure 1a, no discernible exothermic crystallization peak was observed during cooling from 360 to 250 K, confirming AMPD retained a supercooled state without spontaneous nucleation. The exceptional supercooling stability originates from its three-dimensional hydrogen-bonding network, formed through synergistic interactions between the hydroxyl (-OH) and amino (-NH_2) groups, which effectively suppresses molecular rearrangement and crystalline nucleation [17,18]. During the subsequent heating process (blue curve, Figure 1a), AMPD exhibited two distinct phase transitions. The first was an exothermic peak at 290 K ($\Delta H_{\mathrm{exo}} = -154.9$ J/g), corresponding to the crystallization of the supercooled β-phase into the low-temperature α-phase. The second was an endothermic peak at 360 K (ΔH_{endo} = 209.8 J/g), indicating the phase transition from α- to β-phase, where AMPD reverts from the crystalline solid to the plastic crystalline state. The structural features and transition pathway are further illustrated in Figure 1b, which provides a visual summary of the reversible phase evolution between the α-phase, β-phase, and the metastable supercooled state. This phase behavior highlights the dynamic stabilization of both the crystalline and plastic crystal states by the hydrogen-bonding network during thermal energy storage and release [8].

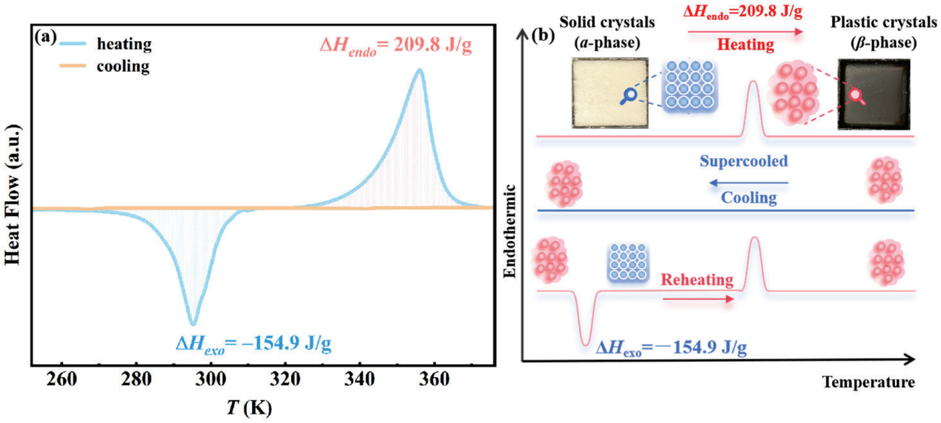

Figure 1. (**a**) The heat flow curve of AMPD as a function of temperature. The yellow curve represents the cooling process, while the blue curve corresponds to the subsequent heating process. ΔH_{exo} and ΔH_{endo} denote the exothermic and endothermic enthalpy changes, respectively. The negative values of ΔH_{exo} indicate heat release. (**b**) Schematic illustration of the structural changes among the ordered α-phase, the plastic crystalline β-phase, and the metastable supercooled β-phase during thermal cycling.

To investigate the effect of sample mass on the phase transition behavior of AMPD, four different sample masses (m_1 = 3.68 mg, m_2 = 11.42 mg, m_3 = 15.48 mg, and m_4 = 16.14 mg) were subjected to DSC analysis under a uniform heating and cooling rate of 10 K/min. Figure 2a,b present the variations in exothermic enthalpy with temperature and the exothermic enthalpy per unit mass for the samples of different masses during the β- to α-phase transition. Figure 2c,d show the variations in endothermic enthalpy with temperature, and the endothermic enthalpy per unit mass for the samples of different masses during the α- to β- phase transition. Larger samples demonstrated progressively higher enthalpy values, culminating in the exothermic enthalpy changes $\Delta H_{\text{exo}} = -156.3$ J/g and $\Delta H_{\text{endo}} = 247.9$ J/g for m_4 compared to $\Delta H_{\text{exo}} = -92.1$ J/g, and an endothermic enthalpy change $\Delta H_{\text{endo}} = 192.8$ J/g for m_1. The 69.6% increase in ΔH_{exo} and 28.5% rise in ΔH_{endo} reflected the influence of sample mass on total energy release, consistent with the cumulative effect of latent heat content in larger samples. The observed trends can be explained by classical nucleation theory (CNT) and thermal transport dynamics [19,20]. As shown in Equation (1), according to CNT, the nucleation energy barrier (expressed per unit mass), ΔG^*, is inversely proportional to the sample volume (V):

$$\Delta G^* = \frac{16\pi\gamma^3}{3\Delta {G_v}^2} \propto \frac{1}{V} \tag{1}$$

where γ represents the interfacial energy and ΔG_v denotes the volumetric free energy difference. As the sample volume increases, the nucleation energy barrier decreases, promoting heterogeneous nucleation and leading to more complete crystallization of the α-phase. This effect was evident in the 69.6% increase in ΔH_{exo} from m_1 to m_4, which corresponded to an enhanced probability of nucleation at interfacial regions due to amplified thermal gradients. In the smaller samples, minimal internal thermal gradients create a uniform temperature field, suppressing heterogeneous nucleation and leading to incomplete crystallization, resulting in lower exothermic enthalpy release [21].

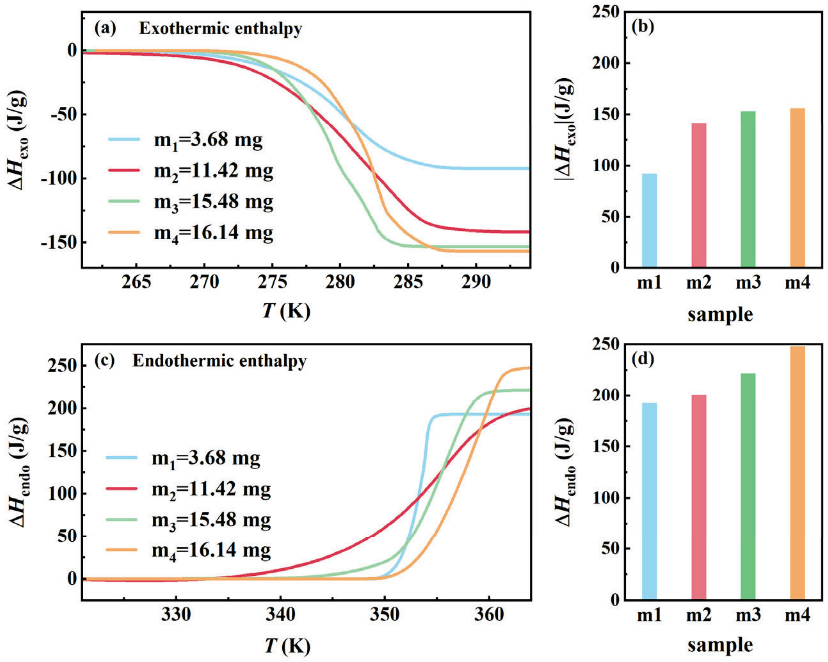

Figure 2. Enthalpy changes during the phase transition of AMPD with varying sample masses. (**a**) Enthalpy changes curves as a function of temperature during the reheating process. (**b**) Variations in exothermic enthalpy change (absolute value) for samples of different masses. (**c**) Enthalpy changes curves as a function of temperature during the heating process. (**d**) Variations in endothermic enthalpy change for samples of different masses.

Thermodynamically, the enthalpy change ΔH associated with the solid–solid phase transition involves both internal energy and entropy (ΔS) contributions, according to the relation $\Delta H = \Delta G + T\Delta S$. Although ΔS cannot be quantitatively determined in this study, its effect on phase stability was implied in the reversible transition behavior observed for AMPD. Based on CNT, the nucleation energy barrier ΔG^* determined the possibility of crystallization. While ΔG^* was inversely related to the sample volume, larger AMPD samples exhibited enhanced supercooling stability due to a reduced surface-to-volume ratio, which decreased the availability of heterogeneous nucleation sites. This effect prolonged the retention of the metastable β-phase in larger systems, consistent with the observed thermal behavior.

A similar trend was observed for endothermic enthalpy that increased with the sample mass, which could be attributed to differences in molecular rearrangement kinetics during reheating [22]. In the smaller samples, where heat is uniformly distributed, the transition from the α- to β-phase occurs more efficiently, requiring relatively lower energy input. In contrast, the larger samples exhibit spatially inhomogeneous temperature distributions, leading to asynchronous phase transitions across different regions. Some domains require additional thermal energy to fully complete molecular rearrangement and establish the plastic crystalline phase, resulting in a progressive increase in ΔH_{endo} with the sample mass. Table S1 presents the exothermic and endothermic enthalpy changes per unit mass for each sample during phase transition. These enthalpy differences reflected the kinetic asymmetry between melting and crystallization, where incomplete nucleation and molecular disorder during cooling led to a lower ΔH_{exo} compared to the full enthalpy release during heating.

To elucidate the effect of cooling rate on the phase transition behavior of AMPD, DSC measurements were conducted at the controlled cooling rates of 2, 5, 10, and 20 K/min, followed by a uniform reheating rate of 10 K/min. This experimental design emphasized the influence of cooling rates while maintaining consistent reheating conditions, enabling a direct comparison of the nucleation dynamics and phase stability. Quantitative phase transition parameters are summarized in Table S2. The cooling rate-dependent behavior can be explained through the CNT. As shown in Equation (2), the nucleation rate J is expressed as follows:

$$J = J_0 \exp\left(-\frac{\Delta G^*}{k_B T}\right) \tag{2}$$

where γ is the interfacial energy and ΔG_v is the volumetric free energy difference between phases [19–21]. Increasing the cooling rate from 2 to 20 K/min enhanced supercooling, which elevated ΔG_v (thermodynamic driving force), while reducing the critical nucleation barrier ΔG^*. The formed dual effect amplifies stochastic nucleation events, which was consistent with the broadening exothermic peaks and emergent doublet feature at 20 K/min (Figure 3a). Spatial heterogeneity in crystallization, evidenced by the expanded phase transition temperature range ΔT from 21.5 K (2 K/min) to 27.8 K (20 K/min), arises from thermal gradients under rapid cooling. These gradients induce localized variations in ΔG_v, promoting heterogeneous nucleation at high-energy interfaces rather than homogeneous bulk crystallization. Concurrently, incomplete molecular alignment during fast cooling generates structural defects in the metastable β-phase domains. These defects (e.g., misaligned hydrogen bonds and lattice vacancies) lower the activation energy for the transition from β- to α-phase by providing pre-existing nucleation pathways. This proposed possible mechanism explains the significant reduction in endothermic enthalpy ΔH_{endo} from 209.8 J/g (2 K/min) to 171.4 J/g (20 K/min) (Figure 3c), aligning with defect-mediated transitions in hydrogen-bonded systems [23–25].

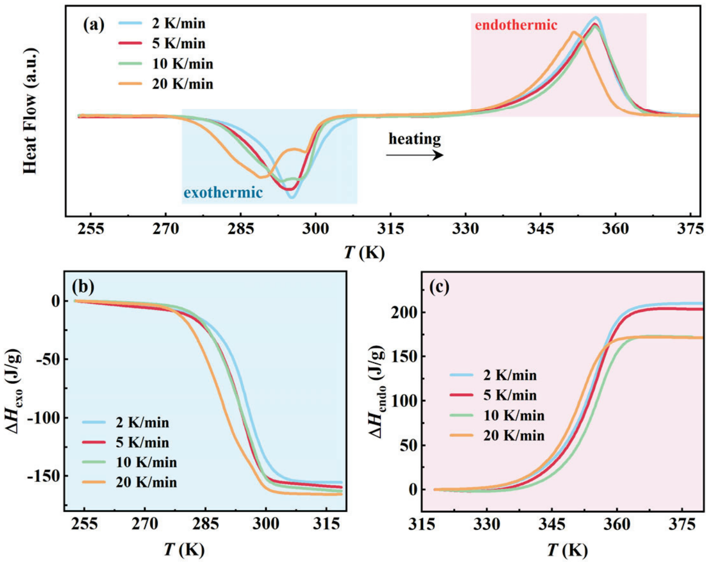

Figure 3. The effect of different cooling rates on the phase transition of AMPD: (**a**) Heat flow curves during heating at a fixed rate of 5 K/min after cooling at different rates, and (**b**,**c**) the variations in exothermic and endothermic enthalpy with temperature during the heating process, respectively.

In contrast to the variable endothermic behavior, the exothermic enthalpy change ΔH_{exo} exhibited minimal variation with cooling rates, ranging from -154.9 J/g (2 K/min) to 165.4 J/g (20 K/min) (Figure 3b), which suggested that α-phase crystallization, once nucleated, progresses as a thermodynamically controlled process dominated by equilibrium phase growth rather than kinetic constraints [26]. The phase transition termination temperature T_e remained constrained within a narrow range from 301.5 to 304.8 K, reflecting the thermodynamic equilibrium boundary of β-phase dissociation. The temperature invariance, coupled with the stable ΔH_{exo} values, confirmed that the final phase composition is governed by thermodynamic stability thresholds. The decoupling between nucleation onset (T_s depression) and phase termination (T_e stability) reflected the interaction between the kinetic constraints and thermodynamic equilibrium in hydrogen-bonded plastic crystals, consistent with classical nucleation theory and phase stability analysis.

To investigate the kinetic–thermodynamic interaction during the crystallization process of AMPD, we performed ten thermal cycles at controlled cooling rates (2 and 10 K/min), with a fixed heating rate of 10 K/min as shown in Figure 4, revealing distinct structural evolution pathways governed by molecular reorganization dynamics. The quantitative phase transition parameters are summarized in Table S3. As shown in Figure 4a–c, for the slow-cooled group (2 K/min), the exothermic enthalpy ΔH_{exo} increased progressively from -170.1 to -182.7 J/g over ten cycles, accompanied by a narrow crystallization temperature range from 281.1–297.8 to 284.3–299.1 K. An enhancement of 7.4% in the energy release aligned with the configurational entropy minimization principle in plastic crystals [27], where the prolonged molecular reorganization time reduces lattice defects. The upward shift in the crystallization onset temperature T_s reflected reduced nucleation barriers due to iterative annealing, which was consistent with the earlier observations on the extended reorganization time enhancing crystallinity in the larger samples. In contrast, as shown in Figure 4d–f, the rapid cooling (10 K/min) initially generated metastable configurations, evidenced by a decreased ΔH_{exo} (-154.1 J/g) and broadened crystallization range (277.1–301.6 K). Remarkably, ΔH_{exo} was restored to -181.6 J/g after ten cycles (17.8% enhancement), with the range stabilizing at 284.5–300.4 K. The above recovery originates from thermally activated hydrogen-bond reorganization, where the repeated phase transitions eliminate disordered domains through cooperative -OH/-NH$_2$ rearrangement, which is analogous to structural relaxation in hydrogen-bonded polymers. Despite the initial differences, both the cooling rates ultimately led to nearly identical thermodynamic states, with a ΔH_{exo} difference of less than 1% and a ΔT variation below 2%. The results suggested that the slower cooling promotes defect minimization through equilibrium-driven crystallization, while the faster cooling facilitates kinetic recovery via cyclic hydrogen-bond reorganization. This dual-pathway mechanism aligns well with the defect-annealing models in hydrogen-bonded plastic crystals. Furthermore, the enhanced cycling stability of AMPD, compared to the well-known neopentyl glycol system, highlights its structural adaptability, where its hydroxyl-rich framework enables efficient energy dissipation under thermal stress.

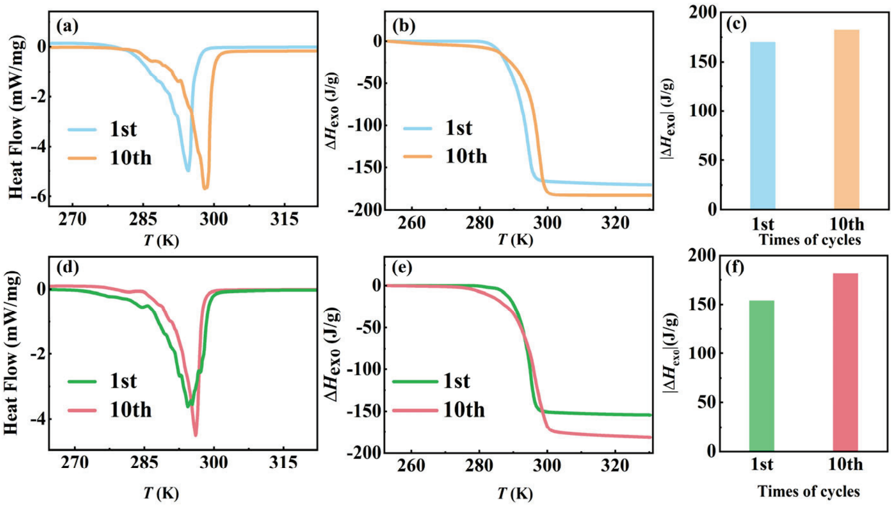

Figure 4. The effect of cooling rates on the exothermic phase transition of AMPD during thermal cycling. (**a**) Heat flow curves and (**b**) enthalpy changes as functions of temperature for a cooling rate of 2 K/min, and (**c**) comparison of the absolute enthalpy changes after ten thermal cycles at 2 K/min. (**d**) Heat flow curves and (**e**) enthalpy changes as functions of temperature for a cooling rate of 10 K/min, and (**f**) comparison of the absolute enthalpy changes after ten thermal cycles at 10 K/min.

An investigation of the phase transition behavior in AMPD revealed a remarkable supercooling persistence, where the high-temperature plastic crystalline β-phase remained metastable at room temperature (~298 K) for several months without spontaneous heat release. However, mechanical stimuli (e.g., needle insertion) disrupted the metastability, as shown in Figure S1, triggering rapid heat release. The thermal or mechanical dual-trigger mechanism positions AMPD as a promising candidate for intelligent thermal management systems, particularly in the applications requiring on-demand energy release. To assess the thermal regulation potential of AMPD, a simplified experimental setup was designed using two metal containers (2 cm × 2 cm × 0.5 cm) filled with AMPD samples of different masses (m_1 = 1125 and m_2 = 2250 mg). The samples were first heated to 380 K to ensure complete transition to the β-phase, followed by natural cooling to ambient temperature while continuously recording their temperature profiles to track heat dissipation dynamics. In the absence of external intervention, both samples exhibited linear temperature decay (Figure 5a,b), consistent with passive heat dissipation governed by thermal conduction and phase transition kinetics. However, when an external trigger was applied at 333.16 K (60 °C), simulating a thermal regulation threshold, the system behavior changed markedly. Nucleation was initiated near the trigger site, inducing rapid latent heat release and forming distinct temperature plateaus (Figure 5c–e). The plateau durations, 149 s for m_1 and 337 s for m_2, increased with the sample mass, which aligned with the increases in total latent heat, determined by the product of the sample mass and the specific latent heat. This behavior reflected the additive nature of energy storage in phase change systems, rather than the differences in intrinsic material properties. This mechanically triggered phase transition highlights the unique capability of AMPD for active thermal regulation. By strategically timing the external stimuli, the system can maintain target temperatures without continuous energy input, offering an energy-efficient and controllable thermal management solution. These findings confirmed that AMPD enables temporal decoupling between energy storage and release, and supports dual-trigger activation via both thermal input and mechanical stimulation.

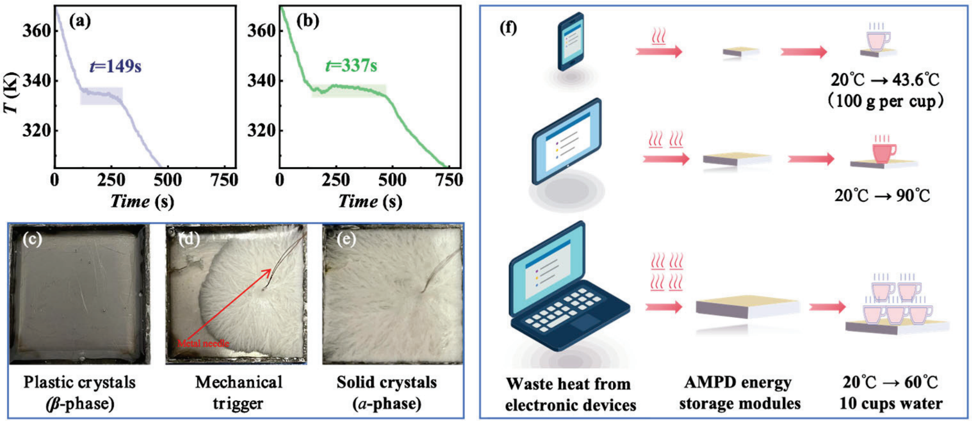

Figure 5. The temperature evolution of AMPD samples during cooling and mechanical triggering. (**a**) m_1 = 1125 mg and (**b**) m_2 = 2250 mg. (**c**) Supercooled plastic crystalline state. (**d**) Phase transition upon triggering at 333.16 K (~60 °C). (**e**) Solid crystalline state after phase transition. (**f**) The application of AMPD in electronic devices (mobile phones, tablets, and laptops) for waste heat recovery, and its secondary utilization for water heating.

Based on the phase transition characteristics and energy storage behavior of AMPD, we developed a modular waste heat recovery system that leverages its high latent heat capacity ($\Delta H_{exo} = -159.5$ J/g, averaged across the cooling rates of 2–20 K/min) and mechanically triggered crystallization for efficient thermal energy harvesting and controlled release. The

AMPD modules can be directly attached to electronic devices, such as smartphones and tablets, to absorb waste heat through solid–solid phase transitions. In off-grid scenarios, stored thermal energy can be instantaneously released via mechanical triggering to supply warm water (40–60 °C) or hot water (80–100 °C), addressing diverse daily needs. As shown in Figure 5f, to meet diverse thermal management needs, three AMPD modules were designed for standard electronic devices, with the specific parameters detailed in Table S4. The smartphone module ($15 \times 7.5 \times 0.5$ cm^3, 63.4 g), with a thermal storage capacity of 10.11 kJ, was capable of heating 100 g of water from 20 to 43.6 °C for instant warm water supply. The tablet module ($21 \times 18.6 \times 0.5$ cm^3, 220.0 g), with a thermal storage capacity of 35.09 kJ, heated 100 g water from 20 to 90 °C for prolonged heat retention without boiling risks. The laptop module ($38 \times 25 \times 1$ cm^3, 1069.8 g), with a thermal storage capacity of 170.63 kJ, enabled the simultaneous heating of ten 100 g water portions (one cup each) from 20 °C to 60.8 °C, supporting multi-user operation in parallel. Compared to conventional electric kettles (400 W, 5-min heating), AMPD modules eliminated electricity consumption, reducing CO_2 emissions by 1.5 kg/month (assuming three daily uses and carbon emission factor: 0.5 kg CO_2/kWh). The plug-and-play design ensures compatibility with diverse electronics, enhancing energy utilization efficiency.

3. Materials and Methods

The compound 2-amino-2-methyl-1,3-propanediol (AMPD, purity: 98%) was purchased from Sigma-Aldrich (Shanghai) Trading Co., Ltd. (Shanghai, China) and used without further purification. To eliminate any residual moisture, the sample was thoroughly dried at 60 °C for 24 h in a vacuum oven (0.1 MPa) and then stored in a desiccator to prevent moisture reabsorption. Thermogravimetric analysis (TGA) of the dried sample revealed no significant mass loss below 150 °C, confirming the absence of volatile residues. Additionally, control DSC tests performed on samples dried for 12 and 24 h showed negligible variation (<1.5%) in latent heat and transition temperatures, indicating stable thermal behavior under the selected drying conditions.

The phase transition behavior of AMPD was characterized using differential scanning calorimetry (DSC 4000, PerkinElmer Pyris Diamond, Waltham, MA, USA). All measurements were conducted under a nitrogen atmosphere to minimize oxidation and external environmental influences. The temperature control accuracy of the instrument is ±0.1 °C. The heating and cooling rates were systematically varied between 2 and 20 K/min to examine their effects on phase transition kinetics. The sample was placed in high-purity aluminum oxide crucibles, which were hermetically sealed with lids to prevent possible volatilization during thermal cycling. In terms of the data processing, background correction was performed to eliminate baseline drift and improve measurement accuracy.

4. Conclusions

This study systematically investigated the phase transition characteristics of AMPD and its potential in energy storage applications. The results demonstrated that AMPD undergoes a reversible solid-state phase transition during cooling, with its phase transition temperature range and exothermic enthalpy change being influenced by the cooling rate and sample mass. The faster cooling rates suppressed crystal nucleus formation, resulting in a greater supercooling degree and lower exothermic enthalpy change, while the slower cooling rates facilitated molecular ordering and enhanced crystallinity, thereby reducing supercooling and improving the exothermic capacity. Furthermore, the simulated application scenarios confirmed the triggerable exothermic characteristics in AMPD, where external triggers induced the rapid recovery of molecular ordering, generating stable plateau regions during the exothermic process that exhibited excellent thermal stability and controllable energy release. This research reveals that AMPD, as a supercooled phase change energy storage material, demonstrates an interaction mechanism between microscopic molecular rearrangement and adjustable phase transition properties, providing the guidance for its application in thermal management and the energy storage fields.

Supplementary Materials: The following supporting information can be downloaded at: https://www.mdpi.com/article/10.3390/molecules30102206/s1, Figure S1. Schematic illustration of the phase transition of AMPD during the heating–cooling–reheating process. During heating from state (a) to state (b), the solid crystalline α-phase undergoes a phase transition into the plastic crystalline β-phase, accompanied by an endothermic enthalpy change. In the subsequent cooling process from state (b) to state (c), the plastic crystalline phase remains in a supercooled state at room temperature due to the absence of spontaneous crystallization. The supercooled plastic crystalline β-phase can revert to the solid crystalline α-phase either through reheating, as observed in the transition from state (c) to state (a), or by mechanical triggering, as demonstrated in state (d), both of which are associated with an exothermic enthalpy change. Table S1. Enthalpy changes during phase transition of AMPD samples with different masses, and ΔH_{exo} and ΔH_{endo} represent exothermic and endothermic enthalpy changes, respectively; negative values of ΔH_{exo} indicate heat release; Table S2. The phase transition parameters of AMPD at different cooling rates, and Ts and Te represent the onset and end temperatures of phase transition, respectively; ΔT is the phase transition temperature range; Table S3. Thermal cycling performance of AMPD at different cooling rates. Table S4. Performance parameters of AMPD modules for different electronic devices.

Author Contributions: X.W.: Conceptualization, methodology, formal analysis, writing—original draft, funding acquisition. J.B.: Conceptualization, writing—review and editing. X.Z.: Formal analysis, funding acquisition. X.S.: Formal analysis, funding acquisition. Z.X.: Formal analysis. H.Y.: Writing—review and editing, funding acquisition. All authors have read and agreed to the published version of the manuscript.

Funding: This work was supported by the Key Program of the Natural Science Foundation of Colleges and Universities in Anhui Province (Grant No. 2024AH051722), the High-level Talent Research Start-up Program (Grant No. GCCRCKYQDJ-823045), the University-level Quality Engineering Program (Grant Nos. 2023hsjyxm11, 2024hskc17, and 2024hsjc07), the Anhui Province College Students' Innovation Training Program (Grant Nos. 202410381001 and S201410381033), the Anhui Provincial Key Research and Development Plan (Grant Nos. 2022a05020010 and 202004a050200), the Anhui Province Postdoctoral Research Activities Funding Project (Grant No. 2022B625), and the Provincial Quality Engineering Project of Higher Education Institutions of Anhui Province (Grant No. 2023zybj047).

Institutional Review Board Statement: Not applicable.

Informed Consent Statement: Not applicable.

Data Availability Statement: The original contributions presented in this study are included in the article/Supplementary Materials. Further inquiries can be directed to the corresponding authors.

Conflicts of Interest: The authors declare no conflicts of interest.

References

1. Zhou, D.; Zhao, C.Y.; Tian, Y. Review on thermal energy storage with phase change materials (PCMs) in building applications. *Appl. Energy* **2012**, *92*, 593–605. [CrossRef]
2. Sharma, A.; Tyagi, V.V.; Chen, C.R.; Buddhi, D. Review on thermal energy storage with phase change materials and applications. *Renew. Sustain. Energy Rev.* **2009**, *13*, 318–345. [CrossRef]
3. Xiao, X.; Zhang, P.; Li, M. Preparation and thermal characterization of paraffin/metal foam composite phase change material. *Appl. Energy* **2013**, *112*, 1357–1366. [CrossRef]
4. Zhao, Y.; Zou, B.; Zhang, T.; Jiang, Z.; Ding, J.; Ding, Y. A comprehensive review of composite phase change material based thermal management system for lithium-ion batteries. *Renew. Sustain. Energy Rev.* **2022**, *167*, 112667. [CrossRef]

5. Huang, J.; Luo, Y.; Weng, M.; Yu, J.; Sun, L.; Zeng, H.; Liu, Y.; Zeng, W.; Min, Y.; Guo, Z. Advances and applications of phase change materials (PCMs) and PCMs-based technologies. *ES Mater. Manuf.* **2021**, *13*, 23–39. [CrossRef]
6. Zhao, X.; Zou, D.; Wang, S. Flexible phase change materials: Preparation, properties and application. *Chem. Eng. J.* **2022**, *431*, 134231. [CrossRef]
7. Farid, M.; Khudhair, A.M.; Razack, S.A.K.; Al-Hallaj, S. A review on phase change energy storage: Materials and applications. *Therm. Energy Storage Phase Change Mater.* **2004**, *45*, 1597–1615. [CrossRef]
8. Liu, Y.; Deng, Y.; Zheng, J.; Wu, F.; Lu, J.; Sun, S.; Wu, D.; Wu, T. Role and influence of hydrogen bonds in composite phase change materials: A critical review. *Sol. Energy Mater. Sol. Cells* **2022**, *248*, 112031. [CrossRef]
9. Zhang, K.; Zhang, Z.; Pan, H.; Wang, H.; Zhao, X.; Qi, J.; Zhang, Z.; Song, R.; Yu, C.; Huang, B.; et al. Taming heat with tiny pressure. *Innovation* **2024**, *5*, 100577. [CrossRef]
10. Han, G.G.D.; Li, H.; Grossman, J.C. Optically-controlled long-term storage and release of thermal energy in phase-change materials. *Nat. Commun.* **2017**, *8*, 1446. [CrossRef]
11. Yang, S.; Shi, H.Y.; Liu, J.; Lai, Y.-Y.; Bayer, Ö.; Fan, L.-W. Supercooled erythritol for high-performance seasonal thermal energy storage. *Nat. Commun.* **2024**, *15*, 4948. [CrossRef] [PubMed]
12. Li, B.; Kawakita, Y.; Ohira-Kawamura, S.; Sugahara, T.; Wang, H.; Wang, J.; Chen, Y.; Kawaguchi, S.I.; Kawaguchi, S.; Ohara, K.; et al. Colossal barocaloric effects in plastic crystals. *Nature* **2019**, *567*, 506–510. [CrossRef] [PubMed]
13. Baek, J.I.; Yoon, J.H. Solubility of carbon dioxide in aqueous solutions of 2-amino-2-methyl-1,3-propanediol. *J. Chem. Eng. Data* **1998**, *43*, 635–637. [CrossRef]
14. Tong, B.; Tan, Z.-C.; Liu, R.-B.; Meng, C.-G.; Zhang, J.-N. Thermodynamic investigation of a solid–solid phase change material: 2-amino-2-methyl-1,3-propanediol by calorimetric methods. *Energy Convers. Manag.* **2010**, *51*, 1905–1910.
15. Zhang, Z.Y.; Yang, M.L. Heat capacity and phase transition of 2-amino-2-methyl-1,3-propanediol from 280 K to the melting point. *Thermochim. Acta* **1990**, *169*, 263–269. [CrossRef]
16. Zhang, Z.Y.; Xu, Y.P. Measurement of the thermal conductivities of 2-amino-2-methyl-1,3-propanediol (AMP), 2-amino-2-hydroxymethyl-1,3-propanediol (TRIS) and the mixture (AMP+ TRIS, mole ratio 50: 50) in the temperature range from 20 °C to their supermelting temperatures. *Sol. Energy* **2001**, *71*, 299–303. [CrossRef]
17. Sharma, R.K.; Ganesan, P.; Tyagi, V.V.; Metselaar, H.S.C.; Sandaran, S.C. Developments in organic solid–liquid phase change materials and their applications in thermal energy storage. *Energy Convers. Manag.* **2015**, *95*, 193–228. [CrossRef]
18. Kahwaji, S.; White, M.A. Organic phase change materials for thermal energy storage: Influence of molecular structure on properties. *Molecules* **2021**, *26*, 6635. [CrossRef]
19. Prestipino, S.; Laio, A.; Tosatti, E. Systematic improvement of classical nucleation theory. *Phys. Rev. Lett.* **2012**, *108*, 225701. [CrossRef]
20. Tanaka, K.K.; Diemand, J.; Angélil, R.; Tanaka, H. Free energy of cluster formation and a new scaling relation for the nucleation rate. *J. Chem. Phys.* **2014**, 140. [CrossRef]
21. Van Duijneveldt, J.S.; Frenkel, D. Computer simulation study of free energy barriers in crystal nucleation. *J. Chem. Phys.* **1992**, *96*, 4655–4668. [CrossRef]
22. Liu, Y.P.; Lynch, G.C.; Truong, T.N.; Lu, D.H.; Truhlar, D.G.; Garrett, B.C. Molecular modeling of the kinetic isotope effect for the [1,5]-sigmatropic rearrangement of cis-1,3-pentadiene. *J. Am. Chem. Soc.* **1993**, *115*, 2408–2415. [CrossRef]
23. Shi, G.; Li, S.; Shi, P.; Gong, J.; Zhang, M.; Tang, W. Distinct pathways of solid-to-solid phase transitions induced by defects: The case of dl-methionine. *IUCrJ* **2021**, *8*, 584–594. [CrossRef]
24. Tang, Y.; Ouyang, M. Tailoring properties and functionalities of metal nanoparticles through crystallinity engineering. *Nat. Mater.* **2007**, *6*, 754–759. [CrossRef] [PubMed]
25. Roy, S.; Choi, W.; Jeon, S.; Kim, D.-H.; Kim, H.; Yun, S.J.; Lee, Y.; Lee, J.; Kim, Y.-M.; Kim, J. Atomic observation of filling vacancies in monolayer transition metal sulfides by chemically sourced sulfur atoms. *Nano Lett.* **2018**, *18*, 4523–4530. [CrossRef]
26. Oxtoby, D.W. Nucleation of first-order phase transitions. *Acc. Chem. Res.* **1998**, *31*, 91–97. [CrossRef]
27. Angell, C.A. Relaxation in liquids, polymers and plastic crystals—Strong/fragile patterns and problems. *J. Non-Cryst. Solids* **1991**, *131*, 13–31. [CrossRef]

Disclaimer/Publisher's Note: The statements, opinions and data contained in all publications are solely those of the individual author(s) and contributor(s) and not of MDPI and/or the editor(s). MDPI and/or the editor(s) disclaim responsibility for any injury to people or property resulting from any ideas, methods, instructions or products referred to in the content.

molecules

Article

Synergistic Effect of Anionic-Tuning and Architecture Engineering in $BiPO_4@C$ Anode for Durable and Fast Potassium Storage

Heying Chu, Yong Li, Yuanjie Liu, Xueping Chai, Hongzhou Zhang * and Jingchuan Zhang *

College of Mechanical and Electronic Engineering, Tarim University, Alar 843300, China;
chuheying@taru.edu.cn (H.C.); deyuzhijia@163.com (Y.L.); 120050023@taru.edu.cn (Y.L.);
haixueping@taru.edu.cn (X.C.)
* Correspondence: shenzhouxing@taru.edu.cn (H.Z.); zhangjingchuan@taru.edu.cn (J.Z.)

Abstract: Bismuth-based materials that adhere to the alloy/dealloy reaction mechanism are regarded as highly promising anode materials for potassium-ion batteries due to their high volume-specific capacity and moderate reaction potentials. However, their commercial viability has been limited by the effects of structural collapse due to volume distortion and impeded electron conduction, resulting in rapid capacity decline. In this work, a carbon-coated nanosized $BiPO_4$ rod ($BiPO_4@C$) was designed and fabricated to overcome the aforementioned challenges through the architecture engineering and anionic-tuning strategy. In particular, the nanosized nanorods significantly reduce the volume expansion; the incorporation of the bulk and open-skeleton anion $PO_4{}^{3-}$ serves to mitigate the considerable volume distortion and generates the high ionic conductivity product (K_3PO_4) to ameliorate the poor ionic transport due to the structural deformation. The elaborated $BiPO_4$ rods exhibit high specific capacity (310.3 mAh g^{-1}, at 500 mA g^{-1}), excellent cycling stability (over 700 cycles at 500 mA g^{-1}) and superior rate performance (137.8 mAh g^{-1}, at 1000 mA g^{-1}). Systematic ex-situ XRD and TEM, as well as kinetic tests, have revealed the "conversion-multistep alloying" reaction process and the "battery-capacitance dual-mode" potassium storage mechanism. Moreover, the thick electrodes showed excellent specific capacity and rate performance, demonstrating their significant application potential in the next generation of SIBs.

Keywords: bismuth phosphate; nanostructures; architecture engineering; anionic-tuning; potassium-ion batteries

1. Introduction

The contradiction between the limited lithium resources (0.0017 wt% in the earth's crust) and the rapidly expanding energy storage and electric vehicle markets has considerably constrained the further development of lithium-ion batteries (LIBs) [1]. Therefore, the development of new energy storage devices with low-cost and high-specific energy is an effective means to accelerate the development of the energy storage market. The abundance of potassium resources (2.09% in the earth's crust), the maturity of the processing technology, the low electrochemical potential (K^+/K: −2.93 V vs. E^o), and the well-known rocking chair charging/discharging mechanism have collectively positioned potassium-ion batteries (PIBs) as a promising next-generation "beyond Li-ion" battery [2,3]. However, the process of matching the large radius of K^+ (1.38 Å) with conventional electrode materials leads to problems such as slow ion migration and high volume strain [4,5]. Consequently, there is an urgent requirement to develop anode materials with a robust structure and a high ability to tolerate volume strain, as well as to obtain electrode materials with ultra-long cycle stability and rapid potassiation/depotassiation capabilities.

In terms of anode materials, the potassium storage capacity and cycling stability of graphite are much lower than that of commercial LIBs due to the drastic volume distortion that occurs during K^+ insertion/extraction [6]. Metal-based materials (e.g., Sn [7,8], Sb [9,10], Bi [11,12], and binary/ternary alloys [13,14]) capable of alloying with K^+ have attracted considerable attention due to their high conductivity, considerable theoretical specific capacity and safe redox potential. Among these materials, layered bismuth shows promising prospects for K^+-storage due to its advantageous characteristics, including a high volumetric theoretical specific capacity (385 mAh g^{-1}), non-toxicity, high electrical conductivity, large lattice spacing, and moderate discharge voltage [15]. However, the gradual alloying process with K^+ inevitably causes significant volume strain (390%), which further leads to microstructural collapse and rapid deterioration of cycling performance [16]. Many strategies have been attempted to overcome the above problems, such as compositing with carbon media to mitigate the volume strain exerted on the active particles and reduce particle fragmentation [17,18], Construction of special micro-nanostructures to accommodate volume expansion and contraction through the incorporation of buffer spaces to avoid rupture of the outer stable solid electrolyte interphase (SEI) films [19,20]; Anion auxiliary strategies (Bi_2O_3 [21], Bi_2S_3 [22], Bi_2Se_3 [23], Bi_2O_2Se [24], $Bi_2Se_{3-x}Se_x$ [25]) to prevent agglomeration of metal elements and relieve structural stresses anchored by bonding with anions. Undeniably, the aforementioned subtle enhancement strategies have largely mitigated the damage to the electrode structure caused by volume distortion and significantly improved the cycling stability of Bi-based electrodes. Nevertheless, the scalability of this intricate process remains a significant challenge, and the difficulty of disrupting the electron conduction path during volume expansion and contraction has yet to be overcome. Furthermore, the poor conductivity of the discharge products of Bi-based chalcogenides and the strong evolution and shuttle effects (K_2S and K_2Se) in the anion tuning process are often overlooked, which are again the culprits for the capacity degradation of Bi-based electrodes.

Herein, a carbon-coated nanosized $BiPO_4$ rod ($BiPO_4$@C) was synthesized by a simple hydrothermal method to mitigate the drastic alloying reaction and improve ionic conductivity. Specifically, the small-sized nanorods reduce the transport distance of K^+ and electrons within the solid phase, eliminate the size dependence, and mitigate the volume distortion. The introduction of the large-sized ${PO_4}^{3-}$ with a highly thermally stable and open P-O octahedral framework structure serves to buffer the significant volume distortion of the Bi anode during the alloying/dealloying process. Crucially, the discharge product (K_3PO_4) is generated in situ with high ionic conductivity, which boosts the electronic conductivity in damaged structures. Furthermore, the carbon coating improves the conductivity of the phosphate electrode and acts as an armor against structural degradation. As a consequence of these properties, the $BiPO_4$@C electrode exhibits high specific capacity, excellent cycling stability and rate performance. Post-mortem analysis demonstrates the conversion-multistep alloying reaction mechanism. The kinetic tests verify the "battery-capacitor" dual-mode potassium storage behavior. Therefore, the synergistic strategy of anion tuning and nanosize effect in this work provides a promising avenue for the development of rapid and stable anodes for PIBs.

2. Results and Discussion

2.1. Synthesis and Structural Characterization

Figure 1a illustrates a facile synthetic approach for $BiPO_4$@C nanorod via a one-step hydrothermal process, in which $Bi(NO_3)_3$ and $NH_4H_2PO_4$ were employed as the sources of Bi and P, respectively, while ethylene glycol (EG) was served as both the reaction medium and the carbon source. According to the literature, Bi^{3+} ions in solutions tend to be hydrolyzed to produce various hydroxides, depending on the composition of the solution [26]. Meanwhile, under mild heating, $NH_4H_2PO_4$ molecules can be decomposed to form H_3PO_4. [27,28] Subsequent high temperature and pressure processes lead to the formation of $BiPO_4$ nanorods. Based on the above analyses, we believe that the following reactions occur in the water/ethylene glycol mixture:

$$Bi(NO_3)_3 + 3H_2O \rightarrow Bi(OH)_3 + 3HNO_3 \tag{1}$$

$$NH_4H_2PO_4 \rightarrow H_3PO_4 + NH_3\uparrow \tag{2}$$

$$Bi(OH)_3 + H_3PO_4 \rightarrow BiPO_4 + 3H_2O \tag{3}$$

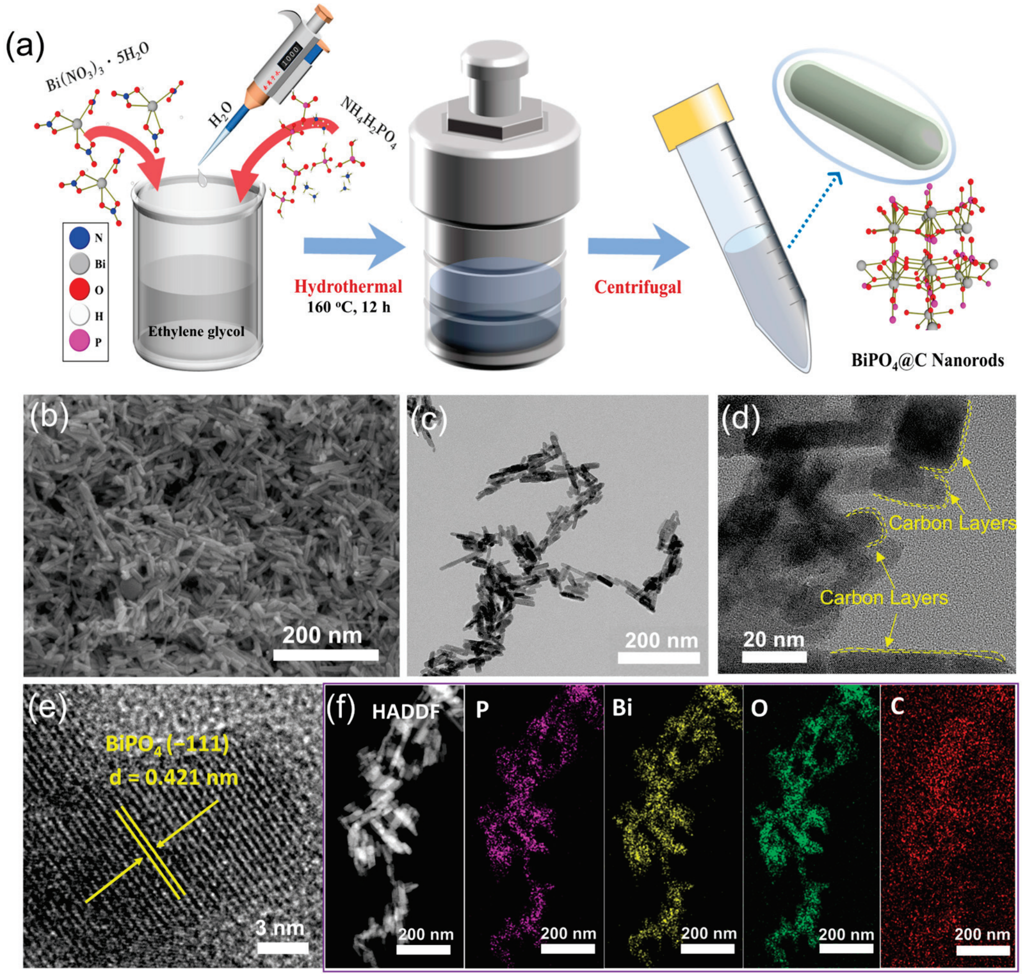

Figure 1. (**a**) Schematic of the fabrication process of $BiPO_4$@C composite. (**b**) SEM, (**c**,**d**) TEM, (**e**) HRTEM images, and corresponding (**f**) HADDF and EDS mapping images of the obtained $BiPO_4$@C.

The microscopic morphology of $BiPO_4$@C was investigated by scanning electron microscopy (SEM) and transmission electron microscopy (TEM). First, the effects of raw material concentration, reaction time and reaction temperature on the morphology of $BiPO_4$@C composites were systematically investigated. As shown in Figures S1–S3, the diameter and length of $BiPO_4$@C nanorods increase with increasing reaction concentration and reaction temperature, while the reaction time significantly restricts the morphology of the material. Taking all factors into consideration, we set the optimum raw material concentration, reaction time and temperature to 0.5 mmol, 160 °C, and 12 h, respectively. As shown in Figure 1b,c, $BiPO_4$@C exhibits a nanosized rod-like structure with a length of approximately 50–80 nm and a diameter of 15–20 nm. Interestingly, as shown in Figure 1d, each $BiPO_4$ nanorod exhibits a monocrystal structure with well-defined lattice fringes, and the surface of the nanorods is encapsulated with an ultra-thin carbon layer. Furthermore, the high-resolution TEM (HRTEM) image in Figure 1e clearly shows a set of periodic lattice fringes with a spacing of 0.421 nm, corresponding to the (-111) plane of monoclinic $BiPO_4$ (PDF# 04-010-5606). Meanwhile, the energy dispersive spectroscopy (EDS) mapping results indicate that the elements Bi, P and O are distributed uniformly in the $BiPO_4$@C nanorod composites (as shown in Figure 1f).

X-ray diffraction (XRD), Raman spectra, Fourier transform infrared spectroscopy (FTIR), and X-ray photoelectron spectroscopy (XPS) were used to determine the physical phase and structural information of $BiPO_4$@C. As shown in Figures 2a and S4 and Table S1, the XRD results indicated that the diffraction peaks of $BiPO_4$@C were consistent with the pure phase of monoclinic $BiPO_4$ (PDF# 04-010-5606). Subsequently, Raman spectra (Figure 2b) monitored a set of characteristic absorption peaks in the range of 300–1700 cm^{-1}, wherein the peaks located at 395, 543, and 600 cm^{-1} can be ascribable to PO_4^{3-}, while the peaks appearing at 972 and 1026 cm^{-1} can ascribe to the symmetric ($\upsilon1$) and asymmetric ($\upsilon2$) scaling modes of PO_4^{3-}, respectively [29]. Two other characteristic peaks that appear at 1356 and 1587 cm^{-1} can be attributed to disordered graphitic carbon (D-bond) and sp^2 hybridized graphic carbon (G-bond) of the C component, respectively. Obviously, a lower intensity ratio (I_D/I_G) value (0.37) for $BiPO_4$@C indicates a regular graphitic structure and high electrical conductivity, which can significantly improve the poor electrical conductivity inherent in phosphate materials. Moreover, the FTIR spectra revealed the presence of chemical bonding information within the wavenumber range of 500 to 3700 cm^{-1} for $BiPO_4$@C composites (as shown in Figure 2c). The results indicated that the absorption peaks at 530 and 601 cm^{-1} were indicative of the vibrational absorption of $\delta(PO_4^{3-})$, while the absorption peak at 1072 cm^{-1} was attributed to the $\upsilon3$ asymmetric stretching vibration of the P-O bond [30,31]. The three absorption peaks situated between 2750 and 2950^{-1} are ascribed to the symmetric and antisymmetric stretching vibrations of the C−H bond in the $-CH_3$, while the vibrational absorption peaks of the benzenoid ring skeleton appear between 1459 and 1650 cm^{-1}. Furthermore, the XPS survey spectrum clearly shows signals corresponding to the Bi, P, O, and C elements in $BiPO_4$@C composites, as illustrated in Figure 2d. Specifically, the two peaks observed at 165.1 eV and 159.8 eV in the high-resolution Bi 4f can correspond to Bi 4f $_{5/2}$ and Bi 4f $_{7/2}$, respectively (Figure 2e) [12,29]. Additionally, the P 2p spectrum (Figure 2f) demonstrated the emergence of a prominent peak associated with the P 2p $_{3/2}$ (at 133.7 eV) [29,32]. The high-resolution O 1s spectrum is split into two peaks at 531.2 and 533.1 eV, which are attributed to P-O and C-O bonds, respectively (Figure 2g) [29,32]. Additionally, we detected the characteristic peaks of the C=O (288.7 eV), C-O (286.3 eV), and C-C (284.8 eV) bonds in the C 1s spectrum, respectively, as shown in Figure 2h [33,34]. It is noteworthy that the presence of C-O bonding indicates that the ultrafine $BiPO_4$ particles can be chemically bonded to form a linkage with the carbon layer, which will undoubtedly facilitate electron transfer and enhance the rate performance. Subsequently, the content of the carbon-protective layer in $BiPO_4$@C was then determined by thermogravimetric analysis (TGA) test. As illustrated in Figure 2i, the mass remained constant up to 450 °C, after which a rapid mass loss (reduction of ~6.48 wt%) occurred in the range from 450 °C to 600 °C. In light of the TGA result and the deep oxidation products ($BiPO_4$, as shown in Figure S5), the calculated contents of the product $BiPO_4$ and carbon matrix in $BiPO_4$@C composite are 93.58 and 6.42%, respectively. A small amount of carbon layer with high graphitization can improve the conductivity of $BiPO_4$, alleviate the volume effect in the electrochemical process, and further improve the potassium-ion storage performance of $BiPO_4$@C electrode without excessively reducing the specific capacity of the active component.

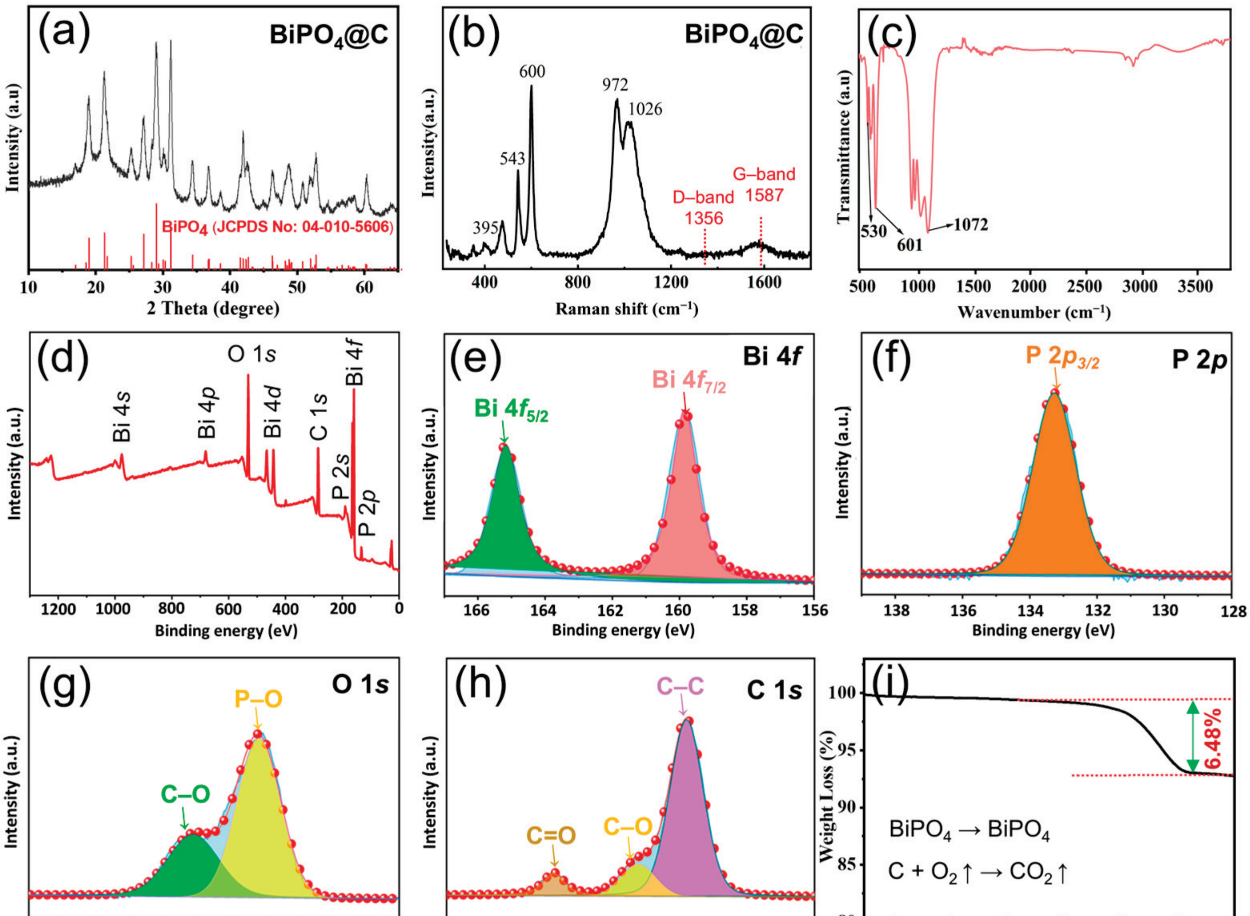

Figure 2. (**a**) XRD pattern, (**b**) Raman spectra, (**c**) FTIR spectra, (**d**) XPS survey spectra, high-resolution XPS spectra of (**e**) Bi 4f, (**f**) P 2p, (**g**) O 1s, (**h**) C 1s, and (**i**) TGA curve of $BiPO_4$@C composite.

2.2. Electrochemical Properties

The potassium ion storage performance of $BiPO_4$@C ultrafine nanorods and reference sample (commercial micro-sized $BiPO_4$, morphology and crystalline phase are shown in Figure S6) was investigated in button-type half-cells and coupled with potassium metal as the counter electrode. Figure 3a depicts the cyclic voltammetry (CV) curves of the $BiPO_4$@C electrode within the voltage range of 0.01 to 1.6 V at a scan rate of 0.1 mV s^{-1}. A reduction peak at 0.96 V was observed in the initial cathodic scan, corresponding to the conversion reaction to produce Bi element and K_3PO_4 ($BiPO_4 + 3\,K^+ + 3\,e^- \rightarrow K_3PO_4 + Bi$), as well as the formation of SEI layer [31]. Furthermore, a subsequent peak located at 0.09 V is associated with the alloying reaction to produce K_3Bi ($3\,Bi + K^+ + e^- \rightarrow K_3Bi$). Subsequently, three anodic peaks located at 0.60, 0.79, and 1.12 V were detected due to the gradual dealloying reaction ($K_3Bi \rightarrow K_xBi \rightarrow Bi$) [29]. During successive scans, the reduction peak at 0.96 V disappeared, suggesting an irreversible transformation process. Undoubtedly, the high ionic conductivity of K_3PO_4 is always maintained around the Bi particles, thereby accelerating the K^+ conduction kinetics by repairing the ion transport channels. In subsequent cycles, the electroreception process of the Bi-metal gradually evolved into a unique, multi-step alloy/dealloy process, exhibiting three pairs of oxidation/reduction peaks at 1.12/0.84, 0.79/0.35 and 0.6/0.14 V, respectively. [29,31]. Comfortingly, the alloying/dealloying reaction is highly reversible in terms of the positions and shapes of the CV curves, indicating the strong structural stability of $BiPO_4$@C. Furthermore, the voltage platforms in the galvanostatic charge-discharge (GCD) curve (Figure 3b) are well consistent with the redox peaks observed in the CV curves, confirming the proposed mechanism of initial "conversion-alloying/dealloying" and the subsequent "alloying–dealloying" reactions.

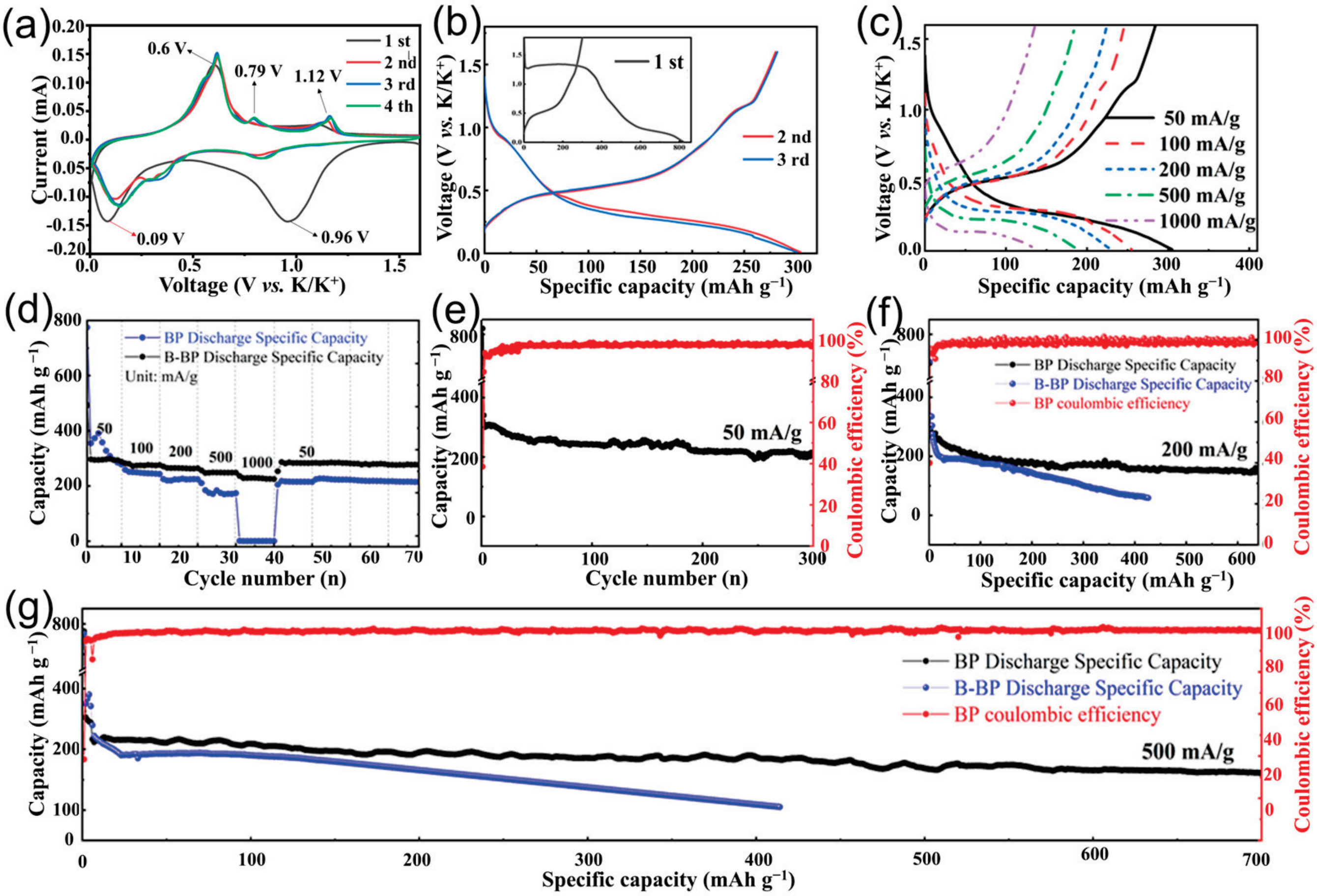

Figure 3. (**a**) CV curves at 0.1 mV s^{-1} and (**b**) galvanostatic charge/discharge curves at 0.2 A g^{-1} of the $BiPO_4$@C electrode. (**c**) Cycling performances at 50 mA/g. (**d**) Rate performances and (**e**) corresponding discharge/charge profiles at various current densities of $BiPO_4$@C electrode. Long cycling performances at (**f**) 200 mA/g and (**g**) 500 mA/g.

Additionally, the $BiPO_4$@C electrode displays a low polarization potential (Figure 3c) and excellent rate performance (Figure 3d). Accordingly, the specific charging capacities at 50, 100, 200, 500 and 1000 mA g^{-1} current density were 307.2, 254.9, 229.5, 187.9 and 137.8 mAh g^{-1}, respectively, which are significantly higher than those of commercial $BiPO_4$ electrodes and other reported Bi-based compound anode materials (Figure S7) [35–39]. The superior rate performance can be attributed to the short and efficient ion transport path provided by the nanostructuring effect and the accelerated ion transport kinetics provided by the fast ion conductor intermediate (K_3PO_4). It is encouraging to note that following multiple current shocks, the $BiPO_4$@C electrode still exhibited a reversible capacity of 278.2 mAh g^{-1} when the current density was returned to 50 mA g^{-1}, substantiating the fast electron/ion transport capacity and robust structure of the $BiPO_4$@C electrode. Subsequent cycling performance tests highlighted the high specific charge capacity and exceptional electrochemical stability of the $BiPO_4$@C electrode. As illustrated in Figure 3e, the $BiPO_4$@C electrode exhibits an initial charge capacity of 310.3 mAh g^{-1} and reaches a specific capacity of 216 mAh g^{-1} after 300 cycles at a current density of 50 mA g^{-1} with a slower average decay rate of 0.101% per cycle. Not surprisingly, the reversible capacities of the $BiPO_4$@C electrode after 600 cycles at 200 and 500 mA g^{-1} were an astonishing 161 mAh g^{-1} and 142 mAh g^{-1}, respectively (Figure 3f,g). Nevertheless, the specific capacitance of the micro-sized $BiPO_4$ electrode rapidly decreases due to the fact that the unprotected large-area structure cannot accommodate the large volume distortion that occurs during repeated alloying and dealloying. In addition, even at a current density of 1000 mA/g, the $BiPO_4$@C electrode demonstrated stable operation over 150 cycles, maintaining a specific capacity of 171 mAh g^{-1} (Figure S8). These superior reversibility rate properties far exceed those of some previously reported phosphate anode electrodes [32,40,41].

To elucidate the robust cycle stability of the $BiPO_4$@C electrode, we added the structural tests of the electrode surface and cross-section with multiple sets and performed a statistical analysis of the volume expansion. As expected, the $BiPO_4$@C electrode surface retained an intact structure even after 100 cycles (Figure S9a,b), whereas commercial micro-sized $BiPO_4$ electrodes exhibited obvious structural fragmentation (Figure S10a,b). Figure S9c,d shows the cross-sectional changes of the $BiPO_4$@C electrodes before and after cycling. Specifically, the thickness of the $BiPO_4$@C electrode is 20.31 μm before potassium insertion. After repeated potassiation/depotassiation, the thickness increases to 29.74 μm, and the corresponding volume expansion rate is 46.4%. In contrast, the commercial micro-sized $BiPO_4$ electrode showed a volume expansion of 95.5%, and the electrode showed obvious signs of loosening and cracking (Figure S10c,d). It is clear that the $BiPO_4$@C electrode, which combines the nanoscale effect and carbon-constrained structure, has significant resistance to volume expansion, which is the key to achieving stable potassium-ion storage. In addition, Electrochemical Impedance Spectroscopy (EIS) tests were carried out under different cycle conditions (Figure S11). Clearly, at high frequencies, the $BiPO_4$@C electrode has a smaller semicircle, which means a lower impedance. Especially after the formation of the SEI film during the first cycle, the impedance decreases significantly and gradually stabilizes even after 50 to 100 cycles (Figure S11a). In contrast, the $BiPO_4$ electrode consistently showed a large semicircle (Figure S11b), which can be attributed to the large interfacial impedance due to continuous volume expansion and electrode cracking. Overall, further testing confirms that the $BiPO_4$@C electrode combines both nanoscale dimensions and carbon layer properties, is highly resistant to the volume strain inherent in alloy–dealloy reactions, achieves a robust structure and significantly improves cycle stability.

2.3. Kinetic Analysis

To ascertain the origin of the excellent rate performance of the $BiPO_4$@C electrode, further tests were carried out on the kinetic and pseudocapacitive behavior. In detail, as depicted in Figure 4a, the five CV curves obtained at different sweep rates (0.1, 0.2, 0.6, 0.8, and 1.0 mV/s) show similar profiles and regular change trends of the redox peaks. The capacitive effect is calculated from the relationship between the measured peak current (i) and the sweep rate (v) ($i = av^{b}$), where b is the slope of the plot of log i versus log v. The atypical diffusion-controlled process corresponds to $b = 0.5$, while $b = 1.0$ indicates surface induced capacitive behavior. Furthermore, Figure 4b shows that the *b* values of the several peaks are distributed between 0.61 and 0.75, suggesting that the $BiPO_4$@C electrode follows a "battery-capacitance dual-mode" potassium storage mechanism dominated by surface capacitive behavior. Moreover, the proportion of capacitance-controlled and diffusion-controlled processes contributing to the total specific capacity can also be quantified according to the equation of $i = k_1 v + k_2 v^{1/2}$, where $k_1 v$ and $k_2 v^{1/2}$ are to be assigned as the relative contributions of the capacitive and intercalation processes, respectively. As expected, the capacitive percentage was observed to be 31, 31, 43, 49 and 60% at scanning rates of 0.1, 0.2, 0.6, 0.8, and 1.0 mV s^{-1}, respectively (Figure 4c,d). The high capacitive behavior is primarily attributable to the abundant surface reaction sites afforded by the ultrafine structure of $BiPO_4$@C and the adsorption/desorption capacity of K^+ by the ultrathin carbon layer, undoubtedly resulting in fast K-ion storage kinetics and ultralong cycling life. Meanwhile, the galvanostatic intermittent titration technique (GITT) measurements were carried out to identify the underlying causes of the superior K-ion storage kinetics obtained in the $BiPO_4$@Celectrode. As depicted in Figure 4e, the GITT curve of the $BiPO_4$@C electrode exhibits a high specific capacity, low electrochemical polarization and standard redox potential. Moreover, from the pulse current time (s), potential difference (ΔE_S) and electrode parameters in the collected GITT profiles, the potassium-ion diffusion coefficient (D_{K+}) is calculated. The calculated D_{K+} values during discharging (4.20×10^{-13}~3.95×10^{-12} cm^2 s^{-1}) and charging (1.2×10^{-12}~1.65×10^{-11} cm^2 s^{-1}) are significantly higher than micro-sized $BiPO_4$ electrode (discharging: 7.8×10^{-13}~1.82×10^{-14} cm^2 s^{-1}, charging: 1.2×10^{-13}~3.5×10^{-11} cm^2 s^{-1}) (Figures 4f and S12), also significantly exceeds some of the reported phosphate anodes [42–44]. The high K^+ values indicate fast potassiation and depotassiation kinetics and excellent rate performance. The rapid potassium storage capacity of well-designed ultra-fine $BiPO_4$@C electrodes can be attributed to their ingenious structural configuration, which provides an abundance of K^+ insertion sites and a short K^+ migration path, thereby accelerating the K^+ reaction kinetics (as summarized in Figure S13).

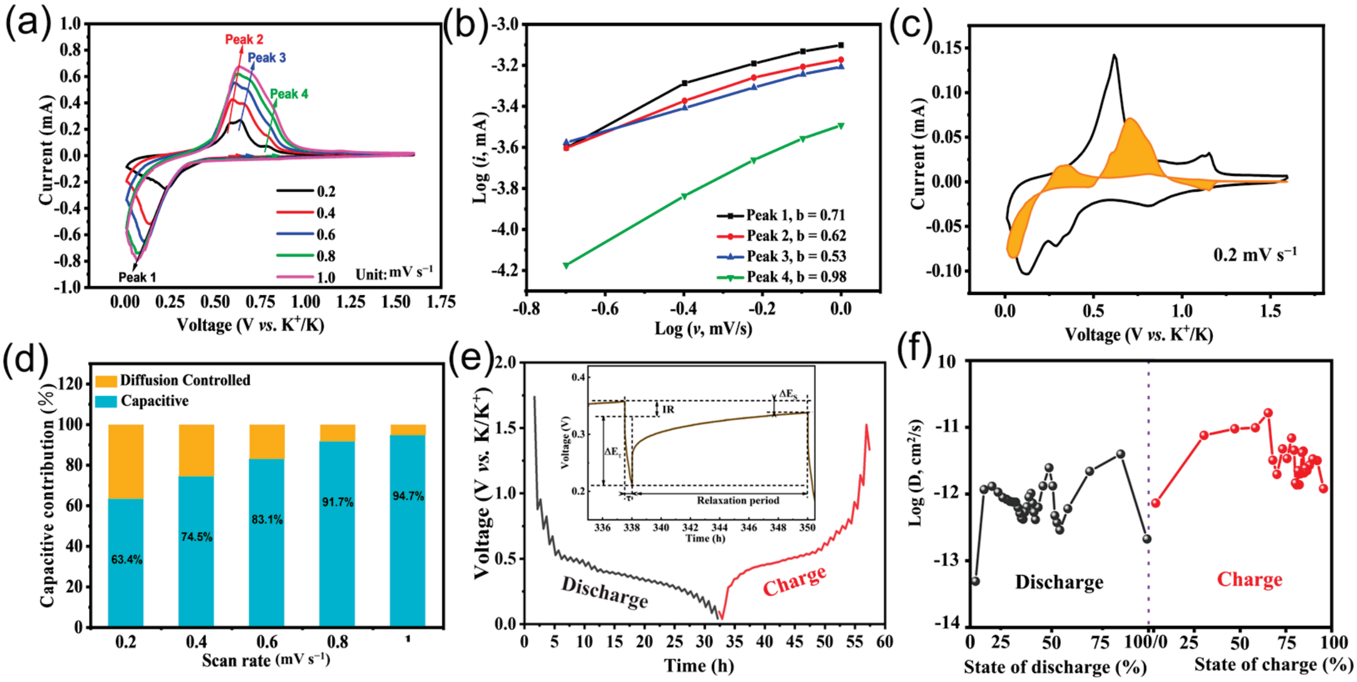

Figure 4. (**a**) CV curves at various scan rates, (**b**) the relationship between log (i) and log (v), and (**c**,**d**) contribution ratios of the capacitive-controlled capacity of the $BiPO_4$@C electrode. (**e**) GITT curves and (**f**) the calculated potassium-ion diffusion coefficients of the $BiPO_4$@C.

2.4. Electrochemical Mechanism

Systematic ex-situ XRD and TEM testing were further employed to reveal the potassium storage mechanism of the $BiPO_4$@C electrode. As depicted in Figure 5a, the $BiPO_4$@C electrode exhibits a series of diffraction peaks located at 21.3°, 25.5°, 27.1°, 28.3°, 29.1°, 31.2°, 34.4°, 36.8°, and 36.8° at open circuit voltage (OCV), which are attributed to the (−111), (020), (200), (002), (120), (−112), (−202), and (112) crystal planes of monoclinic $BiPO_4$. As the discharge progresses, the diffraction peak of $BiPO_4$ gradually diminishes, and three characteristic peaks (located at 27.3°, 38.1°, and 39.8°) corresponding to the metal Bi emerges at 0.7 V, indicating a conversion reaction of $BiPO_4$ ($BiPO_4 \rightarrow Bi$). Subsequently, the metal Bi is gradually alloyed into KBi_2 (31.1° and 32.6°) at 0.4 V and further converted to K_3Bi (28.6°) at 0.01 V ($Bi \rightarrow KBi_2 \rightarrow K_3Bi$). In the reverse charge process, the derivative peak of KBi_3 gradually disappears and converts into KBi_2 at 0.5 V before ultimately converting back to metallic Bi at 1.5 V, suggesting a gradual dealloying process ($K_3Bi \rightarrow KBi_2 \rightarrow Bi$). Subsequently, the ex-situ TEM test results provided further confirmed the experimental findings. Figure 5b,c clearly shows that the $BiPO_4$@C electrode produced uniform nanoparticles when discharged to 0.01 V, with crystal plane spacings of 0.20 and 0.311 nm, corresponding to the (400) crystal plane of K_3PO_4 and the (220) crystal phase of K_3Bi, respectively. Meanwhile, the (202) and (104) crystal planes of K_3Bi and the (200) and (422) crystal planes of K_3PO_4 were identified by selected area electron diffraction (SAED) (Figure 5d). Upon reverse charging to 1.6 V, ultrafine metallic Bi particles belonging to the (012) and (014) crystal planes were successively detected (Figure 5e–g), thereby demonstrating the excellent reversibility of the stepwise alloying-dealloying reaction of the $BiPO_4$@C electrode. To sum up, the in-situ/ex-situ test results combined with the CV curves reveal the reversible conversion and stepwise alloying/dealloying reaction mechanism of the $BiPO_4$@C electrode. The detailed evolution process of the mechanism is illustrated in Figure 5h and described as follows:

Stage I: (OCV–0.8 V, Conversion reaction and the formation of SEI layer):

$$BiPO_4 + 3\,K^+ + 3\,e^- \rightarrow K_3PO_4 + Bi$$

Stage II: (0.8–0.01 V, Step-alloying reaction):

$$2\,Bi + K^+ + e^- \rightarrow KBi_2$$

$$KBi_2 + 5\,K^+ + 5\,e^- \rightarrow 2\,K_3Bi$$

Stage III: (0.01–0.5 V, Dealloying reaction):

$$2\,K_3Bi - 5\,K^+ - 5\,e^- \rightarrow KBi_2$$

Stage IV: (0.5–1.6 V, Dealloying reaction):

$$KBi_2 - K^+ - e^- \rightarrow 2\,Bi$$

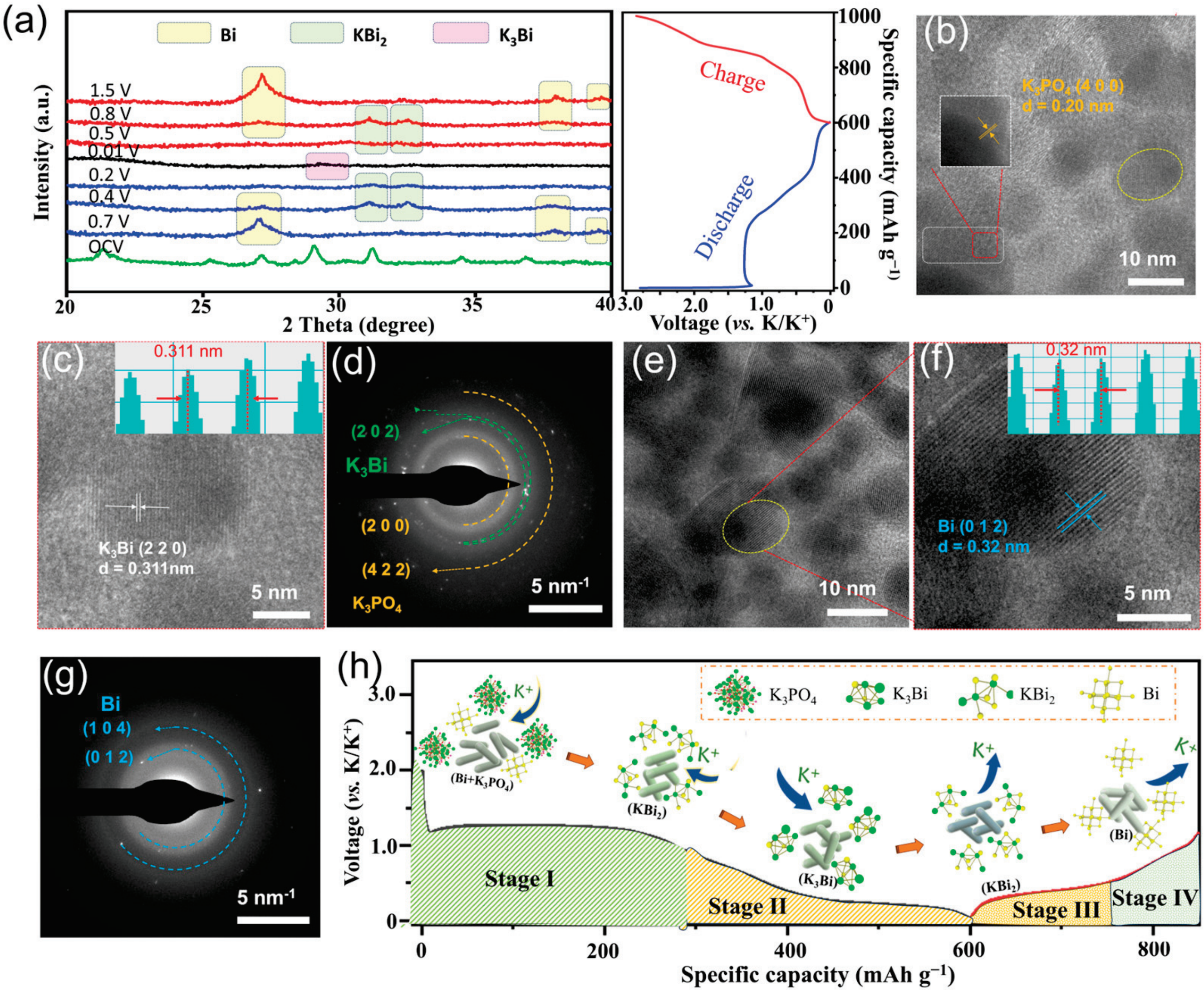

Figure 5. Investigation of the reaction mechanism of the BiPO$_4$@C anode: (**a**) In-situ XRD and corresponding discharge-charge curve. (**b**,**c**) HRTEM images and (**d**) SAED pattern after discharge to 0.01 V. (**e**,**f**) HRTEM images and (**g**) SAED pattern after charge to 1.6 V. (**h**) Illustration of the reaction mechanism of the BiPO$_4$@C anode.

2.5. Application Potential

To fully demonstrate the application potential of BiPO$_4$@C, we have re-prepared thick electrodes (about 4.0 mg/cm^2) and investigated their potassium storage performance. As shown in Figure S14, the BiPO$_4$@C thick electrode showed high specific capacity and superior cycling stability, maintaining 218.8 mAh g^{-1} after 80 cycles at 50 mA g^{-1} (Figure S14a), 180.9 mAh g^{-1} after 200 cycles at 200 mA g^{-1} (Figure S14b), and 130.3 mAh g^{-1} after 80 cycles at 1000 mA g^{-1} (Figure S14c). Impressively, the thick electrode demonstrated excellent rate performance, with capacities of 280.1, 219.9, 194.8, 152.4, and 102.6 mAh g^{-1} at 50–1000 mA g^{-1}, respectively (Figure S14d). Compared to the commercial BiPO$_4$ thick electrode, the BiPO$_4$@C thick electrode has significantly better structural advantages, as evidenced by its specific capacity, capacity retention rate and rate performance at various current densities (Figure S15). Overall, the BiPO$_4$@C electrodes maintained excellent cycling stability and rate performance even at the increased loading mass of 4.0 mg cm^{-2}, which also confirms its potential for commercialization. The excellent performance is attributed to the nanosized BiPO$_4$ significantly reducing the volume strain and increasing the embedded potassium sites; the incorporation of the bulk and open-skeleton anion PO_4^{3-} serves to mitigate the considerable volume distortion and generates the high ionic conductivity product (K_3PO_4) to ameliorate the poor ionic transport due to the structural deformation.

3. Experimental

3.1. Sample Preparation

Synthesis of $BiPO_4$@C nanorods. All chemicals were analytical reagent grade and used as received without further treatment. $BiPO_4$@C nanorods were synthesized using a typical solvothermal method. First, 0.5 mmol $Bi(NO_3)_3$ (99%, Aladdin Reagent Co., Ltd., Shanghai, China) and 0.5 mmol $NH_4H_2PO_4$ (99%, Aladdin Reagent Co., Ltd., China) were dissolved in 30 mL of ethylene glycol (99%, Aladdin Reagent Co., Ltd., China) with stirring for 6 h. Then, 1 mL of deionized (DI) water was added and stirred rapidly for 5 min. The mixture was transferred to a 50 mL autoclave and heated at 160 °C for 12 h. The $BiPO_4$ nanorods were washed six times by centrifugation with ethanol and DI water. Finally, they were dried overnight at 80 °C.

3.2. Electrochemical Measurements

The working electrodes were prepared by mixing active materials, Super P, and polyvinylidene fluoride (PVDF) in a weight ratio of 7:2:1 with N-methyl-2-pyrrolidone (NMP) as solvent. The CR2032 half-cells were assembled with K-metal, glass fiber (Whatman), and 3 M potassium bis(fluorosulfonyl)imide (KFSI) in dimethyl ether (DME) as the counter electrodes, the separators, and the electrolyte, respectively. Cyclic voltammetry (CV) and electrochemical impedance spectroscopy (EIS, frequency range from 1.0×10^5 to 0.1 Hz) tests were performed on an Autolab instrument (PGSTAT 302). Galvanostatic charge-discharge tests were performed on a Neware battery tester (Neware CT-4008). The mass loading of the active materials ($BiPO_4$@C) was about 1.2 mg cm^{-2}. And the specific capacity was based on the mass of $BiPO_4$@C.

4. Conclusions

In summary, we have integrated the dual strategies of architecture engineering and anion tuning to construct an ultrathin carbon-coated $BiPO_4$ nanorods ($BiPO_4$@C) electrode to suppress volume distortion and unclog electron transport pathways. The ultrathin nanorods provided a substantial number of electrochemical reaction sites, negated the size-related volume strain effect, and also shortened the ion transport distance. Meanwhile, the incorporation of an ultrathin carbon layer and bulk PO_4^{3-} served to defend and buffer the volume expansion associated with the alloying-dealloying process, thereby markedly enhancing the cycling stability of the $BiPO_4$@C anode. Significantly, the in-situ generated K_3PO_4 with high ionic conductivity acts as a bridge to unblock the electron/ion transport pathway and significantly improves the rate performance. Moreover, the preparation and testing of thick electrodes confirmed the excellent electrochemical performance and application potential of $BiPO_4$@C electrodes. Thus, this work highlights the significance of architecture engineering and anion-tuning strategy in rationally designing high-performance electrodes for K-ion batteries.

Supplementary Materials: The following supporting information can be downloaded at: https://www.mdpi.com/article/10.3390/molecules30030729/s1, Figure S1: SEM images of $BiPO_4$@C composites with different raw material concentrations; Figure S2: SEM images of $BiPO_4$@C composites at different reaction temperatures; Figure S3: SEM images of $BiPO_4$@C composites at different reaction times; Figure S4: XRD patterns and Rietveld refinement plots of $BiPO_4$@C; Figure S5: XRD pattern of $BiPO_4$@C residue after the TGA test; Figure S6: SEM image and XRD patterns of commercial micro-sized $BiPO_4$; Figure S7: Comparison of rate performance between $BiPO_4$@C anode and the previously reported Bi-based compound anode in PIBs.; Figure S8: Cycling performances of (a) $BiPO_4$@C and (b) commercial micro-sized $BiPO_4$ anodes at a current density of 1.0 A g^{-1}; Figure S9: Surface and cross-sectional SEM images of the $BiPO_4$@C electrode after 100 cycles; Figure S10: Surface and cross-sectional SEM images of the $BiPO_4$ electrode after 100 cycles; Figure S11: EIS results of the (a) $BiPO_4$@C electrode and (b) commercial micro-sized $BiPO_4$ electrode before and after different cycles at 500 mA g^{-1}; Figure S12: (a) GITT curves, (b) the corresponding detailed voltage response in a single current pulse, and the K^+ diffusion coefficient values (D_{K+}) during the (c) discharge and (d) charge process; Figure S13: Schematic illustration of potassium-ion diffusion in the nanosize structure; Table S1: Crystallographic parameters from Rietveld refinement for the XRD pattern of $BiPO_4$@C.

Author Contributions: Conceptualization, H.C. and H.Z.; methodology, H.C.; investigation, Y.L. (Yong Li) and Y.L. (Yuanjie Liu); resources, X.C.; writing—original draft preparation, H.C.; writing—review and editing, H.Z. and J.Z.; All authors have read and agreed to the published version of the manuscript.

Funding: This research was funded by the Science and Technology Program of XPCC (NO.2023AB031; NO.2023AA007) and the Xinjiang Production and construction corps new energy industry innovation research institute construction project (NO.2023-02-20240106).

Institutional Review Board Statement: Not applicable.

Informed Consent Statement: Not applicable.

Data Availability Statement: The dataset is available upon request from the authors.

Acknowledgments: The authors thank all the help from their laboratory companions.

Conflicts of Interest: The authors declare no conflicts of interest.

References

1. Zhou, W.; Mo, Y.; Gao, P.; Wang, K.X.; Ke, J.L.; Liu, Z.; Chen, S.; Liu, J.L. Decoupling Interfacial Kinetics Realizes 5C Fast Charging of Potassium-Ion Batteries Using Graphite Anode. *Adv. Funct. Mater.* **2024**, *34*, 2312994. [CrossRef]
2. Chen, C.; Zhong, J.; Deng, H.L.; Wei, Q.L.; Shen, X.H.; Jia, X.X.; Li, S.Y.; Zhang, Q.S.; Zhu, J.; Lu, B.A.; et al. Advanced Potassium-Ion Batteries with High Areal Capacity. *CCS Chem.* **2024**, *6*, 1011–1023. [CrossRef]
3. Tian, Y.S.; Zeng, G.B.; Rutt, A.; Shi, T.; Kim, H.; Wang, J.Y.; Koettgen, J.; Sun, Y.Z.; Ouyang, B.; Chen, T.; et al. Promises and Challenges of Next-Generation "Beyond Li-ion" Batteries for Electric Vehicles and Grid Decarbonization. *Chem. Rev.* **2021**, *121*, 1623–1669. [CrossRef]
4. Ma, M.; Chong, S.K.; Yao, K.; Liu, H.K.; Dou, S.X.; Huang, W. Advanced anode materials for potassium batteries: Sorting out opportunities and challenges by potassium storage mechanisms. *Matter* **2023**, *6*, 3220–3273. [CrossRef]
5. Wang, J.L.; Huang, Z.J.; Zhang, W.; Li, Q.H.; Liang, Z.X.; Lu, J.J.; Lin, Z.Y.; Wang, G.; Wu, J.X.; Huang, S.M. Balancing Graphitic Nanodomains and Heteroatom Doping in Hard Carbons Toward High Capacity and Durable Potassium-Ion Battery Anodes. *Adv. Funct. Mater.* **2024**, *34*, 2409937. [CrossRef]
6. Xiao, Z.T.; Wang, X.P.; Meng, J.S.; Wang, H.; Zhao, Y.L.; Mai, L.Q. Advances and perspectives on one-dimensional nanostructure electrode materials for potassium-ion batteries. *Mater. Today* **2022**, *56*, 114–134. [CrossRef]
7. He, Y.N.; Xu, Y.F.; Zhang, M.; Xu, J.Z.; Chen, B.B.; Zhang, Y.X.; Bao, J.C.; Zhou, X.S. Confining ultrafine SnS nanoparticles in hollow multichannel carbon nanofibers for boosting potassium storage properties. *Sci. Bull.* **2022**, *67*, 151–160. [CrossRef]
8. Luo, W.D.; Feng, Y.H.; Shen, D.Y.; Zhou, J.; Gao, C.T.; Lu, B.A. Engineering Ion Diffusion by CoS@SnS Heterojunction for Ultrahigh-Rate and Stable Potassium Batteries. *ACS Appl. Mater. Interfaces* **2022**, *14*, 16379–16385. [CrossRef]
9. Lin, X.P.; Xue, F.F.; Zhang, Z.G.; Li, Q.H. Sb nanoparticles encapsulated in N-doped carbon nanotubes as freestanding anodes for high-performance lithium and potassium ion batteries. *Rare Met.* **2023**, *42*, 449–458. [CrossRef]
10. Chong, S.K.; Ma, M.; Yuan, L.L.; Qiao, S.Y.; Dong, S.H.; Liu, H.K.; Dou, S.X. Hierarchical Encapsulation and Rich sp(2) N Assist Sb_2Se_3-Based Conversion-Alloying Anode for Long-Life Sodium- and Potassium-Ion Storage. *Energy Environ. Mater.* **2023**, *6*, e1245. [CrossRef]
11. Zhang, P.; Wei, Y.; Zhou, S.J.; Soomro, R.A.; Jiang, M.C.; Xu, B. A metal-organic framework derived approach to fabricate in-situ carbon encapsulated Bi/Bi_2O_3 heterostructures as high-performance anodes for potassium ion batteries. *J. Colloid Interf. Sci.* **2023**, *630*, 365–374. [CrossRef]

12. Yang, Y.L.; Wang, J.; Liu, S.Q.; Zhu, W.W.; Ye, G.Y.; Yi, X.H.; Lu, B.A. Nature of bismuth and antimony based phosphate nanobundles/graphene for superior potassium ion batteries. *Chem. Eng. J.* **2022**, *435*, 134746. [CrossRef]
13. Liu, G.P.; Sun, Z.P.; Shi, X.Y.; Wang, X.Y.; Shao, L.Y.; Liang, Y.H.; Lu, X.Y.; Liu, J.W.; Guo, Z.P. 2D-Layer-Structure Bi to Quasi-1D-Structure $NiBi_3$: Structural Dimensionality Reduction to Superior Sodium and Potassium Ion Storage. *Adv. Mater.* **2023**, *35*, 2305551. [CrossRef]
14. Xu, J.Y.; Lai, C.L.; Duan, L.P.; Zhang, Y.X.; Xu, Y.F.; Bao, J.C.; Zhou, X.S. Anchoring ultrafine CoP and CoSb nanoparticles into rich N-doped carbon nanofibers for efficient potassium storage. *Sci. China Mater.* **2022**, *65*, 43–50. [CrossRef]
15. Lin, Z.Y.; Zhang, W.; Peng, J.; Li, Q.H.; Liang, Z.X.; Wang, G.Y.; Wang, J.L.; Wang, G.; Huang, Z.J.; Huang, S.M. Synergistic Regulation of Polyselenide Dissolution and Na-Ion Diffusion of Se-Vacancy-Rich Bismuth Selenide toward Ultrafast and Durable Sodium-Ion Batteries. *Adv. Energy Mater.* **2024**, *14*, 2402110. [CrossRef]
16. Wang, G.Y.; Li, Q.H.; Zhang, W.; Wu, J.W.; Fan, W.B.; Wang, L.X.; Liang, Z.X.; Huang, Z.J.; Lin, Z.Y.; Wang, G.; et al. Unveiling the Synergy of Architecture and Anion Vacancy on Bi_2Te_{3-x}@NPCNFs for Fast and Stable Potassium Ion Storage. *ACS Appl. Mater. Interfaces* **2024**, *16*, 13858–13868. [CrossRef]
17. Zhao, X.X.; Zhang, C.L.; Yang, G.W.; Wu, Y.H.; Fu, Q.; Zhao, H.P.; Lei, Y. Bismuth selenide nanosheets confined in thin carbon layers as anode materials for advanced potassium-ion batteries. *Inorg. Chem. Front.* **2021**, *8*, 4267–4275. [CrossRef]
18. Yao, J.; Zhang, C.L.; Yang, G.W.; Sha, M.; Dong, Y.L.; Fu, Q.; Wu, Y.H.; Zhao, H.P.; Wu, M.K.; Lei, Y. Bismuth Nanoparticles Confined in Carbonaceous Nanospheres as Anodes for High-Performance Potassium-Ion Batteries. *ACS Appl. Mater. Interfaces* **2021**, *13*, 31766–31774. [CrossRef]
19. Sun, X.P.; Zhang, B.; Chen, M.; Wang, L.; Wang, D.B.; Man, R.X.; Iqbal, S.; Tian, F.; Qian, Y.T.; Xu, L.Q. Space-confined growth of Bi_2Se_3 nanosheets encapsulated in N-doped carbon shell lollipop-like composite for full/half potassium-ion and lithium-ion batteries. *Nano Today* **2022**, *43*, 101408. [CrossRef]
20. Hsieh, Y.Y.; Tuan, H.Y. Architectural van der Waals Bi_2S_3/Bi_2Se_3 topological heterostructure as a superior potassium-ion storage material. *Energy Storage Mater.* **2022**, *51*, 789–805. [CrossRef]
21. Wang, Z.Y.; Duan, C.Q.; Wang, D.; Dong, K.Z.; Luo, S.H.; Liu, Y.G.; Wang, Q.; Zhang, Y.H.; Hao, A.M. BiSb@Bi_2O_3/SbO_x encapsulated in porous carbon as anode materials for sodium/potassium-ion batteries with a high pseudocapacitive contribution. *J. Colloid Interf. Sci.* **2020**, *580*, 429–438. [CrossRef]
22. Zou, Z.G.; Wang, Q.; Zhu, K.; Ye, K.; Wang, G.L.; Cao, D.X.; Yan, J. Ultrathin-Walled Bi_2S_3 Nanoroll/MXene Composite toward High Capacity and Fast Lithium Storage. *Small* **2022**, *18*, 2106673. [CrossRef] [PubMed]
23. Sun, Z.; Liu, M.; Khan, R.; Huang, L.; Wu, Y.; Zhou, Y. Strain engineering of Bi_2Se_3 anode for ultrafast sodium storage. *Mater. Today Chem.* **2023**, *29*, 101401. [CrossRef]
24. Wu, Z.B.; Liang, G.M.; Wu, J.X.; Pang, W.K.; Yang, F.H.; Chen, L.B.; Johannessen, B.; Guo, Z.P. Synchrotron X-Ray Absorption Spectroscopy and Electrochemical Study of Bi_2O_2Se Electrode for Lithium-/Potassium-Ion Storage. *Adv. Energy Mater.* **2021**, *11*, 2100185. [CrossRef]
25. Lin, J.Y.; Lu, S.J.; Zhang, Y.F.; Zeng, L.X.; Zhang, Y.; Fan, H.S. Selenide-doped bismuth sulfides ($Bi_2S_{3-x}Se_x$) and their hierarchical heterostructure with ReS_2 for sodium/potassium-ion batteries. *J. Colloid Interf. Sci.* **2023**, *645*, 654–662. [CrossRef]
26. Wang, Y.J.; Li, L.P.; Li, G.S. One-step synthesis of $SbPO_4$ hollow spheres by a self-sacrificed template method. *RSC Adv.* **2012**, *2*, 12999–13006. [CrossRef]
27. Jiang, Q.T.; Li, X.F.; Hao, Y.C.; Zuo, J.X.; Duan, R.X.; Li, J.; Cao, G.Q.; Wang, J.J.; Wang, J.; Li, M.; et al. Double-layer phosphates coated Mn-based oxide cathodes for highly stable potassium-ion batteries. *Energy Storage Mater.* **2023**, *58*, 101–109.
28. Jiang, Q.; Li, X.; Hao, Y.; Zuo, J.; Duan, R.; Li, J.; Cao, G.; Wang, J.; Wang, J.; Li, M.; et al. Oxygen-Vacancy-Assisted Dual Functional Surface Coatings Suppressing Irreversible Phase Transition of Li-Rich Layered Oxide Cathodes. *Adv. Funct. Mater.* **2025**, *35*, 2400670. [CrossRef]
29. Wu, J.W.; Wang, G.Y.; Zhang, W.; Wang, L.X.; Peng, J.; Li, Q.H.; Liang, Z.X.; Fan, W.B.; Wang, J.Z.; Huang, S.M. Universal architecture and defect engineering dual strategy for hierarchical antimony phosphate composite toward fast and durable sodium storage. *J. Energy Chem.* **2024**, *90*, 110–119. [CrossRef]
30. Wang, H.Q.; Gou, L.; Jing, W.F.; An, D.; Li, Y.; Wang, M.; Li, N.; Hu, S.L.; He, Y.B. Highly microporous $SbPO_4$/BC_x hybrid anodes for sodium-ion batteries. *Mater. Adv.* **2020**, *1*, 206–214. [CrossRef]
31. Pan, J.; Chen, S.L.; Fu, Q.; Sun, Y.W.; Zhang, Y.C.; Lin, N.; Gao, P.; Yang, J.; Qian, Y.T. Layered-Structure $SbPO_4$/Reduced Graphene Oxide: An Advanced Anode Material for Sodium Ion Batteries. *ACS Nano* **2018**, *12*, 12869–12878. [CrossRef] [PubMed]
32. Hu, J.X.; Li, H.Z.; Zheng, J.Q.; Lai, Y.Q.; Zhang, Z.A. An advanced $BiPO_4$/super P anode material for high-performance potassium-ion batteries. *Chem. Commun.* **2021**, *57*, 13178–13181. [CrossRef]
33. Hu, J.X.; Xie, Y.Y.; Zheng, J.Q.; Lai, Y.Q.; Zhang, Z.A. Unveiling nanoplates-assembled Bi_2MoO_6 microsphere as a novel anode material for high performance potassium-ion batteries. *Nano Res.* **2020**, *13*, 2650–2657. [CrossRef]
34. Tong, H.G.; Chen, S.; Tu, J.W.; Zeng, X.H.; Wang, C.L.; Wang, P.C.; Chen, Q.W. Bi_2O_3 particles embedded in carbon matrix as high-performance anode materials for potassium ion batteries. *J. Power Sources* **2022**, *549*, 232140. [CrossRef]

35. Chong, S.K.; Yuan, L.L.; Zhou, Q.W.; Wang, Y.K.; Qiao, S.Y.; Li, T.; Ma, M.; Yuan, B.Y.; Liu, Z.Q. Bismuth Telluride Nanoplates Hierarchically Confined by Graphene and N—Doped C as Conversion-Alloying Anode Materials for Potassium—Ion Batteries. *Small* **2023**, *19*, 2303985. [CrossRef]
36. Yuan, L.L.; Zhou, Q.W.; Li, T.; Wang, Y.K.; Liu, Z.Q.; Chong, S.K. Promoting superior K—Ion storage of Bi_2S_3 nanorod anode via graphene physicochemical protection and electrolyte stabilization effect. *Appl. Energy* **2022**, *322*, 119471. [CrossRef]
37. Diwakar, K.; Rajkumar, P.; Subadevi, R.; Arjunan, P.; Sivakumar, M. Electrospun assisted antimony phosphate ($SbPO_4$) anode for elevated performance in sodium and lithium ion charge storage application. *J. Alloys Compd.* **2021**, *870*, 159317. [CrossRef]
38. Li, Q.; Zhang, W.; Peng, J.; Zhang, W.; Liang, Z.X.; Wu, J.W.; Feng, J.J.; Li, H.X.; Huang, S.M. Metal–Organic Framework Derived Ultrafine Sb@Porous Carbon Octahedron via In Situ Substitution for High-Performance Sodium-Ion Batteries. *ACS Nano* **2021**, *15*, 15104–15113. [CrossRef]
39. Li, Q.; Zhang, W.; Peng, J.; Yu, D.D.; Liang, Z.X.; Zhang, W.; Wu, J.W.; Wang, G.Y.; Li, H.X.; Huang, S.M. Nanodot-in-Nanofiber Structured Carbon-Confined Sb_2Se_3 Crystallites for Fast and Durable Sodium Storage. *Adv. Funct. Mater.* **2022**, 2112776. [CrossRef]
40. Lee, Y.; Kang, J.M.; Ahn, J.; Ko, W.; Park, H.Y.; Lee, S.; Lee, S.; Yoo, J.K.; Kim, J. A high-energy conversion-type cathode activated by amorphization for Li rechargeable batteries. *J. Mater. Chem. A* **2022**, *10*, 20080–20089. [CrossRef]
41. Ou, M.; Ling, Y.; Ma, L.; Liu, Z.H.; Luo, D.Q.; Xu, L.M. Synthesis and Li-storage property of flower-like $SbPO_4$ microspheres. *Mater. Lett.* **2018**, *224*, 100–104. [CrossRef]
42. Li, Q.H.; Yu, D.D.; Peng, J.; Zhang, W.; Huang, J.L.; Liang, Z.X.; Wang, G.Y.; Li, H.X.; Xiong, S.Y.; Wang, J.Z.; et al. Efficient Polytelluride Anchoring for Ultralong-Life Potassium Storage: Combined Physical Barrier and Chemisorption in Nanogrid-in-Nanofiber. *Nano-Micro Lett.* **2024**, *16*, 77. [CrossRef] [PubMed]
43. Deng, S.; Li, C.; Feng, W.; Cao, Y.; Tian, X.; Bi, H.; Zhou, S.; Wong, C.-P.; Dong, Y. Ultra-small ZnS enhanced by Fe-N-C for advanced potassium-ion hybrid capacitors: Electronic transfer dynamics and ion adsorption capability. *Nano Energy* **2023**, *106*, 108065. [CrossRef]
44. Sha, M.; Liu, L.; Zhao, H.; Lei, Y. Anode materials for potassium-ion batteries: Current status and prospects. *Carbon Energy* **2020**, *2*, 350–369. [CrossRef]

Disclaimer/Publisher’s Note: The statements, opinions and data contained in all publications are solely those of the individual author(s) and contributor(s) and not of MDPI and/or the editor(s). MDPI and/or the editor(s) disclaim responsibility for any injury to people or property resulting from any ideas, methods, instructions or products referred to in the content.

molecules

MDPI

Article

A Spontaneous Complexation–Exfoliation Strategy for a Flexible Anode Towards Superior Durable and Ultrafast Lithium-Ion Batteries

Heying Chu [1], Jingchuan Zhang [1], Pengsen Zhao [1], Yong Li [1], Zhaoxia Liu [2,*] and Hongzhou Zhang [1,*]

[1] College of Mechanical and Electronic Engineering, Tarim University, Alar 843300, China; chuheying@taru.edu.cn (H.C.); zhangjingchuan@taru.edu.cn (J.Z.); zpstaru@163.com (P.Z.); deyuzhijia@163.com (Y.L.)
[2] College of Mechanical and Electronic Engineering, Wuhan Donghu University, Wuhan 430017, China
* Correspondence: liuzhaoxia@wdu.edu.cn (Z.L.); shenzhouxing@taru.edu.cn (H.Z.)

Abstract: Transition metal oxides are considered promising anode materials for high performance flexible electrodes due to their abundant reserves and excellent specific capacity. However, their inherent low conductivity, large volume effect, and poor cycling performance limit their applications. Herein, we report a novel “spontaneous complexation and exfoliation” strategy for the fabrication of flexible MnO NCs@rGO thin-film electrodes, which overcomes the aforementioned drawbacks and pushes the mechanical flexibility and lithium-ion (Li^+) storage performance to a higher level. The combination of large-area few-layer reduced graphene oxide (rGO) films and ultrafine MnO nanocrystals (MnO NCs) provides a high density of electrochemical active sites. Notably, the layer-by-layer embedded structure not only enables the MnO NCs@rGO electrodes to withstand various mechanical deformations but also produces a strong synergistic effect of enhanced reaction kinetics by providing an enlarged electrode/electrolyte contact area and reduced electron/ion transport resistance. The elaborately designed flexible MnO NCs@rGO anode provides a specific capacity of about 1220 mAh g^{-1} over 1000 cycles, remarkable high-rate capacity (50.0 A g^{-1}), and exceptional cycling stability. Finally, the assembled flexible lithium-ion full cells achieve zero capacity loss during repeated large-angle bending, demonstrating immense potential as a high-performance flexible energy storage device. This work provides valuable insights into unique structural designs for durable and ultrafast lithium ion batteries.

Keywords: flexible electrode; free-standing; spontaneous complexation and exfoliation; layer-embedded structure; high rate; lithium-ion batteries

1. Introduction

Rapid advances in electronics have contributed significantly to the development of portable and wearable electronic devices that require high-performance batteries to operate [1,2]. Currently, the technology landscape is accelerating the shift towards flexibility and health-centric designs in electronic products [3]. The advent of bendable displays and chips in electronic devices has paved the way for innovative, flexible applications [4]. To achieve this vision, however, a crucial enabler is the cooperation of flexible energy storage devices. Lithium-ion batteries (LIBs) are currently widely used in small and medium-sized portable electronic products due to a number of advantageous characteristics, including high energy density, high output voltage, long cycle lifespan, and environmental friendliness [5]. However, there are still significant challenges to overcome in the application of flexible devices, particularly the necessity to combine electrode materials with favorable mechanical durability, minimal weight, elevated specific capacity, extended cycle life, and optimal safety [6].

Commercial LIBs are currently characterized by a substantial degree of bulk and weight [7,8], which can be attributed to the utilization of a considerable number of collectors, binders, and conductive agents. Compared to conventional electrodes, the self-supporting flexible electrodes eliminate the necessity for these inactive components. This increases the specific capacitance, reduces the cost and weight of the electrode material, and provides the opportunity for improved flexibility and processability [9]. Graphite, a traditional anode material, is inadequate for meeting the requirements of future high-specific-energy and high-capacity batteries due to its low theoretical specific capacity (372 mAh g^{-1}) and poor rate performance [10]. Other intercalated anode materials (such as $Li_4Ti_5O_{12}$ and TiO_2), known as "volumetric zero strain" materials, exhibit extremely long cyclic stability, but are limited by poor conductivity and high reaction potential [11–13]. Therefore, it is imperative to design and fabricate a new generation of flexible electrodes with higher reversible capacity, high-rate performance, long life, and low cost. Transition metal oxides, including CoO [14], Co_3O_4 [15,16], Fe_2O_3 [17], Fe_3O_4 [18,19], SnO_2 [20–22], NiO [23], MnO [24–26], and MoO_2 [27,28], etc., which exhibit high theoretical specific capacities, have emerged as potential candidates for high-performance anode materials. Among these, MnO nanocrystals have received increasing attention due to their numerous favorable properties, including relatively lower electrode potentials (1.032 V vs. Li^+/Li), high theoretical capacity, abundant reserves, and environmental compatibility [25]. However, the inherent low conductivity and the huge volume expansion of MnO electrodes during electrochemical processes result in structural collapse, rapid capacity decay, and difficulty withstanding high current charging. Furthermore, the discharge products, namely metallic Mn and Li_2O particles, are prone to agglomeration and precipitation. Researchers have endeavored to address these issues using a variety of means [24]. Of these, nanosizing and carbon-coating strategies are considered to be the most effective [29–31]. Nanosized particles can increase the electrochemical active sites and shorten the Li^+ transport distance, while carbon-coating can improve the conductivity, prevent the agglomeration of metal particles, and serve as a bulk strain relief layer to maintain the stability of the electrode material structure. However, the challenge remains in regards to achieving an ultrafine nanoparticle with a perfect carbon coating that exhibits optimal performance.

Herein, an "autonomous chelation and exfoliation" film-forming method was developed at room temperature, resulting in a layer-by-layer embedded flexible self-supported MnO NCs@rGO nanocomposite film after subsequent sintering. Specifically, the ultrafine MnO NCs are uniformly dispersed and confined within the rGO films, thereby forming a large-area three-dimensional ordered conductive network. The elaborately prepared MnO NCs@rGO film electrode perfectly inherits the advantages of rGO, including a thin layer, good conductivity, low weight, large specific surface area, and robust mechanical properties. Additionally, it effectively overcomes the inherent limitations of MnO, such as low conductivity, a huge volume effect, and rapid capacity decline. As an anode material for LIBs, the MnO NCs@rGO film displays ultra-high specific capacity, excellent cycling stability (1220 mAh g^{-1} over 1000 cycles), and exceptional rate performance (336.6 mAh g^{-1} at 50.0 A g^{-1}). Ultimately, the assembled flexible LIBs' full cells (MnO NCs@rGO//$LiCoO_2$) demonstrate remarkable flexibility and zero-diminished electrochemical stability. This study offers a valuable methodology for the development of ultra-light, flexible, and high-performance electrode materials for LIBs.

2. Results

2.1. Synthesis and Structural Characterization

Figure 1a illustrates the fabrication process of MnO NCs@rGO flexible films. A solution comprising manganese salts and graphene oxide (GO) is automatically chelated, deposited, and forms a dense film on a glass substrate under the reducing stimulus of HI acid [32]. Subsequently, the film is automatically stripped from the glass plate by infiltration into water. Following the high-temperature reduction process, the MnO NCs@rGO film is obtained. The delicate fabrication process of MnO NCs@rGO film can be attributed to the following aspects: firstly, the positive Mn^{2+} bond spontaneously interacts (interactions between -O···M and -COO···M) with GO, containing abundant oxygen-containing functional groups (-OH, -COOH, -O-) and electronegativity, and ultimately homogeneously anchors onto the surface of the GO nanosheets. Subsequently, the strong complexation and reduction property of the I^- ions promotes the colloidal association of GO, forming a large, dense rGO composite film. Finally, the composite films with free oxidized functional groups exhibit notable hydrophobicity, thereby enabling the spontaneous exfoliation from water (Figure S1, with an area of about 33 cm × 15 cm).

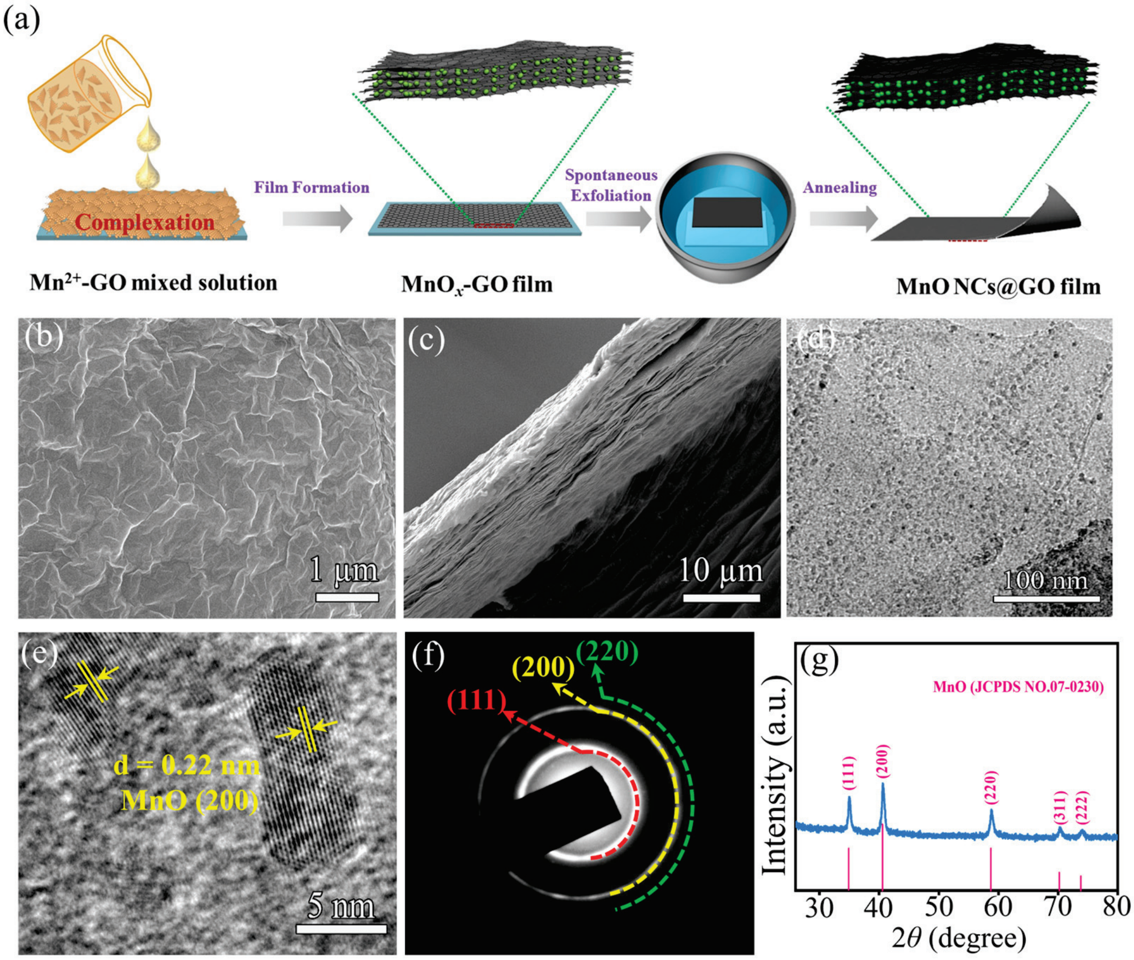

Figure 1. (**a**) Schematic diagram of the synthesis process of flexible MnO NCs@rGO thin films. (**b**) Surface and (**c**) cross-section SEM images, (**d**) TEM image, (**e**) HRTEM image, (**f**) corresponding SAED pattern, and (**g**) XRD pattern of flexible MnO NCs@rGO film.

Figure S2 shows a piece of MnO NCs@rGO film material with an area of 19 cm × 8 cm. It is evident that the composite film remains intact and dense, exhibiting notable flexibility and the ability to be bent randomly at large angles. In detail, the surface of the MnO NCs@rGO flexible film is rich and uniformly distributed with wrinkles formed by the interconnection of ultrathin rGO layers (as shown in Figure 1b). The smooth surface indicates that the MnO NCs exhibit an ultrafine particle size and are firmly embedded in the rGO interlayers. Furthermore, the cross-sectional scanning electron microscope (SEM) image (Figure 1c) clearly demonstrates that the thickness of the MnO NCs@rGO film is approximately 20 μm and consists of a uniform stacking of ultrathin rGO sheets, with a certain degree of interlayer spacing. This layer-embedded structure avoids MnO agglomeration and precipitation, enhances electrolyte wetting, facilitates rapid electron transport, inhibits the volume expansion of the active material during charging and discharging, and improves the mechanical stability and electrochemical lifetime. In contrast, the manganese oxide that was not protected by rGO exhibited a significant agglomeration phenomenon (as shown in Figure S3).

In order to gain insight into the existence form, distribution, and crystal structure of MnO NCs in the ultrathin layer structure of rGO, transmission electron microscopy (TEM), selected area electron diffraction (SAED), and X-ray diffraction (XRD) were employed. The TEM test results, as shown in Figures 1d and S4, demonstrate that the ultrafine MnO nanocrystals (with particle sizes of approximately 5~10 nm) are uniformly distributed on the surfaces of the ultrathin rGO layers. Moreover, the monodisperse MnO NCs display a discernible distance between them, indicating that the oxygen-containing functional groups in the GO effectively inhibit the agglomeration of the MnO NCs, even during the high-temperature reduction process. An appropriate spacing can also effectively prevent particle agglomeration during the charge/discharge cycling process, thereby enhancing the cycling stability of the material. Furthermore, the high-resolution TEM (HRTEM) images show an obvious lattice spacing of 0.318 nm (Figure 1e), corresponding to the (200) crystal plane of the cubic phase of MnO (JCPDS No. 07-0230) [33]. The corresponding SAED pattern in Figure 1f also identifies several crystal planes of MnO, including (200), (220), and (111). Subsequent XRD results (as shown in Figure 1g) display a series of diffraction peaks at 34.9, 40.5, 58.7, 70.2, and 73.8° corresponding to the (111), (200), (220), (311), and (222) crystal planes, which are consistent with the results for cubic MnO [33]. The broad diffraction peaks also suggest that the MnO nanoparticles are relatively small in size.

A systematic characterization was conducted using Raman, thermogravimetric-differential thermal analysis (TG-DTA), and X-ray photoelectron spectroscopy (XPS) tests to further clarify the state and content of MnO, as well as the presence of valence states of each element in the flexible MnO NCs@rGO thin films. Two distinct characteristic peaks located at 1333 and 1578 cm^{-1}, observed in the Raman results, can assigned to the D- and G-bands of carbon [34], respectively (Figure 2a). The corresponding I_D/I_G ratio is 1.17, indicating that the MnO NCs@rGO composite displays a higher density of defects and active sites. Furthermore, the contents of carbon and MnO in the MnO NCs@rGO composite were determined by the TG-DTA in air. As illustrated in Figure 2b, a pronounced decline in mass is observed in the 400–650 °C range, followed by a gradual increase in the 650–800 °C range, which is attributed to the oxidation reactions of MnO and C, respectively, as follows: (1) $C + O_2 \rightarrow CO_2\uparrow$; (2) $2MnO + O_2 \rightarrow 2MnO_2$. The DTA curves display a pronounced exothermic peak at about 520 °C, indicative of the combustion of rGO, while a less intense exothermic peak at about 600 °C is suggestive of the oxidation of MnO. In light of the aforementioned results, the contents of MnO and rGO in MnO NCs@rGO are calculated to be 58.1% and 41.9%, respectively. In addition, the characteristic signals of Mn ($2p_{1/2}$, $2p_{3/2}$, and 3s), O (1s), and C (1s) were identified in the full XPS spectrum (Figure S5). In Figure 2c, the high-resolution spectrum of the C 1s peaks can be fitted to four peaks. The strongest peak at 284.4 eV is attributed to graphitic carbon in rGO, while the other three weaker peaks are ascribed to the C-O bond (286.2 eV), the C=O bond (287.9 eV), and the O-C=O bond (289.0 eV), respectively [35]. A spin-energy separation of 6.0 eV for the Mn 3s doublet (as shown in Figure 2d) indicates that the Mn in the MnO NCs@rGO has a charge state of ~2. The Mn 2p spectrum, as shown in Figure 2e, can be divided into two peaks, located at 642.1 and 653.5 eV, which correspond to Mn $2p_{3/2}$ and Mn $2p_{1/2}$, respectively. Furthermore, the two peaks observed at 530.9 and 532.9 eV in the O 1s spectrum are ascribed to the Mn–O bonds and the surface oxidation layer of the rGO matrix (C–O–C) (Figure 2f) [36].

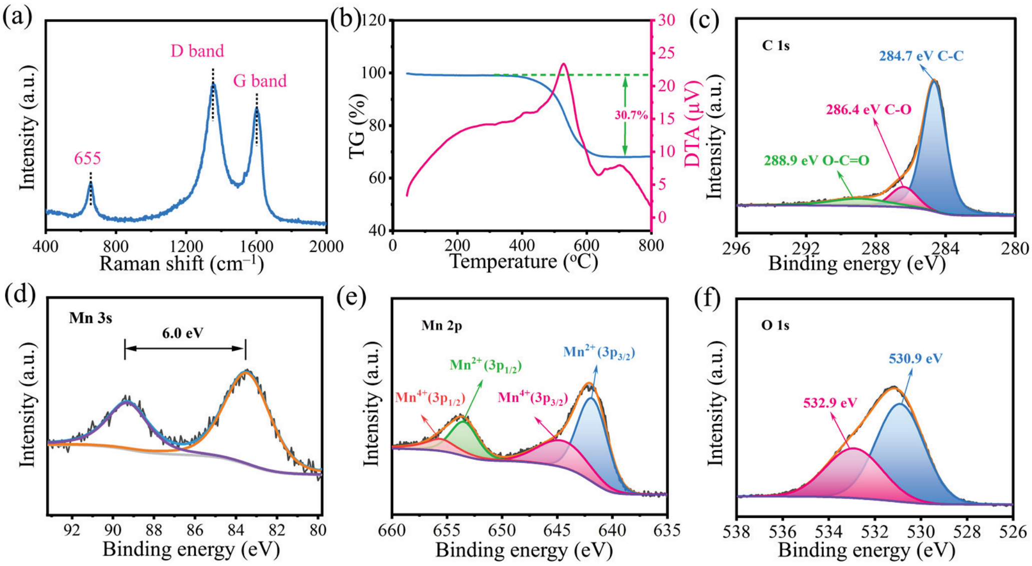

Figure 2. Material characterization of the MnO NCs@rGO film. (**a**) Raman spectra; (**b**) TG-DTA curve obtained at a heating rate of 10 °C $\min^{-1}$ in flowing air. High-resolution XPS spectra of (**c**) C 1s, (**d**) Mn 3s, (**e**) Mn 2p, and (**f**) O 1s.

2.2. Electrochemical Properties

A series of coin-type half-cells were assembled and coupled with Li metal as the counter electrode to evaluate the electrochemical behavior of the MnO NCs@rGO film electrode. Figures S6 and S7 present the crystalline phase and thin-layered structure of rGO, as well as optical photographs of the flexible self-supported structure of the MnO NCs@rGO film electrode. Figure 3a depicts the initial five cyclic voltammetry (CV) profiles of the MnO NCs@rGO film electrode within the voltage range of 0.01–3.0 V (vs. Li/Li^+) at a scan rate of 0.1 mV s^{-1}. In the initial cathodic loop, two cathodic peaks are observed at 0.68 and 0.26 V, which can be attributed to the reduction of Mn^{2+} to Mn^0, accompanied by the formation of Li_2O ($MnO + 2Li^+ + 2e^- \rightarrow Mn + Li_2O$) and the formation of the solid electrolyte interphase (SEI) layer [37,38]. Two additional peaks, situated at 1.41 and 1.14 V, may be due to the reduction of residual high-valent manganese oxide (MnO_x, $2 < x < 3$) on the surface of the rGO and the passivation reaction of the collector [38]. During the oxidative stage, two peaks at 1.33 V and 2.34 V are indicative of the gradual oxidative reaction of Mn^0, with a minor proportion of Mn^{2+} undergoing transformation to the valence of Mn^{x+} at elevated potentials [39]. Following the microstructural recombination of the electrode materials after the initial lithiation process, the reduction/oxidation peaks corresponding to MnO (located at 0.88/1.33 V) in the 2nd to 5th cycles were confirmed. In parallel, the reduction/oxidation peaks of Mn^{x+} were gradually weakened as a result of the microstructural reorganization of the electrode material. As illustrated in Figure 3b, the voltage plateau of the galvanostatic charge/discharge (GCD) curves coincides with the position of the redox peak observed in the CV results. The initial discharge and charge capacities of the MnO NCs@rGO film electrode were determined to be 1830 and 1160 mAh g^{-1}, respectively, with an initial Coulombic efficiency of 65% (based on the total mass of the MnO NCs@rGO film electrode). The irreversible capacity loss observed during the initial cycles was primarily attributed to the consumption of active lithium ions involved in the formation of the solid electrolyte interface (SEI) film. Subsequently, the Coulomb efficiency gradually increased, approaching 100% after three cycles, while the discharge and charge curves were essentially coincident. In terms of cycling stability, the MnO NCs@rGO film anode maintains a specific capacity of 1121 mAh g^{-1} after 200 cycles at a low current density of 0.2 A g^{-1}, with a capacity retention rate of about 96.8% (Figure 3c). In comparison, the MnO electrode demonstrated a tendency towards rapid capacity decline, while the pure rGO paper exhibited a considerably lower capacity than that of the MnO NCs@rGO film anode (Figures S8 and S9). Surprisingly, the specific capacity of the MnO NCs@rGO film anode remained stable after 1000 charge/discharge cycles at 500 mA g^{-1} (as shown in Figure 3d). Moreover, it showed a slight increase, which has been documented for numerous transition metal oxide anode materials [39,40]. This phenomenon can be attributed to the nanosizing of active materials, the expansion of the specific surface area, and the enhancement of electrochemical sites during high-current charging and discharging [41]. In contrast, the two opposing electrodes (MnO and rGO anodes) showed a rapid decrease in capacitance at the outset of the electrochemical reaction and maintained a very low capacitance thereafter, which can be attributed to structural instability (Figure S10).

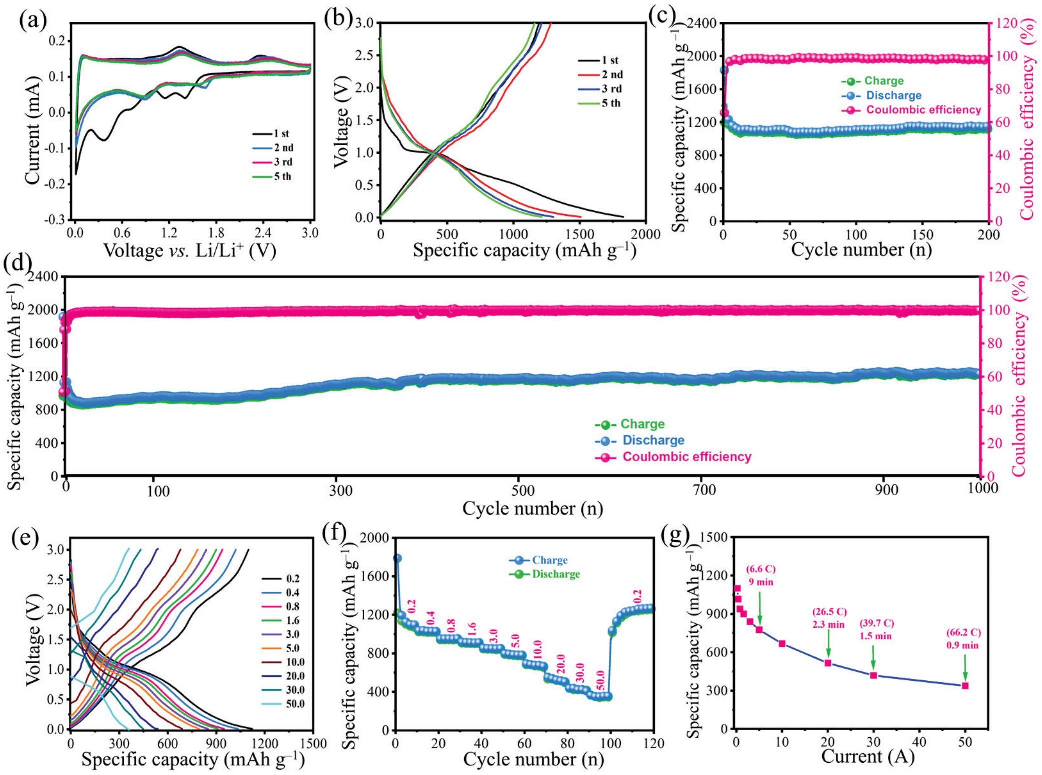

Figure 3. Electrochemical performance of the flexible MnO NCs@rGO film electrode: (**a**) CV curves 0.1 mV s^{-1}; (**b**) galvanostatic charge/discharge profiles and cycling performance at (**c**) 200 mA g^{-1} and (**d**) 500 mA g^{-1}; (**e**) galvanostatic charge/discharge profiles, (**f**) rate capability, and (**g**) corresponding relationship between current density and charge/discharge time at different current densities from 0.2 A to 50 A g^{-1}.

Furthermore, Figure 3e,f illustrates the constant GCD and rate performance curves at different current densities (0.2–50.0 A g^{-1}). Clearly, the voltage plateaus of the GCD curves are obvious, and with increasing current density, the plateaus regularly weaken, but these plateau positions remain relatively stable, which is attributed to the superconductivity reducing the electrochemical polarization. Figure 3f shows the excellent rate performance of the MnO NCs@rGO film electrode, exhibiting charge-specific capacities of 1100, 1015, 938.5, 899, 838.7, 775.4, 667, 515, 418.5, and 336.6 mAh g^{-1} at current densities of 0.2, 0.4, 0.8, 1.6, 3.0, 5.0, 10.0, 20.0, 30.0, and 50.0 A g^{-1}, respectively, which are much higher than those of the MnO, rGO electrodes (Figure S11) and electrode materials, based on those reported for MnO [6,24–27,37,40]. Surprisingly, even at an ultra-high current density of 50.0 A g^{-1} (equivalent to 66.2 C), the MnO NCs@rGO film electrodes demonstrate a reversible capacity of 336.6 mAh g^{-1}, which corresponds to the completion of a charge/discharge time of only 0.9 min (Figure 3g). The ultra-high current tolerance and corresponding ultra-high capacity indicate that the MnO NCs@rGO anodes possess exceptionally robust structural stability. The unrivalled rate performance and structural stability of the MnO NCs@rGO film anode are significantly superior to those reported for MnO_x-based electrodes (Table S1). As anticipated, the favorable cycling stability and excellent rate performance indicate a promising potential application in future high-specific-energy lithium-ion secondary batteries.

2.3. Electrochemical Reaction Mechanism

Furthermore, ex situ XRD tests were employed to investigate the detailed lithium-ion storage mechanism of the MnO NCs@rGO film anode, as shown in Figure S12. A diffraction peak is consistently present at 43.3°, attributed to the copper current collector (JCPDS No. 99-0034). The initial characteristic peaks at around 34.9 and 40.5 correspond to the (111) and (200) crystal planes, respectively, of the cubic phase of MnO (JCPDS No. 07-0230). Obviously, the diffraction peaks of MnO gradually weakened and disappeared at 0.38 V during discharge and were regenerated during subsequent charging. Meanwhile, the diffraction peaks corresponding to the rGO (002) crystal surface (located at 21.2°) gradually shifted to a smaller angle during the discharge process, confirming the expansion of the interlayer spacing, which can be attributed to the intercalation and adsorption of lithium ions within the interlayers. On the contrary, the (002) peak recovers to 21.2° after charging back to 3.0 V, indicating the outstanding structural stability and electrochemical reversibility of the MnO NCs@rGO film electrode. Combined with the CV test results, it can be concluded that MnO in the MnO NCs@rGO electrodes follows a stepwise conversion–reversion conversion reaction mechanism, while rGO undergoes an intercalation–adsorption reaction process.

2.4. Kinetic Analysis

To gain further insight into the underlying mechanisms for the excellent rate performance of the MnO NCs@rGO film electrodes, a series of cyclic voltammetry tests and galvanostatic intermittent titration technique (GITT) tests were performed at different scan speeds. The corresponding Li-ion storage behavior and Li^+ diffusion coefficient (D_{Li+}) was then summarized. In the CV curves (as shown in Figure 4a), the reduction and oxidation peaks of the MnO NCs@rGO film electrode shifted in opposite directions with an increasing scan rate (from 0.2 to 1.0 mV s^{-1}). The calculated *b*-values of the linear fits corresponding to the reduction (peak 1, peak 2) and oxidation (peak 3, peak 4) peaks are 0.98, 0.81, 0.77, and 0.88, respectively (Figure 4b), suggesting that the MnO NCs@rGO film electrodes follow the pseudo-capacitance-dominated "capacitor-battery" dual-type lithium storage mechanism [42,43]. Moreover, the capacitance contributions of the MnO NCs@rGO film electrodes were calculated to be 61.4%, 67.1%, 71.8%, 74.7%, and 79.7% for the scan rates of 0.2, 0.4, 0.6, 0.8, and 1.0 mV s^{-1}, respectively (Figure 4c,d). The high pseudocapacitance is mainly due to the abundant active surface area afforded by the layered rGO and the ultrafine MnO particles, as well as the presence of highly active electrochemical reaction sites provided by the MnO NCs. Subsequently, the diffusion coefficient of Li^+ in the MnO NCs@rGO film electrode was evaluated after 20 cycles using the GITT, applying a series of pulse currents at 0.02 A g^{-1} for 30 min (τ) and allowing it to remain stationary for 30 min. As depicted in Figure 4e, both the MnO NCs@rGO film and the MnO electrodes exhibit similar potential distribution trends throughout the entire discharging/charging processes, indicating the same Li-ion storage mechanism. The calculated D_{Li+} of MnO NCs@rGO was found to be 5.98×10^{-12}–2.97×10^{-11} cm^2 s^{-1}, which significantly higher than that of MnO (3.22×10^{-12}–5.53×10^{-12} cm^2 s^{-12}) (Figure 4f). The aforementioned kinetic analyses have demonstrated that the MnO NCs@rGO film electrode with a layer-embedded structure can significantly accelerate Li^+ transport, thus resulting in its superior rate performance and lithium storage kinetics. In summary, the exceptional electrochemical performance of MnO NCs@rGO film electrodes can be attributed to the ingenious structural design, as illustrated below: (1) the large-area rGO nanosheets and ultrafine MnO nanoparticles provide abundant electrochemical active sites; (2) the rGO-based film possesses an abundant fold-like structure to provide a sufficient attachment interface for the MnO, also providing a volume-release space for repeated charge/discharge processes; (3) the layer-by-layer embedded three-dimensional structure promotes electrolyte infiltration and storage and shortens the distance for ion transport; (4) most importantly, the strong synergistic effect between rGO nanosheets and MnO NCs significantly improves the ability of the composite electrode to withstand mechanical deformation, expands the electrode/electrolyte contact area, reduces the electron/ion transport resistance, and improves the reaction kinetics.

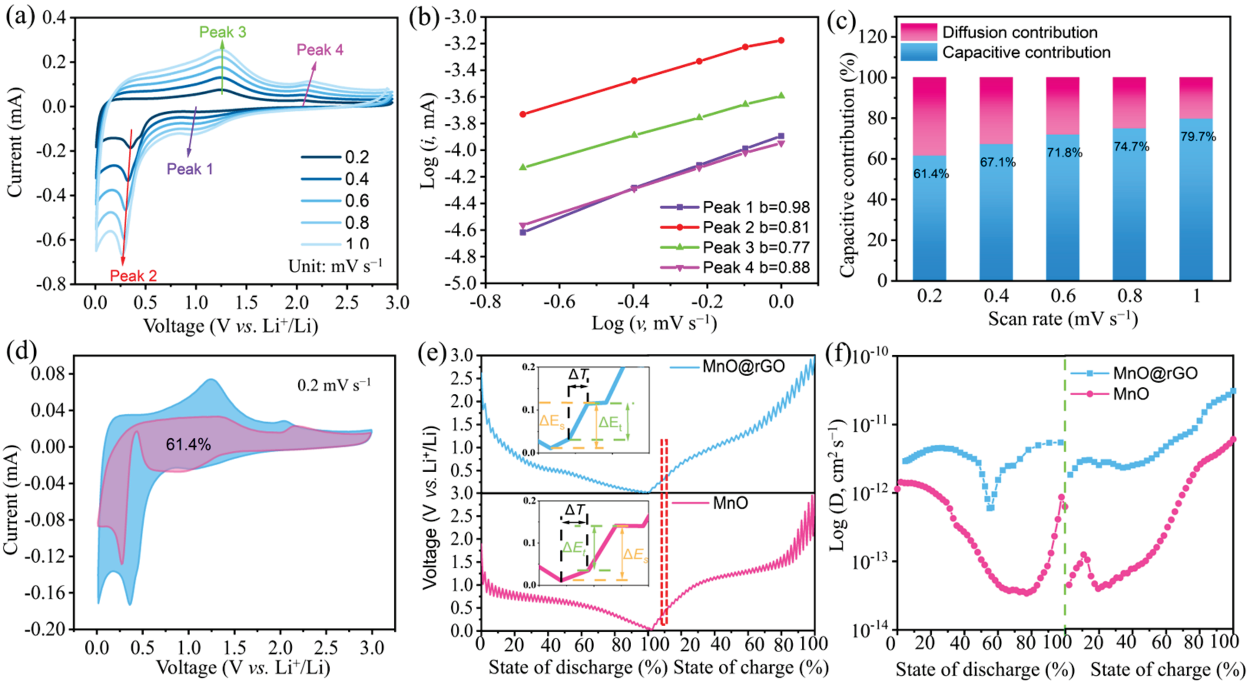

Figure 4. Dynamic behavior analysis of the flexible MnO NCs@rGO film electrode: (**a**) CV curves at various scan rates, (**b**) the relationship between log *i* and log *v*, (**c**,**d**) capacity contribution ratios of capacitive-controlled behavior of the flexible MnO NCs@rGO film electrode. (**e**) GITT curves and (**f**) corresponding D_{Li+} values for the MnO NCs@rGO film and MnO electrodes.

2.5. Flexible Full-Cell Assembly and Electrochemical Properties

In light of the aforementioned exceptional electrochemical properties, remarkable flexibility, and robust mechanical properties, the MnO NCs@rGO film electrode has essentially fulfilled the criteria for high-performance electrode materials in flexible LIBs. To assess the practicality of the MnO NCs@rGO film anode when coupled with the $LiCoO_2$ cathode and an aluminum-coated plastic film shell, a flexible lithium-ion full cell (MnO NCs@rGO//$LiCoO_2$) was constructed after vacuum encapsulation. As illustrated in Figure 5a, the size of the flexible full cell is 5.5 ×7.5 × 0.1 cm. Long strips of aluminum and copper foil are employed to facilitate contact with a limited portion of the electrode materials and are used as battery tabs for the cathode and anode of the full cell. Initially, a low current density of 20 mA^{-1} was applied during the initial galvanostatic charge/discharge process, which is considered as the cell formation process. In order to optimize the cell capacity, the voltage range of the full cells was set to 0.5–3.9 V. Figure 5b,c shows the GCD curves and cycle performance results of the MnO NCs@rGO//$LiCoO_2$ full cell at different bending angles under 200 mA g^{-1}, with each bending angle performed for 10 cycles. It can be observed that the initial charge-/discharge-specific capacities of the MnO NCs@rGO//$LiCoO_2$ full cell were 2015 and 1195 mAh g^{-1}, respectively, with a Coulombic efficiency of approximately 60% (Figure 5b). Following the bending of the flexible full cell to 30 °, 60 °, 90 °, and 180 ° and subsequent reversible restoration to 90 °, 60 °, 30 °, and 0 °, respectively, the reversible capacity remained almost constant (Figure 5c), confirming the excellent flexibility and stable electrochemical stability of the MnO NCs@rGO//$LiCoO_2$ full cell. The additional stability test, as illustrated in Figure 5d, demonstrated that the charge-specific capacity of the MnO NCs@rGO//$LiCoO_2$ full cell remained at approximately 941.8 mAh g^{-1} over 200 cycles at 500 mA g^{-1}, with a capacity retention rate of nearly 100%. It is noteworthy that the full cell exhibited a consistently high Coulombic efficiency, exceeding 99% throughout the cycling period. In order to assess the practicality of the full cell, it was bent and connected to an array of about 100 LEDs, which were successfully illuminated (Figure S13). These favorable results in terms of bending performance and electrochemical stability indicate that the MnO NCs@rGO//$LiCoO_2$ full cells have the potential for commercialization in flexible and wearable optoelectronic devices.

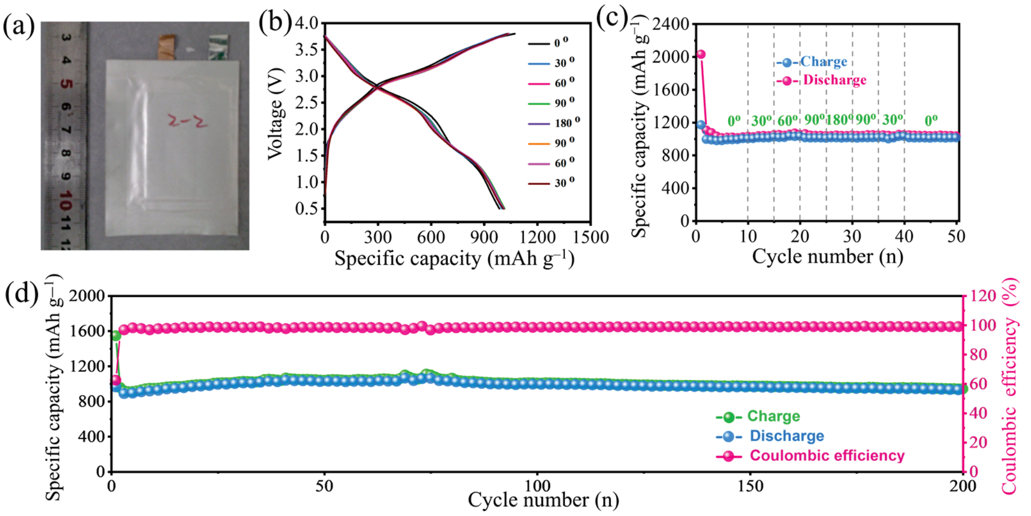

Figure 5. (**a**) Photograph, (**b**) GCD curves, and (**c**) corresponding cycling performance of the flexible full cell with different bend statuses. (**d**) Long-term cycling performance and Coulombic efficiency of the full cell at a current density of 500 mA g^{-1}.

3. Conclusions

In summary, we have successfully synthesized a layer-embedded structured, flexible MnO NCs@rGO thin-film electrode using a novel "spontaneous complexation–exfoliation" strategy. This method utilizes the nucleophilicity of GO surface functional groups and the surface hydrophobicity of rGO to achieve the spontaneous complexation–exfoliation process, thereby indicating its feasibility for simple and large-scale application. Benefiting from the synergistic effect of the thin film, its flexibility, the strong mechanical properties of rGO, and the numerous active sites and high capacity of ultrafine MnO NCs, the flexible MnO NCs@rGO anodes completely overcame the inherent drawbacks of MnO electrodes, including low conductivity, huge volume effect, and rapid capacity degradation. Consequently, the lithium storage capacity and fast charge/discharge capability have reached new heights. Most impressively, the assembled soft-pack lithium-ion battery can withstand full-angle bending without any capacity loss. These results demonstrate the rationality and broad application prospects of the layered embedded structure.

Supplementary Materials: The following supporting information can be downloaded at: https://www.mdpi.com/article/10.3390/molecules30010133/s1, Figure S1: Photograph of the MnOx-rGO intermediate and flexible MnO NCs@rGO film.; Figure S2: SEM image and XRD patterns of MnO; Figure S3: HR-TEM image of the flexible MnO NCs@rGO film; Figure S4: XRD pattern and SEM image of rGO; Figure S5: Photograph of the flexible free-standing MnO NCs@rGO electrode; Figure S6: GCD profiles and cycling performance of the MnO anode at 0.2 A g^{-1}; Figure S7: GCD profiles and cycling performance of the rGO anode at 0.2 A g^{-1}; Figure S8: Cycling performance of the MnO and rGO anode at 0.5 A g^{-1}; Figure S9: Rate performance of the MnO and rGO anode at different current densities from 0.2 A to 50.0 A g^{-1}; Figure S10: Photograph of the flexible MnO NCs@rGO//$LiCoO_2$ full cell, powering an array of 100 LEDs. Refs. [44–46] are cited in the Supplementary Materials.

Author Contributions: Conceptualization, H.C. and H.Z.; methodology, H.C. and Z.L.; investigation, J.Z. and P.Z.; resources, Y.L.; writing—original draft preparation, H.C.; writing—review and editing, H.Z. and Z.L. All authors have read and agreed to the published version of the manuscript.

Funding: This research was supported by the Science and Technology Program of XPCC (No. 2023AB031; No. 2023AA007) and the Xinjiang Production and Construction Corps New Energy Industry Innovation Research Institute Construction Project (No. 2023-02-20240106).

Institutional Review Board Statement: Not applicable.

Informed Consent Statement: Not applicable.

Data Availability Statement: Dataset available upon request from the authors.

Acknowledgments: The authors wish to thank the laboratory associates for their assistance.

Conflicts of Interest: The authors declare no conflicts of interest.

References

1. Liu, Y.; He, K.E.; Chen, G.; Leow, W.R.; Chen, X. Nature-inspired structural materials for flexible electronic devices. *Chem. Rev.* **2017**, *117*, 12893–12941. [CrossRef] [PubMed]
2. Xiao, Q.H.Q.; Yang, J.L.; Wang, X.D.; Deng, Y.R.; Han, P.; Yuan, N.; Zhang, L.; Feng, M.; Wang, C.A.; Liu, R.P. Carbon-based flexible self-supporting cathode for lithium-sulfur batteries: Progress and perspective. *Carbon Energy* **2021**, *3*, 271–302. [CrossRef]
3. Khan, Y.; Ostfeld, A.E.; Lochner, C.M.; Pierre, A.; Arias, A.C. Monitoring of Vital Signs with Flexible and Wearable Medical Devices. *Adv. Mater.* **2016**, *28*, 4373. [CrossRef]
4. Zhang, Y.; Zhao, Y.; Ren, J.; Weng, W.; Peng, H. Advances in wearable fiber-shaped lithium-ion batteries. *Adv. Mater.* **2016**, *28*, 4524–4531. [CrossRef] [PubMed]
5. Nguyen, Q.H.; Nguyen, Q.H.; So, S.; Hur, J. Efficient TiC-C hybrid conductive matrix for ZnTe anode in Lithium-ion storage. *Appl. Surf. Sci.* **2020**, *534*, 147679. [CrossRef]
6. Liu, W.J.; Zhang, X.; Xu, Y.N.; Wang, L.; Li, Z.; Li, C.; Wang, K.; Sun, X.Z.; An, Y.B.; Wu, Z.S.; et al. 2D Graphene/MnO Heterostructure with Strongly Stable Interface Enabling High-Performance Flexible Solid-state Lithium-Ion Capacitors. *Adv. Funct. Mater.* **2022**, *32*, 2202342. [CrossRef]
7. Xia, J.; Zhang, X.; Yang, Y.G.; Wang, X.; Yao, J.N. Electrospinning fabrication of flexible, foldable, and twistable $Sb_2S_3/TiO_2/C$ nanofiber anode for lithium ion batteries. *Chem. Eng. J.* **2021**, *413*, 127400. [CrossRef]
8. Qian, G.Y.; Liao, X.B.; Zhu, Y.X.; Pan, F.; Chen, X.; Yang, Y. Designing Flexible Lithium-Ion Batteries by Structural Engineering. *ACS Energy Lett.* **2019**, *4*, 690–701. [CrossRef]
9. Wang, H.; Yang, X.; Wu, Q.; Zhang, Q.; Chen, H.; Jing, H.; Wang, J.; Mi, S.-B.; Rogach, A.L.; Niu, C. Encapsulating silica/antimony into porous electrospun carbon nanofibers with robust structure stability for high-efficiency lithium storage. *ACS Nano* **2018**, *12*, 3406–3416. [CrossRef] [PubMed]
10. Zhao, W.Y.; Bai, M.; Li, S.W.; Tang, X.Y.; Wu, W.W.; Sun, C.C.; Yin, X.K.; Zhou, J.; Yuan, S.; Ma, Y. Integrated Thin Film Battery Design for Flexible Lithium Ion Storage: Optimizing the Compatibility of the Current Collector-Free Electrodes. *Adv. Funct. Mater.* **2019**, *29*, 1903542. [CrossRef]

11. Opra, D.P.; Sinebryukhov, S.L.; Modin, E.B.; Sokolov, A.A.; Podgorbunsky, A.B.; Ziatdinov, A.M.; Ustinov, A.Y.; Mayorov, V.Y.; Gnedenkov, S.V. Manganese, Fluorine, and Nitrogen Co-Doped Bronze Titanium Dioxide Nanotubes with Improved Lithium-Ion Storage Properties. *Batteries* **2023**, *9*, 229. [CrossRef]
12. Toigo, C.; Arbizzani, C.; Pettinger, K.-H.; Biso, M. Study on Different Water-Based Binders for $Li_4Ti_5O_{12}$ Electrodes. *Molecules* **2020**, *25*, 2443. [CrossRef]
13. Opra, D.P.; Sokolov, A.A.; Sinebryukhov, S.L.; Tkachenko, I.A.; Ziatdinov, A.M.; Gnedenkov, S.V. Electronic Structure, Optical and Magnetic Properties of Oxygen-Deficient Gray $TiO_{2-\delta}$(B). *Inorganics* **2022**, *10*, 184. [CrossRef]
14. Wang, S.H.; Teng, J.; Xie, Y.Y.; Wei, Z.W.; Fan, Y.A.; Jiang, J.J.; Wang, H.P.; Liu, H.G.; Wang, D.W.; Su, C.Y. Embedding CoO nanoparticles in a yolk–shell N-doped porous carbon support for ultrahigh and stable lithium storage. *J. Mater. Chem.* **2019**, *7*, 4036–4046. [CrossRef]
15. Chang, X.Q.; Zhu, Q.Z.; Zhao, Q.; Zhang, P.; Sun, N.; Soomro, R.A.; Wang, X.X.; Xu, B. 3D Porous Co_3O_4/MXene Foam Fabricated via a Sulfur Template Strategy for Enhanced Li/K-Ion Storage. *ACS Appl. Mater. Interfaces* **2023**, *15*, 7999–8009. [CrossRef] [PubMed]
16. Zhang, C.L.; Lu, B.R.; Cao, F.H.; Yu, Z.L.; Cong, H.P.; Yu, S.H. Hierarchically structured Co_3O_4@carbon porous fibers derived from electrospun ZIF-67/PAN nanofibers as anodes for lithium ion batteries. *J. Mater. Chem. A* **2018**, *6*, 12962. [CrossRef]
17. Zhang, S.L.; Guan, B.Y.; Wu, H.B.; Lou, X.W. Metal-Organic Framework-Assisted Synthesis of Compact Fe_2O_3 Nanotubes in Co_3O_4 Host with Enhanced Lithium Storage Properties. *Nano-Micro Lett.* **2018**, *10*, 44. [CrossRef]
18. Guo, S.S.; Koketsu, T.; Hu, Z.W.; Zhou, J.; Kuo, C.Y.; Lin, H.J.; Chen, C.T.; Strasser, P.; Sui, L.J.; Xie, Y.; et al. Mo-Incorporated Magnetite Fe_3O_4 Featuring Cationic Vacancies Enabling Fast Lithium Intercalation for Batteries. *Small* **2022**, *18*, 2203835. [CrossRef] [PubMed]
19. Xu, X.J.; Shen, J.D.; Li, F.K.; Wang, Z.S.; Zhang, D.C.; Zuo, S.Y.; Liu, J. Fe_3O_4@C Nanotubes Grown on Carbon Fabric as a Free-Standing Anode for High-Performance Li-Ion Batteries. *Chem. Eur. J.* **2020**, *26*, 14708–14714. [CrossRef]
20. Wang, J.K.; Wang, H.K.; Yao, T.H.; Liu, T.; Tian, Y.P.; Li, C.; Li, F.; Meng, L.J.; Cheng, Y.H. Porous N-doped carbon nanoflakes supported hybridized SnO_2/Co_3O_4 nanocomposites as high-performance anode for lithium-ion batteries. *J. Colloid Interf. Sci.* **2020**, *560*, 546–554. [CrossRef]
21. Zhan, G.H.; Liao, W.H.; Hu, Q.Q.; Wu, X.H.; Huang, X.Y. Rational Engineering of p-n Heterogeneous ZnS/SnO_2 Quantum Dots with Fast Ion Kinetics for Superior Li/Na-Ion Battery. *Small* **2023**, *19*, 2300534. [CrossRef] [PubMed]
22. Rodriguez, J.R.; Hamann, H.J.; Mitchell, G.M.; Ortalan, V.; Gribble, D.; Xiong, B.; Pol, V.G.; Ramachandran, P.V. Interconnected Sn@SnO_2 Nanoparticles as an Anode Material for Lithium-Ion Batteries. *ACS Appl. Nano Mater.* **2023**, *6*, 11070–11076. [CrossRef]
23. Xu, L.Q.Y.; Zhang, X.X.; Chen, R.J.; Wu, F.; Li, L. P-Doped Ni/NiO Heterostructured Yolk-Shell Nanospheres Encapsulated in Graphite for Enhanced Lithium Storage. *Small* **2022**, *18*, 2105897. [CrossRef] [PubMed]
24. Yan, L.; Zong, L.S.; Zhang, Z.J.; Li, J.X.; Wu, H.Z.; Cui, Z.Y.; Kang, J.L. Oxygen vacancies activated porous MnO/graphene submicron needle arrays for high-capacity lithium-ion batteries. *Carbon* **2022**, *190*, 402–411. [CrossRef]
25. Lin, J.; Zeng, C.H.; Lin, X.M.; Xu, C.; Xu, X.; Luo, Y.F. Metal-Organic Framework-Derived Hierarchical MnO/Co with Oxygen Vacancies toward Elevated-Temperature Li-Ion Battery. *ACS Nano* **2021**, *15*, 4594–4607. [CrossRef] [PubMed]
26. Zou, Y.N.; Dong, A.Q.; Guo, Z.X.; Ye, L.; Cui, Y.H.; Guo, M.Y.; Zhao, L.J.; Jiang, Q. MnO/Mn_2O_3 Nanowires Coated by Porous N-Doped Carbon for Long-Cycle and High-Rate Lithium-Ion Batteries. *ACS Appl. Nano Mater.* **2020**, *3*, 5612–5624. [CrossRef]
27. Zhong, M.; Li, L.L.; Zhao, K.; Peng, H.; Xu, S.X.; Su, B.T.; Wang, D.H. Metal–organic framework-engaged synthesis of core–shell MoO_2/ZnSe@N-C nanorods as anodes in high-performance lithium-ion batteries. *New J. Chem.* **2021**, *45*, 12064–12070. [CrossRef]
28. Lu, X.; Wang, P.; Liu, K.; Niu, C.M.; Wang, H.K. Encapsulating nanoparticulate Sb/MoO_x into porous carbon nanofibers via electrospinning for efficient lithium storage. *Chem. Eng. J.* **2018**, *336*, 701–709. [CrossRef]
29. Li, Q.H.; Zhang, W.; Peng, J.; Zhang, W.; Liang, Z.X.; Wu, J.W.; Feng, J.J.; Li, H.; Huang, S.M. Metalorganic framework derived ultrafine Sb@Porous carbon octahedron via in situ substitution for high-performance sodium-ion batteries. *ACS Nano* **2021**, *15*, 15104–15113. [CrossRef] [PubMed]
30. Li, Q.H.; Peng, J.; Zhang, W.; Wang, L.X.; Liang, Z.X.; Wang, G.; Wu, J.W.; Fan, W.B.; Li, H.; Wang, J.L.; et al. Manipulating the polytellurides of metallic telluride for ultra-stable potassium-ion storage: A case study of carbon-confined $CoTe_2$ nanofibers. *Adv. Energy Mater.* **2023**, *16*, 2300150. [CrossRef]
31. Zhang, W.; Wang, X.W.; Wong, K.W.; Zhang, W.; Chen, T.; Zhao, W.; Huang, S.M. Rational design of embedded $CoTe_2$ nanoparticles in freestanding N-doped multichannel carbon fibers for sodium-ion batteries with ultralong cycle lifespan. *ACS Appl. Mater. Interfaces* **2021**, *13*, 34134–34144. [CrossRef] [PubMed]
32. Zhang, W.; Liu, Y.T.; Chen, C.J.; Li, Z.; Huang, Y.H.; Hu, X.L. Flexible and Binder-Free Electrodes of Sb/rGO and $Na_3V_2(PO_4)_3$/rGO Nanocomposites for Sodium-Ion Batteries. *Small* **2015**, *11*, 3822–3829. [CrossRef]
33. Chen, M.H.; Li, T.Y.; Li, Y.; Liang, X.Q.; Sun, W.F.; Chen, Q.G. Rational Design of a MnO Nanoparticle-Embedded Carbon Nanofiber Interlayer for Advanced Lithium–Sulfur Batteries. *ACS Appl. Energy Mater.* **2020**, *3*, 10793–10801. [CrossRef]

34. Li, Q.H.; Zhang, W.; Peng, J.; Yu, D.D.; Liang, Z.X.; Zhang, W.; Wang, G.; Wu, J.W.; Li, H.; Huang, S.M. Nanodot-in-nanofiber structured carbon-confined Sb2Se3 crystallites for fast and durable sodium storage. *Adv. Funct. Mater.* **2022**, *32*, 2112776. [CrossRef]
35. Lin, Z.Y.; Zhang, W.; Peng, J.; Li, Q.H.; Liang, Z.X.; Wang, G.Y.; Wang, J.L.; Wang, G.; Huang, Z.J.; Huang, S.M. Synergistic Regulation of Polyselenide Dissolution and Na-Ion Diffusion of Se-Vacancy-Rich Bismuth Selenide toward Ultrafast and Durable Sodium-Ion Batteries. *Adv. Energy Mater.* **2024**, *14*, 2402110. [CrossRef]
36. Wang, J.L.; Huang, Z.J.; Zhang, W.; Li, Q.H.; Liang, Z.X.; Lu, J.J.; Lin, Z.Y.; Wang, G.; Wu, J.X.; Huang, S.M. Balancing Graphitic Nanodomains and Heteroatom Doping in Hard Carbons Toward High Capacity and Durable Potassium-Ion Battery Anodes. *Adv. Funct. Mater.* **2024**, *34*, 2409937. [CrossRef]
37. Yu, J.; Luo, J.D.; Zhang, H.; Zhang, Z.; Wei, J.C.; Yang, H.Y. Renewable agaric-based hierarchically porous cocoon-like MnO/Carbon composites enable high-energy and high-rate Li-ion batteries. *Electrochim. Acta* **2019**, *322*, 134757. [CrossRef]
38. Yang, C.; Yao, Y.; Lian, Y.B.; Chen, Y.J.; Shah, A.; Zhao, X.H.; Chen, M.Z.; Peng, Y.; Deng, Z. A Double-Buffering Strategy to Boost the Lithium Storage of Botryoid MnOx/C Anodes. *Small* **2019**, *15*, 1900015. [CrossRef] [PubMed]
39. Huang, S.J.; Li, H.P.; Xu, G.B.; Liu, X.; Zhang, Q.; Yang, L.W.; Cao, J.X.; Wei, X.L. Porous N-doped carbon sheets wrapped MnO in 3D carbon networks as high-performance anode for Li-ion batteries. *Electrochim. Acta* **2020**, *342*, 136115. [CrossRef]
40. Hou, C.X.; Wang, J.; Zhang, W.B.; Li, J.J.; Zhang, R.H.; Zhou, J.J.; Fan, Y.Q.; Li, D.J.; Dang, F.; Liu, J.Q.; et al. Interfacial Superassembly of Grape-Like MnO-Ni@C Frameworks for Superior Lithium Storage. *ACS Appl. Mater. Interfaces* **2020**, *12*, 13770–13780. [CrossRef]
41. Chen, P.H.; Zhou, W.Y.; Xiao, Z.J.; Li, S.Q.; Chen, H.L.; Wang, Y.C.; Wang, Z.B.; Xi, W.; Xia, X.G.; Xie, S.S. In situ anchoring MnO nanoparticles on self-supported 3D interconnected graphene scroll framework: A fast kinetics boosted ultrahigh-rate anode for Li-ion capacitors. *Energy Storage Mater.* **2020**, *33*, 298–308. [CrossRef]
42. Liang, Z.X.; Li, Q.H.; Zhang, W.; Yu, D.D.; Zhang, W.; Wu, J.W.; Wang, G.Y.; Fan, W.B.; Wang, J.L.; Huang, S.M. Pomegranate-inspired porous SnSe/ZnSe@C anode: A stress-buffer nanostructure for fast and ultrastable sodium-ion storage. *J. Energy Chem.* **2020**, *75*, 369–377. [CrossRef]
43. Zhao, W.M.; Zhang, W.; Lei, Y.X.; Wang, L.X.; Wang, G.Y.; Wu, J.W.; Fan, W.B.; Huang, S.M. Dual-Type Carbon Confinement Strategy: Improving the Stability of $CoTe_2$ Nanocrystals for Sodium-Ion Batteries with a Long Lifespan. *ACS Appl. Mater. Interfaces* **2022**, *14*, 6801–6809. [CrossRef] [PubMed]
44. Li, Q.H.; Yu, D.D.; Peng, J.; Zhang, W.; Huang, J.L.; Liang, Z.X.; Wang, G.Y.; Li, H.X.; Xiong, S.Y.; Wang, J.Z.; et al. Efficient Polytelluride Anchoring for Ultralong-Life Potassium Storage: Combined Physical Barrier and Chemisorption in Nanogrid-in-Nanofiber. *Nano-Micro Lett.* **2024**, *16*, 77. [CrossRef] [PubMed]
45. Peng, B.; Xu, S.; Lv, Z.; Zhang, S.; Gao, Y.; Lin, T.; Huang, F. Toward Extremely Fast Charging Through Boosting Intercalative Redox Pseudocapacitance: A $SbCrSe_3$ Anode for Large and Fast Sodium Storage. *Adv. Energy Mater.* **2022**, *13*, 2203187. [CrossRef]
46. Dong, C.; Shao, H.; Zhou, Y.; Du, W.; Li, L.; Sun, J.; Yan, Z.; Hu, Z.; Chou, S.; Jiang, F. Construction of ZnS/Sb_2S_3 Heterojunction as an Ion-Transport Booster toward High Performance Sodium Storage. *Adv. Funct. Mater.* **2022**, *33*, 2211864. [CrossRef]

Disclaimer/Publisher's Note: The statements, opinions and data contained in all publications are solely those of the individual author(s) and contributor(s) and not of MDPI and/or the editor(s). MDPI and/or the editor(s) disclaim responsibility for any injury to people or property resulting from any ideas, methods, instructions or products referred to in the content.

molecules

Article

Encapsulation Engineering of Sulfur into Magnesium Oxide for High Energy Density Li–S Batteries

Sunny Choudhary [1,*], Nischal Oli [1], Shweta Shweta [1], Satyam Kumar [1], Mohan K. Bhattarai [1], Carlos Alberto Malca-Reyes [2], Rajesh K. Katiyar [1], Balram Tripathi [1,3], Liz M. Díaz-Vázquez [2], Gerardo Morell [1] and Ram S. Katiyar [1,*]

[1] Department of Physics, University of Puerto Rico at Río Piedras, San Juan, PR 00931, USA
[2] Department of Chemistry, University of Puerto Rico at Río Piedras, San Juan, PR 00931, USA
[3] Department of Physics, S.S. Jain Subodh P.G. (Autonomous) College, Jaipur Rajasthan 302004, India
* Correspondence: souryabhardwaj@gmail.com (S.C.); ram.katiyar@upr.edu (R.S.K.)

Abstract: This study addresses the persistent challenge of polysulfide dissolution in lithium–sulfur (Li–S) batteries by introducing magnesium oxide (MgO) nanoparticles as a novel additive. MgO was integrated with sulfur using a scalable process involving solid-state melt diffusion treatment followed by planetary ball milling. XRD measurements confirmed that sulfur (S_8) retains its orthorhombic crystalline structure (space group F_{ddd}) following the MgO incorporation, with minimal peak shifts indicating slight lattice distortion, while the increased peak intensity suggests enhanced crystallinity due to MgO acting as a nucleation site. Additionally, Raman spectroscopy demonstrated sulfur's characteristic vibrational modes consistent with group theory (point group D_2h) and highlighted multiwalled carbon nanotube (MWCNT′s) D, G, and 2D bands, with a low I_D/I_G ratio (0.47), which indicated low defects and high crystallinity in the prepared cathode. The S–MgO composite cathode exhibited superior electrochemical behavior, with an initial discharge capacity (950 mA h g^{-1} at 0.1 C), significantly improved compared to pristine sulfur's. The presence of MgO effectively mitigated the polysulfide shuttle effect by trapping polysulfides, leading to enhanced stability over 400 cycles and the consistent coulombic efficiency of over 99.5%. After 400 cycles, EDS and SEM analyses confirmed the structural integrity of the electrode, with only minor fractures and slight sulfur content loss. Electrochemical impedance spectroscopy further confirmed the enhanced performance.

Keywords: vibrational modes in Li–S; sulfur–MgO composite; energy storage applications; cyclic stability; morphology sulfur cathode; polysulfides

1. Introduction

Lithium–sulfur (Li–S) batteries are expected to be the basis for next-generation high-energy rechargeable batteries due to their high theoretical specific capacity (1673 mA h g^{-1}), high theoretical specific energy (2567 Wh kg^{-1}), and low cost. Although the sulfur cathode has recently been operated beyond the topotactic discharge voltage for Li–S to obtain high capacities of around 900 mA h g^{-1} and more, their applications are hindered by several technical challenges [1–3], including rapid capacity fading, low coulombic efficiency, and irreversible active mass loss. An effective way to overcome these challenges is to bind the Li_2S_x species to host materials in order to suppress the polysulfide shuttle, thus enhancing the cycling stability of the Li–S batteries. An ideal anchoring material should (1) exhibit robust but not too strong of a chemical interaction with the Li_2S_x species (0.8–2.0 eV including Van der Waals interactions) to effectively trap them; (2) keep the species intact to prevent their dissolution into the electrolyte; (3) have a large and sufficient active region to accommodate sulfur volumetric expansion; and (4) possess a small characteristic dimension of the sulfur electrode to avoid pulverization. Therefore, it is imperative to control the volume fluctuations of sulfur upon cycling, suppress the dissolution of the intermediate

Molecules **2024**, *29*, 5116. https://doi.org/10.3390/molecules29215116 https://www.mdpi.com/journal/molecules

polysulfides, and improve the ionic/electronic conductivities of sulfur and relevant metal sulfides [4–8]. Figure 1 shows the schematic and electrochemical reaction mechanism of the Li–S batteries.

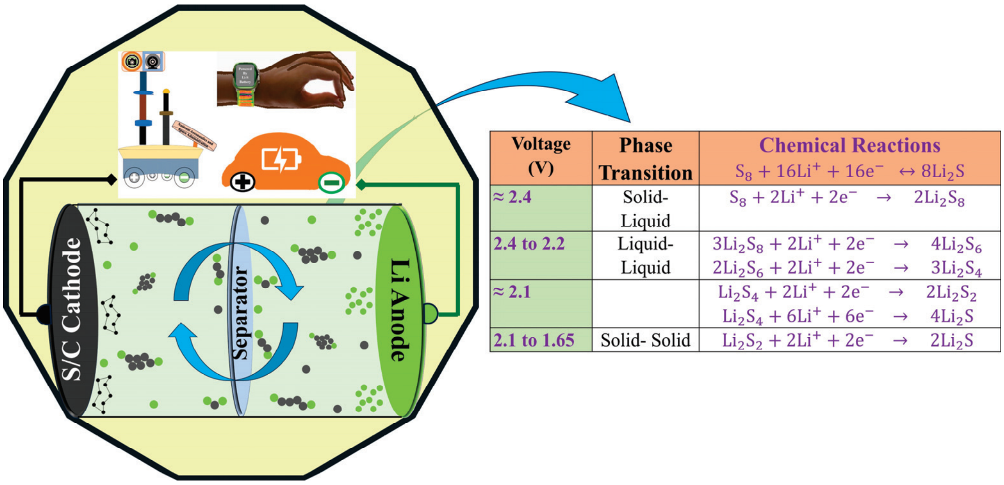

Voltage (V)	Phase Transition	Chemical Reactions $S_8 + 16Li^+ + 16e^- \leftrightarrow 8Li_2S$
≈ 2.4	Solid-Liquid	$S_8 + 2Li^+ + 2e^- \rightarrow 2Li_2S_8$
2.4 to 2.2	Liquid-Liquid	$3Li_2S_8 + 2Li^+ + 2e^- \rightarrow 4Li_2S_6$ $2Li_2S_6 + 2Li^+ + 2e^- \rightarrow 3Li_2S_4$
≈ 2.1		$Li_2S_4 + 2Li^+ + 2e^- \rightarrow 2Li_2S_2$ $Li_2S_4 + 6Li^+ + 6e^- \rightarrow 4Li_2S$
2.1 to 1.65	Solid- Solid	$Li_2S_2 + 2Li^+ + 2e^- \rightarrow 2Li_2S$

Figure 1. Schematic of Li–S battery and Electrochemical classification.

The theoretical density of sulfur is about 2.07 g cm^{-3}, notably lower than that of the typical cathode materials in conventional Li–ion batteries, $LiCoO_2$ (5.1 g cm^{-3}), $LiNi_xCo_xMn_xO_2$ NMC (4.8–5.3 g cm^{-3}), and $LiMn_2O_4$ LMO (4.3 g cm^{-3}). To enhance the volumetric capacity of sulfur cathodes, it is essential to utilize host materials that possess higher density and improved functionality. Transition metal oxides, exhibiting densities between 3.5 and 5.1 g cm^{-3}, provide a significant benefit in enhancing the overall volumetric capacity. Magnesium oxide (MgO), possessing a theoretical density of 3.58 g cm^{-3}, serves as an appropriate additive for sulfur–based cathodes, facilitating an optimal balance between high density and functionality. The substantial specific surface area (150–300 m^2 g^{-1}), resulting from its nanostructured form, enhances the cycling stability. The interaction of MgO with lithium polysulfides (LiPSs) improves structural integrity, facilitates the conversion of LiPS, and reduces the shuttle effect, resulting in enhanced electrochemical performance [9,10].

Moreover, the incorporation of functional groups [11–14] such as oxygen, nitrogen, boron, and sulfur into carbon structures has demonstrated an improvement in polysulfide adsorption via both chemical bonding and physical confinement. This dual interaction diminishes the shuttle effect considerably, resulting in enhanced cycle stability and increased sulfur utilization. Table 1 delineates that many oxides have been effectively functionalized as additives or incorporated into sulfur cathodes, showcasing significant promise for future commercial use in Li–S batteries [15].

Table 1. Current state–of–the–art oxide materials for enhancing cathode performance in Li–S batteries.

Oxides as Cathode Additive	Mechanism	Experimental Findings	Reference
Al_2O_3/S composite	Adsorbs LiPSs, enhancing cycle performance.	660 mA h g^{-1} over 25th cycle	[16]
TiO_2/S composite	Traps LiPSs and improves sulfur retention and cycle life	850 mA h g^{-1} (0.5 C, 200 cycles) ~97%	[17]
$Mg_{0.6}Ni_{0.4}O$/S composite	Prevents LiPS dissolution, enhancing redox reactions and durability	1185 mA h g^{-1} (50 cycles)	[18]
MCM/Nb_2O_5 composite	Adsorbs polysulfides, reducing shuttle effect and improving sulfur retention	650 mA h g^{-1} (2 C, 500 cycles) ~98%	[19]

Table 1. *Cont.*

Oxides as Cathode Additive	Mechanism	Experimental Findings	Reference
NiO–CNT/S composite	Polysulfide adsorption reduces capacity fade and enhances cycle stability	609 mA h g^{-1} (0.1 C, 160 cycles) ~96%	[20]
SnO_2/S composite	Strong polysulfide adsorption, limiting shuttle effect and improving retention	550 mA h g^{-1} (0.1 C, 700 cycles) ~95%	[21]
CeO_2/S composite	Traps LiPSs, reducing shuttle effect and improving capacity	611 mA h g^{-1} (0.5 C, 200 cycles), 3.5 mg/cm^2 high loading ~99%	[22]
MoO_2@CNT/S composite	Polysulfide capture and catalytic conversion, improving sulfur utilization	540 mA h g^{-1} (1 C, 700 cycles) ~97%	[23]
Co_3O_4/S composite	Adsorbs and catalyzes polysulfide conversion, reducing capacity fade	694 mA h g^{-1} (0.2 C, 550 cycles) ~98%	[24]
rGO@ZnO/S composite	High surface area for polysulfide trapping, enhancing sulfur retention	674 mA h g^{-1} (1 C, 400 cycles) ~96%	[25]
Fe_3O_4/S composite	Strong polysulfide adsorption, reducing shuttle effect and stabilizing sulfur	610 mA h g^{-1} (1 C, 1000 cycles) ~98%	[26]
MnO_2@rGO/S composite	Traps and catalyzes polysulfide conversion, improving cycle stability	578 mA h g^{-1} (0.2 C, 100 cycles) ~95%	[27]
S/MgO–MWCNT–Super P	Traps LiPSs, reducing shuttle effect and improving reversibility	~600 mA h g^{-1} over 200 cycles at 0.1 C, ~650 mA h g^{-1} at 1 C; ~99.5%	Present study

Metal oxides typically demonstrate low electrical conductivity, thereby restricting the efficiency of electrochemical reactions that involve anchored polysulfides on their surfaces. For effective utilization, these polysulfides need to diffuse towards neighboring conductive carbon materials. The diffusion of anchored polysulfides across metal oxide surfaces is a critical factor in the design of effective interlayers for sulfur-based batteries. Research [9,28,29] integrating density functional theory (DFT) calculations with experimental validations identifies MgO as a suitable candidate owing to its robust polysulfide-binding capability and minimal diffusion energy barrier, thereby effectively mitigating the polysulfide shuttle and improving the overall battery performance.

This study aims to develop and investigate a novel S/MgO–carbon composite interlayer to enhance the performance of Li–S batteries by addressing key challenges, particularly the polysulfide shuttle effect, which leads to capacity fading and reduced efficiency. The integration of MgO nanoparticles with multiwall carbon nanotubes (MWCNTs) and Super P carbon black enhances the trapping and reutilization of polysulfides. Structural analyses employing X–ray diffraction (XRD), Raman spectroscopy, Fourier transform infrared (FT–IR) spectroscopy, and scanning electron microscopy (SEM) validated the uniform dispersion of MgO, which effectively confines polysulfides and improves the structural integrity. Electrochemical tests, including galvanostatic charge–discharge (GCD) and cyclic voltammetry (CV), revealed improved rate capability and cycle life, with stable capacity retention (~600 mA h g^{-1} over 200 cycles) and high coulombic efficiency (CE) (~99.5%). These findings demonstrate MgO's role in enhancing sulfur utilization, mitigating the polysulfide shuttle, and improving the overall battery longevity.

The incorporation of MgO into sulfur cathodes has demonstrated significant improvements in suppressing the polysulfide shuttle effect, leading to enhanced cycling stability and sulfur utilization in Li–S batteries. MgO as a functional additive is expected to endow the cathode with stronger chemical confinement against polysulfide shuttling. In addition to exploring other transition metal oxides and composite materials to enhance battery performance, future research could investigate the application of these improved Li–S batteries in space. The unique environmental conditions of space, such as extreme temperatures, vacuum, and radiation, present challenges for battery technologies, but the high energy density and improved cycling stability of MgO–enhanced Li–S batteries make them attractive candidates for space missions. Optimizing the design to ensure stability under these harsh conditions could enable their use in space exploration, satellites, and lunar or Martian habitats, where long-duration energy storage is critical. Additionally, fine–tuning the particle size and surface modification of MgO may enhance its interaction with polysulfides, providing opportunities to develop next–generation Li–S batteries with even greater capacity retention, energy density, and long–term stability.

2. Results and Discussion

2.1. Structural Measurements

2.1.1. X-Ray Diffraction (XRD)

The XRD patterns of pristine sulfur (S) and S/MgO are shown in Figure 2a. The sulfur patterns exhibit sharp, well-defined peaks, specifically prominent at about 23.11°, 25.81°, and 27.70°, which correspond to (222), (026), and (206), respectively. These are the characteristic peaks of the orthorhombic crystal structure of sulfur (S_8) [30]. We observed many other reflections, indicated with (hkl) values in Figure 2a. These peaks signify the high crystalline nature and phase purity of sulfur (ICDD/JCPDS reference file 01–07–1888). These peaks remain prominent in the S/MgO composite sample, confirming that sulfur retains its crystallinity after the incorporation of MgO nanoparticles. In addition to sulfur's peaks, the prepared sample shows distinct peaks at 36.92°, 42.91°, and 63.28° (inset: Figure 2b), attributed to the cubic phase of MgO (ICDD/JCPDS reference file 00–043–1022) [31,32], confirming the successful incorporation into the composite. We observed minimal peak shifting (Figure 2b) to a higher angle in the S/MgO sample (222 peak from 23.11° to 23.15°) (Figure S2), suggesting minor lattice distortion, which might be due to the interaction between sulfur and MgO. Thus, the intensity of the S/MgO prepared (Figure S1) sample is relatively high compared to pristine sulfur, indicating that the presence of MgO nanoparticles enhances the crystallinity of sulfur [33,34]. This leads to MgO acting as a nucleation site, facilitating the crystallization process of sulfur and leading to the stabilization of the sulfur structure. The improved crystallinity and structural stability are beneficial for enhancing the performance of the composite material regarding the application of Li–S batteries [34]. To confirm the phase of the composite materials, we refined the spectra utilizing the HighScore plus software 3.0.5 to analyze the phase, sulfur consisting of the F_{ddd} space group (orthorhombic structure), and MgO as the secondary phase of the $F_{m\bar{3}m}$ space group of the cubic crystal structure, and the refinement maintains the goodness–of–fit factor at less than 3%.

2.1.2. Scanning Electron Microscopy (SEM)

Figure 2c,d shows the SEM images of the S/MgO and S/MgO–MWCNTs–Super P composites, respectively. In the S/MgO composite, the sulfur matrix appears to be uniformly dispersed with the MgO nanoparticles across the surface, preventing sulfur agglomeration and contributing to the overall structural uniformity of the composite, as observed in the XRD analysis. The S/MgO–MWCNTs–Super P composite, however, displays a more complex morphology, with the MWCNTs forming a fibrous network (shown in Figure 2d) intertwined with sulfur and MgO particles, while Super P contributes to a porous, conductive matrix (also shown in Figure S3) [34–36]. This interconnected structure enhances electron transport, with the MgO particles remaining well-integrated.

The morphology suggests an optimized composite for high conductivity and stability, typically required for Li–S battery applications.

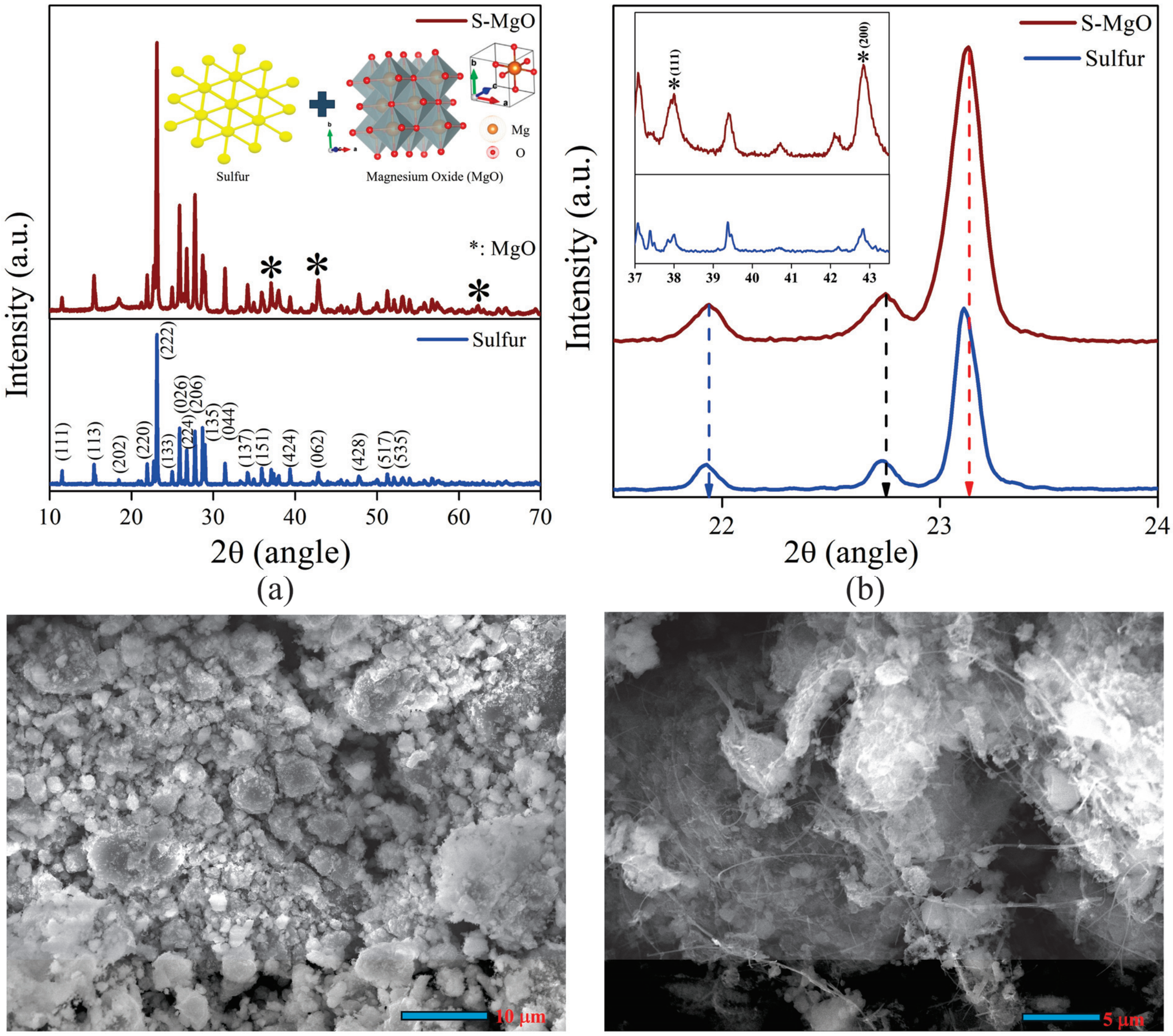

(a) (b)

(c) (d)

Figure 2. (**a**) XRD patterns of sulfur and S/MgO (inset: Vesta images of sulfur and MgO), (**b**) minimal peak shifting (inset: peaks of MgO), (**c**) SEM images of S/MgO, and (**d**) S/MgO–MWCNTs–Super P composite material.

2.1.3. Raman Analysis

Figure 3a–d shows the Raman spectra of the pristine sulfur, MWCNT (inset: super P), S/MgO, and S/MgO–MWCNTs–Super P, respectively. However, studies [37–40] indicated the D_4d and D_2h [38,41–43] point group for the analysis of the Raman spectra of pristine sulfur. For our measurement, we utilized the D_2h point group and F_{ddd} space group for α-sulfur of crystalline form. We discussed in detail how the sulfur modes are assigned to specific symmetry in the vibrational mode analysis section of the Supplementary Information (SI). In Figure 3a, there are various Raman active modes, at about 150, 183, 245, 436 cm^{-1}, corresponding to non-totally symmetric bending/stretching vibrations with B_{1g}, B_{2g}, B_{3g} symmetries. Additionally, the modes at 216 and 470 cm^{-1} correspond to symmetric stretching vibrations with A_g symmetry [38,41].

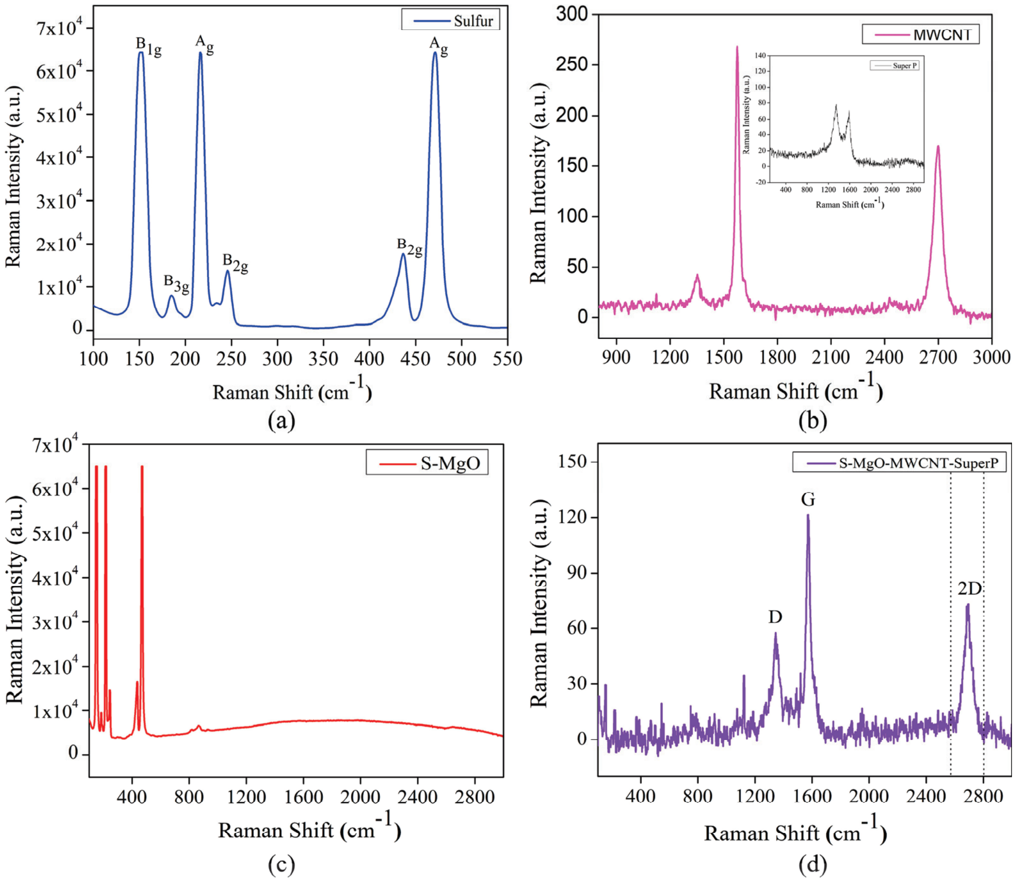

Figure 3. Raman spectra of (**a**) pristine sulfur, (**b**) MWCNT (inset: Super P), (**c**) S/MgO, and (**d**) S/MgO–MWCNTs–Super P.

Regarding the Raman spectra of the MWCNT and Super P shown in Figure 3b, the MWCNT spectra exhibit characteristic peaks at about 1350 cm^{-1} (D–band), which signify the defects/disorder in the sp^2 carbon lattice around 1580 cm^{-1} (G–band), suggesting in-plane vibrations of sp^2–hybridized carbon atoms, and 2700 cm^{-1} (2D band), which is an overtone of the d-band and broader due to the structure of the MWCNT composite [44–46]. For the mixture of S/MgO and S/MgO–MWCNTs–Super P, Raman spectra are also shown in Figure 3c,d. In the S/MgO, peaks between 150 cm^{-1} and 500 cm^{-1} predominately show sulfur vibrational active modes. The absence of significant peaks beyond 500 cm^{-1} reflects the lack of observable raman activity for MgO, which typically has a very low Raman cross-section due to its ionic nature and simple vibrational modes that are often raman-inactive or weakly active. Therefore, MgO does not contribute prominently to the spectrum, and the flat signal beyond sulfur's peaks confirms MgO's minimal contribution to the raman scattering in this composite. In the mixing of all the precursors, Figure 3d shows characteristic carbon peaks of D, G, and 2D bands at about 1350, 1580, and 2683 cm^{-1}, respectively. Significantly, the comparable intensity of the D band to that of the G band in our study serves as a clear indicator of the presence of defects within the examined specimen. The calculated ratio between the intensities of the D and G bands (I_D/I_G) is determined to be 0.47, suggesting low–level defects in the sample alongside a higher degree of crystallinity. This observed I_D/I_G ratio provides valuable quantitative insight into the structural characteristics of the examined material, emphasizing the coexistence of defects and a well–defined crystalline structure within the analyzed carbon nanotube sample. This low value of the ratio indicates that MWCNTs retain a substantial degree of crystallinity, even after the incorporation of S and MgO [47–49].

2.1.4. Fourier Transform Infrared Spectroscopy

As we discussed regarding the vibrational mode's activity in the pristine sulfur (SI section), there are modes B_{1u}, B_{2u}, and B_{3u}, which are IR–active, not Raman-active, and only A_u mode, which is neither Raman nor IR active, called silent mode. FT–IR is a well-established spectroscopic technique that is low in cost with simple operation but has yet to be implemented in Li–S batteries under electrochemical evaluation to monitor Li–S batteries. Recent work [50] has established that this technique could be used to detect different LiPS species based on the S–S vibrational mode. Figure 4a shows the spectrum of pristine sulfur, demonstrates the peak about 470 cm^{-1}, a characteristic signal of S_8, and can be attributed to the stretching of S–S bonds, which is more likely consistent with theB_{1u}/B_{3u} IR active mode, predicted by group theory for the D_2h point group [51,52]. Additionally, we observed the other signature mode around 840 cm^{-1}, which likely corresponds to the bending mode or deformation mode of the S_8 ring structure because of the bending, wagging, or twisting modes generally observed in this region. This peak might be attributed to the B_{2u}/B_{3u} mode, where sulfur atoms might be undergone out of the plane distortions [42,52,53]. This phenomenon tends to increase the electrical conductivity and catalytic reaction efficiency [54,55]. In Figure 4b, the main peak for identifying Mg=O is observed at 434 cm^{-1} from the stretching bond [56]. The peaks at 1488 cm^{-1} and 1406 cm^{-1} are the bending vibrations of the water molecules due to the humidity in the S/MgO formation process since they are rapidly chemisorbed on the surface of the MgO, as well as the CO_2 bound to a sulfur [57,58]. Additionally, the other characteristic peaks of sulfur are observed at 464 cm^{-1} and 854 cm^{-1}, and the interactions between sulfur and the MgO molecule in the formation of sulfites and sulfates are shown in the peaks at 1106 and 996 cm^{-1}, respectively [59]. However, with the MgO composite electrodes, it is found that there are two key absorption regions that provide insightful redox information: the S–S vibrational modes approaching the far–IR region (~470 cm^{-1}) and the symmetric SO_3 stretch vibrational mode of the triflate anion (~854 cm^{-1}). Both regions show cyclic evolution during reactions, indicating the disappearance of polysulfides and changes in the triflate ion coordination state, respectively.

In the case of S–MWCNT–Super P, the spectrum indicates new chemical ligands together with sulfur. We observed the characteristic peaks of sulfur at 840 cm^{-1} and 464 cm^{-1}; this last peak was displaced by the S–C interactions; in addition, there is the presence of the S–OR (ester group) that can be identified in the peak at 878 cm^{-1} [55]. The peaks shown are associated with C–S, C–C, and C=C bonds, as indicated in the peaks at 1054, 1274, and 1398 cm^{-1} [55], which include the stretching of the sulfate and sulfonated groups, and the peaks at 1550 and 1506 cm^{-1} would be the stretching vibrations of the C–C and C=C bonds [60] characteristic of MWCNTs. Moreover. Figure 4d shows the S/MgO and mixing of the MWCNT/Super P combination. The structure reveals the combination of the signals, where we can observe the presence of the new material in the interaction, the S ions with peaks at 840 and 434 cm^{-1}, the characteristic signal of MgO at 434 cm^{-1}, and the C=C and C–C interactions at 1560 cm^{-1} and 1400 cm^{-1}, respectively.

The formation of the structures between the S-MWCNT and S-MgO is a benefit regarding the use of electrodes for Li–S batteries because both structures can prevent the formation of polysulfides in the cell electrolyte, improving the conductivity and structural stability during multiple charges and discharges. The combination could improve the overall properties, such as improved structural stability for increased electrical conductivity and better containment of the polysulfide formation within the battery electrolyte, resulting in higher energy density.

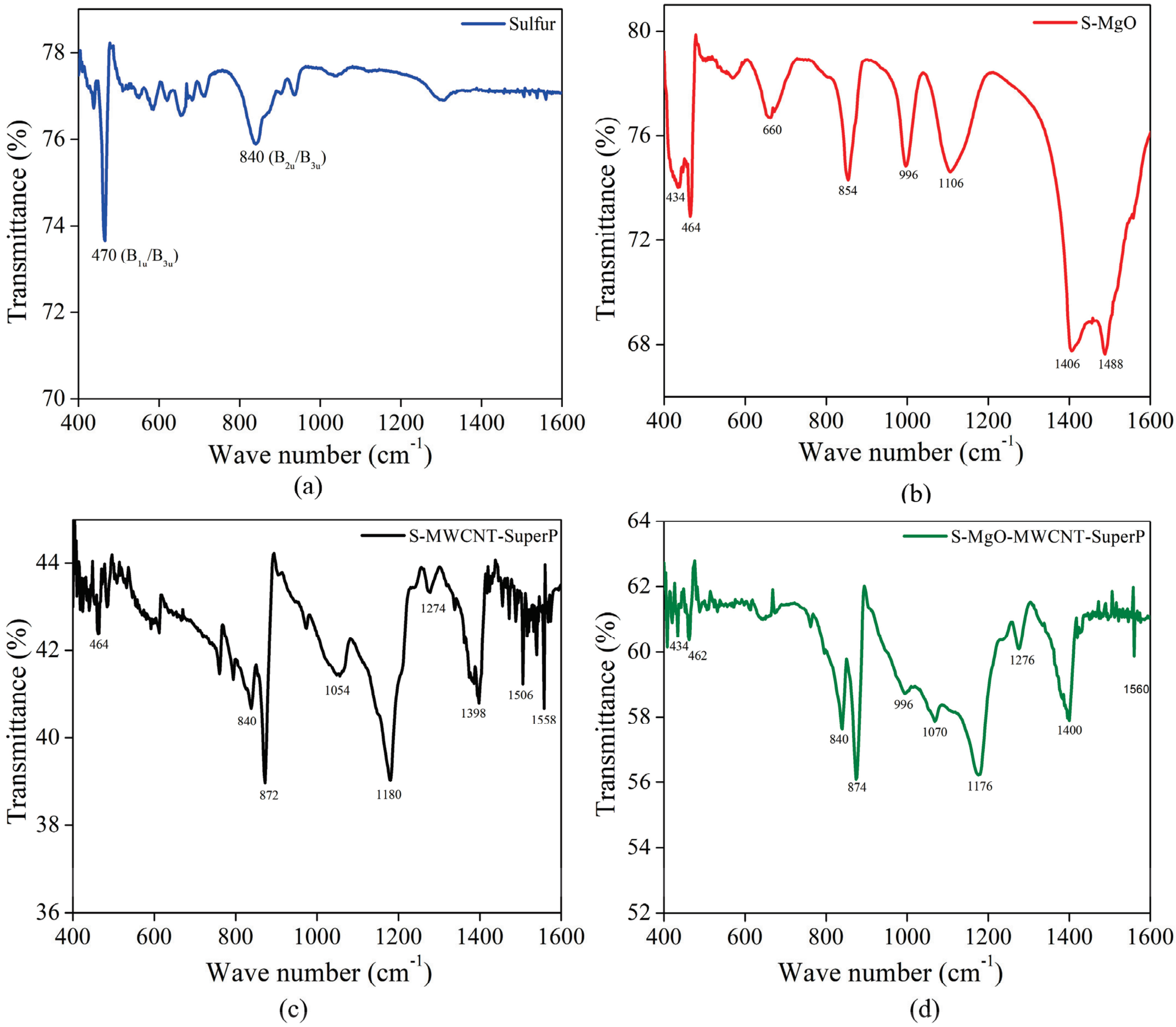

Figure 4. FT–IR spectra of (**a**) pristine sulfur, (**b**) S/MgO, (**c**) S–MWCNT–Super P, and (**d**) S/MgO–MWCNTs–Super P composite.

2.2. Electrochemistry

In Li–S batteries, electrochemical measurements play a crucial role in understanding the mechanisms of sulfur redox reactions, polysulfide formation, and overall battery performance. The electrochemical behavior of the sulfur in the battery is characterized by a series of phase transitions and chemical reactions as lithium ions (Li^+) interact with the sulfur to form different polysulfide intermediates. Figure 1 also highlights the well–known electrochemical reactions involved in the Li–S batteries. Electrochemical techniques such as galvanostatic charge–discharge (GCD) cycling, cyclic voltammetry (CV), and electrochemical impedance spectroscopy (EIS) provide insight into the kinetics of these redox processes, battery capacity, and stability over time.

Figure 5 shows GCD profiles of the assembled coin cells of (a) S/MWCNT/Super P/PVDF and (b) S-MgO/MWCNTs/Super P/PVDF, highlighting the characteristic two plateau discharge behavior evident of the typical behavior of Li–S batteries. The first plateau observed at 2.3 V corresponds to the reduction of elemental sulfur (S_8) to long–chain polysulfides (Li_2S_6 to Li_2S_4), while the second plateau around 2.1 V is associated with further reduction to insoluble Li_2S_2/Li_2S, consistent with the reported literature on sulfur electrochemistry in Li–S cells [61–63]. The cell demonstrated an initial discharge capacity of 950 mA h g^{-1} while incorporating MgO other than the pristine sulfur (600 mA h g^{-1} initial cycles at 0.1 C rate), demonstrating more stable configurations over 400 cycles. The cycling performance and rate of the battery depend on many parameters, like the used electrolyte and its quantity, the active material's stability and compatibility with the current collector, the applied current for charge and discharge, etc. In the present manuscript, the main focus was to control the polysulfide formation in the Li–S battery via the encapsulation engineering of sulfur with the MgO additive regarding the cathode. However, capacity retention was observed with various C rates. In the S/MgO composite, we still observed the two–stage plateau, but the MgO additive played a crucial role in mitigating the polysulfide shuttle effect by chemically absorbing polysulfides and reducing the dissolution into electrolytes. This interaction between the MgO and polysulfides prevents the loss of active sulfur material and enhances the utilization, consistent with the state of the art [34,64,65]. Furthermore, the fabricated cell exhibited a stable nature, as evidenced by the CE consistently exceeding 99.5%, depicted in Figure 5c. Figure 5d shows the cyclic performance and respective CE of the assembled coin cell, demonstrating the impact of varying C rates (C/10 to 1 C) on the electrochemical behavior. We observed a specific discharge capacity ≅1000 mA h g^{-1} at a lower C/10 rate, which retained its capacity ~650 mA h g^{-1} at 1 C upon increasing the current and resumed the pattern of the original capacity while decreasing the current. This natural phenomenon of batteries might be due to kinetic limitations and incomplete redox reactions as high current densities reduce the time for full sulfur conversion and lead to lower specific capacities [4,47,49,66,67]. Moreover, the recovery of the specific capacity occurs upon returning to lower C values, which suggests a robust structure of the composite, enabling reversible sulfur reactions and stable performance over extended cycles (Figure S5) [68]. Notably, CE remains at about 99.5% throughout all the cycles, signifying highly reversible electrochemical reactions and minimal loss of active material, supported by the polysulfide–trapping capability of MgO, which prevents dissolution and enhances the battery performance. The S/MgO–MWCNT–Super P composite demonstrates significant improvements in sulfur retention and cycling stability compared to earlier oxide–based composites. Oxides like TiO_2, CeO_2, and Fe_3O_4 (Table 1) have demonstrated effectiveness in enhancing sulfur cathode performance. In contrast, the current study achieves a stable discharge capacity of approximately 600 mA h g^{-1} over 200 cycles at 0.1 C and maintains around 650 mA h g^{-1} at 1 C, alongside a high CE of ~99.5%. The results demonstrate comparability to, and in certain instances surpass, the performance of the established oxide composites, such as TiO_2/S (850 mA h g^{-1} at 0.5 C), CeO_2/S (611 mA h g^{-1} at 0.5 C), and Fe_3O_4/S (610 mA h g^{-1} at 1 C). The S/MgO–MWCNT–Super P composite demonstrates superior rate capability, high stability, and improved sulfur utilization, highlighting its potential as a viable candidate for the advancement of Li–S battery technologies, especially in applications that demand both high energy density and long-term stability.

After the cycling of the cell, we conducted the investigation of the EDS and SEM (Figure 6) of the S/MgO composite electrode for uncycled and after 400 cycles, indicating significant structural and compositional alterations that highlight the electrode's stability. In the pristine electrode, MgO nanoparticles were found to be randomly and sparsely distributed on the surface of the micrometer–sized sulfur particles (Figure S4). Remarkably, the electrodes remained intact even after 400 cycles, a notable achievement considering that sulfur electrodes typically face challenges in sustaining extended cycles without additives [34,64]. Notably, there is no evidence of fracture observed in the pristine sample, whereas some signature of fracture becomes apparent after the completion of 400 cycles, underscoring the protective role of MgO nanoparticles in maintaining the structural integrity of the electrode during the cycling process. From the EDS analysis of the cycled cathode, it shows a reduction in the sulfur content from 23% to 21%, suggesting sulfur loss, likely attributed to the dissolution of polysulfides into the electrolyte, a prevalent issue in Li–S batteries that contributes to loss of active material and capacity degradation over prolonged cycles. The increase in the oxygen content indicates a possible interaction between MgO and polysulfides, which may lead to the formation of sulfur–oxygen complexes or other oxygen containing byproducts [69–71]. The interaction between MgO and polysulfides is influenced by MgO's significant chemical affinity for polysulfides, which aids in confining them within the cathode matrix, thus reducing their migration—an essential factor for improving the long–term electrochemical stability of Li–S batteries. The results highlight the dual role of MgO as a conductive matrix and chemical adsorbent for polysulfides, enhancing the sulfur retention and cycling performance. Furthermore, the capacity of MgO to capture polysulfides may lead to an enhanced oxygen signature detected in EDS analysis as increased formation of oxidized species is probable during the cycling process. This behavior reinforces the role of MgO in stabilizing the sulfur cathode and mitigating capacity fade.

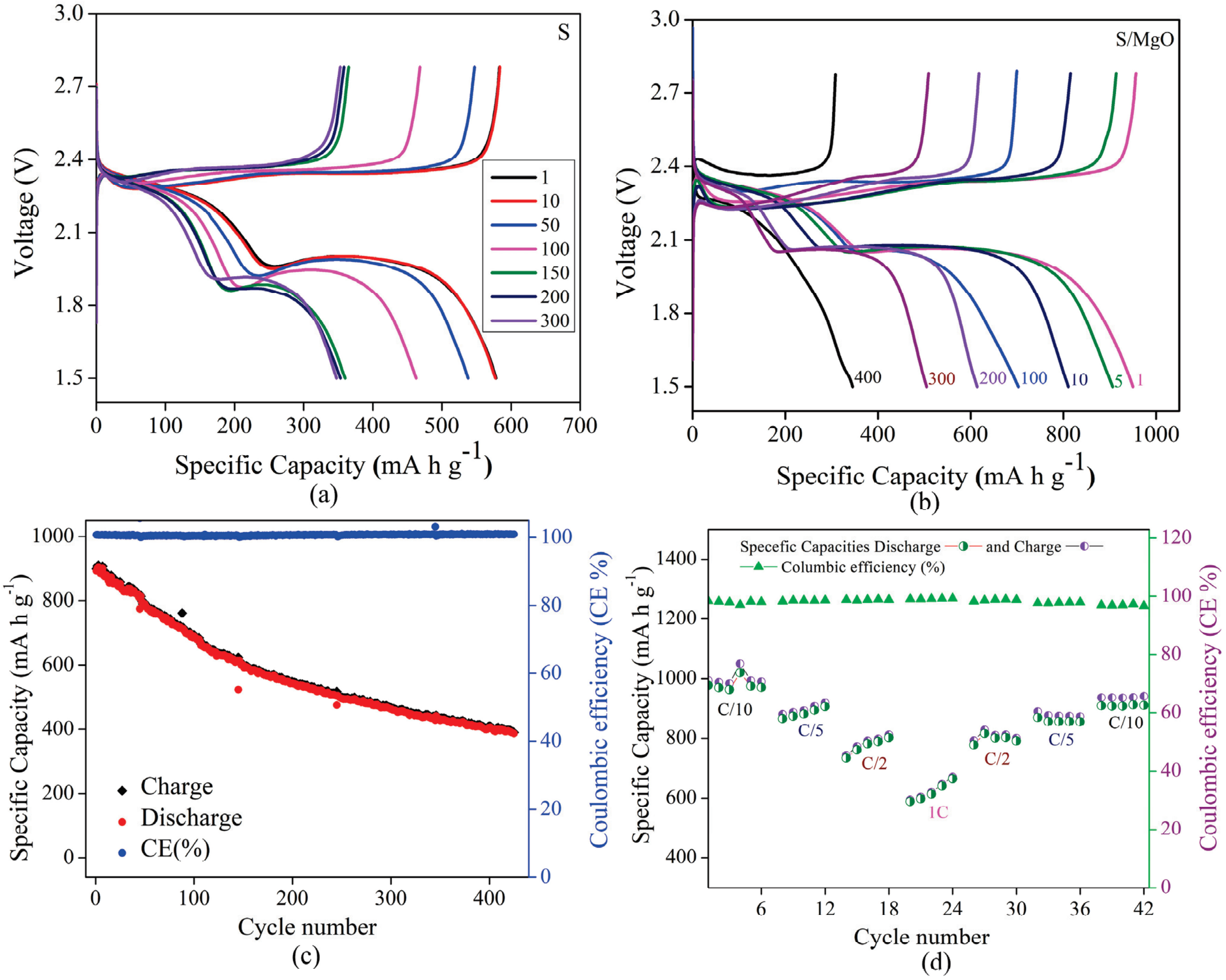

Figure 5. Galvanostatic charge–discharge profile: (**a**) S cathode (without MgO), (**b**) S/MgO composite cathode and (**c**) discharge–specific capacities of S/MgO composite cathode, and (**d**) rate performance of S/MgO composite cathode in Li–S coin cell.

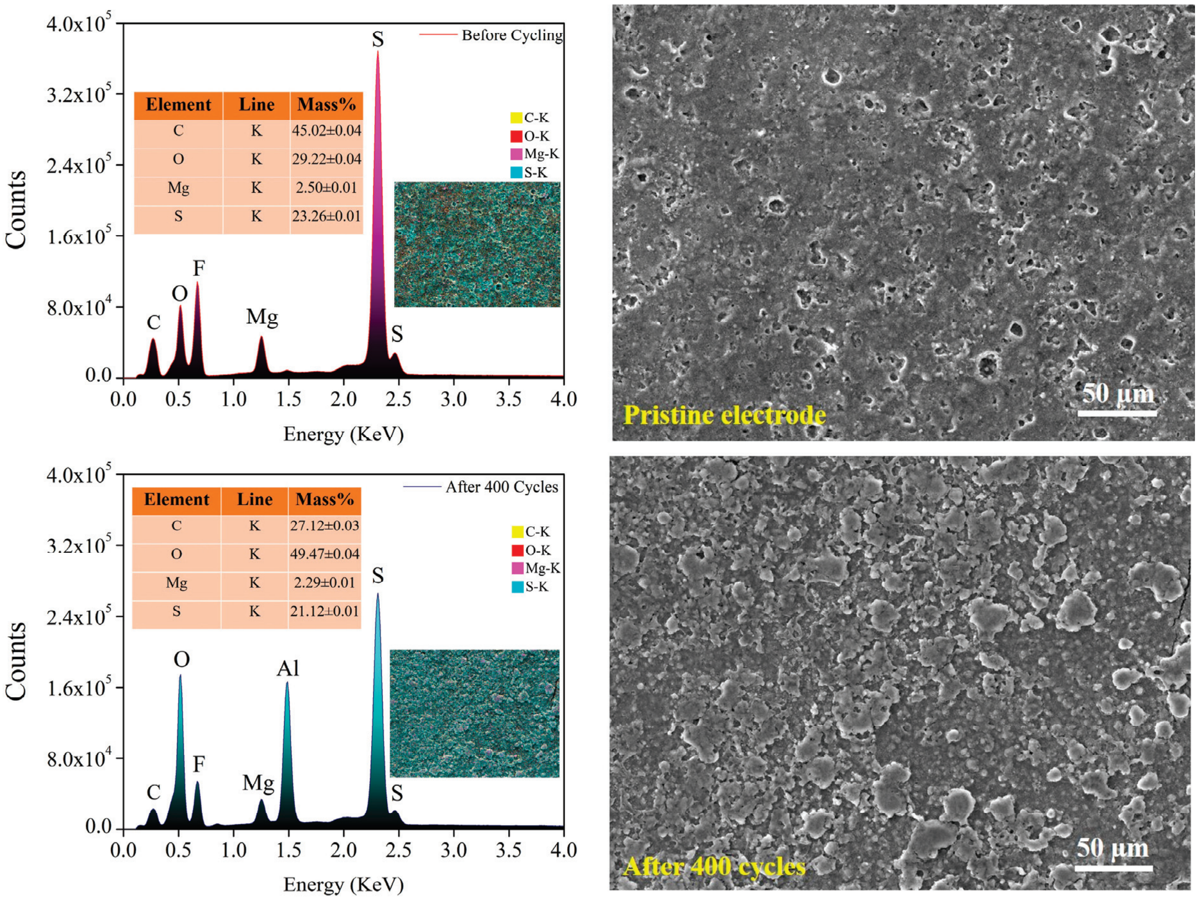

Element	Line	Mass%
C	K	45.02±0.04
O	K	29.22±0.04
Mg	K	2.50±0.01
S	K	23.26±0.01

Element	Line	Mass%
C	K	27.12±0.03
O	K	49.47±0.04
Mg	K	2.29±0.01
S	K	21.12±0.01

Figure 6. SEM–EDS images of pristine and after 400 cycles of S/MgO cathode.

The cyclic voltammetry (CV) profiles (Figure 7a,b) further confirm these findings, showing stable redox activity of sulfur before and after 400 cycles, with MgO effectively trapping polysulfides and maintaining electrode conductivity. The higher current density after 400 cycles suggests improved ionic and electronic pathways provided by MWCNT and Super P. The electrochemical characteristics of a pristine electrode, as reported in the literature [66,72,73], reveal two reduction peaks at 1.95 V and 2.2 V, along with a single oxidation peak at 2.45 V, indicative of the typical sulfur reduction and oxidation processes. The subsequent investigation of the CV characteristics after 400 cycles, within the operating voltage range of 1.5–2.78 V, shows a stable electrochemical performance regarding the reduction. The essentially coincident CV curves after the first cycle suggest sustained stability. Moreover, the observed shifting in the peaks implies alterations in the thermodynamics of the sulfur reduction and Li–S oxidation, hinting at potential improvements in energy barriers. The two reduction peaks are associated with sulfur reduction reactions, progressing from sulfur to lithium polysulfides (Li_2S_n, $4 < n < 8$), and further reduction to Li_2S_2/Li_2S. The oxidation peak corresponds to the reaction from Li_2S to lithium polysulfides. The stability regarding the oxidation and reduction peaks indicates that the S–MgO composite electrode Li–S cell exhibits significant electrochemical performance, reinforcing its suitability for practical applications [9,21,26,27,73]. Electrochemical impedance spectroscopy (EIS) (Figure 7c) further confirmed the enhanced performance, with a decrease in solution resistance (from 11.77 Ω to 3.9 Ω) and charge transfer resistance (from 185 Ω to 156 Ω), signifying improved ionic conductivity and efficient charge transfer [74]. In the process of the electrochemical reaction in electrodes, the Li–ion distributions at the surface and inside the electrode differ, which manifests as a Li–ion concentration gradient and drives Li–ion diffusion. In most cases, Li diffusion plays an import role in the kinetic process that occurs in the electrode materials because the diffusion determines the reaction velocity of electrode materials and thus the rate performance of the electrode. However, the increased diffusion impedance at low frequencies points to diffusion limitations, likely due to polysulfide accumulation or solid electrolyte interphase (SEI) growth after extended cycling. These findings reinforce the suitability of the S–MgO composite for long-term Li–S battery applications as it effectively mitigates the shuttle effect and enhances sulfur utilization [59,63,73].

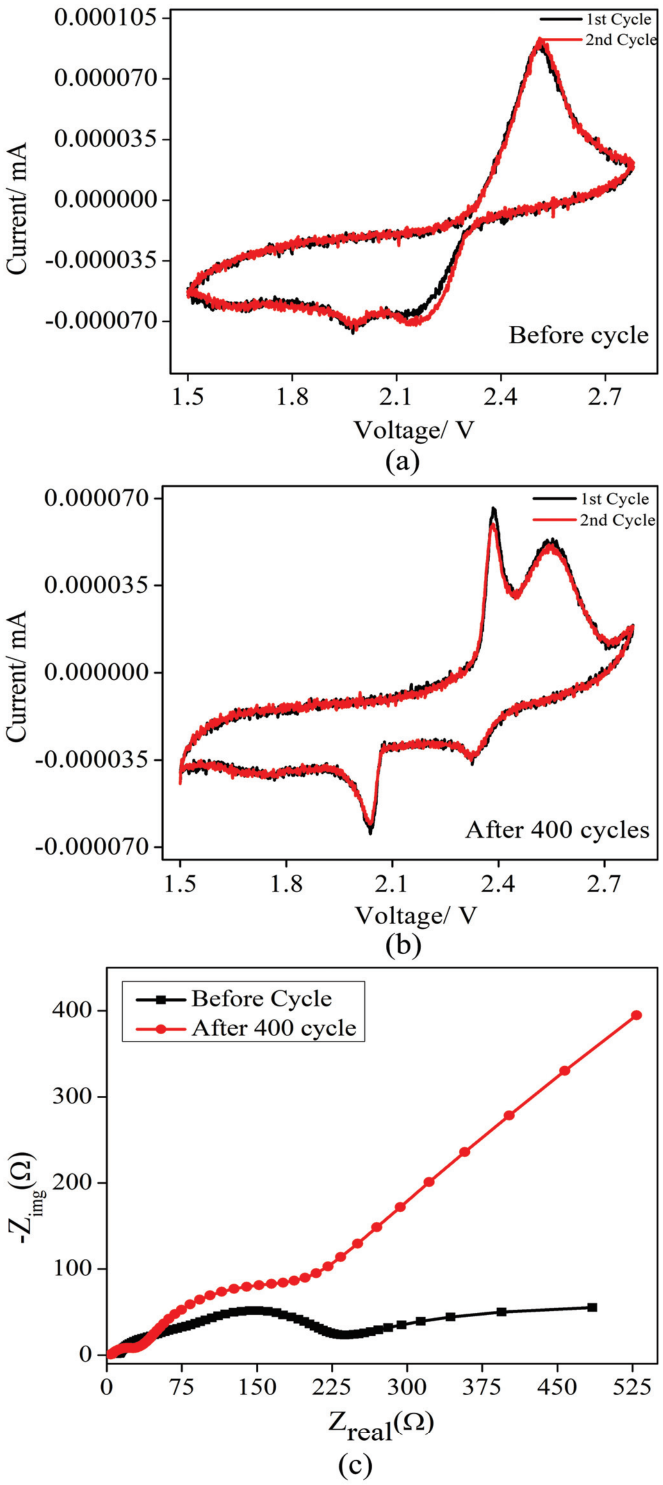

Figure 7. Cyclic voltammetry (CV) of (**a**) uncycled cathode, (**b**) after 400 cycles, and (**c**) EIS performance of S–MgO.

3. Materials and Methods

3.1. Materials

We utilized the following materials in our study, sourced from Sigma-Aldrich unless otherwise noted: magnesium oxide (MgO, nanopowder, $\leq$50 nm particle size), Super-P carbon black, sulfur (S, 99.5–100.5%), polyvinylidene fluoride (PVDF, Mw 1000–1200 kg mol^{-1}, Solef 5130, Solvay, Brussels, Belgium), 1,3-dioxolane (DOL, 99%), 1,2-dimethoxyethane (DME, 99.5%), bis(trifluoromethane) sulfonamide lithium (LiTFSI, 99.95% trace metals basis), and lithium nitrate ($LiNO_3$, 99.99%, trace metals basis). Additionally, the polymer-based separator used for coating was polyphenylene ether (PPE, Celgard Chemicals, Charlotte, NC, USA). All materials were used as received, without further purification. We would like to clarify that the mention of company names is solely for the purpose of accurately describing the materials/ instruments used in our research and does not imply any form of advertisement or endorsement.

3.2. Cathode Preparation, Electrolyte Preparation, and Li–S Coin Cell Assembly

In the cathode, compositions are represented as $(S_{0.9}MgO_{0.1})_{0.6}$ + $(MWCNT)_{0.2}$ + $(Super\ P)_{0.1}$ + $(PVDF)_{0.1}$. Figure 8 illustrates the approach for cathode preparation, wherein we initially combine 90% sulfur with 10% MgO using ball milling. Subsequently, 60% of this mixture was amalgamated with 20% MWCNT and formed into pellets for further processing by the heat diffusion technique in the autoclave and kept in an oven at 150 °C for 6 h. Subsequently, during the preparation of the slurry, 10% Super P and 10% PVDF (solution with NMP) were included, and the combination was crushed in an agate mortar until homogenous. To attain the optimal viscosity for electrode preparation, the addition of 1–2 mL of NMP is advised. Additionally, we prepared the pristine sulfur cathode as $(S)_{0.6}$ + $(MWCNT)_{0.2}$ + $(Super\ P)_{0.1}$ + $(PVDF)_{0.1}$. All components were stirred together in a slurry maker until a homogeneous slurry was obtained. The slurry was evenly spread over an aluminum sheet using a doctor blade machine, then dried at 60 °C for 16 h in a vacuum oven. A die cutter with a 10 mm diameter (MTI Corporation, Richmond, CA, USA) was used to punch the electrodes, and their weight was measured. The electrodes were then transferred into an Ar–filled glove box (MBraun, Garching bei München, Germany) for coin cell assembly. The active mass loading of the final electrodes was approximately 1.1–1.4 mg cm^{-2}, and cell was crimped utilizing MTI's Digital Pressure Controlled Electric Crimper for CR20XX Coin Cells (Ar Glovebox Compatible) MSK-160E (Richmond, CA, USA) and pressure were maintained from 0.831–0.835 T.

Electrolyte Preparation and Assembly of Coin Cell 2032

For efficient trapping of polysulfides, a 1 M solution of bis(trifluoromethane) sulfonamide lithium (LiTFSI) in a solvent mixture of 1,3-dioxolane (DOL) and 1,2-dimethoxyethane (DME) in a 1:1 ratio was employed as the electrolyte. Initially, dried the LiTFSI and lithium nitrite ($LiNO_3$) overnight at 65–70°C to remove the possible moisture. Subsequently, 2 wt% of lithium nitrite ($LiNO_3$) was added to enhance the electrolyte's performance. The fixed amount of electrolyte in various coin cells was maintained at 11–12 µL mg^{-1} of active sulfur material. This tailored electrolyte composition was designed to optimize the performance of the Li–S battery system in the experimental setup. Coin cells were assembled using CR2032 components sourced from Landt Instrument, including a cathode cap, anode cap, spring, and spacer. The setup also included a polypropylene (PP) separator (Celgard 2400, 16 mm), LiTFSI electrolyte, and Li chips (0.6 mm thick, supplied by MSE). A Li chip was employed as the counter electrode (anode) in the half-cell configuration for Li–S batteries. The coin cell assembly steps are shown in Figure S6.

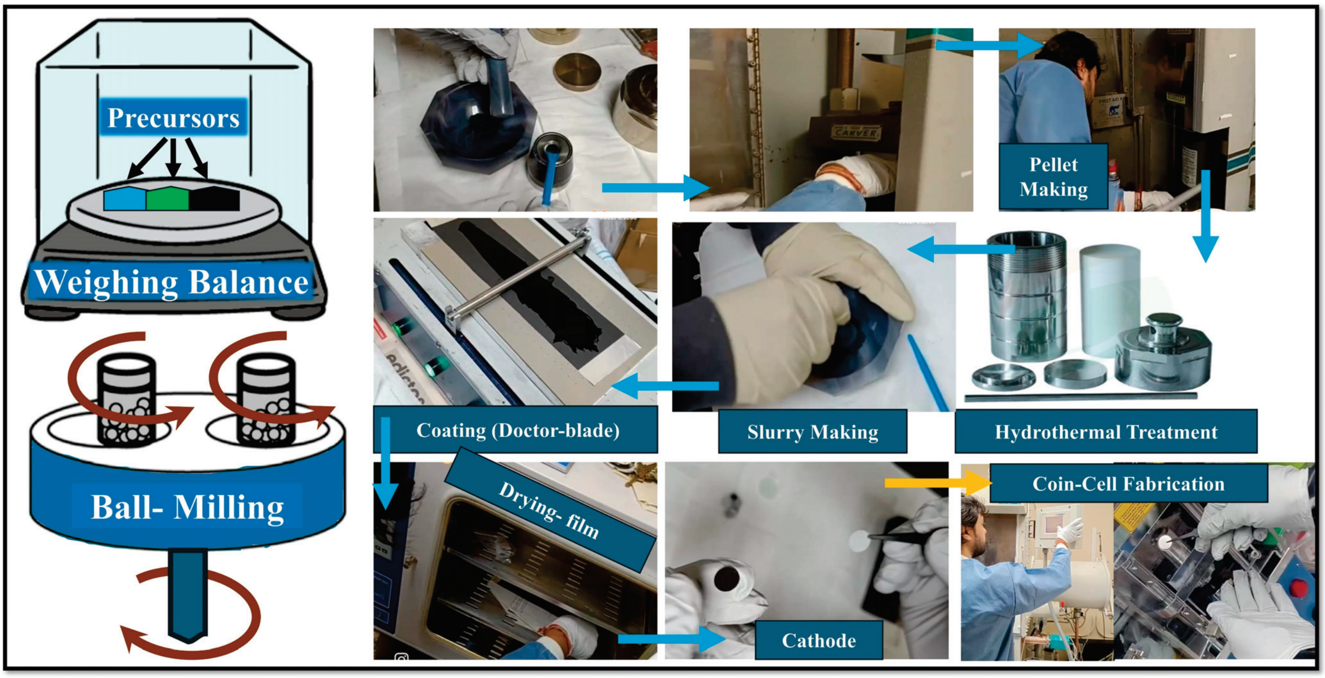

Figure 8. Schematics of cathode preparation.

3.3. Characterization

The crystal structure was analyzed using an X-ray diffractometer (XRD, Rigaku Smart Lab, Tokyo, Japan) with CuK_a radiation and a wavelength (λ) of 1.5405 Å. The instrument was configured in Bragg–Brentano (θ–2θ) geometry, scan rate 0.01, 2θ 10–70°, operated at 40 kV and 44 mA, power 1.76 kW, and measurement error ±0.01. To analyze the data, we utilized Highscore Plus software 3.0.5 for peak matching and phase confirmation, visualized using Vesta. Scanning electron microscopy (SEM) images and energy dispersive X–ray spectroscopy (EDS) spectra were acquired with a JOEL JEM–1400Plus (Peabody, MA, USA) microscope equipped with a LaB6 thermionic source operating at 120 kV. For the analysis of normal modes of vibration, Raman and Fourier transform infrared spectroscopy (FT–IR) spectra were utilized. Raman spectra were recorded from 100 to 3000 cm^{-1} using a Horiba-Jobin T64000 spectrometer (Longjumeau, France) in backscattering geometry, with an excitation wavelength of 514.5 nm (a confocal microscope with an 80× objective with a numerical aperture of 0.9). We utilized the suitable power (1–2 mW on prepared sample) for the prepared sample based on the spectra observation and sample nature. Also, FTIR spectra of samples were recorded by UATR HR Spectrum Two Perking Elmer (Shelton, CT, USA). Data spectra were obtained in the range of 400–4000 cm^{-1} using 32 scans and resolutions of 2 cm^{-1}.

Additionally, electrochemical evaluations, including charge–discharge profiles, cycling stability, cyclic voltammetry, and electrochemical impedance spectroscopy (EIS), were conducted to comprehensively assess the battery performance. Galvanostatic charge–discharge (GCD) rate performance curves were obtained using the multi-channel battery test system CT3002A (Landt, Vestal, NY, USA) in a voltage range of 1.5–2.78 V (vs. Li/Li^+), applying various currents. Cyclic voltammetry (CV) tests were conducted to evaluate the cycling performance and stability of the cathode material using an Arbin instrument at scan rates (0.1 mV/s). Electrochemical impedance spectroscopy (EIS) measurements, conducted before and after cycling at the open circuit voltage (OCV), utilized a signal amplitude of 10 mV within a wide frequency range, using a Gamry Instrument (Interface 1010E Potentiostat/Galvanostat/ZRA, 26081; Warminster, PA, USA).

4. Conclusions

This study shows that MgO significantly improves the stability and discharge capacity of Li–S batteries by functioning as a polysulfide–trapping agent. It sequesters dissolved polysulfide intermediates from the sulfur cathode, thereby enabling the active material to persist in electrochemical reactions. Structural and electrochemical analyses, such as XRD, Raman, FT–IR spectroscopy, and cyclic voltammetry, validate the role of MgO in reducing the polysulfide shuttle effect and enhancing sulfur utilization. Incorporating MgO into the sulfur matrix diminishes capacity fading and enhances long–term cycling stability. Following 400 cycles, the S–MgO composite retains its structural integrity, as demonstrated by the SEM and EDS analyses, revealing only slight sulfur loss and an increase in the oxygen content attributable to interactions between sulfur and MgO. The composite demonstrates stable redox behavior and attains a high CE of 99.5%, indicating that MgO serves as an effective additive for enhancing the lifespan and efficiency of Li–S batteries. The results demonstrate that MgO is a promising additive for advancing Li–S battery technologies by enhancing both capacity retention and cycling stability.

Supplementary Materials: The following supporting information can be downloaded at: https://www.mdpi.com/article/10.3390/molecules29215116/s1, the supplementary materials include the following tables and figures: Tables: Table S1 (Standard character table for D_2h point group symmetry), Table S2 (Total characters representation in D_2h point group), Table S3 (Translational characters in D_2h point group), Table S4 (Rotational characters in D_2h point group), and Table S5 (Vibrational characters in D_2h point group). Figures: Figure S1 (XRD spectra (2q vs intensity) of (a) pristine sulfur and (b) S/MgO), Figure S2 (Peak shifting of 222 peak around 23 degrees), Figure S3 (SEM images of sulfur and composites), Figure S4 (SEM image of S-MgO), Figure S5 (Rate performance of Li–S coin cell with continuous cycling), and Figure S6 (Assembly of 2032 coin cell for Li–S batteries).

Author Contributions: Conceptualization, S.C., B.T. and R.S.K.; Methodology, S.C., N.O., S.S. and S.K.; Software, S.C., S.S. and B.T.; Data curation, S.C., N.O., S.S., S.K., M.K.B., C.A.M.-R. and R.K.K.; Formal analysis, S.C., N.O., S.S., S.K., M.K.B., C.A.M.-R., R.K.K. and B.T.; Visualization, S.C. and R.S.K.; Resources, L.M.D.-V., G.M. and R.S.K.; Writing—original draft, S.C.; Writing—review & editing, M.K.B., R.K.K., B.T., L.M.D.-V. and R.S.K.; Validation, L.M.D.-V., G.M. and R.S.K.; Supervision, R.S.K.; Project administration, G.M. and R.S.K.; Funding acquisition, G.M. and R.S.K. All authors have read and agreed to the published version of the manuscript.

Funding: This study was supported by the National Science Foundation Established Program to Stimulate Competitive Research (NSF-EPSCoR) Center for the Advancement of Wearable Technologies (CAWT) through grant # OIA-1849243, PR NASA EPSCoR grant # 80NSSC24M0107, as well as NASA MIRO PR-SPRInT grant # 80NSSC19M0236.

Institutional Review Board Statement: Not applicable.

Informed Consent Statement: Not applicable.

Data Availability Statement: The data presented in this study is available on request from the corresponding author.

Acknowledgments: We are deeply appreciative of the exceptional assistance provided by William Perez during the investigations. Furthermore, we would like to express our gratitude to Alejandro Parodi from MCC in Cupey, Puerto Rico, for his invaluable contributions to the SEM and EDS measurements.

Conflicts of Interest: The authors declare no conflicts of interest.

References

1. Ji, X.; Lee, K.T.; Nazar, L.F. A highly ordered nanostructured carbon–sulphur cathode for lithium-sulphur batteries. *Nat. Mater.* **2009**, *8*, 500–506. [CrossRef] [PubMed]
2. Zheng, G.; Yang, Y.; Cha, J.J.; Hong, S.S.; Cui, Y. Hollow carbon nanofiber-encapsulated sulfur cathodes for high specific capacity rechargeable lithium batteries. *Nano Lett.* **2011**, *11*, 4462–4467. [CrossRef]

3. Wang, H.; Yang, Y.; Liang, Y.; Robinson, J.T.; Li, Y.; Jackson, A.; Cui, Y.; Dai, H. Graphene-wrapped sulfur particles as a rechargeable lithium-sulfur battery cathode material with high capacity and cycling stability. *Nano Lett.* **2011**, *11*, 2644–2647. [CrossRef] [PubMed]
4. Manthiram, A.; Chung, S.H.; Zu, C. Lithium-sulfur batteries: Progress and prospects. *Adv. Mater.* **2015**, *27*, 1980–2006. [CrossRef]
5. Rosenman, A.; Markevich, E.; Salitra, G.; Aurbach, D.; Garsuch, A.; Chesneau, F.F. Review on Li-Sulfur Battery Systems: An Integral Perspective. *Adv. Energy Mater.* **2015**, *5*, 1500212. [CrossRef]
6. Wang, J.; Xie, K.; Wei, B. Advanced engineering of nanostructured carbons for lithium-sulfur batteries. *Nano Energy* **2015**, *15*, 413–414. [CrossRef]
7. Zhang, S.; Ueno, K.; Dokko, K.; Watanabe, M. Recent Advances in Electrolytes for Lithium-Sulfur Batteries. *Adv. Energy Mater.* **2015**, *5*, 1500117. [CrossRef]
8. Xu, R.; Lu, J.; Amine, K. Progress in Mechanistic Understanding and Characterization Techniques of Li-S Batteries. *Adv. Energy Mater.* **2015**, *5*, 1500408. [CrossRef]
9. Kang, H.; Shin, J.; Kim, T.H.; Lee, Y.; Lee, D.; Lee, J.; Kim, G.; Cho, E. Metal-Organic Framework-Derived Magnesium Oxide@Carbon Interlayer for Stable Lithium-Sulfur Batteries. *ACS Sustain. Chem. Eng.* **2023**, *11*, 1344–1354. [CrossRef]
10. Liu, Y.T.; Liu, S.; Li, G.R.; Yan, T.Y.; Gao, X.P. High Volumetric Energy Density Sulfur Cathode with Heavy and Catalytic Metal Oxide Host for Lithium-sulfur Battery. *Adv. Sci.* **2020**, *7*, 1903693. [CrossRef]
11. Gu, X.; Tong, C.J.; Lai, C.; Qiu, J.; Huang, X.; Yang, W.; Wen, B.; Liu, L.M.; Hou, Y.; Zhang, S. A porous nitrogen and phosphorous dual-doped graphene blocking layer for high performance Li-S batteries. *J. Mater. Chem. A* **2015**, *3*, 16670–16678. [CrossRef]
12. Zhou, G.; Paek, E.; Hwang, G.S.; Manthiram, A. Long-life Li/polysulphide batteries with high sulphur loading enabled by lightweight three-dimensional nitrogen/sulphur-codoped graphene sponge. *Nat. Commun.* **2015**, *6*, 7760. [CrossRef]
13. Qiu, Y.; Li, W.; Zhao, W.; Li, G.; Hou, Y.; Liu, M.; Zhou, L.; Ye, F.; Li, H.; Wei, Z.; et al. High-rate, ultralong cycle-life lithium/sulfur batteries enabled by nitrogen-doped graphene. *Nano Lett.* **2014**, *14*, 4821–4827. [CrossRef]
14. Xie, Y.; Meng, Z.; Cai, T.; Han, W.Q. Effect of Boron-Doping on the Graphene Aerogel Used as Cathode for the Lithium-sulfur Battery. *ACS Appl. Mater. Interfaces* **2015**, *7*, 25202–25210. [CrossRef]
15. Chen, Y.; Wang, T.; Tian, H.; Su, D.; Zhang, Q.; Wang, G. Advances in lithium-sulfur batteries: From academic research to commercial viability. *Adv. Mater.* **2021**, *33*, 2003666. [CrossRef]
16. Choi, Y.J.; Jung, B.S.; Lee, D.J.; Jeong, J.H.; Kim, K.W.; Ahn, H.J.; Cho, K.K.; Gu, H.B. Electrochemical properties of sulfur electrode containing nano Al_2O_3 for lithium/sulfur cell. *Phys. Scr.* **2007**, 62. [CrossRef]
17. Zhang, Z.; Li, Q.; Zhang, K.; Chen, W.; Lai, Y.; Li, J. Titanium-dioxide-grafted carbon paper with immobilized sulfur as a flexible free-standing cathode for superior lithium-sulfur batteries. *J. Power Sources* **2015**, *290*, 159–167. [CrossRef]
18. Song, M.S.; Han, S.C.; Kim, H.S.; Kim, J.H.; Kim, K.T.; Kang, Y.M.; Ahn, H.J.; Dou, S.X.; Lee, J.Y. Effects of Nanosized Adsorbing Material on Electrochemical Properties of Sulfur Cathodes for Li/S Secondary Batteries. *J. Electrochem. Soc.* **2004**, *151*, A791. [CrossRef]
19. Tao, Y.; Wei, Y.; Liu, Y.; Wang, J.; Qiao, W.; Ling, L.; Long, D. Kinetically-enhanced polysulfide redox reactions by Nb_2O_5 nanocrystals for high-rate lithium-sulfur battery. *Energy Environ. Sci.* **2016**, *9*, 3230–3239. [CrossRef]
20. Jia, X.; Liu, B.; Liu, J.; Zhang, S.; Sun, Z.; He, X.; Li, H.; Wang, G.; Chang, H. Fabrication of NiO-carbon nanotube/sulfur composites for lithium-sulfur battery application. *RSC Adv.* **2021**, *11*, 10753–10759. [CrossRef]
21. Liu, J.; Zhu, M.; Shen, Z.; Han, T.; Si, T.; Hu, C.; Zhang, H. A Polysulfides-Confined All-in-One Porous Microcapsule Lithium-Sulfur Battery Cathode. *Small* **2021**, *17*, 2103051. [CrossRef] [PubMed]
22. Ma, L.; Chen, R.; Zhu, G.; Hu, Y.; Wang, Y.; Chen, T.; Liu, J.; Jin, Z. Cerium Oxide Nanocrystal Embedded Bimodal Micromesoporous Nitrogen-Rich Carbon Nanospheres as Effective Sulfur Host for Lithium-Sulfur Batteries. *ACS Nano* **2017**, *11*, 7274–7283. [CrossRef] [PubMed]
23. Choi, C.; Lee, D.Y.; Park, J.B.; Kim, D.W. Separators Modified Using MoO_2@Carbon Nanotube Nanocomposites as Dual-Mode Li-Polysulfide Anchoring Materials for High-Performance Anti-Self-Discharge. *ACS Sustain. Chem. Eng.* **2020**, *8*, 15134–15148. [CrossRef]
24. Liu, R.; Guo, F.; Zhang, X.; Yang, J.; Li, M.; Miaomiao, W.; Liu, H.; Feng, M.; Zhang, L. Novel "bird-Nest" Structured Co_3O_4/Acidified Multiwall Carbon Nanotube (ACNT) Hosting Materials for Lithium-Sulfur Batteries. *ACS Appl. Energy Mater.* **2019**, *2*, 1348–1356. [CrossRef]
25. Jian, Z.; Zhang, S.; Guan, X.; Li, J.; Li, H.; Wang, W.; Xing, Y.; Xu, H. ZnO quantum dot-modified rGO with enhanced electrochemical performance for lithium-sulfur batteries. *RSC Adv.* **2020**, *10*, 32966–32975. [CrossRef]
26. Su, Z.; Chen, M.; Pan, Y.; Liu, Y.; Xu, H.; Zhang, Y.; Long, D. Expediting polysulfide catalytic conversion for lithium-sulfur batteries via in situ implanted ultrafine Fe_3O_4 nanocrystals in carbon nanospheres. *J. Mater. Chem. A* **2020**, *8*, 24117–24127. [CrossRef]
27. Pan, H.; Cheng, Z.; Zhang, X.; Wan, K.; Fransaer, J.; Luo, J.; Wübbenhorst, M. Manganese dioxide nanosheet functionalized reduced graphene oxide as a compacted cathode matrix for lithium-sulphur batteries with a low electrolyte/sulphur ratio. *J. Mater. Chem. A* **2020**, *8*, 21824–21832. [CrossRef]
28. Chen, H.; Tang, H. Interfacial insights for divergent dendrite formation mechanisms in lithium and magnesium anodes. *J. Mater. Chem. A* **2024**, *12*, 22584–22596. [CrossRef]

29. Liang, Q.; Wang, S.; Yao, Y.; Dong, P.; Song, H. Transition Metal Compounds Family for Li-S Batteries: The DFT-Guide for Suppressing Polysulfides Shuttle. *Adv. Funct. Mater.* **2023**, *33*, 2300825. [CrossRef]
30. Rettig, S.; Trotter, J. Refinement of the structure of orthorhombic sulfur, α-S_8. *Acta Crystallogr. Sect. C Cryst. Struct. Commun.* **1987**, *43*, 2260–2262. [CrossRef]
31. Balakrishnan, G.; Velavan, R.; Batoo, K.M.; Raslan, E.H. Microstructure, optical and photocatalytic properties of MgO nanoparticles. *Res. Phys.* **2020**, *16*, 103013. [CrossRef]
32. McCarthy, G.J.; Martin, K.J.; Holzer, J.M.; Grier, D.G.; Syvinski, W.M.; Nodland, D.W. Calculated Patterns in X-Ray Powder Diffraction Analysis. *Adv. X-Ray Anal.* **1991**, *35*, 17–23. [CrossRef]
33. Guzmán, M.; Reyes, G.; Agulló, N.; Borrós, S. Synthesis of Zn/Mg oxide nanoparticles and its influence on sulfur vulcanization. *J. Appl. Polym. Sci.* **2011**, *119*, 2048–2057. [CrossRef]
34. Ponraj, R.; Kannan, A.G.; Ahn, J.H.; Kim, D.W. Improvement of Cycling Performance of Lithium-Sulfur Batteries by Using Magnesium Oxide as a Functional Additive for Trapping Lithium Polysulfide. *ACS Appl. Mater. Interfaces* **2016**, *8*, 4000–4006. [CrossRef]
35. Ma, D.; Zhu, R.; Ruan, F.; Sonamuthu, J.; Zhang, Q.; Sun, M.; Li, H.; Cai, Y. Rational design of hierarchical C-MgO@ZnO nanofiber as sulfur host for high-performance lithium-sulfur batteries. *J. Mater. Sci.* **2020**, *55*, 5534–5544. [CrossRef]
36. Duong, T.H.Y.; Nguyen, T.N.; Oanh, H.T.; Dang Thi, T.A.; Giang, L.N.T.; Phuong, H.T.; Anh, N.T.; Nguyen, B.M.; Tran Quang, V.; Le, G.T.; et al. Synthesis of magnesium oxide nanoplates and their application in nitrogen dioxide and sulfur dioxide adsorption. *J. Chem.* **2019**, *2019*, 4376429. [CrossRef]
37. Eckert, B.; Steudel, R. Molecular spectra of sulfur molecules and solid sulfur allotropes. In *Elemental Sulfur und Sulfur-Rich Compounds II. Topics in Current Chemistry*; Springer: Berlin/Heidelberg, Germany, 2003; Volume 231, p. 3198. [CrossRef]
38. Domingo, C.; Montero, S. Raman intensities of sulphur α-S_8. *J. Chem. Phys.* **1981**, *74*, 862–872. [CrossRef]
39. Ward, A.T. Raman spectroscopy of sulfur, sulfur-selenium, and sulfur-arsenic mixtures. *J. Phys. Chem.* **1968**, *72*, 4133–4139. [CrossRef]
40. Ward, A.T. Crystal-field splitting of fundamentals in the Raman spectrum of rhombic sulfur. *J. Phys. Chem.* **1968**, *72*, 744–746. [CrossRef]
41. Wu, H.L.; Huff, L.A.; Gewirth, A.A. In situ Raman spectroscopy of sulfur speciation in lithium–sulfur batteries. *ACS Appl. Mater. Interfaces* **2015**, *7*, 1709–1719. [CrossRef]
42. Han, S.; Czernuszewicz, R.S.; Spiro, T.G. Vibrational Spectra and Normal Mode Analysis for [2Fe-2S] Protein Analogues Using 34S, 54Fe, and 2H Substitution: Coupling of Fe-S Stretching and S-C-C Bending Modes. *J. Am. Chem. Soc.* **1989**, *111*, 3496–3504. [CrossRef]
43. Steudel, R. *Elemental Sulfur and Sulfur-Rich Compounds II*; Springer: Berlin/Heidelberg, Germany, 2003; Volume 248.
44. Costa, S.; Borowiak-Palen, E.; Kruszynska, M.; Bachmatiuk, A.; Kalenczuk, R.J. Characterization of carbon nanotubes by Raman spectroscopy. *Mater. Sci. Pol.* **2008**, *26*, 433–441.
45. Puech, P.; Flahaut, E.; Bassil, A.; Juffmann, T.; Beuneu, F.; Bacsa, W.S. Raman bands of double-wall carbon nanotubes: Comparison with single- and triple-wall carbon nanotubes, and influence of annealing and electron irradiation. *J. Raman Spectrosc.* **2007**, *38*, 714–720. [CrossRef]
46. Zhang, F.; Hou, P.X.; Liu, C.; Wang, B.W.; Jiang, H.; Chen, M.L.; Sun, D.M.; Li, J.C.; Cong, H.T.; Kauppinen, E.I.; et al. Growth of semiconducting single-wall carbon nanotubes with a narrow band-gap distribution. *Nat. Commun.* **2016**, *7*, 11160. [CrossRef] [PubMed]
47. Shweta, S.; Bhattarai, M.K.; Kumar, S.; Choudhary, S.; Morell, G.; Katiyar, R.S. Enhanced rate capability in lithium-sulfur batteries using hybrid carbon nanotubes and NZFO-coated separator. *J. Electroanal. Chem.* **2024**, *966*, 118396. [CrossRef]
48. Katiyar, R.K.; Zuluaga Gomez, C.C.; Katiyar, S.; Tripathi, B.; Morell, G.; Weiner, B.R.; Katiyar, R.S. Capacity Retention Through a Separator Coated with Bifunctional Ferroelectric Nanoparticles and Modified Cathodes for Li-S Batteries. *Chem. Sel.* **2023**, *8*, e202300614. [CrossRef]
49. Bhattarai, M.K.; Tripathi, B.; Shweta, S.; Kumar, S.; Zuluaga-Gómez, C.C.; Katiyar, R.K.; Weiner, B.R.; Katiyar, R.S.; Morell, G. Effective polysulfide control in lithium-sulfur batteries utilizing $BiFeO_3$ nanoparticles. *Appl. Mater.* **2024**, *12*, 051125. [CrossRef]
50. Saqib, N.; Silva, C.J.; Maupin, C.M.; Porter, J.M. A Novel Optical Diagnostic for In Situ Measurements of Lithium Polysulfides in Battery Electrolytes. *Appl. Spectrosc.* **2017**, *71*, 1593–1599. [CrossRef]
51. Ferrari, P.; Berden, G.; Redlich, B.; Waters, L.B.; Bakker, J.M. Laboratory infrared spectra and fragmentation chemistry of sulfur allotropes. *Nat. Commun.* **2024**, *15*, 5928. [CrossRef]
52. Nakamoto, K. *Infrared and Raman Spectra of Inorganic and Coordination Compounds, Part B Applications in Coordination, Organometallic, and Bioinorganic Chemistry*, 6th ed.; Wiley: Hoboken, NJ, USA, 2009. [CrossRef]
53. Puspitasari, I.; Mutmainah, W.; Nobel, M.P.; Hidayat, S. Purification of Natural Sulfur up to the Analyst Grade to qualify for Li-Sulfur Battery Applications. *J. Phys. Conf. Ser.* **2024**, *2780*, 012021. [CrossRef]
54. Rasheed, H.K.; Kareem, A.A. Effect of Multiwalled Carbon Nanotube Reinforcement on the Opto-Electronic Properties of Polyaniline/c-Si Heterojunction. *J. Opt. Commun.* **2021**, *42*, 25–29. [CrossRef]
55. Shuit, S.H.; Tan, S.H. Feasibility study of various sulphonation methods for transforming carbon nanotubes into catalysts for the esterification of palm fatty acid distillate. *Energy Convers. Manag.* **2014**, *88*, 1283–1289. [CrossRef]

56. Song, G.; Ma, S.; Tang, G.; Wang, X. Ultrasonic-assisted synthesis of hydrophobic magnesium hydroxide nanoparticles. *Colloids Surf. A Physicochem. Eng. Asp.* **2010**, *364*, 99–104. [CrossRef]
57. Salman, K.D.; Abbas, H.H.; Aljawad, H.A. Synthesis and characterization of MgO nanoparticle via microwave and sol-gel methods. *J. Phys. Conf. Ser.* **2021**, *1973*, 012104. [CrossRef]
58. Selvam, N.C.S.; Kumar, R.T.; Kennedy, L.J.; Vijaya, J.J. Comparative study of microwave and conventional methods for the preparation and optical properties of novel MgO-micro and nano-structures. *J. Alloys Compd.* **2011**, *509*, 9809. [CrossRef]
59. Sternig, A.; Diwald, O.; Gross, S.; Sushko, P.V. Surface decoration of MgO nanocubes with sulfur oxides: Experiment and theory. *J. Phys. Chem. C* **2013**, *117*, 7727–7735. [CrossRef] [PubMed]
60. Fan, J.J.; Fan, Y.J.; Wang, R.X.; Xiang, S.; Tang, H.G.; Sun, S.G. A novel strategy for the synthesis of sulfur-doped carbon nanotubes as a highly efficient Pt catalyst support toward the methanol oxidation reaction. *J. Mater. Chem. A* **2017**, *5*, 19467–19475. [CrossRef]
61. Liang, X.; Hart, C.; Pang, Q.; Garsuch, A.; Weiss, T.; Nazar, L.F. A highly efficient polysulfide mediator for lithium-sulfur batteries. *Nat. Commun.* **2015**, *6*, 5682. [CrossRef]
62. Bruce, P.G.; Freunberger, S.A.; Hardwick, L.J.; Tarascon, J.-M. Tarascon, Li-O_2 and Li-S batteries with high energy storage. *Nat. Mater.* **2012**, *11*, 19–29. [CrossRef]
63. Santos, A.; Fernandes, R.C.; Vicentini, R.; Aguiar, J.P.; Da Silva, L.M.; Zanin, H. On the electrochemical properties of lithium sulfur batteries. *J. Energy Storage* **2023**, *71*, 108203. [CrossRef]
64. Kiai, M.S. Magnesium oxide as an additive with polymeric sulfur cathode and modified glass fiber separator for high performance lithium-sulfur batteries. *ChemRxiv* **2021**. [CrossRef]
65. Wang, P.; Xi, B.; Zhang, Z.; Song, N.; Chen, W.; Feng, J.; Xiong, S. Dual-Functional MgO Nanocrystals Satisfying Both Polysulfides and Li Regulation toward Advanced Lithium-Sulfur Full Batteries. *Small* **2021**, *17*, 2103744. [CrossRef] [PubMed]
66. Chung, S.H.; Manthiram, A. High-performance Li–S batteries with an ultra-lightweight MWCNT-coated separator. *J. Phys. Chem. Lett.* **2014**, *5*, 1978–1983. [CrossRef] [PubMed]
67. He, J.; Manthiram, A. A review on the status and challenges of electrocatalysts in lithium-sulfur batteries. *Energy Storage Mater.* **2019**, *20*, 55–70. [CrossRef]
68. Zhang, S.S. Liquid electrolyte lithium/sulfur battery: Fundamental chemistry, problems, and solutions. *J. Power Sources* **2013**, *231*, 153–162. [CrossRef]
69. Zheng, Y.; Yi, Y.; Fan, M.; Liu, H.; Li, X.; Zhang, R.; Li, M.; Qiao, Z.A. A high-entropy metal oxide as chemical anchor of polysulfide for lithium-sulfur batteries. *Energy Storage Mater.* **2019**, *23*, 678–683. [CrossRef]
70. Li, Y.; Guo, S. Material design and structure optimization for rechargeable lithium-sulfur batteries. *Matter* **2021**, *4*, 1142–1188. [CrossRef]
71. Pang, Q.; Shyamsunder, A.; Narayanan, B.; Kwok, C.Y.; Curtiss, L.A.; Nazar, L.F. Tuning the electrolyte network structure to invoke quasi-solid state sulfur conversion and suppress lithium dendrite formation in Li-S batteries. *Nat. Energy* **2018**, *3*, 783–791. [CrossRef]
72. Xue, W.; Shi, Z.; Suo, L.; Wang, C.; Wang, Z.; Wang, H.; So, K.P.; Maurano, A.; Yu, D.; Chen, Y. Intercalation-conversion hybrid cathodes enabling Li-S full-cell architectures with jointly superior gravimetric and volumetric energy densities. *Nat. Energy* **2019**, *4*, 374–382. [CrossRef]
73. Sun, W.; Sun, X.; Peng, Q.; Wang, H.; Ge, Y.; Akhtar, N.; Huang, Y.; Wang, K. Nano-MgO/AB decorated separator to suppress shuttle effect of lithium-sulfur battery. *Nanoscale Adv.* **2019**, *1*, 1589–1597. [CrossRef]
74. Dharmaraj, V.R.; Sarkar, A.; Yi, C.-H.; Iputera, K.; Huang, S.-Y.; Chung, R.-J.; Hu, S.-F.; Liu, R.-S. Battery performance amelioration by introducing a conducive mixed electrolyte in rechargeable Mg-O_2 batteries. *ACS Appl. Mater. Interfaces* **2023**, *15*, 9675–9684. [CrossRef] [PubMed]

Disclaimer/Publisher's Note: The statements, opinions and data contained in all publications are solely those of the individual author(s) and contributor(s) and not of MDPI and/or the editor(s). MDPI and/or the editor(s) disclaim responsibility for any injury to people or property resulting from any ideas, methods, instructions or products referred to in the content.

molecules

Article

Carbonized Ganoderma Lucidum/V_2O_3 Composites as a Superior Cathode for High-Performance Aqueous Zinc-Ion Batteries

Guilin Zeng [1,2], Zhengda Li [1,*], Shaohua Jiang [3] and Wei Zhou [1,*]

[1] Hunan Key Laboratory of Applied Environmental Photocatalysis, Changsha University, Changsha 410022, China; zglhut@163.com
[2] College of Materials and Advanced Manufacturing, Hunan University of Technology, Zhuzhou 412007, China
[3] Jiangsu Co-Innovation Center of Efficient Processing and Utilization of Forest Resources, International Innovation Center for Forest Chemicals and Materials, College of Materials Science and Engineering, Nanjing Forestry University, Nanjing 210037, China; shaohua.jiang@njfu.edu.cn
* Correspondence: 0736a@163.com (Z.L.); zhouwei_csu@163.com (W.Z.)

Abstract: In response to the suboptimal electrochemical performance of low-valence vanadium oxides, Ganoderma lucidum biomass-derived carbon@V_2O_3 (V_2O_3@CGL) composites were prepared by evaporative self-assembly technology and high-temperature calcination. In the prepared composites, V_2O_3 effectively encapsulates CGL, serving as a support for V_2O_3 and enhancing electrical conductivity and structural stability. This results in improved overall performance for the composites. They revealed satisfactory electrochemical properties when assembled in aqueous zinc-ion batteries (AZIBs). The preliminary discharge specific capacity of the V_2O_3@CGL-2 (VOCG-2) composite electrode reached 407.87 mAh g^{-1} at 0.05 A g^{-1}. After 1000 cycles, the capacity retention is 93.69% at 3 A g^{-1}. This research underscores the feasibility of employing V_2O_3 and abundantly available biomass for high-performance AZIB cathodes.

Keywords: V_2O_3; carbonized; biomass; cathode; AZIBs; capacity retention

1. Introduction

Severe environmental pollution and energy shortages have compelled us to develop inexpensive and renewable storage devices for energy [1,2]. Lithium-ion batteries, as a type of secondary battery, are currently one of the most widely used energy storage devices on account of their satisfactory energy density and long cycle life [3,4]. Nonetheless, concerns about safety and limited resources, such as lithium metal, have driven the exploration of new battery systems. In recent years, water-based metal-ion batteries (e.g., zinc, sodium, potassium, magnesium, and calcium) have shown enormous possibilities in energy storage, considering the abundant reserves of metal resources on earth and their inherent safety [5].

Among these options, AZIBs have garnered significant curiosity from researchers worldwide because of their rich sources, non-toxicity, high safety, low REDOX potential (−0.76 V), and excellent theoretical capacity (approximately 820 mAh g^{-1}) [6–9]. However, research on AZIBs is still in its early stages, and it is challenging to find positive electrode materials suitable for reversible Zn^{2+} embedding or de-embedding, restricting the development of AZIB systems. Previous studies on AZIB cathode materials have focused on Prussian blue analogues with a cubic open frame structure [10]. However, this has a limited capacity (about 60 mAh g^{-1}), which hinders further development. Manganese oxides, such as MnO_2, α-Mn_2O_3, and Mn_3O_4, have considerable voltage and desirable capacity. Nonetheless, the dissolution of manganese in the electrolyte leads to poor cycling performance [11–13].

Among AZIB cathode materials, vanadium-based materials have been extensively researched for their high specific capacity, vast resources, and excellent cycle stability [14–17]. For instance, Hu et al. [18] obtained porous V_2O_5 material (P-V_2O_5) by pyrolyzing V-MOF. As the cathode for AZIBs, the P-V_2O_5 electrode manifested a capacity of 120 mAh g^{-1} at 2 A g^{-1}. They also demonstrated that the formation of V_2O_5 nanoflakes and the reorganization with carbon can increase cycle stability. Mai et al. [19] successfully developed $Na_2V_6O_{16}\cdot 1.63H_2O$ material that is highly suitable for Zn^{2+} embedding and removal, demonstrating a noteworthy specific capacity of 352 mAh g^{-1} and a desirable long-cycle stability with a capacity retention of 90% for 6000 cycles at 0.05 A g^{-1}.

Although well developed in small-scale production, the above synthesis methods are still far from commercialization due to their complexity, the high cost of electrolyte and electrode materials, and unsustainable carbon sources [20,21]. Therefore, the search for cheap, abundant, and renewable raw materials gradually gains popularity. Biomass, a carbon-rich precursor, has been extensively researched in various applications because of its inherent benefits, such as environmental friendliness, abundant renewable resources, and economic benefits [22–24].

In this study, the Ganoderma lucidum biomass was first activated using KOH ultrasonic solvent and calcination. The observed V_2O_3@CGL composites exhibited a large specific surface area and numerous mesopores, which furnished abundant active sites and efficient channels for reversible storage of Zn^{2+}. Three Ganoderma lucidum biomass-derived carbon/V_2O_3 composites were prepared as positive electrodes for AZIBs, with the economical 3M $ZnSO_4$ serving as the electrolyte. The VOCG-2 composite electrode displayed outstanding durability with a satisfactory capacity retention of 93.69% after 1000 cycles at 3 A g^{-1}. SEM analysis confirmed that the VOCG-2 composite electrode maintained a steady morphology during circulation. These findings suggest VOCG-2 composites offer promising potential for fast and long-lasting storage of Zn^{2+}.

2. Results

Through XRD investigations, detailed information regarding the crystal structure of the V_2O_3@CGL composites was obtained. Figure 1a illustrates the XRD patterns of the V_2O_3@CGL composites, displaying a broad diffraction peak at approximately $2\theta = 24.5°$, which is consistent with the (002) plane of amorphous carbon [25]. The peak intensity of this diffraction peak diminishes with the reduction of carbon in the composites. No additional noteworthy residual phases were detected, implying that there is no noticeable impact of CGL on the crystal structure of V_2O_3. In addition, the diffraction peaks centered at 65.2°, 53.9°, 41.3°, 36.3°, 33.0°, and 24.3°, correspond to the (300), (116), (113), (110), (104), and (012) diffraction planes, respectively, of the rhombic crystalline phase of V_2O_3 (PDF#84-0316), evidencing the successful synthesis of the V_2O_3 phase.

Figure 1b reveals a typical FT-IR spectrum of the V_2O_3@CGL composites. The peaks situated at 2853 and 2922 cm^{-1} denote the presence of residual C-H groups [26]. The peak observed at 2367 cm^{-1} corresponds to an asymmetric stretching vibration of C-O, which is attributed to CO_2 adsorption on KBr and is negligible [27]. The H-O bending vibration and H-O stretching vibration can be identified at 1625 and 3423 cm^{-1}, respectively, which may be because of certain water molecules adsorbed on the surface and embedded in the composite interlayers [28]. Furthermore, the peaks located at 801 and 584 cm^{-1} are ascribed to the symmetric and asymmetric stretching vibrations of the V-O-V bond [29–31]. The signal at 987 cm^{-1} is related to the symmetric stretching of V^{3+}=O, suggesting the presence of V_2O_3 [32,33]. Based on the above analysis, the synthesized V_2O_3@CGL composites consist of V_2O_3 and biomass-derived carbon, which coincides with the results of the XRD.

The porosity and specific surface area of electrode materials are critical for ion diffusion. Therefore, N_2 adsorption/desorption isotherm experiments were carried out. As depicted in Figure 1c,d, the three V_2O_3@CGL composites exhibit typical IV isotherms followed by H_3-type hysteresis loops, suggesting that the materials include a significant number of mesoporous pores in the samples. The average pore diameter, pore volume, and specific surface area of the three V_2O_3@CGL composites are summarized in Table 1. Among them, the specific surface area of VOCG-3 composite is as high as 174.2683 cm^2 g^{-1}, which is significantly larger than VOCG-1 (154.9935 $cm^2\ g^{-1}$) and VOCG-2 (164.5602 $cm^2\ g^{-1}$), suggesting that with a higher content of V_2O_3, the specific surface area will increase. Additionally, the pore sizes of the three V_2O_3@CGL composites range from 2 to 43 nm (see Figure 2d). The abundant mesoporous structure and large specific surface area facilitate rapid storage of Zn^{2+}. Furthermore, a suitable pore size distribution promotes ion diffusion, thereby enhancing the magnification performance of V_2O_3@CGL composites [34].

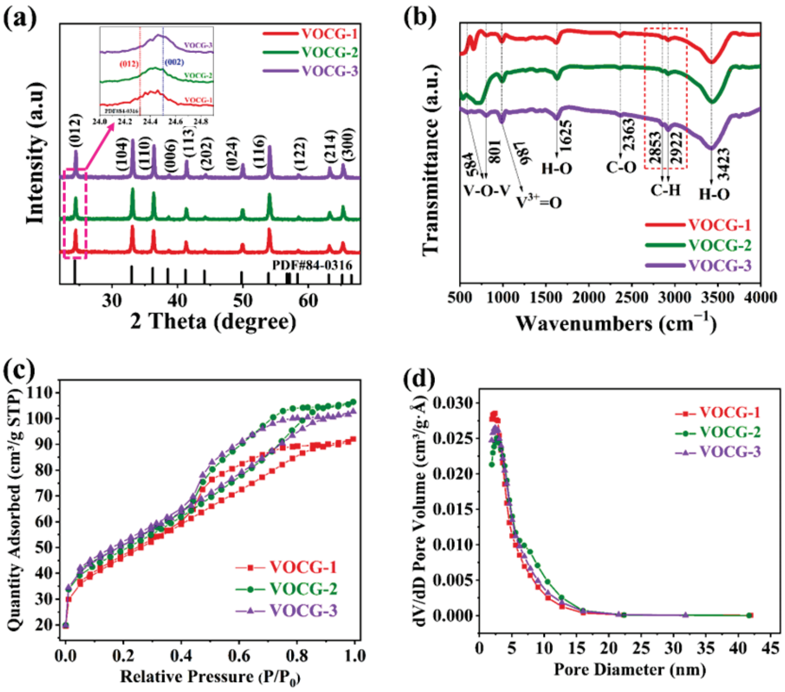

Figure 1. (**a**) XRD patterns; (**b**) FT-IR spectrum; (**c**) N_2 absorption/desorption isotherms; and (**d**) pore size distribution of the V_2O_3@CGL composites. Inset images show the (012) and (002) diffraction planes of the V_2O_3@CGL composites.

Table 1. Pore volume, specific surface area, and average pore size of the V_2O_3@CGL composites.

Sample	Pore Volume ($cm^3\ g^{-1}$)	Specific Surface Area ($m^2\ g^{-1}$)	Average Pore Size (Å)
VOCG-1	0.1424	154.9935	3.6760
VOCG-2	0.1647	164.5602	4.0040
VOCG-3	0.1589	174.2683	3.6465

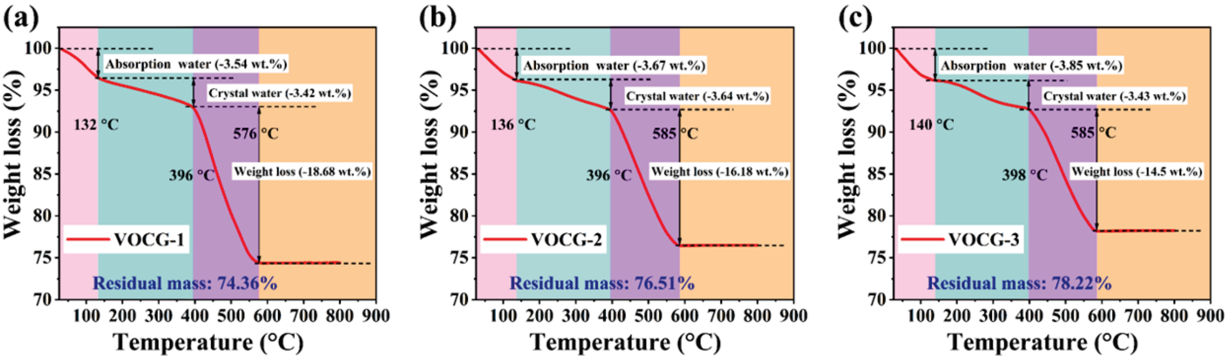

Figure 2. TGA curves of (**a**) VOCG-1, (**b**) VOCG-2, and (**c**) VOCG-3 composites.

To ascertain the weight percentage of every ingredient in the V_2O_3@CGL composites, a TGA test was carried out at 25–800 °C in nitrogen, as illustrated in Figure 2. The three

TGA curves exhibit three distinct weightlessness stages. The first two stages occur at room temperature to about 136 °C and 400 °C, respectively, which are associated with the release of structural water and adsorbed water in the V_2O_3@CGL composites. The mass loss in the first two stages of VOCG-1, VOCG-2, and VOCG-3 was 6.96%, 7.31%, and 7.28%, respectively. The third stage of weightlessness occurs at about 400–580 °C, which is related to the combustion of CGL in the V_2O_3@CGL composites. The weightlessness in the third stage for VOCG-1, VOCG-2, and VOCG-3 composites was 18.68%, 16.18%, and 14.5%, respectively. According to the data obtained from the TGA, the mass content of CGL and V_2O_3 in VOCG-1, VOCG-2, and VOCG-3 was 18.68% and 74.36%, 16.18% and 76.51%, and 14.5% and 78.22%, respectively.

The surface elemental composition, electronic states, and bonding states of the V_2O_3@CGL composites were studied by means of XPS spectroscopy. As depicted in Figure 3a, V, O, and C elements were detected in the XPS measurement spectra. The bonding state of V, C, and O was further evaluated by the V 2p, C 1s, and O 1s peaks. As displayed in Figure 3b, the peaks are located at 288.58, 285.76, and 284.77 eV, respectively, matching the O=C-O^-, C-O, and C-C bonds of C 1s, which are derived from CGL [35–37]. Figure 3c exhibits three contributions from the fitted O 1s peaks, with binding energies of 533.06, 531.6, and 530.33 eV, attributed to the O=C-O^-, C-OH, and V-O bonds [22,38,39], respectively. The V 2p peak of the V_2O_3@CGL composites (Figure 3d) is decomposed into two peaks at 523.78 and 516.8 eV, corresponding to V $2p_{1/2}$ and V $2p_{3/2}$, proving the presence of V_2O_3 [40–42].

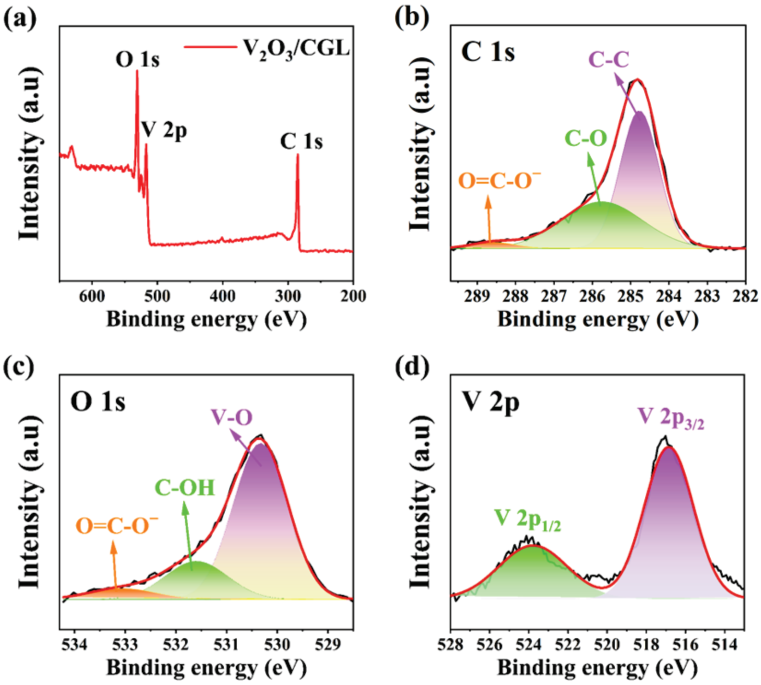

Figure 3. (**a**) XPS survey spectra; at high-resolution: (**b**) C 1s, (**c**) O 1s, and (**d**) V 2p XPS spectra of the V_2O_3@CGL composites.

Figure 4 illustrates the SEM pictures of the V_2O_3@CGL composites. The CGL in the V_2O_3@CGL composites reveals an irregular three-dimensional porous structure with diameters ranging from 30 to 300 µm. V_2O_3 is observed to be encapsulated on the surface of the CGL or entering its pores. The surface of VOCG-1 composite is relatively smooth, with the exposed Ganoderma lucidum biomass-derived carbon visible, while the surfaces of VOCG-2 and VOCG-3 composites are relatively rough. Notably, VOCG-3 is completely covered by V_2O_3, with the bare Ganoderma lucidum biomass-derived carbon barely discernible. This indicates that VOCG-1 composite contains the least amount of V_2O_3, while VOCG-3 composite contains the greatest amount of V_2O_3. Furthermore, CGL can provide a carbon skeleton for V_2O_3, effectively overcoming the adverse effects of V_2O_3 aggregation and volume expansion during charging and discharging, thus enhancing the zinc storage performance [43]. Moreover, the elemental mapping of the V_2O_3@CGL composites is presented in Figure 5, which reveals that the C, O, and V elements are homogeneously dispersed in the V_2O_3@CGL composites. This, together with the XRD and XPS data presented above, provides evidence that the synthesis of the V_2O_3@CGL composites was successful. It is notable that a comparison of the brightness of the elemental maps of the three composites reveals that the VOCG-1 composite has the highest concentration of carbon and the lowest concentration of vanadium, while the VOCG-3 composite has the lowest concentration of carbon and the highest concentration of vanadium. This indicates that the VOCG-1 composite has the lowest vanadium pentoxide content, while the VOCG-3 composite has the highest V_2O_3 content.

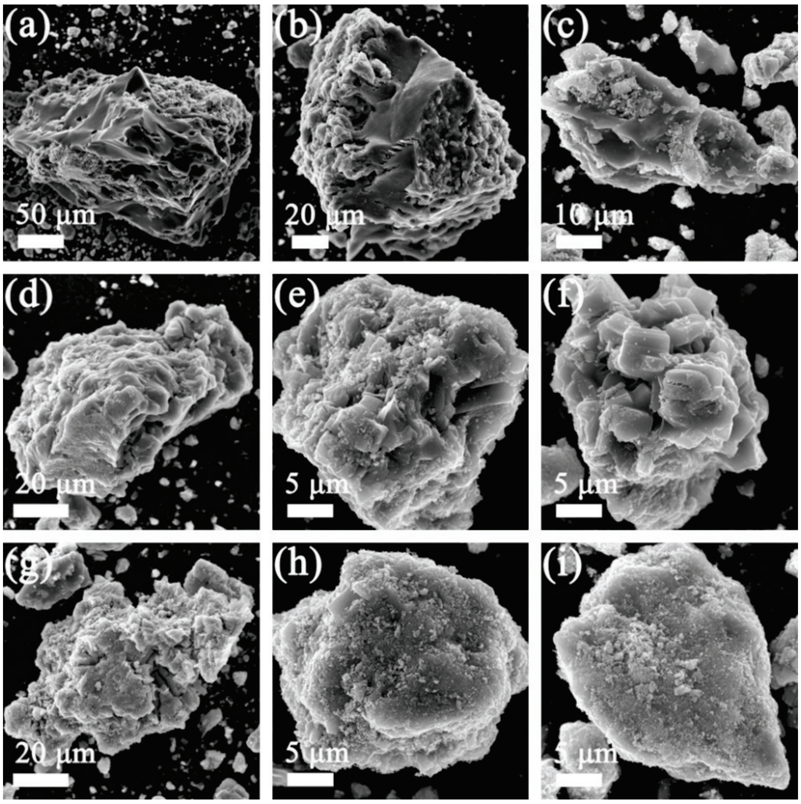

Figure 4. SEM pictures of (**a**–**c**) VOCG-1, (**d**–**f**) VOCG-2, and (**g**–**i**) VOCG-3 composites.

The HRTEM map and the corresponding selected area electron diffraction (SAED) diagram of the V_2O_3@CGL composites are presented in Figure 6. The majority of the lattice fringes of the V_2O_3@CGL composites are more pronounced. The corresponding crystallographic spacing is approximately 2.18 Å, which is consistent with the (113) crystallographic plane of V_2O_3, thereby confirming the presence of V_2O_3 in the V_2O_3@CGL composites. Furthermore, the SAED diagram of the V_2O_3@CGL composites is presented in Figure 6b. The presence of significant diffraction rings at the (012), (104), (110), and (113) facets of V_2O_3 was observed, which was in accordance with the XRD results. This once again demonstrates that V_2O_3 exhibits excellent crystallinity.

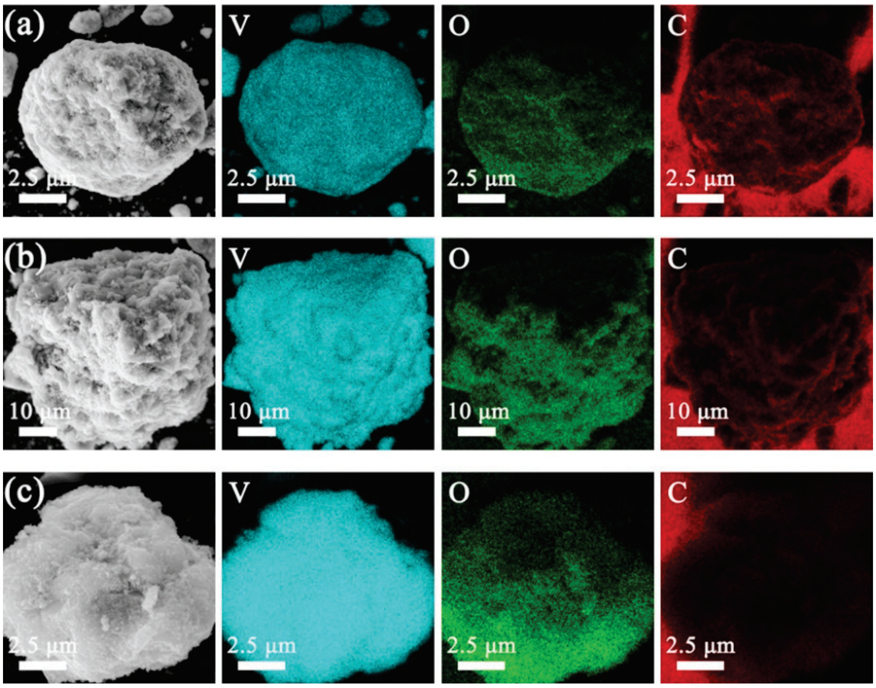

Figure 5. SEM and elemental mapping images of (**a**) VOCG-1, (**b**) VOCG-2, and (**c**) VOCG-3 composites.

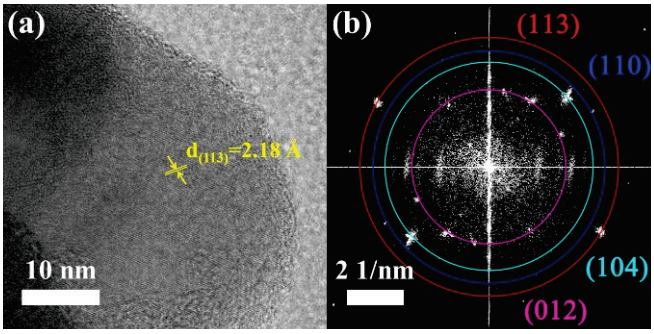

Figure 6. (**a**) HRTEM map and (**b**) SAED diagram of the V_2O_3@CGL composites.

3. Discussion

GCD measurements were performed on the V_2O_3@CGL composite electrodes within the range 0.2–1.8 V at 0.05 A g^{-1}. The resulting GCD profiles for the first five turns are presented in Figure 7a–c. The two pairs of redox voltage plateaus observed at 0.58/0.88 and 0.98/1.21 V on both the charge and discharge curves correspond to the CV curves below. The initial discharge specific capacity of the VOCG-2 composite electrode can be observed to reach 407.88 mAh g^{-1}, which is considerably greater than that of VOCG-1 (307.64 mAh g^{-1}) and VOCG-3 (357.43 mAh g^{-1}). Although only V_2O_3 provides the specific capacity in the composites, a high proportion of V_2O_3 does not necessarily exhibit the highest specific capacity. This is due to the poor structural stability and intrinsic lack of electrical conductivity of V_2O_3. Therefore, the discharge specific capacity of V_2O_3 can be effectively optimized by the addition of an appropriate amount of CGL.

Figure 7d illustrates the rate capability of the V_2O_3@CGL composite electrodes at varying current densities. The current density is incrementally raised from 0.05 C to 3 C and subsequently decreased to 0.05 C (specific multiplicity values are listed in Figure 7d). The discharge specific capacity exhibited a gradual decline as the current density increased. The average discharge specific capacities of VOCG-2 were 344.48, 316.61, 302.85, 290.84, 279.03, and 272.00 mAh g^{-1}, respectively, which were significantly higher than those of VOCG-1 and VOCG-2. This indicates that VOCG-2 is superior in multiplicity performance.

Upon the return of the current density to 0.05 C, the discharge specific capacity of VOCG-2 also recovered to 356.23 mAh g^{-1}, which was 91.21% of the initial value. In contrast, the discharge specific capacity of VOCG-1 was only 81.33% (235.17 mAh g^{-1}) and that of VOCG-3 was 86.55% (293.50 mAh g^{-1}) of the initial value. The VOCG-1 and VOCG-2 electrodes exhibited a capacity of only 81.33% (235.17 mAh g^{-1}) and 86.55% (293.50 mAh g^{-1}) of the initial value, respectively. The aforementioned outcomes demonstrate that the VOCG-2 electrode exhibits excellent reversibility. Moreover, the crystal structure of the VOCG-2 electrode exhibits enhanced stability. The exceptional multiplicity performance of VOCG-2 may be attributed to the incorporation of CGL, which enhances the structural stability and conductivity of the electrode, facilitating the rapid (de)intercalation of carriers.

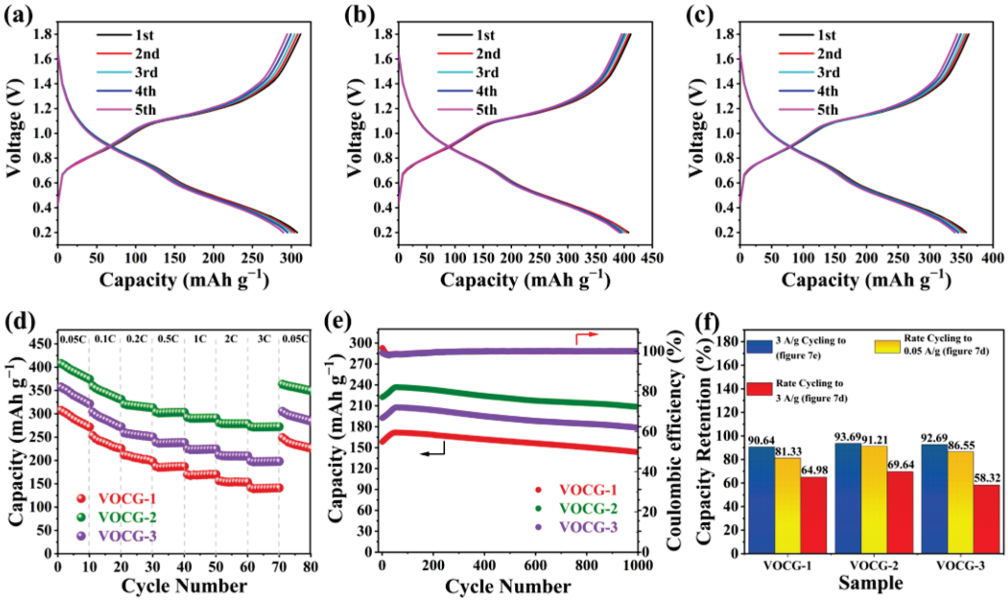

Figure 7. GCD profiles of (**a**) VOCG-1, (**b**) VOCG-2, and (**c**) VOCG-3 composites in the original five cycles; (**d**) rate; (**e**) cycling properties; and (**f**) capacity retention after 1000 cycles at 3 A g^{-1} (blue), capacity retention after rate cycling to 3 A g^{-1} (yellow) and rate cycling back to 0.05 A g^{-1} (red) of the three samples.

Figure 7e illustrates the cycling properties of the three V_2O_3@CGL composites at 3 A g^{-1}. The capacities of all three composite electrodes exhibited a gradual increase over the initial 60 cycles, in agreement with vanadium-based materials reported in the literature, and may be related to the gradual electrochemical activation. The first discharge specific capacity of the VOCG-2 composite electrode was 222.41 mAh g^{-1}, which was considerably superior to that of the VOCG-1 (158.32 mAh g^{-1}) and VOCG-3 (192.55 mAh g^{-1}) composite electrodes. After 56 cycles, the specific capacity of the VOCG-2 electrode reached a maximum of 236.71 mAh g^{-1}. However, the maximum discharge specific capacities of the VOCG-1 and VOCG-3 composite electrodes were only 171.69 and 207.68 mAh g^{-1}, respectively, after 53 and 58 cycles, which were significantly lower than that of the VOCG-2 electrode. Moreover, the reversible specific capacity of the VOCG-2 electrode was obtained at 208.38 mAh g^{-1} after 1000 cycles, with a capacity retention of 93.69%. In contrast, the specific capacities of the VOCG-1 and VOCG-3 electrodes were somewhat lower, at 143.51 mAh g^{-1} and 178.46 mAh g^{-1}, respectively. Moreover, the capacity retentions were not as good as those of VOCG-2, at 90.65% and 92.67%, respectively. Consequently, the VOCG-2 electrode exhibits superior cycling stability. The exceptional electrochemical property of the VOCG-2 electrode is attributed to the CGL, which not only improves the electrode's conductivity but also provides a well-developed pore structure that facilitates the diffusion of ions, thereby ensuring an optimal ion diffusion rate.

The CV curves were utilized to evaluate the electrochemical process kinetics of the V_2O_3@CGL electrode within the range 0.2–1.8 V, as depicted in Figure 8a. The three CV curves possess similar shapes, with two pairs of distinct coupled REDOX peaks placed at about 0.58/0.88 V and 0.98/1.21 V, respectively, indicating that the insertion of Zn^{2+} in the V_2O_3@CGL electrode undergoes a two-step reversible reaction, akin to the previously reported vanadium-based cathodes [6,16,34]. It has been reported that the area and current depicted in the CV curve are closely linked to the obtained capacity [44]. It is easily observed that the area of the VOCG-2 electrode is the largest, while the VOCG-1 electrode has the smallest area. Consequently, the VOCG-2 electrode has the largest specific capacity among them, while the VOCG-1 capacity is relatively lower.

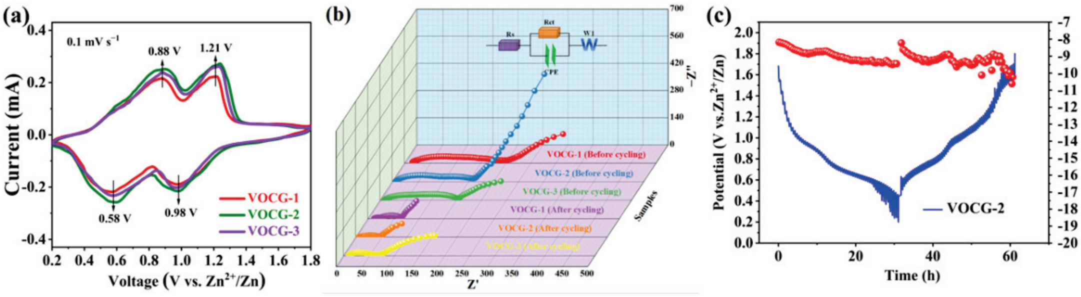

Figure 8. (**a**) CV curves of VOCG-1, VOCG-2, and VOCG-3 composites before and after cycling; (**b**) EIS spectra of the V_2O_3@CGL composite cathodes before and after cycling; and (**c**) GITT curve and corresponding $D_{Zn}{}^{2+}$ values for the VOCG-2 composite cathode.

To further evaluate the charge transfer state of the V_2O_3@CGL composite electrodes, EIS measurements were carried out, and the corresponding Nyquist and EIS plots are depicted in Figure 8b. The three EIS curves exhibit a semicircle at medium-high frequencies and a straight line at low frequencies. The semicircle reflects charge transfer resistance (R_{ct}), while the straight line is related to the ion diffusion process (R_s) within the electrode [45,46]. The equivalent circuit presented in Figure 8b was utilized for fitting, and the detailed fitting data are summarized in Table 2. Notably, the R_{ct} values of the VOCG-2 composite electrode pre- and post-cycling were significantly lower than those of VOCG-1 and VOCG-3, indicating the superior electrical conductivity of the VOCG-2 electrode. Furthermore, the R_{ct} values for all three V_2O_3@CGL electrodes after cycling are notably smaller compared to those before cycling, suggesting improved charge transfer kinetics following multiple cycles.

Table 2. Electrochemical impedance spectra of the three V_2O_3@CGL composites before and after cycling.

Sample	VOCG-1	VOCG-2	VOCG-3
R_{ct} (before cycling)	180.8 Ω	129.8 Ω	141 Ω
R_{ct} (after cycling)	63.47 Ω	40.92 Ω	55.29 Ω
R_s (before cycling)	4.04 Ω	2.56 Ω	3.73 Ω
R_s (after cycling)	7.72 Ω	3.72 Ω	4.48 Ω

To accurately investigate the diffusion kinetics of Zn^{2+} ($D_{Zn}{}^{2+}$) in the VOCG-2 composite electrode, GITT measurements were performed, and $D_{Zn}{}^{2+}$ was calculated using Formula (1):

$$D = \frac{4L^2}{\pi\tau}\left(\frac{\Delta E_s}{\Delta E_t}\right)^2. \tag{1}$$

where ΔE_t is the change in voltage during the continuous current pulse after the i_R drop has been removed and ΔE_s is the change in steady-state potential owing to the current pulse. The electrode thickness is denoted as L, while the relaxation time is represented by τ.

The GITT profile and the calculated D_{Zn}^{2+} values of the VOCG-2 composite electrode are depicted in Figure 8c. It can be observed that the D_{Zn}^{2+} values of the VOCG-2 composite electrode are in the range of $10^{-10.5}$ and 10^{-8} cm^2 s^{-1} during cycling, which is a relatively good level. This indicates that Zn^{2+} has satisfactory diffusion kinetics in the VOCG-2 electrode, which is mainly associated with the natural porous structure of CGL, which can shorten the diffusion path for Zn^{2+} transport and promote its effective transport.

The morphological evolution of the VOCG-2 composite electrode in the pristine state and at different stages was investigated by SEM, as revealed in Figure 9a–f, respectively. The nanoparticles were evenly arranged on the stainless steel foil without agglomerating in their pristine state. After 200 and 400 cycles, the VOCG-2 composite electrode presented little morphological change, suggesting excellent structural stability during cycling. After 600 cycles, slight pulverization and agglomeration appeared on the surface of the VOCG-2 electrode. As charging and discharging continued, the pulverization and agglomeration were more pronounced (see Figure 9e,f), corresponding to the decrease in capacity in Figure 8e. Notably, no cracks or obvious dendrites appeared from the initial state to 1000 cycles (see Figure 9a–f), disclosing the protective mechanism of the array structure of the CGL. Therefore, the resulting VOCG-2 composite has good structural stability, which is advantageous for enhancing the cycle lifetime of AZIBs.

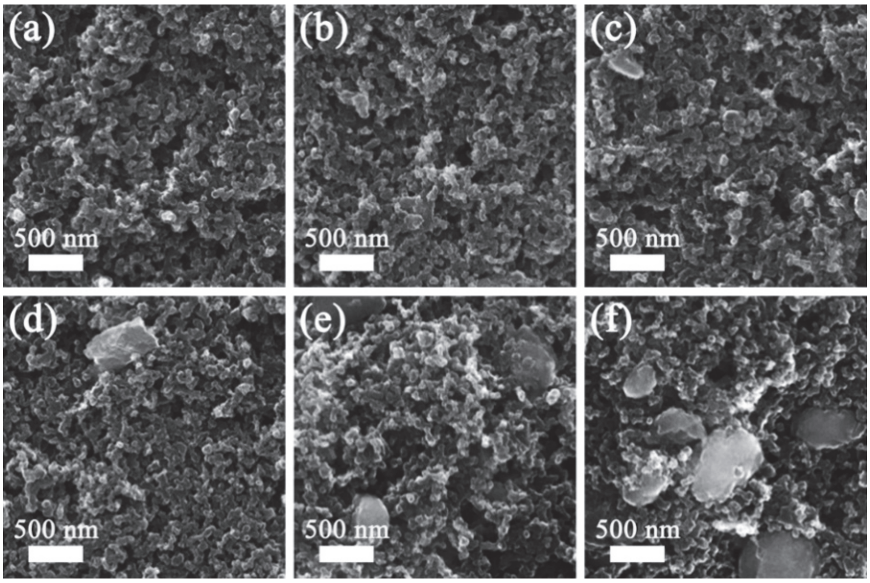

Figure 9. SEM photographs of the VOCG-2 composite electrodes at various stages: (**a**) pristine, (**b**) 200, (**c**) 400, (**d**) 600, (**e**) 800, and (**f**) 1000 cycles.

Table 3 summarizes the electrochemical properties of several previously reported vanadium-based cathodes utilized for AZIB applications. The results reveal that the VOCG-2 composite proposed in this paper has certain advantages, and the desirable electrochemical properties of the VOCG-2 composite electrode can be correlated with the appropriate CGL content to increase the structural stability and electrical conductivity. Furthermore, the plentifully mesoporous structure and large specific surface area of CGL can facilitate the rapid storage of Zn^{2+}.

Table 3. Comparison of the electrochemical properties of the V_2O_3@CGL composite with other vanadium-based AZIB cathode materials that have been previously reported in the literature.

Sample	Cycle Number	Capacity Retention	Current Density (A g^{-1})	Specific Capacity (mAh g^{-1})	Ref.
VOCG-2	1000	93.69%	3	208.38	This work
V_2O_3@carbonized Dictyophora	1000	89.24%	1	151.9	[47]
V_2O_3/carbonized chestnut needle	1000	94.26%	3	213.66	[48]
V_2O_3	100	76.9%	0.1	161	[34]
Polyaniline-intercalated V_2O_5@nH_2O	100	57%	0.1	196	[7]
$Mn_{0.31}V_3O_7$@$1.40H_2O$	500	54%	1	164	[49]
$(NH_4)_xV_2O_5$@nH_2O	50	63%	0.1	235	[50]
V_2O_x@V_2CT_x	200	81.6%	1	87.3	[51]
V_2O_3@carbon nanofibers	1000	80%	0.2	120	[39]
V_6O_{13}@hollow carbon microspheres	1000	76%	1	162.1	[52]
Carbon-coated $NaVPO_4F$	400	94.5%	0.1	87.4	[53]
V_2O_3@amorphous carbon	1600	90.7%	1	116	[6]
V_2O_3@rGO	1000	114%	5	195	[54]
VO_2 hollow nanospheres	860	47.6%	1	143	[15]
δ-$Na_xV_2O_5/VO_2(B)$	200	94%	4	253	[55]
$FeVO_4\cdot nH_2O$@rGO	1000	43.8%	1	92	[12]

Values are estimated from the graphs.

4. Experimental Section

4.1. Preparation of V_2O_3@CGL Composites

The Ganoderma lucidum was repeatedly cleaned with distilled water to remove soil, and placed in a drying oven at 60 °C until it was completely dry. The dried Ganoderma lucidum and KOH were mixed according to the mass ratio of 1:4 with deionized water as the ultrasonic solvent for two hours. It was then transferred to a blast drying oven maintained at 80 °C for the purpose of complete drying, followed by calcination at 600 °C for 2 h in argon to acquire Ganoderma lucidum biomass-derived carbon (CGL).

The detailed synthesis procedure for the V_2O_3@CGL composites is displayed in Figure 10. Firstly, 5.05 g CH_4NO_2 and 7.4 g NH_4VO_3 were dissolved in 100 mL of distilled water, followed by stirring in a water bath at 60 °C for 0.5 h. Subsequently, 40 mL of $C_2H_6O_2$ solution and 0.3 g of CGL were mixed into the above solution, sealed, and left for a week. In order to completely evaporate the water, the mixture was dried in an oven at 80 °C for 48 h. The final stage of the process involved the transfer of the resulting precursors to a corundum crucible and their placement in a tubular furnace. Subsequently, the furnace was heated to 350 °C for 4 h and then heated to 800 °C for 8 h at a rate of 5 °C min^{-1} in an argon environment. This procedure yielded the desired VOCG-3 composite. The mass ratio of NH_4VO_3 to chestnut needle was adjusted in order to prepare the VOCG-1 and VOCG-2 composites by the same method. Table 4 illustrates the quality of the raw materials produced for each sample.

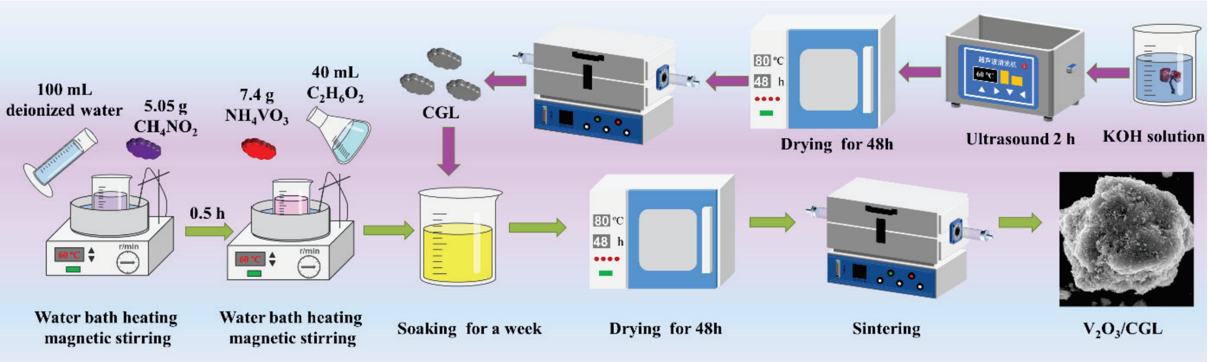

Figure 10. The preparation process of the V_2O_3@CGL composites.

Table 4. Summary of the dosage of raw materials synthesized from each sample.

Sample	CGL	NH_4VO_3	CH_4NO_2	$C_2H_6O_2$	H_2O
VOCG-1	0.3 g	5.04 g	3.43 g	40 mL	100 mL
VOCG-2	0.3 g	6.24 g	4.26 g	40 mL	100 mL
VOCG-3	0.3 g	7.40 g	5.05 g	40 mL	100 mL

4.2. Material Characterization

Detailed information on XRD, TGA, XPS, SEM, HRTEM, and FT-IR testing can be found in our previous paper: 10.3390/molecules28052147 [47]. The isothermal nitrogen adsorption/desorption test was conducted on the samples using an ASAP 2020 tester from Micromeritics, Norcross, GA, USA, maintained at 77 K beneath liquid nitrogen.

4.3. Electrochemical Measurements

In order to prepare the cathode, PVDF (10 w.t.%), acetylene black (20 w.t.%) and active material (70 w.t.%) were successively dispersed in N-methyl-2-pyrrolidone. The resulting mixed slurry was evenly coated on stainless steel foil and dried in a vacuum at 60 °C for 12 h. A CR2025 coin battery was assembled in air with glass fiber adopted as the diaphragm, 3 M $ZnSO_4$ aqueous solution employed as the electrolyte, and commercial zinc foil utilized as the anode. For detailed information on partial electrochemical testing, please refer to our previous paper [47]. The galvanostatic intermittence titration technique (GITT) was carried out using the NETWARE test instrument within the range 0.2–1.8 V.

5. Conclusions

In this study, the V_2O_3@CGL composites were prepared using evaporation self-assembly technology with Ganoderma lucidum as the carbon source and NH_4VO_3 as the metal source. In these V_2O_3@CGL composites, CGL exhibits a porous structure and V_2O_3 provides large capacity, which can increase the electrolytic/cathodic contact area and provide incremental active sites. Moreover, the introduction of CGL increases the mechanical properties, while also making up for V_2O_3's inadequate electrical conductivity. Thus, the V_2O_3@CGL composites possess the ideal electrochemical properties. Specifically, the VOCG-2 composite demonstrated superior initial discharge specific capacity and excellent cycle stability. Furthermore, SEM testing revealed that the VOCG-2 electrode microstructure remained stable without obvious cracks or zinc dendrites during cycling, which contributes to its excellent zinc storage properties. This research introduces an innovative strategy for the enhancement of the electrochemical properties of V_2O_3 and these results will assist in creating affordable high-performance vanadium-based AZIBs.

Author Contributions: Conceptualization, W.Z. and S.J.; methodology, G.Z.; software, G.Z.; validation, G.Z., W.Z. and S.J.; formal analysis, G.Z. and W.Z.; investigation, Z.L.; resources, W.Z.; data curation, Z.L.; writing—original draft preparation, G.Z.; writing—review and editing, W.Z.; visualization, S.J.; supervision, Z.L.; project administration, W.Z.; funding acquisition, W.Z. All authors have read and agreed to the published version of the manuscript.

Funding: The authors gratefully acknowledge the financial support of the Natural Science Foundation of Hunan Province (2022JJ50086).

Institutional Review Board Statement: Not applicable.

Informed Consent Statement: Not applicable.

Data Availability Statement: Data will be made available on request.

Conflicts of Interest: The authors declare no conflicts of interest.

References

1. Shen, C.; Li, X.; Li, N.; Xie, K.; Wang, J.G.; Liu, X.; Wei, B. Graphene-Boosted, High-Performance Aqueous Zn-Ion Battery. *ACS Appl. Mater. Interfaces* **2018**, *10*, 25446–25453. [CrossRef] [PubMed]
2. Fang, G.; Zhou, J.; Pan, A.; Liang, S. Recent Advances in Aqueous Zinc-Ion Batteries. *ACS Energy Lett.* **2018**, *3*, 2480–2501. [CrossRef]
3. Konarov, A.; Voronina, N.; Jo, J.H.; Bakenov, Z.; Sun, Y.-K.; Myung, S.-T. Present and Future Perspective on Electrode Materials for Rechargeable Zinc-Ion Batteries. *ACS Energy Lett.* **2018**, *3*, 2620–2640. [CrossRef]
4. Ming, F.; Liang, H.; Lei, Y.; Kandambeth, S.; Eddaoudi, M.; Alshareef, H.N. Layered $Mg_xV_2O_5{\cdot}nH_2O$ as Cathode Material for High-Performance Aqueous Zinc Ion Batteries. *ACS Energy Lett.* **2018**, *3*, 2602–2609. [CrossRef]
5. Yufit, V.; Tariq, F.; Eastwood, D.S.; Biton, M.; Wu, B.; Lee, P.D.; Brandon, N.P.J.J. Operando visualization and multi-scale tomography studies of dendrite formation and dissolution in zinc batteries. *Joule* **2019**, *3*, 485–502. [CrossRef]
6. Chen, H.; Rong, Y.; Yang, Z.; Deng, L.; Wu, J. V_2O_3@Amorphous Carbon as a Cathode of Zinc Ion Batteries with High Stability and Long Cycling Life. *Ind. Eng. Chem. Res.* **2021**, *60*, 1517–1525. [CrossRef]
7. Zhang, Y.; Xu, L.; Jiang, H.; Liu, Y.; Meng, C. Polyaniline-expanded the interlayer spacing of hydrated vanadium pentoxide by the interface-intercalation for aqueous rechargeable Zn-ion batteries. *J. Colloid Interface Sci.* **2021**, *603*, 641–650. [CrossRef] [PubMed]
8. Niu, Y.; Wang, D.; Ma, Y.; Zhi, L. Cascading V_2O_3/N-doped carbon hybrid nanosheets as high-performance cathode materials for aqueous zinc-ion batteries. *Chin. Chem. Lett.* **2022**, *33*, 1430–1434. [CrossRef]
9. Liu, Y.; Wang, T.; Sun, Y.; Zhang, M.; Gao, G.; Yang, J.; Cai, K. Fast and efficient in-situ construction of low crystalline PEDOT-intercalated V_2O_5 nanosheets for high-performance zinc-ion battery. *Chem. Eng. J.* **2024**, *484*, 149501. [CrossRef]
10. Gao, Q.-L.; Li, D.-S.; Liu, X.-M.; Wang, Y.-F.; Liu, W.-L.; Ren, M.-M.; Kong, F.-G.; Wang, S.-J.; Zhou, R.-C. Biomass-derived mesoporous carbons materials coated by α-Mn_3O_4 with ultrafast zinc-ion diffusion ability as cathode for aqueous zinc ion batteries. *Electrochim. Acta* **2020**, *335*, 135642. [CrossRef]
11. Tang, B.; Shan, L.; Liang, S.; Zhou, J. Issues and opportunities facing aqueous zinc-ion batteries. *Energy Environ. Sci.* **2019**, *12*, 3288–3304. [CrossRef]
12. Lan, B.; Tang, C.; Chen, L.; Zhang, W.; Tang, W.; Zuo, C.; Fu, X.; Dong, S.; An, Q.; Luo, P. $FeVO_4{\cdot}nH_2O$@rGO nanocomposite as high performance cathode materials for aqueous Zn-ion batteries. *J. Alloys Compd.* **2020**, *818*, 153372. [CrossRef]
13. Zhang, W.; Xiao, Y.; Zuo, C.; Tang, W.; Liu, G.; Wang, S.; Cai, W.; Dong, S.; Luo, P. Adjusting the Valence State of Vanadium in VO_2(B) by Extracting Oxygen Anions for High-Performance Aqueous Zinc-Ion Batteries. *ChemSusChem* **2020**, *14*, 971–978. [CrossRef] [PubMed]
14. Kidanu, W.G.; Hur, J.; Choi, H.W.; Kim, M.I.; Kim, I.T. High capacity and inexpensive multivalent cathode materials for aqueous rechargeable Zn-ion battery fabricated via in situ electrochemical oxidation of VO_2 nanorods. *J. Power Sources* **2022**, *523*, 231060. [CrossRef]
15. Liu, Y.; Hu, P.; Liu, H.; Wu, X.; Zhi, C. Tetragonal VO_2 hollow nanospheres as robust cathode material for aqueous zinc ion batteries. *Mater. Today Energy* **2020**, *17*, 100431. [CrossRef]
16. Liu, Y.; Liu, Y.; Wu, X.; Cho, Y.-R. Enhanced Electrochemical Performance of Zn/VO_x Batteries by a Carbon-Encapsulation Strategy. *ACS Appl. Mater. Interfaces* **2022**, *14*, 11654–11662. [CrossRef] [PubMed]
17. Lv, T.-T.; Luo, X.; Yuan, G.-Q.; Yang, S.-Y.; Pang, H. Layered VO_2@N-doped carbon composites for high-performance rechargeable aqueous zinc-ion batteries. *Chem. Eng. J.* **2022**, *428*, 131211. [CrossRef]
18. Ding, Y.; Peng, Y.; Chen, W.; Niu, Y.; Wu, S.; Zhang, X.; Hu, L. V-MOF derived porous V_2O_5 nanoplates for high performance aqueous zinc ion battery. *Appl. Surf. Sci.* **2019**, *493*, 368–374. [CrossRef]
19. Hu, P.; Zhu, T.; Wang, X.; Wei, X.; Yan, M.; Li, J.; Luo, W.; Yang, W.; Zhang, W.; Zhou, L.; et al. Highly durable $Na_2V_6O_{16}{\cdot}1.63H_2O$ nanowire cathode for aqueous zinc-ion battery. *Nano Lett.* **2018**, *18*, 1758–1763. [CrossRef] [PubMed]
20. Hei, J.; Cheng, L.; Fu, Y.; Du, W.; Qian, Y.; Li, J.; Yin, Y.; Wang, N.; Su, L.; Wang, L. Uniformly confined V_2O_3 quantum dots embedded in biomass derived mesoporous carbon toward fast and stable energy storage. *Ceram. Int.* **2023**, *49*, 16002–16010. [CrossRef]
21. He, Z.; Cheng, G.; Jiang, Y.; Li, Y.; Zhu, J.; Meng, W.; Zhou, H.; Dai, L.; Wang, L. Novel 2D porous carbon nanosheet derived from biomass: Ultrahigh porosity and excellent performances toward V^{2+}/V^{3+} redox reaction for vanadium redox flow battery. *Int. J. Hydrogen Energy* **2020**, *45*, 3959–3970. [CrossRef]
22. Li, Y.; Lin, W.; Xue, L.; Xie, J.; Wei, B.; Chen, G.; Chen, D. Facile preparation of V_2O_3/black fungus-derived carbon composite with hierarchical porosity as a promising electrode for lithium/sodium ion batteries. *J. Alloys Compd.* **2022**, *905*, 164258. [CrossRef]
23. Doğan, H.; Taş, M.; Meşeli, T.; Elden, G.; Genc, G. Review on the Applications of Biomass-Derived Carbon Materials in Vanadium Redox Flow Batteries. *ACS Omega* **2023**, *8*, 34310–34327. [CrossRef] [PubMed]
24. Zhai, M.; Ye, J.; Jiang, Y.; Yuan, S.; Li, Y.; Liu, Y.; Dai, L.; Wang, L.; He, Z. Biomass-derived carbon materials for vanadium redox flow battery: From structure to property. *J. Colloid Interface Sci.* **2023**, *651*, 902–918. [CrossRef] [PubMed]
25. Hu, J.; Xie, Y.; Zheng, J.; Li, H.; Wang, T.; Lai, Y.; Zhang, Z. Encapsulating V_2O_3 Nanoparticles in Hierarchical Porous Carbon Nanosheets via C–O–V Bonds for Fast and Durable Potassium-Ion Storage. *ACS Appl. Mater. Interfaces* **2021**, *13*, 12149–12158. [CrossRef] [PubMed]

26. Henry, A.; Hesemann, P.; Alauzun, J.G.; Boury, B. Reductive mineralization of cellulose with vanadium, iron and tungsten chlorides and access to M_xO_y metal oxides and M_xO_y/C metal oxide/carbon composites. *Carbohydr. Polym.* **2017**, *174*, 697–705. [CrossRef] [PubMed]
27. Zheng, J.; Zhang, Y.; Jing, X.; Liu, X.; Hu, T.; Lv, T.; Zhang, S.; Meng, C. Synthesis of amorphous carbon coated on V_2O_3 core-shell composites for enhancing the electrochemical properties of V_2O_3 as supercapacitor electrode. *Colloids Surf. A Physicochem. Eng. Asp.* **2017**, *518*, 188–196. [CrossRef]
28. Feng, Z.; Zhang, Y.; Yu, X.; Yu, Y.; Huang, C.; Meng, C. Aluminum-ion intercalation and reduced graphene oxide wrapping enable the electrochemical properties of hydrated V_2O_5 for Zn-ion storage. *Colloids Surf. A Physicochem. Eng. Asp.* **2022**, *641*, 128473. [CrossRef]
29. Liu, Y.; Pan, Z.; Tian, D.; Hu, T.; Jiang, H.; Yang, J.; Sun, J.; Zheng, J.; Meng, C.; Zhang, Y. Employing "one for two" strategy to design polyaniline-intercalated hydrated vanadium oxide with expanded interlayer spacing for high-performance aqueous zinc-ion batteries. *Chem. Eng. J.* **2020**, *399*, 125842. [CrossRef]
30. Ouyang, D.; Wang, C.; Yang, L.; Zhang, Y.; Wang, Y.-N.; Zhu, H.; Yu, F.; Yin, J. Enhancing Potassium Storage Performance in VO_2/V_2O_3@C Nanosheets by Synergistic Effect of Oxygen Vacancy and C-O-V Bond. *ChemElectroChem* **2022**, *9*, e202200639. [CrossRef]
31. Hu, T.; Liu, Y.; Zhang, Y.; Nie, Y.; Zheng, J.; Wang, Q.; Jiang, H.; Meng, C. Encapsulating V_2O_3 nanorods into carbon core-shell composites with porous structures and large specific surface area for high performance solid-state supercapacitors. *Microporous Mesoporous Mater.* **2018**, *262*, 199–206. [CrossRef]
32. Gou, W.; Kong, X.; Wang, Y.; Ai, Y.; Liang, S.; Pan, A.; Cao, G. Yolk-shell structured V_2O_3 microspheres wrapped in N, S co-doped carbon as pea-pod nanofibers for high-capacity lithium ion batteries. *Chem. Eng. J.* **2019**, *374*, 545–553. [CrossRef]
33. Kim, J.-H.; Kim, Y.-S.; Moon, S.-H.; Park, D.-H.; Kim, M.-C.; Choi, J.-H.; Shin, J.-H.; Park, K.-W. Enhanced electrochemical performance of a selectively formed V_2O_3/C composite structure for Li-ion batteries. *Electrochim. Acta* **2021**, *389*, 138685. [CrossRef]
34. Deng, L.; Chen, H.; Wu, J.; Yang, Z.; Rong, Y.; Fu, Z. V_2O_3 as cathode of zinc ion battery with high stability and long cycling life. *Ionics* **2021**, *27*, 3393–3402. [CrossRef]
35. Liu, X.; Wang, Z.; Niu, Y.; Liu, C.; Chen, H.; Ren, X.; Wang, M.; Lau, W.-M.; Zhou, D. Scalable synthesis of novel V_2O_3/carbon composite as advanced cathode material for aqueous zinc-ion batteries. *Ceram. Int.* **2022**, *48*, 15594–15602. [CrossRef]
36. Liu, C.L.; Liu, Y.; Liu, X.; Gong, Y. Coordination polymer-derived Al^{3+}-doped V_2O_3/C with rich oxygen vacancies for an advanced aqueous zinc-ion battery with ultrahigh rate capability. *Sustain. Energy Fuels* **2022**, *6*, 2020–2037. [CrossRef]
37. Wang, J.; Li, G.; Liu, X.; Ouyang, Q.; Ma, M.; Wang, Q.; Zhang, X.; Fan, Z.; Li, L. In-situ electrochemical oxidization of V_2O_3-C cathode for boosted zinc-ion storage performance. *Appl. Surf. Sci.* **2023**, *616*, 156481. [CrossRef]
38. Wang, Q.; Feng, Q.; Lei, Y.; Tang, S.; Xu, L.; Xiong, Y.; Fang, G.; Wang, Y.; Yang, P.; Liu, J.; et al. Quasi-solid-state Zn-air batteries with an atomically dispersed cobalt electrocatalyst and organohydrogel electrolyte. *Nat. Commun.* **2022**, *13*, 3689. [CrossRef] [PubMed]
39. Liu, X.; Wang, Z.; Niu, Y.; Liu, C.; Chen, H.; Ren, X.; Liu, Z.; Lau, W.-M.; Zhou, D. Electrospun V_2O_3@Carbon Nanofibers as a Flexible and Binder-Free Cathode for Highly Stable Aqueous Zn-Ion Full Batteries. *ACS Appl. Energy Mater.* **2022**, *5*, 3525–3535. [CrossRef]
40. Zhang, H.; Zhang, Y.; Liu, Y.; Shi, X.; Zhang, Y.; Bai, L.; Wang, Q.; Sun, L. Oxygen-Deficient α-MnO_2 Nanotube/Graphene/N, P Codoped Porous Carbon Composite Cathode To Achieve High-Performing Zinc-Ion Batteries. *ACS Appl. Mater. Interfaces* **2022**, *14*, 36668–36678. [CrossRef] [PubMed]
41. Zhao, J.; Zhao, Y.; Yue, W.-C.; Li, X.; Gao, N.; Zhang, Y.-J.; Hu, C.-Q. V_2O_3/VN Catalysts Decorated Free-Standing Multifunctional Interlayer for High-Performance Li-S Battery. *Chem. Eng. J.* **2022**, *441*, 136082. [CrossRef]
42. Chen, H.; Wang, Y.; Liu, C.; Hou, L.; Sun, J.; Yuan, C. Two-dimensional V_2CT_x In-situ Derived Porous V_2O_3@C Flakes Towards Zinc-Ion Capacitors as a Competitive Cathode Material. *ChemNanoMat* **2022**, *9*, e202200394. [CrossRef]
43. Zhang, H.; Yao, Z.; Lan, D.; Liu, Y.; Ma, L.; Cui, J. N-doped carbon/V_2O_3 microfibers as high-rate and ultralong-life cathode for rechargeable aqueous zinc-ion batteries. *J. Alloys Compd.* **2021**, *861*, 158560. [CrossRef]
44. Shin, J.; Jung, H.; Kim, Y.; Kim, J. Carbon-coated V_2O_5 nanoparticles with enhanced electrochemical performance as a cathode material for lithium ion batteries. *J. Alloys Compd.* **2014**, *589*, 322–329. [CrossRef]
45. Duan, Y.; Geng, Z.; Zhang, D.; Wang, Q. In situ electrochemically activated V_2O_3@MXene cathode for a super high-rate and long-life Zn-ion battery. *Dalton Trans.* **2024**, *53*, 7023–7034. [CrossRef] [PubMed]
46. Yin, C.; Wang, H.; Pan, C.; Li, Z.; Hu, J. Constructing MOF-derived V_2O_5 as advanced cathodes for aqueous zinc ion batteries. *J. Energy Storage* **2023**, *73*, 109045. [CrossRef]
47. Zhou, W.; Zeng, G.; Jin, H.; Jiang, S.; Huang, M.; Zhang, C.; Chen, H. Bio-Template Synthesis of V_2O_3@Carbonized Dictyophora Composites for Advanced Aqueous Zinc-Ion Batteries. *Molecules* **2023**, *28*, 2147. [CrossRef] [PubMed]
48. Zeng, G.; Wang, Y.; Lou, X.; Chen, H.; Jiang, S.; Zhou, W. Vanadium oxide/carbonized chestnut needle composites as cathode materials for advanced aqueous zinc-ion batteries. *J. Energy Storage* **2024**, *77*, 109859. [CrossRef]
49. Wu, T.-H.; Li, Y.-M.; Ni, K.-Y.; Li, T.-K.; Lin, W.-S. Vanadium oxides obtained by chimie douce reactions: The influences of transition metal species on crystal structures and electrochemical behaviors in zinc–ion batteries. *J. Colloid Interface Sci.* **2022**, *608*, 3121–3129. [CrossRef] [PubMed]

50. Xu, L.; Zhang, Y.; Zheng, J.; Jiang, H.; Hu, T.; Meng, C. Ammonium ion intercalated hydrated vanadium pentoxide for advanced aqueous rechargeable Zn-ion batteries. *Mater. Today Energy* **2020**, *18*, 100509. [CrossRef]
51. Venkatkarthick, R.; Rodthongkum, N.; Zhang, X.; Wang, S.; Pattananuwat, P.; Zhao, Y.; Liu, R.; Qin, J. Vanadium-Based Oxide on Two-Dimensional Vanadium Carbide MXene (V_2O_x@V_2CT_x) as Cathode for Rechargeable Aqueous Zinc-Ion Batteries. *ACS Appl. Energy Mater.* **2020**, *3*, 4677–4689. [CrossRef]
52. Hu, J.; Chen, H.; Xiang, K.; Xiao, L.; Chen, W.; Liao, H.; Chen, H. Preparation for V_6O_{13}@hollow carbon microspheres and their remarkable electrochemical performance for aqueous zinc-ion batteries. *J. Alloys Compd.* **2021**, *856*, 157085. [CrossRef]
53. Bin, D.; Wang, Y.; Tamirat, A.G.; Zhu, P.; Yang, B.; Wang, J.; Huang, J.; Xia, Y. Stable High-Voltage Aqueous Zinc Battery Based on Carbon-Coated $NaVPO_4F$ Cathode. *ACS Sustain. Chem. Eng.* **2021**, *9*, 3223–3231. [CrossRef]
54. Hong, J.; Xie, L.; Shi, C.; Lu, X.; Shi, X.; Cai, J.; Wu, Y.; Shao, L.; Sun, Z. High-Performance Aqueous Zinc-Ion Batteries Based on Multidimensional V_2O_3 Nanosheets@Single-Walled Carbon Nanohorns@Reduced Graphene Oxide Composite and Optimized Electrolyte. *Small Methods* **2024**, *8*, 2300205. [CrossRef] [PubMed]
55. Pan, D.; Liu, T.; Fu, J.; Liu, H. Superior electrochemical performance of dual-monoclinic δ-$Na_xV_2O_5/VO_2$(B) composite material with enhanced synergistic effects. *J. Alloys Compd.* **2022**, *926*, 166952. [CrossRef]

Disclaimer/Publisher's Note: The statements, opinions and data contained in all publications are solely those of the individual author(s) and contributor(s) and not of MDPI and/or the editor(s). MDPI and/or the editor(s) disclaim responsibility for any injury to people or property resulting from any ideas, methods, instructions or products referred to in the content.

molecules

MDPI

Article

Suitable Stereoscopic Configuration of Electrolyte Additive Enabling Highly Reversible and High—Rate Zn Anodes

Binrui Xu [1], Yong Liu [2,*], Bo Zhao [2,3], Haoming Li [2], Min Liu [1], Huanxiao Mai [1] and Quanan Li [2,4,*]

[1] School of Information Engineering, Henan University of Science and Technology, Luoyang 471023, China; 9906065@haust.edu.cn (B.X.); liuimin1086@163.com (M.L.); mhxgby@163.com (H.M.)
[2] School of Materials Science and Engineering, Provincial and Ministerial Coconstruction of Collaborative Innovation Center for Non—Ferrous Metal New Materials and Advanced Processing Technology, Henan University of Science and Technology, Luoyang 471023, China; bozhao123@haust.edu.cn (B.Z.); lihaoming546123@gmail.com (H.L.)
[3] Key Laboratory of Cluster Science of Ministry of Education, Beijing Key Laboratory of Photoelectronic/Electrophotonic Conversion Materials, School of Chemistry and Chemical Engineering, Beijing Institute of Technology, Beijing 100081, China
[4] Longmen Laboratory, Luoyang 471000, China
* Correspondence: liuyong209@haust.edu.cn (Y.L.); liquanan2016@163.com (Q.L.); Tel.: +86-158-9664-9559 (Y.L.); +86-138-3791-1662 (Q.L.)

Abstract: Electrolyte additive engineering is a crucial method for enhancing the performance of aqueous zinc—ion batteries (AZIBs). Recently, most research predominantly focuses on the role of functional groups in regulating electrolytes, often overlooking the impact of molecule stereoscopic configuration. Herein, two isomeric sugar alcohols, mannitol and sorbitol, are employed as electrolyte additives to investigate the impact of the stereoscopic configuration of additives on the $ZnSO_4$ electrolyte. Experimental analysis and theoretical calculations reveal that the primary factor for improving Zn anode performance is the regulation of the solvation sheath by these additives. Among the isomers, mannitol exhibits stronger binding energies with Zn^{2+} ions and water molecules due to its more suitable stereoscopic configuration. These enhanced bindings allow mannitol to coordinate with Zn^{2+}, contributing to solvation structure formation and reducing the active H_2O molecules in the bulk electrolyte, resulting in suppressed parasitic reactions and inhibited dendritic growth. As a result, the zinc electrodes in mannitol—modified electrolyte exhibit excellent cycling stability of 1600 h at 1 mA cm^{-2} and 900 h at 10 mA cm^{-2}, respectively. Hence, this study provides novel insights into the importance of suitable stereoscopic molecule configurations in the design of electrolyte additives for highly reversible and high—rate Zn anodes.

Keywords: Zn anode; electrolyte additive; stereoscopic configuration; dendrite growth; side reactions

1. Introduction

In contrast to traditional lithium—ion batteries utilizing organic electrolytes, rechargeable aqueous zinc—ion batteries (AZIBs) are being increasingly recognized as a promising replacement for energy storage devices by virtue of their cost effectiveness, reliable security, eco—friendliness, and potentially high power density of zinc metal [1–8]. Nevertheless, the practical application of AZIBs faces significant challenges due to the poor reversibility of the zinc anode during the charge/discharge process in the aqueous electrolyte [9–12]. The coordinated water within the solvation shell of the Zn^{2+} ion and the active H_2O in the aqueous electrolyte trigger severe parasitic reactions on the zinc metal surface, including corrosion and generation of H_2 gas, thereby producing the by—products and exacerbating the inhomogeneous deposition of Zn^{2+} [13–16]. As such, this inevitably leads to a decline in the plating/stripping Coulombic efficiency (CE) and eventually to short circuits, cell bulging, and explosion [17].

Various approaches have been employed to address the mentioned shortcomings of AZIBs, including the manufacture of alloy anode, fabrication of coating layer, design of three—dimensional host, development of innovative electrolyte, and electrolyte modification [18–26]. In particular, modifying the electrolyte stands out as one of the most expedient solutions to advance the commercial viability of AZIBs, owing to its excellent simplicity, reproducibility, and versatility. Current research is primarily focused on the development of electrolyte additives that are based on the regulation of Zn^{2+}—solvation structure and the modification of the interface between the aqueous electrolyte and Zn anode, such as salts, polymers, nanoparticles, and organic molecules [27–32]. For instance, Feng et al. demonstrated that the introduction of DMSO molecule into $ZnSO_4$ electrolyte reduces side reactions in the Zn^{2+}—solvation structure caused by H_2O molecules, optimizes Zn^{2+} nucleation by texturing the (002) plane, and facilitates fine—grained deposition to enhance resistance to side reactions and dendrite formation [33]. Additionally, Guo et al. introduced dopamine as an electrolyte additive, which can adhere to the Zn anode surface to form a protective layer, thereby enhancing the cycling stability of Zn anode to 1000 h under 1 mA cm^{-2} and 1 mAh cm^{-2} [34]. Moreover, Hu et al. proposed an innovative xylitol additive that inhibits the hydrogen evolution reaction (HER), expels active H_2O molecules, accelerates cations migration, and weakens electrostatic interaction through oriented restructuring of hydrogen bonds. The Zn/Zn symmetrical cell utilizing the xylitol—modified electrolyte retained reversible plating/stripping for over 1100 h at 1 mA cm^{-2} and 1 mAh cm^{-2} [35]. Furthermore, Wang et al. utilized ethylene glycol to tune Zn^{2+} coordination environment, thus suppressing detrimental dendrite growth on Zn anode and extending the cycling lifespan to 2668 h at 0.5 mA cm^{-2} and 0.5 mAh cm^{-2} [36].

Although the above—mentioned additives significantly extend the electrochemical performance of zinc electrodes by the regulation of the coordination environment of Zn^{2+} or the modification of the electrolyte—electrode interface, the cycling stability of AZIBs deteriorates sharply under severe test conditions (>2 mA cm^{-2}, >2 mAh cm^{-2}), making them impractical for real—world applications [37,38]. Hence, it is crucial to design efficient additives that address the existing obstacles of AZIBs and satisfy practical needs, especially under harsh test conditions. Furthermore, while the existing research predominantly focuses on the impact of the polar functional groups in these additives, the impact of the molecule stereoscopic configuration of additives is often overlooked. Isomers, compounds with identical molecule formulas and functional groups but different stereoscopic configurations, possess distinct chemical and physical properties, likely influencing their effectiveness as electrolyte additives. Despite this, investigations into the role of stereoscopic configurations on additive performance remain limited, highlighting a significant obstacle in designing efficient electrolyte additives for AZIBs.

Herein, a pair of isomers, mannitol and sorbitol, were incorporated as additives into the aqueous $ZnSO_4$ electrolyte to investigate the impact of the stereoscopic configuration of additive molecules on the performance of AZIBs. Mannitol and sorbitol, despite sharing a similar structure as sugar alcohols with six hydroxyl groups, possess distinct spatial configurations due to the chirality of a carbon atom within the molecules. Experimental analyses and theoretical computations revealed that sugar alcohol molecules displace the coordinated H_2O molecules within the Zn^{2+}—solvation structure, thus restraining the parasitic reactions caused by H_2O on the Zn electrode surface. In addition, the strong binding energy between H_2O and sugar alcohol leads to a reduction in free water surrounding the solvation shell, thereby effectively mitigating spontaneous parasitic reactions and suppressing dendritic growth. The research findings also indicate that the stereoscopic configuration of mannitol is more suitable for the $ZnSO_4$ electrolyte, resulting in Zn/Zn cells exhibiting stable cycling performance for more than 1600 h at 1 mAh cm^{-2} (1 mAh cm^{-2}) and over 900 h even under the harsh condition of 10 mA cm^{-2} (10 mAh cm^{-2}). Therefore, this study suggests a new direction in the design of electrolyte additives, highlighting the critical role of the stereoscopic configuration of additive molecules in regulating the solvation structure of electrolytes.

2. Results and Discussions

2.1. Electrolytes' Characterization

Mannitol and sorbitol, which are isomers of each other, possess six hydroxyl groups that have a strong affinity with charged metal ions, and the stereoscopic configurations of these molecules are shown in Figure S1 [35]. To determine the optimal concentration of sugar alcohol as an electrolyte additive, the cyclic performances of symmetrical Zn/Zn cells with different concentrations of mannitol were measured, as illustrated in Figure S2. Among the tested concentrations, the Zn/Zn cell using a 2 M $ZnSO_4$ electrolyte with 20 mM mannitol exhibited the longest cycling lifespan. Therefore, in order to examine the influence of the stereoscopic configuration of sugar alcohols on the $ZnSO_4$ electrolyte, 20 mM mannitol and sorbitol were individually dissolved in 2 M $ZnSO_4$ aqueous electrolyte (Figure S3) and denoted as $ZnSO_4$@M and $ZnSO_4$@S.

Fourier transform infrared spectrometer (FT—IR)was conducted to practically investigate the regulation of the solvation structure of Zn^{2+} by sugar alcohol additives [39]. Figure 1a,b show that the H—O bending vibration shifts towards higher wavenumbers and the H—O stretching vibration shifts towards lower wavenumbers in the $ZnSO_4$@M and $ZnSO_4$@S electrolytes. This indicated that the addition of sugar alcohols led to the displacement of H_2O molecules from the Zn^{2+}—solvation sheath into the bulk solution phase, augmenting the number of hydrogen bonds [36]. This displacement mechanism suggests that sugar alcohols can coordinate with Zn^{2+} and modify the coordination environment in the $ZnSO_4$ electrolyte [40]. Additionally, the stretching vibration of SO_4^{2-} in the electrolyte shifted upon the introduction of sugar alcohols, indicating a loosened constraint around SO_4^{2-} and highlighting the reconstruction of the Zn^{2+}—solvation structure due to the additives [41].

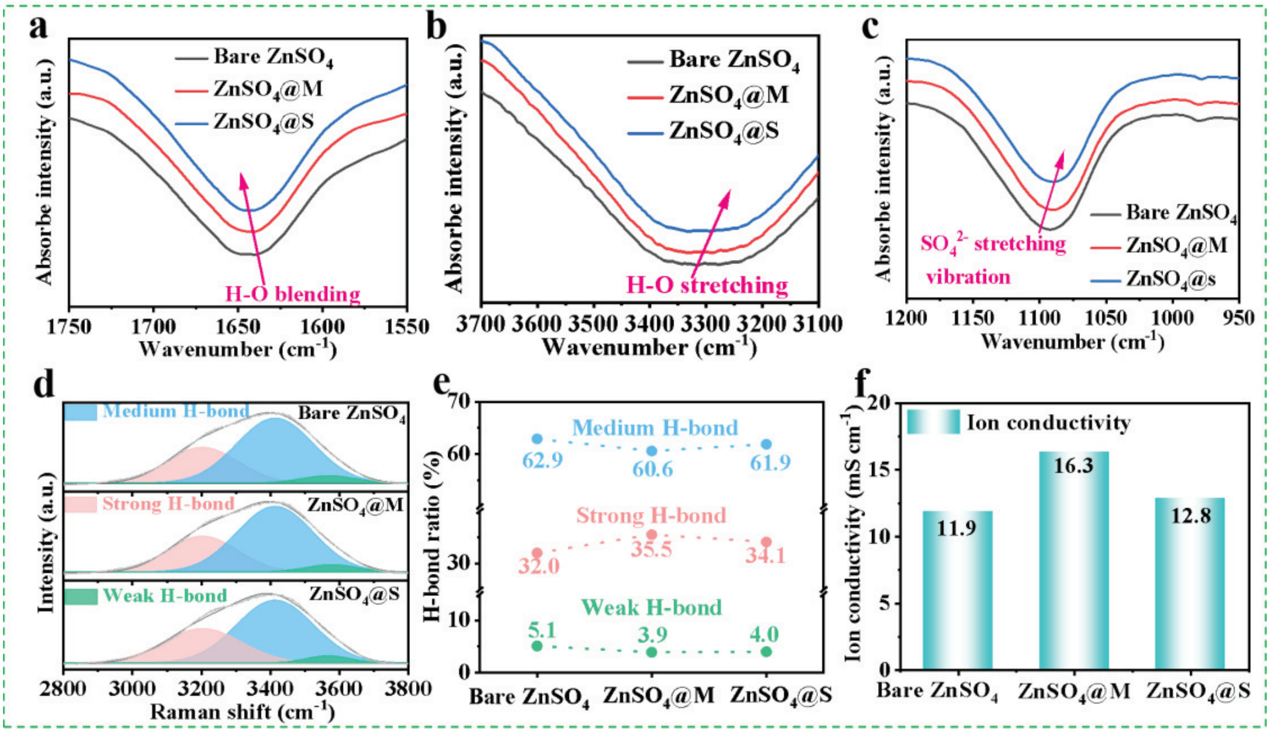

Figure 1. FT—IR spectra of the (**a**) H—O blending vibration, (**b**) H—O stretching vibration, and (**c**) SO_4^{2-} stretching vibration of $ZnSO_4$ electrolytes with/without additive. (**d**) Raman spectra (H—O stretching) of the different electrolytes. (**e**) The percentages of strong, medium, and weak H—bonds in the different electrolytes. (**f**) Ionic conductivities of the different electrolytes.

The electrolyte modification is further determined by the Raman spectroscopy analysis [42]. The Raman spectra of $ZnSO_4$@M and $ZnSO_4$@S electrolytes (Figure S4) show a new peak of C=C vibration (1600–1700 cm^{-1}), which is attributed to the incorporation of sugar alcohols. In addition, the broad peak of H—O stretching vibration (2800–3800 cm^{-1}) was segmented into three different peaks (Figure 1d), each of which corresponds to strong, medium, and weak H—bonds, respectively [43]. Findings from the deconvoluted peak region in Figure 1e indicate that the addition of sugar alcohols, particularly mannitol, led to a decrease in the proportions of medium and weak hydrogen bonds at higher frequency and an increase in the percentage of strong H—bonds at lower frequency. Specifically, mannitol and sorbitol additives were found to strengthen hydrogen bonding interactions, leading to enhanced water cluster stability and reduced active H_2O content in the $ZnSO_4$ electrolyte [44,45]. Furthermore, the slight differences in the changes to hydrogen bonds induced by the two additives may be attributed to variations in their stereoscopic configurations. Moreover, the enhanced ionic conductivity observed in both $ZnSO_4$@M and $ZnSO_4$@S electrolytes (Figure 1f) implied that the modified coordination environment in the presence of additives contributed to a reduction in water activity [31]. Furthermore, Figure S5 illustrates that the cyclic voltammogram (CV) curves of Zn/Zn cell with $ZnSO_4$@M electrolyte in multiple cycles aligned well, indicating the excellent electrochemical stability of mannitol additive [46].

2.2. Theoretical Calculation

To further verify the effect of stereoscopic configuration on the coordination ability of the additive molecules, the binding energies of the Zn^{2+}—H_2O pair (−4.6 eV), Zn^{2+}—mannitol pair (−6.36 eV), and Zn^{2+}—sorbitol pair (−5.73 eV) were calculated using density functional theory (DFT), as illustrated in Figure 2a. The stronger interaction observed between the cationic Zn^{2+} and hydroxyl group from the sugar alcohol molecule suggests that the sugar alcohol preferentially participates in the formation of the Zn^{2+}—solvation structure, which is also supported by the above FT—IR spectra [33]. In addition, Figure 2a also presents the binding energies of the mannitol—H_2O pair, sorbitol—H_2O pair, and H_2O—H_2O pair, where the mannitol—H_2O and sorbitol—H_2O pairs exhibit higher binding energies, particularly the mannitol—H_2O pair. These DFT results indicate a tendency for the reconstruction of the water hydrogen bond network in the $ZnSO_4$ electrolyte, wherein more free H_2O molecules bind with sugar alcohol molecules, as supported by the consistent Raman spectra. Therefore, it can be speculated that the addition of sugar alcohol additive regulates the solvation structure of Zn^{2+} and restructures the H—bond composition in the electrolyte. Furthermore, the greater binding affinity of mannitol towards Zn ions and water molecules, compared to sorbitol, suggests that its steric configuration is more effective in influencing the solvation structure of the $ZnSO_4$ electrolyte.

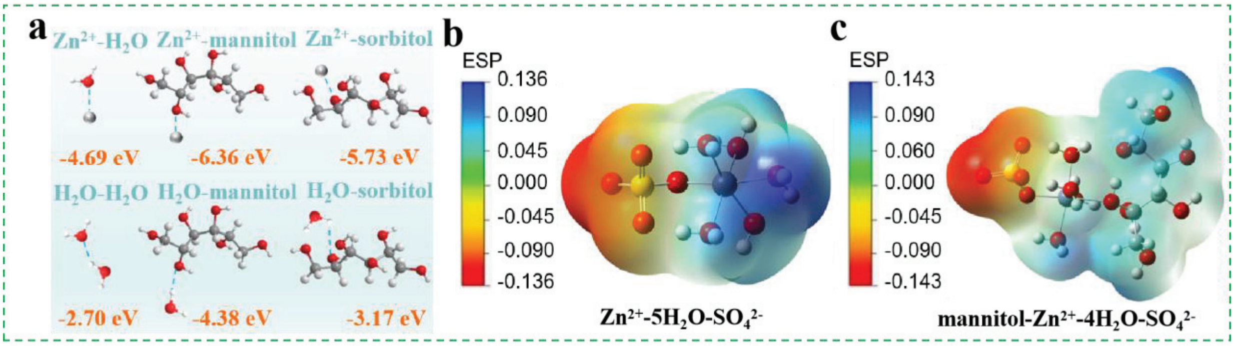

Figure 2. (**a**) The binding energy comparison of various pairs. ESP mapping of the (**b**) Zn^{2+}–$5H_2O$–$SO_4{}^{2-}$ and (**c**) mannitol—Zn^{2+}—$4H_2O$—$SO_4{}^{2-}$ solvation structures.

Notably, Figure 2b,c exhibits that the electrostatic potential of the coordination complex increases when a water molecule is replaced by a sugar alcohol molecule, which results in a more uneven distribution. This uneven distribution helps alleviate electrostatic potential in the vicinity of Zn^{2+} and promotes the rapid transport of Zn^{2+}. Specifically, sites with higher positive electrostatic potential are more appealing to negative sites, thereby favoring the directional reconstruction of H—bonds associated with the mannitol molecule [35]. Additionally, the theoretical geometric parameters of solvation structures are provided in Table S1 and Figure S6 to further elucidate the impact of mannitol additive on the solvation structure of Zn^{2+}. Results show that the addition of mannitol causes a decrease in the average bond length of Zn^{2+}—H_2O and Zn^{2+}—$SO_4{}^{2-}$ bond length, indicating that another part of the structure, apart from the mannitol molecule, becomes more compact, possibly hindering water molecules from participating in the solvation structure. This change in bond lengths also suggested that the symmetry of the entire structure weakens upon the addition of mannitol, making it more stable in an aqueous solution [47,48].

2.3. Cycling Performance

The Zn/Zn symmetrical cells were fabricated to determine the influences of the stereoscopic configuration of sugar alcohol additive on the cyclic stability of the zinc electrode. Figure 3a presents that the Zn/Zn cell with the bare $ZnSO_4$ electrolyte failed rapidly at 1 mA cm^{-2} and 1 mAh cm^{-2}. In contrast, the Zn/Zn cells performed better cyclic performances when mannitol or sorbitol was added, especially the one with $ZnSO_4$@M electrolyte cycled more than 1600 h. Additionally, the $ZnSO_4$@M—containing cell displayed outstanding cycling stability for 900 h at the high test condition of 10 mA cm^{-2} (10 mAh cm^{-2}), outperforming the cells with bare $ZnSO_4$ and $ZnSO_4$@S electrolytes, which cycled for about 85 h and 500 h, respectively (Figure 3b). The different degrees of improvement in the cyclic stability of the Zn anodes show that the stereoscopic configuration of the additive molecule has a significant effect on the cyclic stability of the Zn anode. The comparative data in Figure 3c and Tables S2 and S3 demonstrate that the zinc anode shows superior cycling stability and lower polarization voltage in the $ZnSO_4$@M electrolyte, compared to the previously optimized electrolytes in other studies [11,12,34,35,40,43,49–51]. The results of electrochemical impedance spectroscopy (EIS) (Figure S7 and Figure 3d) further revealed much smaller charge—transfer resistances of the Zn/Zn symmetric cells with sugar alcohols. This indicated that the sugar alcohol additives accelerate electron transport, which helps homogenize the Zn^{2+} distribution in the Zn deposition process [51].

Since CE is a crucial factor in achieving the commercialization of AZIBs, the CEs of the Zn/Cu asymmetric cells utilizing bare $ZnSO_4$, $ZnSO_4$@M, and $ZnSO_4$@S electrolytes were measured and are shown in Figure 3e [52]. The cells with bare $ZnSO_4$ and $ZnSO_4$@S failed after 108 cycles (average CE of 98.68%) and 114 cycles (average CE of 98.99%) at 0.5 mA cm^{-2} and 1 mAh cm^{-2}, respectively. Remarkably, the Zn/Cu cell employing the $ZnSO_4$@M electrolyte outperformed all others with an outstanding average CE of 99.66% sustained over 400 cycles. The voltage profiles in the $ZnSO_4$ electrolytes without/with sugar alcohols during different cycles are compared in Figure 3f–h, where the zinc anode in the $ZnSO_4$@M electrolyte showed high reversibility throughout 400 cycles. Compared to the $ZnSO_4$@S electrolyte, the $ZnSO_4$@M electrolyte significantly enhanced the Zn plating/stripping behaviors, likely due to the suitable stereoscopic configuration of the mannitol molecule, which promotes the reconstruction of the hydrated Zn^{2+}—solvated sheath and the inhibition of dendritic growth and side reactions [53].

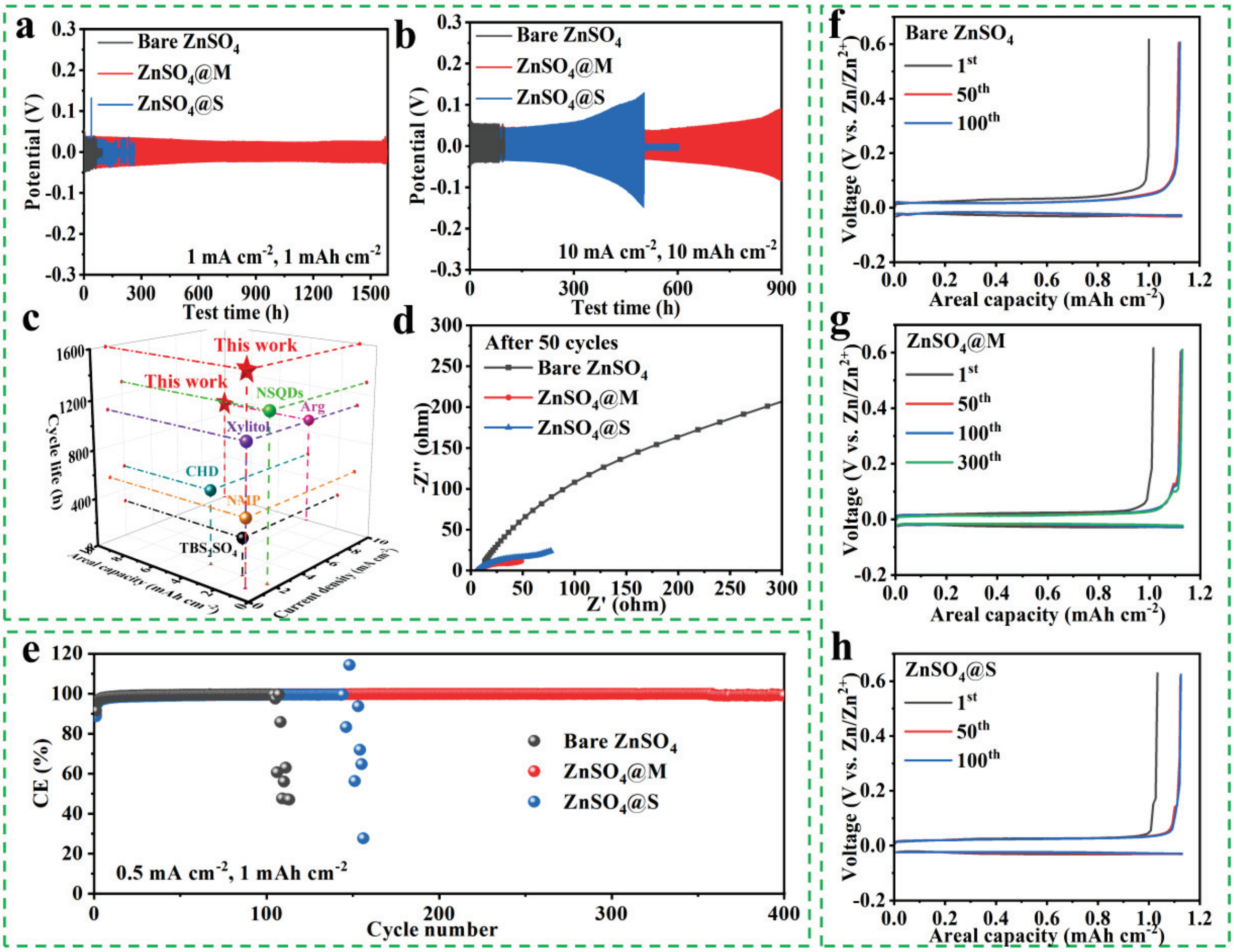

Figure 3. Cyclic performance of Zn/Zn cells with different electrolytes under (**a**) 1 mA cm^{-2} with 1 mAh cm^{-2} and (**b**) 10 mA cm^{-2} with 10 mAh cm^{-2}. (**c**) Comparison of the current density, cycling capacity, and lifetime found in this study and that of other reported Zn/Zn cells with different additives. (**d**) EIS measurements of the Zn/Zn symmetrical cells before the cycling test. (**e**) Cyclic stability of Zn/Cu asymmetrical cells in the different electrolytes at 0.5 mA cm^{-2} with 1 mAh cm^{-2}. (**f**–**h**) Corresponding discharge/charge profiles of Zn/Cu cells at different cycles.

2.4. Zn Deposition Behavior

To further examine the impact of sugar alcohols on the deposition evolution of Zn, the morphologies of zinc foil substrates were compared after 50 cycles. Inhomogeneous Zn deposition with obvious protuberances was observed on the morphology of the Zn foil (Figure 4a) in the bare $ZnSO_4$ electrolyte. In contrast, Figure 4b,c demonstrates that the Zn deposition on the zinc foils in sugar alcohol—modified electrolytes is more uniform, especially in the $ZnSO_4$@M electrolyte [54]. In addition, an in situ optical system was performed to investigate the zinc nucleation and deposition behavior (Figure 4d and Figure S8). Zn protrusions became visible with the increasing electrodeposition time in the bare $ZnSO_4$ electrolyte, eventually inducing the zinc dendrite growth. In comparison, the topography of the Zn plate in the $ZnSO_4$@M electrolyte was always dense and uniform during the continuous deposition, whereas the $ZnSO_4$@S electrolyte resulted in small Zn protrusions and loose deposition [55].

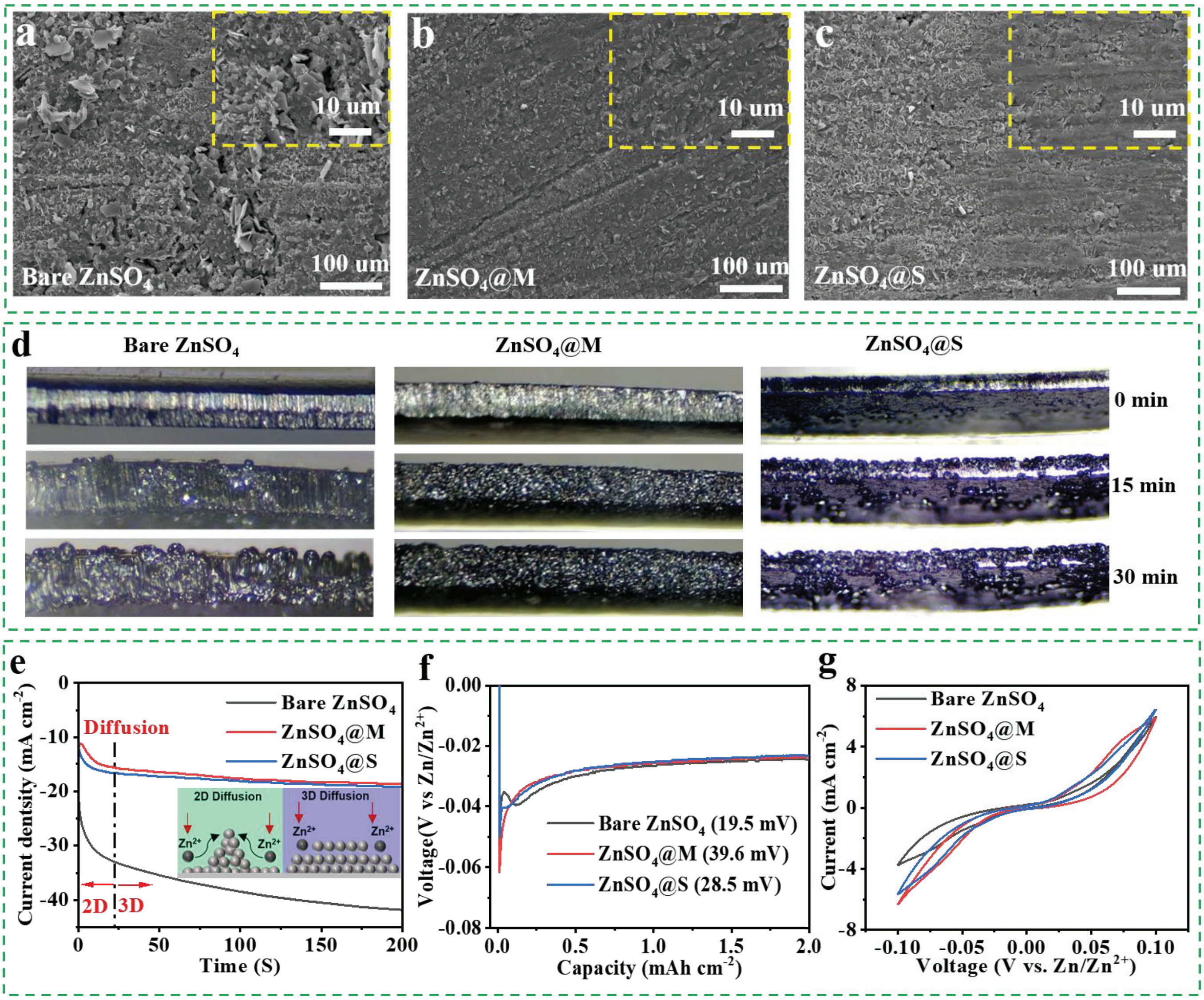

Figure 4. (**a**–**c**) Surface topography measurement of zinc foil substrates after cycling test in bare $ZnSO_4$, $ZnSO_4$@M, and $ZnSO_4$@S electrolytes. (**d**) In situ optical microscopy images of the zinc electrode after 0, 15, and 30 min in bare $ZnSO_4$, $ZnSO_4$@M, and $ZnSO_4$@S electrolytes. (**e**) CA measurement of Zn/Zn symmetrical cells with bare $ZnSO_4$, $ZnSO_4$@M, and $ZnSO_4$@S electrolytes. (**f**) The initial Zn NOPs using the Zn/Cu half cells with various electrolytes. (**g**) CV curves of Zn/Zn symmetric cells with various electrolytes at 5 mV s^{-1}.

The nucleation mechanism of Zn metal in $ZnSO_4$ electrolytes with/without additive was confirmed through the chronoamperometry (CA) measurements [55,56]. Figure 4e exhibits that the zinc electrode in the bare $ZnSO_4$ electrolyte displays a continuously decreased tendency of exchange current density within 200 s, corresponding to a prolonged and rampant two—dimensional (2D) diffusion behavior of zinc deposition, which causes the nonuniform Zn accumulation and vertical growth of dendrites. On the contrary, Zn foils in sugar alcohol—modified electrolytes displayed a constant three—dimensional (3D) diffusion behavior after a short 2D diffusion process for 25 s, indicating that the smooth, dense, and even Zn deposition was maintained over the 200 s duration [57]. The effect of sugar alcohol additives on Zn deposition aligned with findings from in situ optical photographs (Figure 4d) of Zn deposition. Moreover, the Zn nucleation process was further explored through the nucleation overpotential (NOP) analysis of Zn/Cu asymmetrical cells, as illustrated in Figure 4f. The initial NOPs of zinc electrodes in $ZnSO_4$@M and $ZnSO_4$@S electrolytes were found to be 39.6 mV and 28.5 mV, respectively, surpassing the NOP of the bare $ZnSO_4$ electrolyte (19.5 mV). According to classical nucleation theory, a higher NOP encourages the formation of smaller and denser Zn nuclei, potentially leading to fine—grained deposits that result in a compact and uniform surface for subsequent Zn deposition [36]. Furthermore, CV curves with the sugar alcohol additive exhibited much stronger intensities of redox peaks (Figure 4g), indicating the enhanced electrochemical reactivity for Zn deposition [58].

2.5. Inhibition of Side Reactions

To verify the corrosion resistance of the sugar alcohols, the Zn foils were immersed in the bare $ZnSO_4$, $ZnSO_4$@M, and $ZnSO_4$@S electrolytes for 7 days. Figure 5a–c show that the polygonal micro—flakes were distributed on the zinc foil surface in the bare $ZnSO_4$ electrolyte, while no obvious by—products appeared on the surface of the zinc foils in the $ZnSO_4$@M and $ZnSO_4$@S electrolytes. The X-ray diffraction (XRD) pattern (Figure 5d) confirmed that the polygonal by—products observed in the bare $ZnSO_4$ electrolyte were $Zn_4SO_4(OH)_6 \cdot 4H_2O$ induced by the corrosion reaction [59]. However, no undesired diffraction peaks of by—products were observed on the XRD profiles of Zn anodes in the $ZnSO_4$ electrolytes with sugar alcohol additives, indicating the successful prevention of the corrosion reaction induced by H_2O and SO_4^{2-}. Additionally, the corrosion currents (Figure 5e) remarkably decreased in $ZnSO_4$@M and $ZnSO_4$@S electrolytes, demonstrating the more efficient prevention of corrosion reaction by sugar alcohols [60]. Additionally, the potential for HER of electrolytes was evaluated using the linear sweep voltammetry (LSV) measurement, as illustrated in Figure 5f. The HER potential in the bare $ZnSO_4$ electrolyte was recorded to be −112 mV at 20 mA cm^{-2}, while it increased by 12 mV and 4 mV in the $ZnSO_4$@M and $ZnSO_4$@S electrolytes, respectively. This increase suggests that sugar alcohol additives have a more pronounced inhibitory of hydrogen evolution, leading to higher potentials in the modified electrolytes [61].

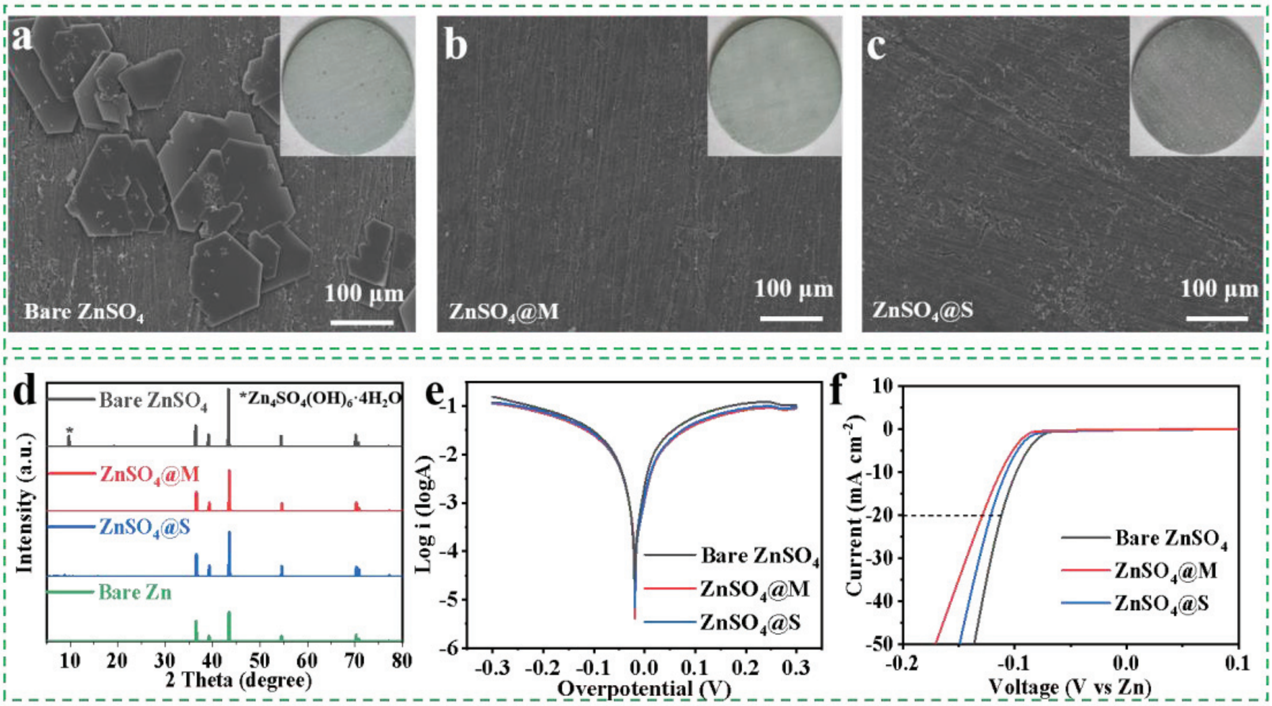

Figure 5. (**a**–**c**) Surface morphology images and optical photographs of zinc foils soaked in the $ZnSO_4$ electrolytes with/without additive for one week. (**d**) XRD patterns of zinc electrodes in the $ZnSO_4$ electrolytes with/without additive after cycling test. (**e**) Linear polarization curves in the $ZnSO_4$ electrolytes with/without additive. (**f**) LSV curves in the ZnSO4 electrolytes with/without additive.

2.6. Working Mechanism of Additive

Upon combining the experimental and theoretical results, a comprehensive understanding of the working mechanism of sugar alcohol additives can be attained. It is acknowledged that Zn^{2+} exists in the aqueous electrolyte as the $[Zn(H_2O)_x]^{2+}$ solvation structure, where the central Zn^{2+} ions function as the Lewis acid site, hydrolyzing H_2O to H^+ and OH^- and inducing side reactions on the zinc anode surface in a mildly acidic environment. Additionally, dendrite growth is another frequent phenomenon during the repeated charge/discharge process (Figure 6). Herein, the introduction of sugar alcohol into the electrolyte alters the electrolyte coordination environment, leading to a partial replacement of H_2O molecules in the solvation shell with sugar alcohol additives. Meanwhile, the added sugar alcohol molecules disrupt the existing hydrogen bond between H_2O molecules in the electrolyte, allowing more free H_2O molecules to be captured by sugar alcohol with hydroxyl groups, reducing the water molecules involved in interface side reactions, lowering proton activity, and thus mitigating parasitic reactions caused by free H_2O. Furthermore, due to the regulation of the Zn^{2+}—solvation sheath by sugar alcohol, the Zn nucleation process requires a slightly higher overpotential, resulting in a homogeneous nuclei distribution and even Zn deposition without dendrites. Notably, among the two sugar alcohol additives employed in this study, mannitol, owing to its more suitable stereoscopic configuration, is utilized as an additive for achieving a Zn anode with superior electrochemical performance.

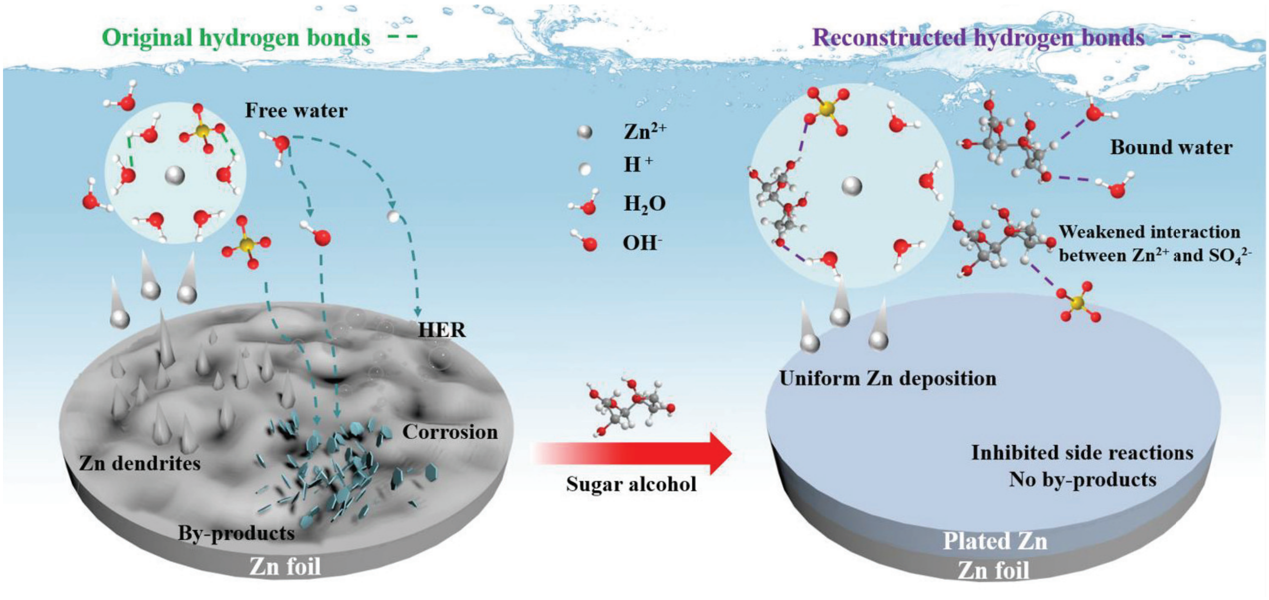

Figure 6. Schematic diagram of hydrated Zn^{2+}—solvation structure at Zn anodes in the $ZnSO_4$ electrolytes with/without additive.

2.7. Electrochemical Properties' Characterization

To demonstrate the practical application of the sugar alcohol additives, full cells were assembled with an $NH_4V_4O_{10}$ cathode (Figure S9) and a Zn anode [58]. Figure 7a exhibits the CV curves for the Zn/$NH_4V_4O_{10}$ full cells. The full cell utilizing $ZnSO_4$@M displayed a larger area compared to that with the bare $ZnSO_4$ electrolyte, which corresponds to the aforementioned improved reaction kinetics [62]. The multi—cycle CV curves (Figure S10) overlapped well, which further elucidated the electrochemical stability of mannitol as an electrolyte additive. Additionally, as shown in Figure S11 and Figure 7b, the R_{ct} reduction in the cells using $ZnSO_4$@M and $ZnSO_4$@S further exemplifies the influences of sugar alcohols on inhibiting dendritic growth and adverse parasitic reactions on the zinc electrode. Another critical factor affecting the performance of AZIBs is their self—discharge characteristics, which can be assessed through the open—circuit voltage of the Zn/$NH_4V_4O_{10}$ full cell after charging and standing for 48 h [63]. Figure 7c reveals that the initial open—circuit voltage (1.4 V) of the $Zn/NH_4V_4O_{10}$ cells incorporated with $ZnSO_4$@M or $ZnSO_4$@S decays to 1.0087 V and 1.0072 V, respectively, while that of the bare cell drops to 1.0029 V. Moreover, Figure 7d shows a low rate performance of the $Zn/NH_4V_4O_{10}$ cell cycling in the bare $ZnSO_4$ electrolyte. This is likely due to the development of an insulating passivation layer on the zinc metal that hinders the interfacial transportation of Zn^{2+} [64–66]. On the other hand, the $Zn/NH_4V_4O_{10}$ cells with $ZnSO_4$@M and $ZnSO_4$@S demonstrated exceptional cycling stability after 800 cycles at 5 A g^{-1}, surpassing the performance of the bare $ZnSO_4$ electrolyte. Meanwhile, unlike the unstable charge/discharge platforms and enlarged over—potential curves observed with the bare $ZnSO_4$ electrolyte, the full cells containing sugar alcohols maintained stable voltage plateaus following multiple cycles without obvious capacity degradation, as illustrated in Figure S12. Furthermore, the morphology image (Figure 7f) of the cycled Zn anode demonstrates the dendrite growth in the bare $ZnSO_4$ electrolyte, while Figure 7g,h shows smooth deposition without noticeable dendrite formation in the sugar alcohol—modified electrolytes.

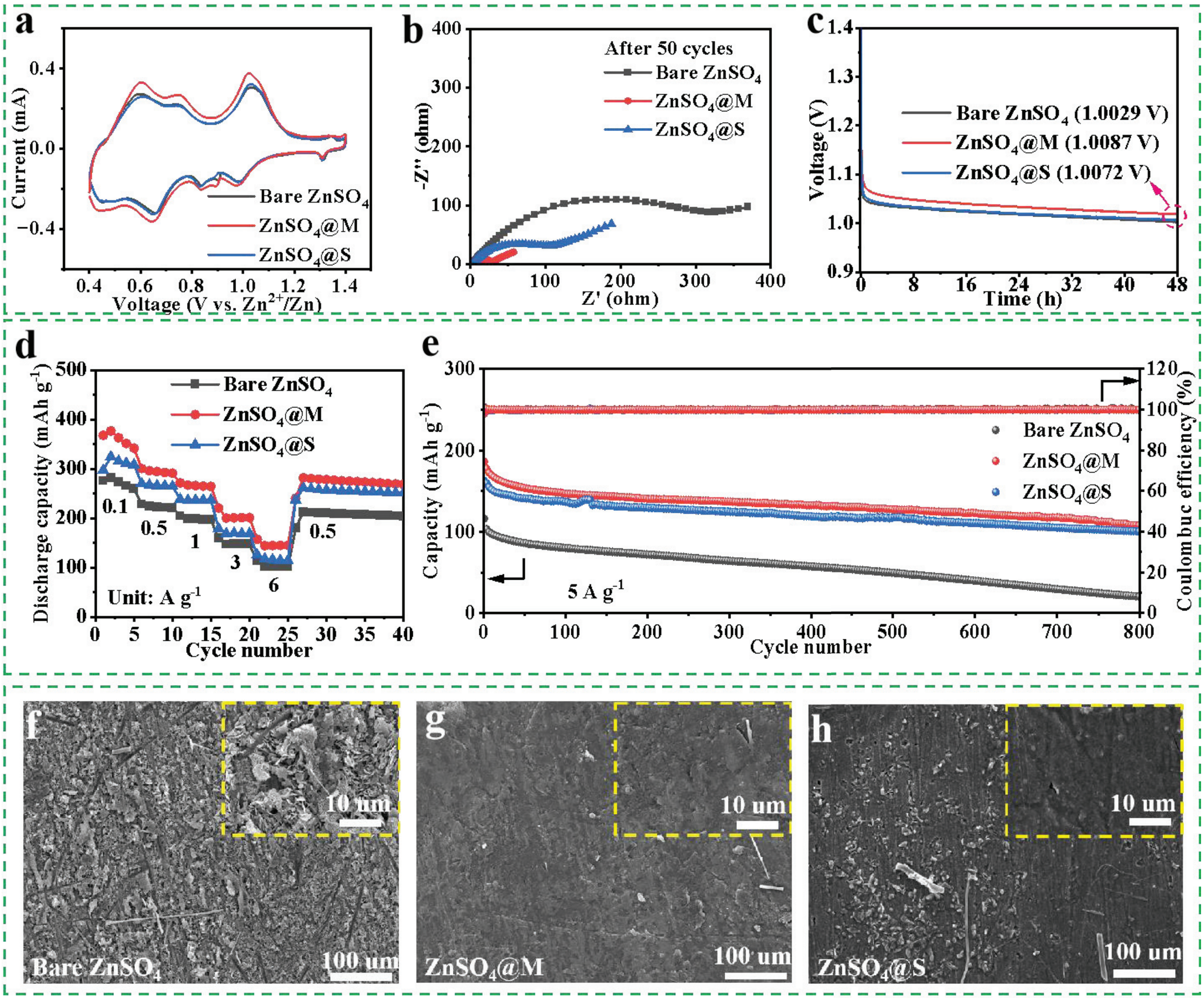

Figure 7. (**a**) CV curves of the $Zn/NH_4V_4O_{10}$ full cells at 0.1 mV s^{-1}. (**b**) Nyquist plots of the $Zn/NH_4V_4O_{10}$ full cells after 50 cycles. (**c**) Time—dependent open—circuit voltages of the $Zn/NH_4V_4O_{10}$ full cells for self—discharge tests. (**d**) Rate performances of the $Zn/NH_4V_4O_{10}$ full cells measured from 0.1 to 6 A g^{-1}. (**e**) Cyclic performances of the $Zn/NH_4V_4O_{10}$ full cells at 5 A g^{-1}. (**f**–**h**) Surface topography measurement of Zn electrodes at the 50th cycle in the $Zn/NH_4V_4O_{10}$ full cells with various electrolytes.

To further explore the universality of sugar alcohol additives, Zn/MnO_2 full cells were assembled using a MnO_2 cathode (Figure S13), and their lifetimes were investigated in different electrolytes, as illustrated in Figure S14. Notably, all sugar alcohol—modified cells exhibited superior capacity retention rates after 800 cycles compared to the bare cell, highlighting the broad applicability of sugar alcohol additives.

3. Experimental Section

3.1. Materials

Zinc sulfate heptahydrate ($ZnSO_4 \cdot 7H_2O$), ammonium metavanadate (NH_4VO_3), oxalic acid ($H_2C_2O_4 \cdot 2H_2O$), potassium permanganate ($KMnO_4$), and 1-methyl-2-pyrrolidinone (NMP) were sourced from Shanghai Aladdin Biochemical Technology Co., Ltd., Shanghai, China. HCl was purchased from Luoyang Haohua Chemical Reagent Co. Ltd., Luoyang, China. Super P carbon was bought from Kluthe Chemical Industrial Co., Ltd., Shanghai, China. Polyvinylidene fluoride (PVDF) was bought from Guangdong Zhuguang New Energy Technology Co., Ltd., Guangdong, China. Mannitol and sorbitol were obtained from Sinopharm Chemical Reagent Co., Ltd., Shanghai, China. All materials were used as received.

3.2. Preparation of Cathode

A 2 M $ZnSO_4$ electrolyte was obtained by dissolving $ZnSO_4 \cdot 7H_2O$ in deionized (DI) water. Mannitol and sorbitol were, respectively, added to the prepared electrolyte to acquire the modified electrolytes.

3.3. Preparation of the Electrolyte

The $NH_4V_4O_{10}$ material was prepared by the traditional hydrothermal method. Firstly, 1.170 g of NH_4VO_3 was added to 35 mL of DI water on a hot plate set to 80 °C and stirred to form a yellowish solution. Next, 1.891 g of $H_2C_2O_4 \cdot 2H_2O$ was slowly dissolved into the solution. Subsequently, the prepared solution was put into a 50 mL Teflon—lined stainless steel autoclave and placed in an oven at 140 °C for 48 h. The precipitates were then filtered and rinsed with DI water and desiccated at 60 °C for 12 h to obtain the $NH_4V_4O_{10}$ powder.

The MnO_2 material was also prepared by the traditional hydrothermal method. A 6 mM quantity of potassium permanganate was dissolved in 60 mL DI water and then stirred evenly. Next, 20 mM HCl was added dropwise to the above solution, and after mixing and stirring, it was poured into a 50 mL Teflon—lined stainless steel autoclave, heated to 140 °C, and kept for 12 h. After the above product was naturally cooled to room temperature, the lower precipitate was washed three times with DI water and alcohol alternately and dried overnight in a vacuum oven to obtain the MnO_2 powder.

The cathodes were fabricated by mixing $NH_4V_4O_{10}$ (or MnO_2), Super P carbon, and PVDF in a weight ratio of 7:2:1, and NMP was added drop by drop. This mixture was then coated on a stainless steel mesh and dried at 80 °C overnight. Lastly, the mesh was cut into round sheets with a diameter of 12 mM, and the mass loading was kept to around 1.7 mg cm^{-2}.

3.4. Characterization

The structure and chemical bond were characterized by a FT—IR spectrometer (Shimadzu, IRTracer—100, Tokyo, Japan). A Raman microscope (Raman, LabRAM HR Evolution, Shanghai, China) with a 532 nm excitation laser line was used to analyze the H—bond network in the $ZnSO_4$ electrolytes. The images revealing the surface morphology of the Zn anodes were acquired by field emission scanning electron microscopy (JSM—7800F, JEOL, Akishima, Japan). The in situ optical images of Zn deposition were collected with an optical microscope (DMSZ8, Ningbo, China). The structural and phase characteristics of the samples were recorded by an XRD diffractometer (Bruker D8 ADVANCE, Cu—kα, λ = 1.5418 Å).

3.5. Electrochemical Measurements

The symmetrical Zn/Zn cells, Zn/Cu asymmetric cells, Zn/$NH_4V_4O_{10}$, and Zn/MnO_2 full cells were assembled in CR2032 coin cells configuration by using 2 M $ZnSO_4$ with or without sugar alcohol additive as the electrolyte and glass fiber as the separator. The cycling, rate, and CE performance of the cells were measured by the Neware battery testing system (BTS—5V20 mA, Shenzhen, China). The electrochemical impedance measurements (EIS) of Zn/Zn symmetric cells were measured across the range of 10^5 Hz to 10^{-2} Hz with an AC amplitude of 5 mV at room temperature on an electrochemical workstation (CHI—660E, Shanghai, China). The specific ionic conductivity was determined using the following equation: $\sigma = l/(R_b{*}S)$, where σ (mS cm^{-1}) is the ionic conductivity, l (cm) is the separator's thickness, R_b (Ω) is the bulk resistance, and S (cm^2) is the separator's area. The LSV measurements were taken using a three—electrode system, with stainless steel working electrodes, and Zn metal reference and counter electrodes, with a change in voltage of 5 mV s^{-1} from 0 V to -0.4 V. The equilibrium redox voltages were obtained by fitting Tafel plots for the Zn/Zn symmetric coin cells at 5 mV s^{-1} across voltages between -0.3 and 0.3 V. The CA measurements were carried out with a constant potential of 10 mV for 200 s to determine Zn deposition behavior. The performance of the CV was conducted at 1 mV s^{-1} across the voltage range between 0.4 and 1.4 V.

3.6. Computational Details

DFT spin—polarized calculations were conducted using the DMol3 package, following the adoption of the generalized gradient approximation (GGA) in the Perdew—Burke—Ernzerhof form and the Semicore Pseudopotential method (DSPP) with the double numerical basis sets plus the polarization functional (DNP) [67–69]. To account for the dispersion interaction, a DFT—D correction with the Grimme scheme was applied [70]. SCF convergence for each electronic energy was set as 1.0×10^{-6} Ha, and the geometry optimization convergence criteria were established at 1.0×10^{-6} Ha for energy, 0.0001 Ha Å–1 for force, and 0.0001 Å for displacement, respectively. The investigation of energy barriers was accomplished through the linear and quadratic synchronous transit methods combined with the conjugated gradient refinement. Furthermore, the adsorption energies (E_{ads}) were computed using $E_{ads} = E_{ad/sub} - E_{ad} - E_{sub}$, where $E_{ad/sub}$, E_{ad}, and E_{sub}, respectively, denote the total energies of the optimized adsorbate/substrate system, the adsorbate in the gas phase, and the clean substrate, respectively. The DFT had also been employed to describe the electrostatic potential (ESP). In this study, the B3LYP—D3(BJ)/6—31G(d,p) theoretical model has been adopted for the structural optimizations. To simulate the solvation effect, the self—consistent reaction field method with the polarized continuum model was utilized. Additionally, the ESP mapping was analyzed via the Multiwfn package 3.7 and VMD package 1.9.4 [71,72].

4. Conclusions

This study utilizes a combination of experimental analysis and theoretical calculations to compare the effects of mannitol and sorbitol, isomers used as additives in the $ZnSO_4$ aqueous electrolyte. Mannitol, with its advantageous stereoscopic configuration, exhibits the strongest binding energy with Zn^{2+} and water molecules. This characteristic enables mannitol to coordinate efficiently with zinc ions, leading to modifications in solvation structure, reduced reactive water content within the electrolyte, and ultimately the prevention of zinc dendrite formation and undesirable side reactions. Consequently, Zn/Zn cells incorporating mannitol show superior long—term stability, with lifetimes extending to 1600 h at 1 mA cm^{-2} (1 mAh cm^{-2}) and 900 h at 10 mA cm^{-2} (10 mAh cm^{-2}). Furthermore, the inclusion of mannitol in Zn/$NH_4V_4O_{10}$ and Zn/MnO_2 full cells results in enhanced cycling performance, better rate capability, and improved capacity retention over extended periods. Thus, this research not only achieves a highly reversible and high—rate Zn anode, but also presents a novel avenue for designing electrolyte additives for aqueous Zn—ion batteries by investigating the stereoscopic configuration of additive molecules.

Supplementary Materials: The following supporting information can be downloaded at: https://www.mdpi.com/article/10.3390/molecules29143416/s1, Figure S1: The stereoscopic configurations of mannitol and sorbitol molecules; Figure S2: Long—term cycling performances of Zn/Zn cells in 2 M $ZnSO_4$ electrolytes with various mannitol contents (0 mM, 10 mM, 20 mM, and 30 mM) at 1 mA cm^{-2} and 1 mAh cm^{-2}; Figure S3: Optical photographs of $ZnSO_4$ electrolytes with/without additives; Figure S4: Raman spectra of the different electrolytes in the range from 1500 cm^{-1} to 1800 cm^{-1}; Figure S5: Multi—cycle CV curves of Zn/Zn symmetric cells with the $ZnSO_4$@Melectrolyte; Figure S6: Different bonds in (a) Zn^{2+}—$5H_2O$—$SO_4{}^{2-}$ and (b) mannitol—Zn^{2+}—$4H_2O$–$SO_4{}^{2-}$; Figure S7: EIS measurements of the Zn/Zn cells before cycling test; Figure S8: The in situ optical microscopy system to observe the Zn anode during the Zn plating process; Figure S9: (a) Morphology image and (b) XRD pattern of $NH_4V_4O_{10}$ powder; Figure S10: Multi—cycle CV curves of Zn/$NH_4V_4O_{10}$ symmetric cells with the $ZnSO_4$@M electrolyte; Figure S11: Nyquist plots of Zn/$NH_4V_4O_{10}$ full cells before cycling test; Figure S12: Voltage profiles of the Zn/$NH_4V_4O_{10}$ full cells at 5 A g^{-1} for different cycles; Figure S13: (a) Morphology image and (b) XRD pattern of MnO_2 powder; Figure S14: Cycling performance of Zn/MnO_2 full cells tested at the current density of 0.5A g^{-1}; Table S1: Bond lengths of the solvation structure of Zn^{2+} with/without mannitol; Table S2: Comparison of this study with other previously reported cycling performances of symmetrical cells; Table S3: Comparison of this study with other previously reported polarization voltages of symmetrical cells at 100 h.

Author Contributions: Conceptualization, B.X. and Y.L.; methodology, B.X.; software, B.Z.; validation, B.X. and M.L.; formal analysis, B.X. and H.M.; investigation, B.X.; resources, Y.L.; data curation, H.M.; writing—original draft preparation, B.X.; writing—review and editing, Y.L.; visualization, B.X. and H.L.; supervision, Q.L. All authors have read and agreed to the published version of the manuscript.

Funding: This research was funded by the Key Science and Technology Program of Henan Province, grant number 232102241020; the Ph.D. Research Startup Foundation of Henan University of Science and Technology, grant number 400613480015; the Postdoctoral Research Startup Foundation of Henan University of Science and Technology, grant number 400613554001; and the Natural Science Foundation of Henan Province, grant number 242300420021.

Institutional Review Board Statement: Not applicable.

Informed Consent Statement: Informed consent was obtained from all subjects involved in the study.

Data Availability Statement: The data presented in this study are available on request from the corresponding author.

Conflicts of Interest: The authors declare no conflicts of interest.

References

1. Yoshino, A. The birth of the lithium—ion battery. *Angew. Chem. Int. Ed.* **2012**, *51*, 5798–5800. [CrossRef] [PubMed]
2. Luo, Z.; Liu, Z.; He, H.; Zhang, Z.; Chen, Y.; Peng, C.; Zeng, J. Suppressing the dissolution of vanadium by organic—inorganic hybrid for aqueous zinc—ion batteries. *J. Mater. Sci. Technol.* **2023**, *145*, 93–100. [CrossRef]
3. Wang, F.; Borodin, O.; Gao, T.; Fan, X.; Sun, W.; Han, F.; Faraone, A.; Dura, J.A.; Xu, K.; Wang, C. Highly reversible zinc metal anode for aqueous batteries. *Nat. Mater.* **2018**, *17*, 543–549. [CrossRef] [PubMed]
4. Jiang, J.; Li, Z.; Pan, Z.; Wang, S.; Chen, Y.; Zhuang, Q.; Ju, Z.; Zhang, X. Recent Progress and Prospects on Dendrite—free Engineerings for Aqueous Zinc Metal Anodes. *Energy Environ. Sci.* **2022**, *6*, e12410. [CrossRef]
5. Zhong, Y.; Xu, X.; Veder, J.-P.; Shao, Z. Self—Recovery Chemistry and Cobalt—Catalyzed Electrochemical Deposition of Cathode for Boosting Performance of Aqueous Zinc—Ion Batteries. *iScience* **2020**, *23*, 100943. [CrossRef]
6. Zhong, Y.; Xu, X.; Liu, P.; Ran, R.; Jiang, S.P.; Wu, H.; Shao, Z. A Function—Separated Design of Electrode for Realizing High—Performance Hybrid Zinc Battery. *Adv. Energy Mater.* **2020**, *10*, 2002992. [CrossRef]
7. Zhong, Y.; Cao, C.; Zhao, L.; Tadé, M.O.; Shao, Z. Optimization of two—dimensional solid—state electrolyte–anode interface by integrating zinc into composite anode with dual—conductive phases. *Green Carbon* **2024**, *2*, 94–100. [CrossRef]
8. Gao, Y.-M.; Liu, Y.; Feng, K.-J.; Ma, J.-Q.; Miao, Y.-J.; Xu, B.-R.; Pan, K.-M.; Akiyoshi, O.; Wang, G.-X.; Zhang, K.-K.; et al. Emerging WS2/WSe2@graphene nanocomposites: Synthesis and electrochemical energy storage applications. *Rare Met.* **2024**, *43*, 1–19. [CrossRef]
9. Tang, B.; Shan, L.; Liang, S.; Zhou, J. Issues and opportunities facing aqueous zinc—ion batteries. *Energy Environ. Sci.* **2019**, *12*, 3288–3304. [CrossRef]
10. Wang, T.; Li, C.; Xie, X.; Lu, B.; He, Z.; Liang, S.; Zhou, J. Anode Materials for Aqueous Zinc Ion Batteries: Mechanisms, Properties, and Perspectives. *ACS Nano* **2020**, *14*, 16321–16347. [CrossRef]

11. Xu, B.-R.; Li, Q.-A.; Liu, Y.; Wang, G.-B.; Zhang, Z.-H.; Ren, F.-Z. Urea—induced interfacial engineering enabling highly reversible aqueous zinc—ion battery. *Rare Met.* **2024**, *43*, 1599–1609. [CrossRef]
12. Xu, B.; Wang, G.; Liu, Y.; Li, Q.; Ren, F.; Ma, J. Co—regulation effect of solvation and interface of pyridine derivative enabling highly reversible zinc anode. *J. Mater. Sci. Technol.* **2025**, *204*, 1–9. [CrossRef]
13. Yang, W.; Yang, Y.; Yang, H.; Zhou, H. Regulating Water Activity for Rechargeable Zinc—Ion Batteries: Progress and Perspective. *ACS Energy Lett.* **2022**, *7*, 2515–2530. [CrossRef]
14. Cheng, H.; Sun, Q.; Li, L.; Zou, Y.; Wang, Y.; Cai, T.; Zhao, F.; Liu, G.; Ma, Z.; Wahyudi, W.; et al. Emerging Era of Electrolyte Solvation Structure and Interfacial Model in Batteries. *ACS Energy Lett.* **2022**, *7*, 490–513. [CrossRef]
15. Nian, Q.; Zhang, X.; Feng, Y.; Liu, S.; Sun, T.; Zheng, S.; Ren, X.; Tao, Z.; Zhang, D.; Chen, J. Designing Electrolyte Structure to Suppress Hydrogen Evolution Reaction in Aqueous Batteries. *ACS Energy Lett.* **2021**, *6*, 2174–2180. [CrossRef]
16. Huang, Q.-X.; Wang, F.; Liu, Y.; Zhang, B.-Y.; Guo, F.-Y.; Jia, Z.-Q.; Wang, H.; Yang, T.-X.; Wu, H.-T.; Ren, F.-Z.; et al. Recent progress of two—dimensional metal—base catalysts in urea oxidation reaction. *Rare Met.* **2024**, *43*, 3607–3633. [CrossRef]
17. Zheng, J.; Huang, Z.; Ming, F.; Zeng, Y.; Wei, B.; Jiang, Q.; Qi, Z.; Wang, Z.; Liang, H. Surface and Interface Engineering of Zn Anodes in Aqueous Rechargeable Zn—Ion Batteries. *Small* **2022**, *18*, 2200006. [CrossRef] [PubMed]
18. Liu, B.; Wang, S.; Wang, Z.; Lei, H.; Chen, Z.; Mai, W. Novel 3D Nanoporous Zn–Cu Alloy as Long—Life Anode toward High—Voltage Double Electrolyte Aqueous Zinc—Ion Batteries. *Small* **2020**, *16*, 2001323. [CrossRef] [PubMed]
19. Guo, N.; Huo, W.; Dong, X.; Sun, Z.; Lu, Y.; Wu, X.; Dai, L.; Wang, L.; Lin, H.; Liu, H.; et al. A Review on 3D Zinc Anodes for Zinc Ion Batteries. *Small Methods* **2022**, *6*, 2200597. [CrossRef]
20. Zhai, P.; Zhai, X.; Jia, Z.; Zhang, W.; Pan, K.; Liu, Y. Inhibiting corrosion and side reactions of zinc metal anode by nano—$CaSiO_3$ coating towards high—performance aqueous zinc—ion batteries. *Nanotechnology* **2023**, *34*, 085402. [CrossRef]
21. Shi, G.; Peng, X.; Zeng, J.; Zhong, L.; Sun, Y.; Yang, W.; Zhong, Y.L.; Zhu, Y.; Zou, R.; Admassie, S.; et al. A Liquid Metal Microdroplets Initialized Hemicellulose Composite for 3D Printing Anode Host in Zn—Ion Battery. *Adv. Mater.* **2023**, *35*, 2300109. [CrossRef] [PubMed]
22. Wang, Y.; Li, Q.; Hong, H.; Yang, S.; Zhang, R.; Wang, X.; Jin, X.; Xiong, B.; Bai, S.; Zhi, C. Lean—water hydrogel electrolyte for zinc ion batteries. *Nat. Commun.* **2023**, *14*, 3890. [CrossRef] [PubMed]
23. Chen, P.; Sun, X.; Pietsch, T.; Plietker, B.; Brunner, E.; Ruck, M. Electrolyte for High—Energy—and Power—Density Zinc Batteries and Ion Capacitors. *Adv. Mater.* **2023**, *35*, 2207131. [CrossRef] [PubMed]
24. Meng, C.; He, W.; Kong, Z.; Liang, Z.; Zhao, H.; Lei, Y.; Wu, Y.; Hao, X. Multifunctional water—organic hybrid electrolyte for rechargeable zinc ions batteries. *Chem. Eng. J.* **2022**, *450*, 138265. [CrossRef]
25. Wang, M.; Wu, X.; Yang, D.; Zhao, H.; He, L.; Su, J.; Zhang, X.; Yin, X.; Zhao, K.; Wang, Y.; et al. A colloidal aqueous electrolyte modulated by oleic acid for durable zinc metal anode. *Chem. Eng. J.* **2023**, *451*, 138589. [CrossRef]
26. Tay, I.R.; Xue, J.; Lee, W.S.V. Methods for Characterizing Intercalation in Aqueous Zinc Ion Battery Cathodes: A Review. *Adv. Sci.* **2023**, *10*, 2303211. [CrossRef] [PubMed]
27. Du, Y.; Li, Y.; Xu, B.B.; Liu, T.X.; Liu, X.; Ma, F.; Gu, X.; Lai, C. Electrolyte Salts and Additives Regulation Enables High Performance Aqueous Zinc Ion Batteries: A Mini Review. *Small* **2022**, *18*, e2104640. [CrossRef] [PubMed]
28. Guo, X.; Zhang, Z.; Li, J.; Luo, N.; Chai, G.-L.; Miller, T.S.; Lai, F.; Shearing, P.; Brett, D.J.L.; Han, D.; et al. Alleviation of Dendrite Formation on Zinc Anodes via Electrolyte Additives. *ACS Energy Lett.* **2021**, *6*, 395–403. [CrossRef]
29. An, Y.; Tian, Y.; Zhang, K.; Liu, Y.; Liu, C.; Xiong, S.; Feng, J.; Qian, Y. Stable Aqueous Anode—Free Zinc Batteries Enabled by Interfacial Engineering. *Adv. Funct. Mater.* **2021**, *31*, 2101886. [CrossRef]
30. Yin, J.; Liu, H.; Li, P.; Feng, X.; Wang, M.; Huang, C.; Li, M.; Su, Y.; Xiao, B.; Cheng, Y.; et al. Integrated electrolyte regulation strategy: Trace trifunctional tranexamic acid additive for highly reversible Zn metal anode and stable aqueous zinc ion battery. *Energy Storage Mater.* **2023**, *59*, 102800. [CrossRef]
31. Zhang, H.; Guo, R.; Li, S.; Liu, C.; Li, H.; Zou, G.; Hu, J.; Hou, H.; Ji, X. Graphene quantum dots enable dendrite—free zinc ion battery. *Nano Energy* **2022**, *92*, 106752. [CrossRef]
32. Liu, Z.; Wang, R.; Ma, Q.; Wan, J.; Zhang, S.; Zhang, L.; Li, H.; Luo, Q.; Wu, J.; Zhou, T.; et al. A Dual—Functional Organic Electrolyte Additive with Regulating Suitable Overpotential for Building Highly Reversible Aqueous Zinc Ion Batteries. *Adv. Funct. Mater.* **2024**, *34*, 2214538. [CrossRef]
33. Feng, D.; Cao, F.; Hou, L.; Li, T.; Jiao, Y.; Wu, P. Immunizing Aqueous Zn Batteries against Dendrite Formation and Side Reactions at Various Temperatures via Electrolyte Additives. *Small* **2021**, *17*, 2103195. [CrossRef] [PubMed]
34. Zeng, X.; Xie, K.; Liu, S.; Zhang, S.; Hao, J.; Liu, J.; Pang, W.K.; Liu, J.; Rao, P.; Wang, Q.; et al. Bio—inspired design of an in situ multifunctional polymeric solid–electrolyte interphase for Zn metal anode cycling at 30 mA cm^{-2} and 30 mA h cm^{-2}. *Energy Environ. Sci.* **2021**, *14*, 5947–5957. [CrossRef]
35. Wang, H.; Ye, W.; Yin, B.; Wang, K.; Riaz, M.S.; Xie, B.-B.; Zhong, Y.; Hu, Y. Modulating Cation Migration and Deposition with Xylitol Additive and Oriented Reconstruction of Hydrogen Bonds for Stable Zinc Anodes. *Angew. Chem. Int. Ed.* **2023**, *62*, e202218872. [CrossRef] [PubMed]
36. Qin, R.; Wang, Y.; Zhang, M.; Wang, Y.; Ding, S.; Song, A.; Yi, H.; Yang, L.; Song, Y.; Cui, Y.; et al. Tuning Zn^{2+} coordination environment to suppress dendrite formation for high—performance Zn—ion batteries. *Nano Energy* **2021**, *80*, 105478. [CrossRef]
37. Zha, Z.; Sun, T.; Li, D.; Ma, T.; Zhang, W.; Tao, Z. Zwitterion as electrical double layer regulator to in—situ formation of fluorinated interphase towards stable zinc anode. *Energy Storage Mater.* **2024**, *64*, 103059. [CrossRef]

38. Li, L.; Jia, S.-F.; Cao, M.-H.; Ji, Y.-Q.; Qiu, H.-W.; Zhang, D. Progress in research on metal—based materials in stabilized Zn anodes. *Rare Metals* **2024**, *43*, 20–40. [CrossRef]
39. Ni, G.; Pan, Z.; Zou, G.; Cao, F.; Qin, L.; Cui, P.; Zhou, C. A multifunctional phenylalanine additive stabilizing zinc anodes in aqueous zinc ion batteries. *J. Mater. Chem. A* **2024**, *12*, 6610–6622. [CrossRef]
40. Gou, Q.; Luo, H.; Zhang, Q.; Deng, J.; Zhao, R.; Odunmbaku, O.; Wang, L.; Li, L.; Zheng, Y.; Li, J.; et al. Electrolyte Regulation of Bio—Inspired Zincophilic Additive toward High—Performance Dendrite—Free Aqueous Zinc—Ion Batteries. *Small* **2023**, *19*, 2207502. [CrossRef]
41. Wu, Z.; Li, M.; Tian, Y.; Chen, H.; Zhang, S.-J.; Sun, C.; Li, C.; Kiefel, M.; Lai, C.; Lin, Z.; et al. Cyclohexanedodecol—Assisted Interfacial Engineering for Robust and High—Performance Zinc Metal Anode. *Nanomicro Lett.* **2022**, *14*, 110. [CrossRef] [PubMed]
42. Yan, Q.; Hu, Z.; Liu, Z.; Wu, F.; Zhao, Y.; Chen, R.; Li, L. Synergistic interaction between amphiphilic ion additive groups for stable long—life zinc ion batteries. *Energy Storage Mater.* **2024**, *67*, 103299. [CrossRef]
43. Li, T.C.; Lim, Y.; Li, X.L.; Luo, S.; Lin, C.; Fang, D.; Xia, S.; Wang, Y.; Yang, H.Y. A Universal Additive Strategy to Reshape Electrolyte Solvation Structure toward Reversible Zn Storage. *Adv. Energy Mater.* **2022**, *12*, 2103231. [CrossRef]
44. Zhi, L.; Li, T.; Liu, X.; Yuan, Z.; Li, X. Functional complexed zincate ions enable dendrite—free long cycle alkaline zinc—based flow batteries. *Nano Energy* **2022**, *102*, 107697. [CrossRef]
45. Cai, S.; Chu, X.; Liu, C.; Lai, H.; Chen, H.; Jiang, Y.; Guo, F.; Xu, Z.; Wang, C.; Gao, C. Water–Salt Oligomers Enable Supersoluble Electrolytes for High—Performance Aqueous Batteries. *Adv. Mater.* **2021**, *33*, 2007470. [CrossRef] [PubMed]
46. Liu, Y.; Feng, K.; Han, J.; Wang, F.; Xing, Y.; Tao, F.; Li, H.; Xu, B.; Ji, J.; Li, H. Regulation of Zn^{2+} solvation shell by a novel N—methylacetamide based eutectic electrolyte toward high—performance zinc—ion batteries. *J. Mater. Sci. Technol.* **2025**, *211*, 53–61. [CrossRef]
47. Ivanova, B.; Spiteller, M. Electrospray ionization stochastic dynamic mass spectrometric 3D structural analysis of ZnII–ion containing complexes in solution. *Inorg. Nano—Met. Chem.* **2022**, *52*, 1407–1429. [CrossRef]
48. Ivanova, B.; Spiteller, M. Crystallographic and theoretical study of the atypical distorted octahedral geometry of the metal chromophore of zinc(II) bis((1R,2R)-1,2-diaminocyclohexane) dinitrate. *J. Mol. Struct.* **2022**, *1248*, 131488. [CrossRef]
49. Bayaguud, A.; Luo, X.; Fu, Y.; Zhu, C. Cationic Surfactant-Type Electrolyte Additive Enables Three-Dimensional Dendrite-Free Zinc Anode for Stable Zinc-Ion Batteries. *ACS Energy Lett.* **2020**, *5*, 3012–3020. [CrossRef]
50. Lu, H.; Zhang, X.; Luo, M.; Cao, K.; Lu, Y.; Xu, B.; Pan, H.; Tao, K.; Jiang, Y. Amino Acid-Induced Interface Charge Engineering Enables Highly Reversible Zn Anode. *Adv. Funct. Mater.* **2021**, *31*, 2103514. [CrossRef]
51. Wang, F.; Lu, H.; Zhu, H.; Wang, L.; Chen, Z.; Yang, C.; Yang, Q.-H. Mitigating the interfacial concentration gradient by negatively charged quantum dots toward dendrite—free Zn anodes. *Energy Storage Mater.* **2023**, *58*, 215–221. [CrossRef]
52. Xiao, J.; Li, Q.; Bi, Y.; Cai, M.; Dunn, B.; Glossmann, T.; Liu, J.; Osaka, T.; Sugiura, R.; Wu, B.; et al. Understanding and applying coulombic efficiency in lithium metal batteries. *Nat. Energy* **2020**, *5*, 561–568. [CrossRef]
53. Ma, Q.; Gao, R.; Liu, Y.; Dou, H.; Zheng, Y.; Or, T.; Yang, L.; Li, Q.; Cu, Q.; Feng, R.; et al. Regulation of Outer Solvation Shell Toward Superior Low—Temperature Aqueous Zinc—Ion Batteries. *Adv. Mater.* **2022**, *34*, 2207344. [CrossRef] [PubMed]
54. Liu, J.; Song, W.; Wang, Y.; Wang, S.; Zhang, T.; Cao, Y.; Zhang, S.; Xu, C.; Shi, Y.; Niu, J.; et al. A polyamino acid with zincophilic chains enabling high—performance Zn anodes. *J. Mater. Chem. A* **2022**, *10*, 20779–20786. [CrossRef]
55. Zhong, Y.; Cheng, Z.; Zhang, H.; Li, J.; Liu, D.; Liao, Y.; Meng, J.; Shen, Y.; Huang, Y. Monosodium glutamate, an effective electrolyte additive to enhance cycling performance of Zn anode in aqueous battery. *Nano Energy* **2022**, *98*, 107220. [CrossRef]
56. Yu, Y.; Zhang, P.; Wang, W.; Liu, J. Tuning the Electrode/Electrolyte Interface Enabled by a Trifunctional Inorganic Oligomer Electrolyte Additive for Highly Stable and High—Rate Zn Anodes. *Small Methods* **2023**, *7*, e2300546. [CrossRef] [PubMed]
57. Han, D.; Wang, Z.; Lu, H.; Li, H.; Cui, C.; Zhang, Z.; Sun, R.; Geng, C.; Liang, Q.; Guo, X.; et al. A Self—Regulated Interface toward Highly Reversible Aqueous Zinc Batteries. *Adv. Energy. Mater.* **2022**, *12*, 2102982. [CrossRef]
58. Zhang, Q.; Luan, J.; Huang, X.; Wang, Q.; Sun, D.; Tang, Y.; Ji, X.; Wang, H. Revealing the role of crystal orientation of protective layers for stable zinc anode. *Nat. Commun.* **2020**, *11*, 3961. [CrossRef] [PubMed]
59. Zhang, S.-J.; Hao, J.; Luo, D.; Zhang, P.-F.; Zhang, B.; Davey, K.; Lin, Z.; Qiao, S.-Z. Dual—Function Electrolyte Additive for Highly Reversible Zn Anode. *Adv. Energy Mater.* **2021**, *11*, 2102010. [CrossRef]
60. Jin, Y.; Han, K.S.; Shao, Y.; Sushko, M.; Xiao, J.; Pan, H.; Liu, W. Stabilizing Zinc Anode Reactions by Polyethylene Oxide Polymer in Mild Aqueous Electrolytes. *Adv. Funct. Mater* **2020**, *30*, 2003932. [CrossRef]
61. Wang, B.; Zheng, R.; Yang, W.; Han, X.; Hou, C.; Zhang, Q.; Li, Y.; Li, K.; Wang, H. Synergistic Solvation and Interface Regulations of Eco—Friendly Silk Peptide Additive Enabling Stable Aqueous Zinc—Ion Batteries. *Adv. Funct. Mater.* **2022**, *32*, 2112693. [CrossRef]
62. Deng, C.; Xie, X.; Han, J.; Lu, B.; Liang, S.; Zhou, J. Stabilization of Zn Metal Anode through Surface Reconstruction of a Cerium—Based Conversion Film. *Adv. Funct. Mater.* **2021**, *31*, 2103227. [CrossRef]
63. Zhou, X.; Li, X.; Li, Z.; Fu, J.; Xu, S.; Zhou, W.; Gui, S.; Wei, L.; Yang, H.; Wu, J.-F.; et al. Ten micrometer thick polyethylene separator modified by α—$LiAlO_2$@γ—Al_2O_3 nanosheets for simultaneous suppression of Li dendrite growth and polysulfide shuttling in Li—S batteries. *Mater. Today Energy* **2022**, *26*, 100990. [CrossRef]
64. Ren, K.; Li, M.; Wang, Q.; Liu, B.; Sun, C.; Yuan, B.; Lai, C.; Jiao, L.; Wang, C. Thioacetamide Additive Homogenizing Zn Deposition Revealed by In Situ Digital Holography for Advanced Zn Ion Batteries. *Nanomicro Lett.* **2024**, *16*, 117. [CrossRef] [PubMed]

65. Duan, A.; Luo, S.; Sun, W. Insight into the development of electrolytes for aqueous zinc metal batteries from alkaline to neutral. *Chin. Chem. Lett.* **2024**, *35*, 108337. [CrossRef]
66. Sun, M.; Wang, Z.; Jiang, J.; Wang, X.; Yu, C. Gelation mechanisms of gel polymer electrolytes for zinc—based batteries. *Chin. Chem. Lett.* **2024**, *35*, 109393. [CrossRef]
67. Delley, B. Hardness conserving semilocal pseudopotentials. *Phys. Rev. B* **2002**, *66*, 155125. [CrossRef]
68. Perdew, J.P.; Burke, K.; Ernzerhof, M. Generalized Gradient Approximation Made Simple. *Phys. Rev. Lett.* **1996**, *77*, 3865–3868. [CrossRef] [PubMed]
69. Delley, B. From molecules to solids with the DMol3 approach. *J. Chem. Phys.* **2000**, *113*, 7756–7764. [CrossRef]
70. Grimme, S. Semiempirical GGA—type density functional constructed with a long—range dispersion correction. *J. Comput. Chem.* **2006**, *27*, 1787–1799. [CrossRef]
71. Lu, T.; Chen, F. Quantitative analysis of molecular surface based on improved Marching Tetrahedra algorithm. *J. Mol. Graphics Modell.* **2012**, *38*, 314–323. [CrossRef] [PubMed]
72. Humphrey, W.; Dalke, A.; Schulten, K. VMD: Visual molecular dynamics. *J. Mol. Graphics Modell.* **1996**, *14*, 33–38. [CrossRef] [PubMed]

Disclaimer/Publisher's Note: The statements, opinions and data contained in all publications are solely those of the individual author(s) and contributor(s) and not of MDPI and/or the editor(s). MDPI and/or the editor(s) disclaim responsibility for any injury to people or property resulting from any ideas, methods, instructions or products referred to in the content.

molecules

MDPI

Review

Opportunities and Challenges of Multi-Ion, Dual-Ion and Single-Ion Intercalation in Phosphate-Based Polyanionic Cathodes for Zinc-Ion Batteries

Lei Cao [1], Tao Du [1,2,*], Hao Wang [1], Zhen-Yu Cheng [1], Yi-Song Wang [1] and Li-Feng Zhou [1,*]

[1] State Environmental Protection Key Laboratory of Eco-Industry, School of Metallurgy, Northeastern University, Shenyang 110819, China; 2371880@stu.neu.edu.cn (L.C.); 2201664@stu.neu.edu.cn (H.W.); 2310690@stu.neu.edu.cn (Z.-Y.C.); wangys@smm.neu.edu.cn (Y.-S.W.)

[2] Engineering Research Center of Frontier Technologies for Low-Carbon Steelmaking (Ministry of Education), School of Metallurgy, Northeastern University, Shenyang 110819, China

* Correspondence: dut@smm.neu.edu.cn (T.D.); zhoulf@smm.neu.edu.cn (L.-F.Z.)

Abstract: Abstract: With the continuous development of science and technology, battery storage systems for clean energy have become crucial for global economic transformation. Among various rechargeable batteries, lithium-ion batteries are widely used, but face issues like limited resources, high costs, and safety concerns. In contrast, zinc-ion batteries, as a complement to lithium-ion batteries, are drawing increasing attention. In the exploration of zinc-ion batteries, especially of phosphate-based cathodes, the battery action mechanism has a profound impact on the battery performance. In this paper, we first review the interaction mechanism of multi-ion, dual-ion, and single-ion water zinc batteries. Then, the impact of the above mechanisms on battery performance was discussed. Finally, the application prospects of the effective use of multi-ion, dual-ion, and single-ion intercalation technology in zinc-ion batteries is reviewed, which has significance for guiding the development of rechargeable water zinc-ion batteries in the future.

Keywords: phosphate-based polyanionic cathode; intercalation/deintercalation mechanisms; zinc-ion batteries

1. Introduction

Energy and the environment are two major issues that must be addressed for the survival of humanity and the development of society today [1]. The continuous depletion of fossil fuels has made energy shortages a significant problem. Thus, there is an urgent need to develop and utilize new types of energy sources [2]. Electrochemical energy sources with high energy and high power have attracted people's attention [3]. Battery storage systems powered by clean energy are crucial for the global economic transition related to carbon neutrality and carbon peaking [4]. Rechargeable batteries have broad application prospects in electric vehicles, mobile devices, and renewable energy sources [5]. The future of the renewable energy integrated grid system requires low-cost, high-safety, and long-cycle-life rechargeable batteries [6]. Among the many rechargeable batteries, lithium-ion batteries are more widely used; however, the problems of limited lithium-ion battery resources [7], high cost, and poor safety [8] have attracted increasing attention. Therefore, finding a new element to supplement lithium-ion batteries has become an urgent issue. Table 1 shows that the atomic radius of zinc is similar to that of lithium. Additionally, zinc has excellent electrochemical properties, with a lower electrode potential and a larger volumetric capacity, making it an attractive option for new types of batteries. Consequently, zinc has gradually received attention. In recent years, zinc-ion batteries have gained traction due to their abundant reserves, low cost, low toxicity, and low electrode potential [9].

Table 1. Comparison of common battery anode elements and their electrochemical properties.

Working Ion	Ionic Radii (Å)	Electrode Potential vs. SHE (V)	Specific Gravimetric Capacity ($mAh \cdot g^{-1}$)	Specific Volumetric Capacity ($mAh \cdot g^{-1}$)
Li^+	0.76	−3.04	3862	2066
Na^+	1.02	−2.71	1166	1129
K^+	1.38	−2.93	685	586
Mg^{2+}	0.72	−2.37	2205	3832
Zn^{2+}	0.74	−0.76	820	5855
Al^{3+}	0.535	−1.66	2980	8046

Aqueous rechargeable batteries use aqueous electrolytes [10]. Compared to conventional lithium-ion and lead-acid batteries, aqueous rechargeable batteries have unique advantages [11]. The aqueous electrolytes used in these batteries have a lower risk of combustion and higher thermal stability than organic solution electrolytes, enhancing battery safety [12]. Their high energy density allows them to store more energy and provide longer operating times [13]. Among the many cathode materials, polyanionic materials are categorized into silicates, phosphates, pyrophosphates, sulfates, and hybrid polyanionic compounds based on the type of anionic groups [14]. Polyanionic compounds have the general formula $A_xB_y(MO_n)_z$, where A stands for alkaline elements (Li, Na, K), B stands for metals (Mn, Ni, Cu, Co, or Zn), and M stands for P, S, Si, Mo, W. These compounds usually consist of BO_6 octahedra and MO_4 tetrahedra sharing oxygen atoms [15]. Compared to transition metal oxides, polyanionic compounds have gained research interest due to their multidimensional ionic diffusion channels, high structural stability during charging and discharging, and tunable intercalation/deintercalation platforms [16]. Currently, the electrodes available in aqueous rechargeable batteries are mainly phosphate-based polyanionic compounds [9], such as $Na_3V_2(PO_4)_3$ [17], $VOPO_4$ [18], and so on, which are composed of aqueous systems with zinc-ion batteries. Compared with other materials, phosphate-based polyanionic cathode materials have unique advantages. For one thing, because of the limitation of water splitting potential, most cathodes could be incompatible with an aqueous rechargeable battery system. By introducing polyanionic groups into a transition metal oxide framework (i.e., inductive effect), the operation potential can be adjusted owing to the bonding strength and covalency of metal−oxygen (M-O). On the other hand. phosphate-based polyanionic cathode materials show high stability again moisture compared to layered oxide cathodes, which boosts the chemical stability of materials. Zinc-ion batteries have received widespread attention in recent years. Analyzing these batteries can explore the performance of cathode materials, determine the mechanism of zinc-ion batteries, and contribute to improving their efficiency.

Multi-ion insertion is a key feature of batteries that can enhance their performance and application areas [19]. The joint action of multiple ions accelerates charge transfer between the positive and negative electrodes, resulting in a higher energy density and faster charge and discharge rates. However, multi-ion insertion also presents challenges, such as side reactions that affect battery performance and structural changes within the battery. Meanwhile, dual-ion insertion and single-ion insertion also have their special advantages and disadvantages. Therefore, a comparative discussion of the insertion of these three types of ions for can help us clarify the ion mechanism of the battery. To facilitate the discussion, these mechanisms are classified in this paper by dividing the action mechanisms of rechargeable zinc batteries into three categories: multi-ion insertion mechanism, dual-ion insertion mechanism, and single-ion insertion mechanism. Under these mechanisms, we discuss the capacity division among multiple ions, the hybrid insertion mechanism of dual ions, and the high electrolyte concentration and H+-free action of single ions. The main relationships are shown in Figure 1, The innermost layer of Figure 1 is a reaction schematic of zinc-ion batteries, and the first layer of circles is the insertion mechanisms of zinc-ion batteries, categorized in this paper as multi-ion insertion mechanism, dual-ion insertion mechanism, and single-ion insertion mechanism. The second layer are the issues worth focusing on corresponding to the above insertion mechanisms, such as the capacity division problem of multiple ions, the hybrid insertion mechanism of dual ions, and the high electrolyte concentration and H^+-free action of single ions. The outermost layer is a summary of the main ideas, which are rechargeable zinc-ion batteries and ionic insertion mechanisms. Ions play a crucial role in aqueous rechargeable zinc batteries, affecting performance and cycle life. This review first summarizes the mechanisms of different ions in these batteries. Then, the mechanisms are systematically classified and comparatively analyzed. Finally, the effective utilization of different ions is discussed to guide the development of water-based rechargeable zinc batteries in the future.

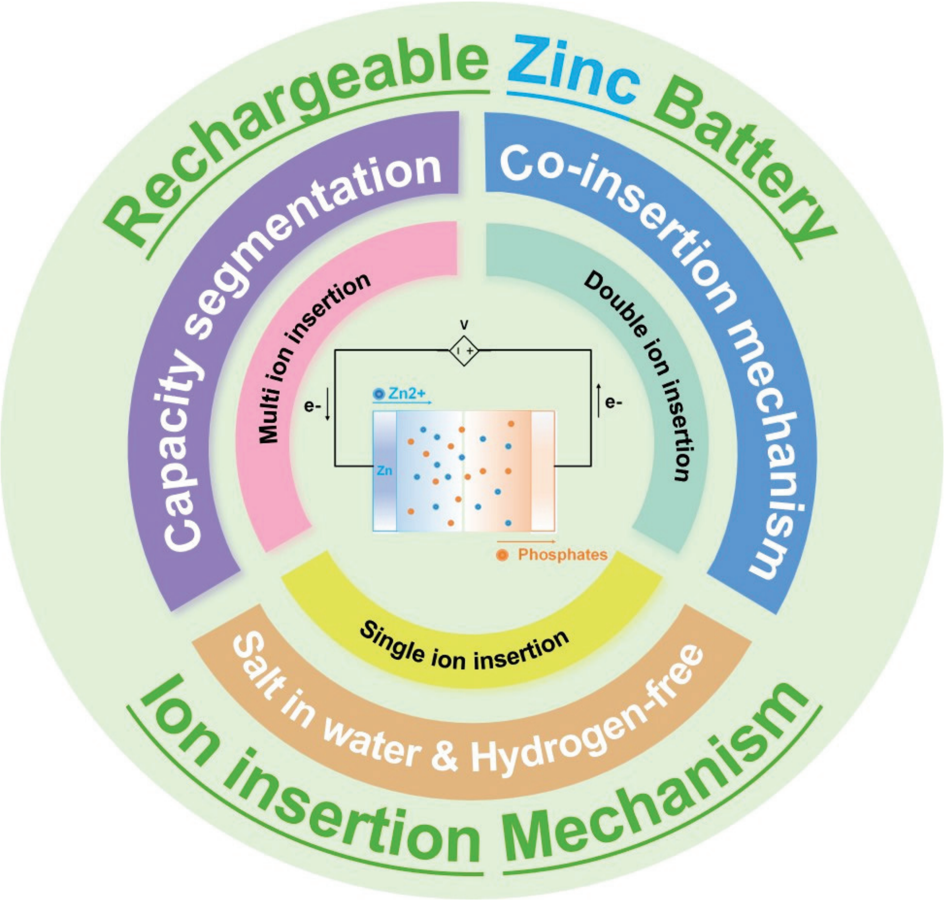

Figure 1. Schematic representation of multiple ion insertion mechanisms in rechargeable zinc phosphate-based batteries.

2. Ion Insertion Mechanism of Rechargeable Zinc Batteries

As shown in Figure 2, the schematic diagrams of batteries with different cationic interactions are presented, along with their advantages and disadvantages. Among them, as shown in the middle row, is the schematic diagram of multi-ion insertion, dual-ion insertion, and single-ion insertion batteries; the row above is the corresponding advantages of these three insertion mechanisms; and the row below is their corresponding disadvantages. The comparison of batteries with different insertion mechanisms provides theoretical support for our discussion. In the case of multiple ions acting together, H^+ is present. In contrast, with single-ion action, the active element in the cell is free of H^+, with Zn^{2+} as its main component. Due to the roles of different ions, the battery exhibits various electrochemical properties. Common cathode materials for zinc-ion batteries and their electrochemical properties are shown in Table 2. There is a significant difference in the performance of different cathode materials under the same electrolyte, and the same cathode material can exhibit varying properties under different electrolytes. Therefore, when exploring battery performance, it is challenging to initially determine the main conditions affecting it due to the variety of factors at play. To facilitate discussion, ion interactions in rechargeable zinc batteries can be categorized into three types: co-action of multiple cations, co-action of dual cations, and the action of a single cation.

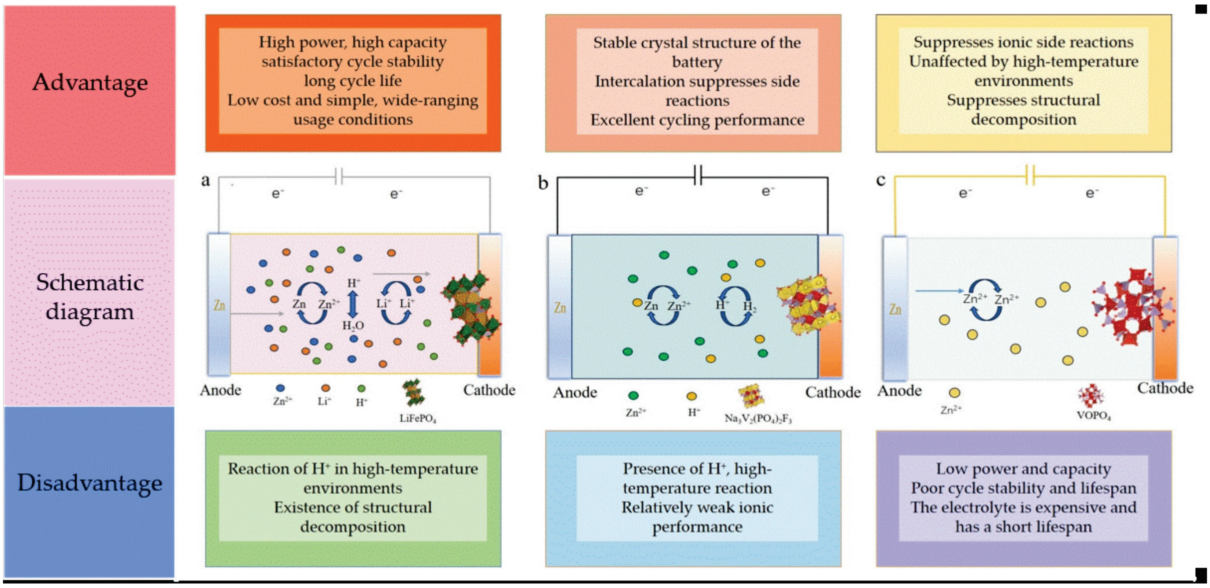

Figure 2. Schematic diagram of different batteries and their advantages and disadvantages. (**a**) Schematic diagram of Zn-$LiFePO_4$ aqueous rechargeable battery; (**b**) schematic diagram of Zn-$Na_3V_2(PO_4)_2F_3$ aqueous rechargeable battery; and (**c**) schematic diagram of Zn-$VOPO_4$ rechargeable battery in the electrolyte 21 M LiTFSI/1 M Zn $(Tr)_2$ solution.

Table 2. Different zinc-ion battery cathode materials and their electrochemical properties.

Cathode	Electrolyte	Voltage/V	Capacity/mAh·g^{-1}	Retention%/Cycles	Number (Acting Ions)	Ref.
$LiFePO_4$	1 M LiOTf + 1 M Zn $(OTf)_2$ + SDBS	0.9–1.4 V	158 (0.5 C)	88.6% at 1 C (100)	3 (Zn^{2+}, Li^+, H^+)	[20]
$LiFePO_4$	4 M $Zn(OTf)_2$ + 2 M $LiClO_4$	0.9–1.4 V	165 (0.2 C)	90% at 0.2 C (285)	2 (Zn^{2+}, H^+)	[21]
$Li_3V_2(PO_4)_3$	1 M Li_2SO_4 + 2 M $ZnSO_4$	0.7–2.1 V	131 (0.2 C)	85.4% at 0.2 C (200)	3 (Zn^{2+}, Li^+, H^+)	[22]
$Na_3V_2(PO_4)_3$	0.5 M $Zn(CH_3COO)_2$	0.8–1.7 V	92 (0.5 C)	74.0% at 0.5 C (100)	3 (Zn^{2+}, Na^+, H^+)	[23]
$Na_3V_2(PO_4)_3$	2 M $Zn(OTf)_2$	0.6–1.8 V	114 (0.05 A·g^{-1})	75.0% at 0.5 A·g^{-1} (200)	3 (Zn^{2+}, Na^+, H^+)	[24]
$Na_3V_2(PO_4)_2F_3$	2 M $Zn(OTf)_2$	0.8–1.9 V	65 (0.08 A·g^{-1})	98.0% at 0.2 A·g^{-1} (600)	2 (Zn^{2+}, H^+)	[25]
$Na_3V_2(PO_4)_2F_3$	3 M $Zn(OTf)_2$	0.2–2.0 V	100 (0.2C)	90.0% at 0.2C (600)	2 (Zn^{2+}, H^+)	[26]
$VOPO_4{\cdot}2H_2O$	21 M LiTFSI + 1 M $Zn(Tr)_2$	0.8–2.1 V	139 (0.1 A·g^{-1})	93.0% at 1 A·g^{-1} (1000)	1 (Zn^{2+})	[27]
$VOPO_4{\cdot}xH_2O$	13 M $ZnCl_2$ + 0.8 M H_3PO_4	0.7–1.9 V	170 (0.1 A·g^{-1})	91.8% at 2 A·g^{-1} (500)	1 (Zn^{2+})	[28]

Table 2. *Cont.*

Cathode	Electrolyte	Voltage/V	Capacity/mAh·g^{-1}	Retention%/Cycles	Number (Acting Ions)	Ref.
$VOPO_4$	4 M $Zn(OTf)_2$ + 0.5 M Me_3EtOTf	0.2–1.9 V	163 (0.05 A·g^{-1})	88.7% at 2 A·g^{-1} (6000)	1 (Zn^{2+})	[29]
$MgV_2O_6{\cdot}1.7H_2O$	0.1 M $Zn(OTf)_2$ in anhydrous acetonitrile + 1% vol water	0.3–1.4 V	425.7 mAh·g^{-1} at 0.2 A·g^{-1}	97% at 0.2 A·g^{-1} (50)	2 (Zn^{2+}, H^+)	[30]

2.1. Multi-Ion Insertion Mechanism of Rechargeable Zinc Batteries

During the charge and discharge processes of rechargeable zinc batteries, multiple ions interact simultaneously. The behavior and properties of ions inside batteries are influenced by multiple factors [31]. Therefore, it is necessary to consider the interactions and effects of various ions comprehensively when discussing the battery mechanism. The electrochemical charge storage mechanism in aqueous zinc-ion batteries is generally the reversible insertion of Zn^{2+} into the host material [32]. This is also the primary mechanism for most polyanion compounds. As shown in Figure 2a, in the rechargeable battery composed of $LiFePO_4$ and Zn, during discharge, Li^+ ions in the mixed electrolyte generate $LiFePO_4$ and insert into the heterostructure ($FePO_4$). Simultaneously, zinc metal loses electrons, forming Zn^{2+} ions that migrate back to the electrolyte.

The primary working mechanism of Zn-$LiFePO_4$ can be represented by the following equations:

$$\text{Cathode, } LiFePO_4 \leftrightarrow e^- + Li^+ + FePO_4; \tag{1}$$

$$\text{Anode, } Zn^{2+} + 2e^- \leftrightarrow Zn; \tag{2}$$

$$\text{Overall, } 2LiFePO_4 + Zn^{2+} \leftrightarrow 2Li^+ + 2FePO_4 + Zn. \tag{3}$$

Research has found that in aqueous electrolytes with polyanion compounds, an H^+ (or Na^+) insertion often occurs alongside a Zn^{2+} insertion [33]. However, many studies on aqueous zinc-ion batteries do not report on H^+. Despite this, H^+ is commonly present in aqueous batteries. For instance, in the Zn-$LiFePO_4$ battery shown in Figure 2a, an analysis of its electrode potential reveals the presence of H^+. Therefore, during the charge and discharge processes, Zn^{2+}, Li^+, and H^+ ions interact simultaneously. Although Zn^{2+} usually predominates over H^+, there are cases where H^+ plays a similar or even dominant role compared to Zn^{2+} and should not be ignored [34]. For example, Wan et al. [28], by analyzing the differential capacity curve (dQ/dV) of a layered $VOPO_4{\cdot}xH_2O$ cathode in different electrolytes, found that H^+ intercalation dominates in an electrolyte composed of 5 m $ZnCl_2$/0.8 m H_3PO_4. Therefore, when discussing the multi-ion insertion mechanism, it is necessary to clarify which ion plays the primary role among the multiple ions. Sometimes, it is also necessary to discuss the situation in which different ions act under different conditions in the same battery. Park et al. [35] studied the differences in the electrochemical behavior of $Na_3V_2(PO_4)_2F_3$ as a cathode material in non-aqueous and aqueous Zn-ion batteries (ZIBs). Their in situ analysis revealed that the observed differences in electrochemical behavior were due to different storage mechanisms. In non-aqueous ZIBs, Zn^{2+} and Na^+ were initially identified as guest ions, but gradually, only Zn^{2+} was present. In contrast, in aqueous ZIBs, H^+ was found to be the dominant guest ion instead of Zn^{2+}. Therefore, the multi-ion insertion mechanism of the battery should be discussed under various conditions to inspire further exploration of the battery's insertion mechanisms.

2.2. Dual-Ion Insertion Mechanism of Rechargeable Zinc Batteries

In addition to the multi-ion insertion mechanism, aqueous zinc-ion batteries also exhibit a dual-ion insertion mechanism, in which Zn^{2+} and another ion act together. This mechanism is simpler than the multi-ion insertion mechanism, as it involves fewer ionic embedding and de-embedding processes. Consequently, it has gained increasing attention. In aqueous zinc-ion batteries, H^+ is inevitable due to the electrolyte's characteristics, so it must be considered in our discussion. Research has shown that in the electrochemical reaction of open-tunnel or layered cathode materials, there is not only the classical Zn^{2+} insertion/extraction mechanism but also a H^+/Zn^{2+} co-insertion/extraction mechanism [36]. The aqueous Zn-$Na_3V_2(PO_4)_2F_3$ rechargeable battery in Figure 2b is a typical battery with Zn^{2+}/H^+ co-insertion. Li et al. [26] synthesized the carbon nanotube-coated $Na_3V_2(PO_4)_2F_3$ aqueous zinc-ion battery (AZIB) anode material with a continuous and interconnected ion transport channel structure. X-ray diffraction (XRD) and X-ray photoelectron spectroscopy (XPS) revealed the Zn^{2+}/H^+ co-intercalation mechanism. The specific mechanism of the reaction was found to be as follows:

During the first charging process: electrochemical reaction,

$$Na_3(VO)_2(PO_4)_2F \leftrightarrow Na_x(VO)_2(PO_4)_2F + (3-x)Na^+ + (3-x)e^- \tag{4}$$

with the chemical reaction

$$Na_3(VO)_2(PO_4)_2F \leftrightarrow VOPO_4 + \text{amorphous byproducts}, \tag{5}$$

and for electrochemical reactions during subsequent charging and discharging processes,

$$Na_x(VO)_2(PO_4)_2F + yZn^{2+} + z\,H^+ + (2y+z)e^- \leftrightarrow Na_xZn_yH_z(VO)_2(PO_4)_2F \tag{6}$$

$$VOPO_4 + aZn^{2+} + bH^+ + (2a+b)e^- \leftrightarrow Zn_aH_bVOPO_4, \tag{7}$$

The reactions indicate the presence of a Zn^{2+}/H^+ co-insertion layer in the cell, with the electrochemical mechanism involving Zn^{2+} insertion followed by H^+ co-insertion. Optimizing the material structure and morphology and adjusting the electrolyte composition provides new insights for related research. The dual-ion insertion mechanism simplifies the complex interactions of multiple ions, enhancing ion embedding and de-embedding, and improving battery stability. Consequently, the dual-ion co-insertion approach has been progressively refined and adopted in various batteries. For instance, researchers have observed significant Zn^{2+}/H^+ co-insertion in oxide cathodes cycled in aqueous media, whereas Zn^{2+} ions alone often prefer non-oxide materials. This difference may be due to the interface nature, which is typically hydroxyl-terminated and hydrated in most oxides and phosphates in aqueous media [37]. Wang et al. reported a novel vanadium-based oxide cathode based on $MgV_2O_6\cdot1.7H_2O$ nanoribbons. Analysis by X-ray photoelectron spectroscopy (XPS), X-ray diffraction (XRD), and inductively coupled plasma optical emission spectroscopy (ICP-OES) revealed an irreversible Mg^{2+}-Zn^{2+} ion-exchange reaction during the initial discharge, followed by an unusual H^+/Zn^{2+} intercalation reaction. In addition, Tao et al. [38] verified Zn^{2+}/H^+ co-insertion/extraction in hydrated zinc vanadium oxide/carbon cloth (ZnVOH/CC) electrodes by off-site transmission electron microscopy (TEM), off-site XPS, and other characterization methods. These findings demonstrate the practical application of the H^+/Zn^{2+} bi-ionic insertion mechanism, paving the way for further exploration of ionic intercalation in batteries.

2.3. Mechanism of Single-Ion Insertion in Rechargeable Zinc Batteries

H^+/Zn^{2+} co-embedding occurs at the cathode of zinc-ion batteries, but methods to inhibit harmful H^+ embedding are limited [34]. Despite an increased focus on aqueous zinc-ion batteries, several issues have emerged. H^+ ion embedding can balance the insertion and removal processes of Zn^{2+} ions, reduce zinc dendrite formation and electrode polarization, and enhance cycling stability and battery lifetime. However, the H^+ embedding mechanism poses challenges. First, H^+ ion embedding can alter the electrode material's structure, causing volume expansion and contraction, which may lead to material breakage and deactivation. Second, side reactions from water decomposition can generate gases, increasing internal gas pressure. Additionally, H^+ poses safety concerns, especially in high-temperature scenarios, and proton insertion can form layered double hydroxide salts (LDHs), such as $Zn_4SO_4(OH)_6{\cdot}5H_2O$, on the surface of metal oxides [32]. These LDHs form an insulating layer that detaches from the electrode over time, leading to active material loss. To address these issues, there has been a growing emphasis on single-ion insertion mechanisms that exclude H^+ embedding. To inhibit H^+ action, modifications to the electrolyte components are often considered, which is why highly concentrated electrolytes have gained attention [39].

Taking Figure 2c as an example, the Zn/$VOPO_4$ aqueous cell uses a 21 M LiTFSI/1 M $Zn(Tr)_2$ solution as the electrolyte, effectively inhibiting H^+ activity within the cell. The energy storage mechanism can be summarized as follows: in the low voltage region (0.8–1.8 V), Zn^{2+} ions are inserted into and extracted from $VOPO_4$. The redox process of lattice oxygen atoms in $VOPO_4$ is not required for the Zn^{2+} ion insertion/extraction but is instead primarily involved in the insertion/extraction of other ions between 1.8 and 2.1 V [27]. Its reaction mechanism is summarized as follows:

$$\text{Cathode, } Zn_xVOPO_{4-}xZn^{2+} - (2x + y)e^- \leftrightarrow VO^{y+}PO_4; \tag{8}$$

$$\text{Anode, } (x + y/2)Zn^{2+} + (x + y/2)e^- \leftrightarrow (x + y/2)Zn; \tag{9}$$

$$\text{Overall, } Zn_xVOPO_4 + y/2Zn^{2+} \leftrightarrow VO^{y+}PO_4 + (x + y/2)Zn^{2+}. \tag{10}$$

By altering the battery's electrolyte, not only was the role of H^+ intercalation modified, but the reversibility of the crystal structure transformation in $VOPO_4$ during charge/discharge cycles was also enhanced through redox reactions. This improvement resulted in excellent capacity retention and a long-term cycle life. This encouraged us to inhibit the role of H^+ by controlling a series of factors, such as the type of electrolyte and even pH, to ultimately achieve a benign application for the battery mechanism.

3. Ionic Properties of Rechargeable Zinc Batteries

In the previous sections, the effects of various ion embedding and de-embedding on rechargeable zinc batteries were examined. The primary focus of subsequent research should be on how these mechanisms impact battery performance. Our analysis reveals that different ion interactions significantly influence the performance of zinc-ion batteries. To facilitate this analysis, this paper categorizes the ionic effects into three types based on previous work: multi-ionic interaction performance, dual-ionic interaction performance, and single-ionic interaction performance.

3.1. Multi-Ion Interaction Properties

Due to the widespread use of aqueous electrolytes, H^+ is unavoidable in batteries; consequently, multi-ion insertion is commonly observed in aqueous zinc-ion batteries [40]. Moreover, due to multi-ion insertion, the performance of batteries is influenced by various factors, complicating the situation within the batteries. To distinguish the factors affecting battery performance, it is essential to compare different batteries to obtain results that meet our needs and identify the main factors influencing battery performance.

Figure 3a shows the charge–discharge curves of the Zn//CH_3COOLi+ $Zn(CH_3COO)_2$// $LiFePO_4$ hybrid battery at different current rates. The capacity at different rates exhibits a regular gradient change, indicating that the Zn-$LiFePO_4$ system demonstrates stability. The perfect recovery of capacity and high efficiency close to 100% indicate that the system has excellent rate performance and a long cycle life, with a continuous current above 20 °C suggesting substantial power output. During charging, Li^+ is de-inserted from the $FePO_4$ matrix, Zn^{2+} is deposited from the electrolyte, and electrons are gained from the current collector. Conversely, during discharge, the opposite process occurs. The associated processes are illustrated in Equations (1)−(3). The system can provide an output voltage of about 1.2 V, with a high expected capacity, satisfactory rate performance, and long cycle life at temperatures above 20 °C. The aqueous zinc battery exhibits a range of excellent properties, and the insertion and de-embedding of various ions enable the battery to achieve substantial power output.

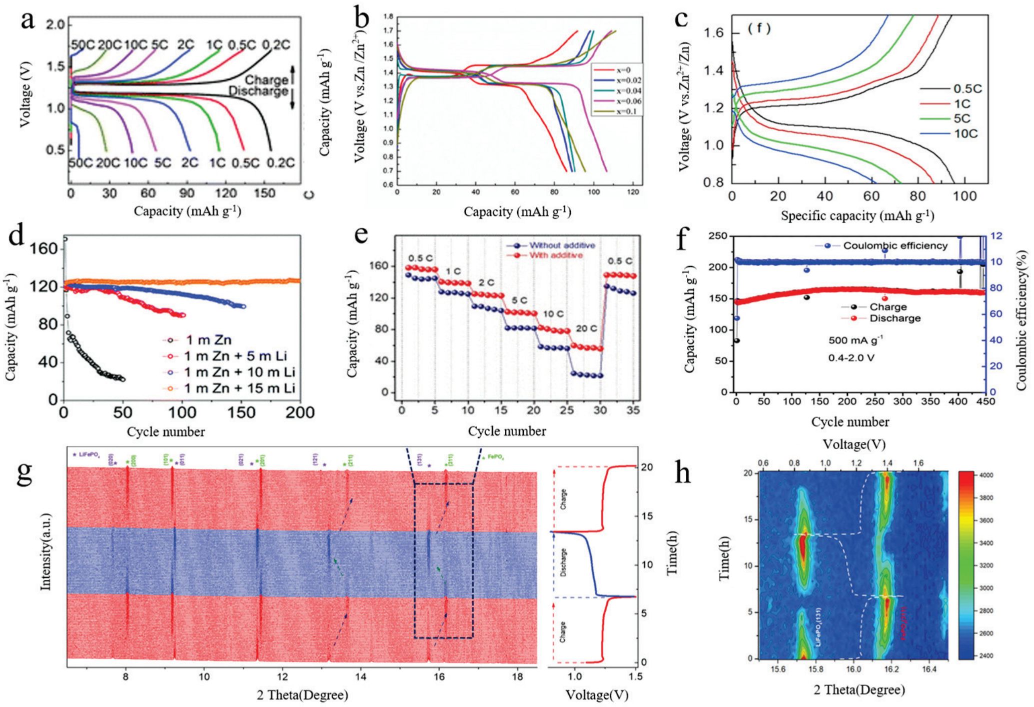

Figure 3. (**a**) Charge-discharge curves of Zn-LiFePO$_4$ [3]; Copyright© 2013 Copyright Clearance Center, Inc. All rights reserved, United Kingdom of Great Britain and Northern Ireland (**b**) Initial charge–discharge curves of $Li_3V_{2-x}Mn_x(PO_4)_3$ (x = 0.00, 0.02, 0.04, 0.06, 0.1) [41]; Copyright© 2023 Advanced Energy Materials, published by Wiley-VCH GmbH, American (**c**) Charge–discharge curves of Zn//0.5 mol L^{-1} + $Zn(CH_3COO)_2$//$Na_3V_2(PO_4)_3$ cell charge/discharge curves [42]; Copyright © 2022, under exclusive license to Springer-Verlag GmbH Germany, part of Springer Nature, Germany (**d**) Cycling stability of $Li_3V_2(PO_4)_3$ cathode with different electrolytes; Copyright© 2016 Elsevier Ltd. All rights reserved. the Netherlands (**e**) Rate capability of LiFePO$_4$ tested in the range of 0.5 to 20 C [43]; Copyright© 2024 Copyright Clearance Center, Inc. All rights reserved, United Kingdom of Great Britain and Northern Ireland (**f**) Cycling performance at 500 mA·g^{-1} in the potential range of $Na_3V_2(PO_4)_3$@C of 0.4~2.0 V [17]. Copyright© 2021, American Chemical Society, American (**g**) The operando synchrotron XRD patterns of the hybrid Zn-LiFePO$_4$ (left) and the corresponding charge–discharge curve (right) [43]. (**h**) Contour plots of the operando synchrotron XRD data, 15.5–16.5°, in which the (131) peak of LiFePO$_4$ is converted to the (311) peak of FePO$_4$ during the initial charge process [43]. Copyright© 2024 Copyright Clearance Center, Inc. All rights reserved, United Kingdom of Great Britain and Northern Ireland.

Adding high-entropy elements to the battery can also significantly improve its electrochemical performance. High-entropy materials (HEMs), which are single-phase crystal structures composed of many different elements, open up a huge space of chemical parameters with an almost unlimited number of element combinations. This versatility enables compounds to meet specific needs and be tailored to desired properties and applications, improving the quality and functionality of the material in a sustainable way. It has broad application prospects because its properties can be adjusted by selecting specific elements and changing the stoichiometry. Appropriate doping of metal elements in the negative electrode can alter the inter-crystalline spacing of the cathode material, alleviate crystal deformation, and enhance conductivity and ion diffusion rates, thereby affecting battery performance. As shown in Figure 3b, metal Mn was doped into the negative electrode

$Li_3V_2(PO_4)_3$ of a zinc battery, and the initial charge/discharge curves were analyzed. The capacities of the battery with $Zn//Li_3V_{2-x}Mn_x(PO_4)_3$ (x = 0.00, 0.02, 0.04, 0.06, and 0.1) were found to be 86.5 $mAh \cdot g^{-1}$ (x = 0), 89 $mAh \cdot g^{-1}$ (x = 0.02), 90 $mAh \cdot g^{-1}$ (x = 0.04), 106 $mAh \cdot g^{-1}$ (x = 0.06), and 95.5 $mAh \cdot g^{-1}$ (x = 0.1) The cell capacity gradually increased with an increase of Mn content, a result attributed to the improvement of the interlayer structure and equilibrium charge of the material by proper Mn doping.

Figure 3c shows the current density of the charge/discharge curves for the Zn-$Na_3V_2(PO_4)_3$ cell under different operating conditions. The specific discharge capacities are 97, 89, 79, and 58 $mAh \cdot g^{-1}$ at 0.5, 1, 5, and 10 C, respectively. The figure indicates that the electrochemical performance of the cell is excellent, allowing it to be charged and discharged at high rates up to 10 C. The specific discharge capacity of the Zn-$Na_3V_2(PO_4)_3$ cell is illustrated in Figure 3c. According to Equations (4)–(7), the battery undergoes charging and discharging involving not only Zn ions but also the embedding and de-embedding of Na ions, along with the valence change of V elements. Their combined action results in good battery performance, suggesting that the interaction between the two cations is significant, prompting further investigation into the mechanism of the aqueous zinc-ion battery.

Cyclic stability is a key performance indicator for electrochemical energy storage and conversion systems. It measures an electrochemical device's ability to maintain stable performance, including capacity, efficiency, and internal resistance, during repeated charging, discharging, or usage. Good cyclic stability is crucial for the long-term reliability of electrochemical systems. It enhances service life, ensures safety and reliability, increases energy density, and reduces maintenance costs. Figure 3d–f illustrate the cyclic stability of various batteries.

The electrolyte plays a crucial role in determining cycling stability [44]. Figure 3d illustrates the cycling performance of the $Li_3V_2(PO_4)_3$ cathode at 200 $mA \cdot g^{-1}$ in various aqueous solutions. The study compared 1 M Zn, 1 M Zn + 5 M Li, 1 M Zn + 10 M Li, and 1 M Zn + 15 M Li, evaluating how different Li concentrations affected cycling stability. The results showed that cycling stability improved with increasing Li concentrations. Notably, the 1 M Zn + 15 M Li system exhibited the highest cycling stability, achieving a reversible capacity of 126.7 $mAh \cdot g^{-1}$ after 200 cycles without significant degradation. The Coulombic efficiency (CE) reached 99.8%. This improvement is attributed to enhanced Li^+ insertion and de-embedding with higher Li concentrations, which likely contributes to the increased cycling stability. The $Zn/Li_3V_2(PO_4)_3$ cell showed reversible Li^+ insertion into the polyanion cathode during cycling, while Zn^{2+} plating and stripping occurred at the anode. These findings suggest that optimizing electrodes and electrolytes could further improve the performance of rechargeable Zn-based batteries.

The addition of additives can also impact the cycling stability of the battery [45]. Figure 3e illustrates the performance of $Zn/LiFePO_4$ batteries with and without additives. Research studies identified sodium dodecylbenzene sulfonate (SDBS) as an additive that enhances the electrochemical behavior of $Zn/LiFePO_4$ hybrid batteries. Applying this additive to the $Zn/LiFePO_4$ cell improved its performance. When evaluating cycling stability, it was found that at a high current rate of 20 C, the capacity of the $Zn/LiFePO_4$ cell without the additive was only 22.5 $mAh \cdot g^{-1}$, with a capacity retention of about 15.3% compared to 0.5 C. In contrast, the cell with the electrolyte additive maintained a capacity of 57.8 $mAh \cdot g^{-1}$ at the same current rate. Further analysis revealed that this additive not only suppressed Zn dendrite growth by controlling the Zn plating pattern but also accelerated lithium-ion diffusion at the $LiFePO_4$ cathode/electrolyte interface. With the additive, Zn^{2+} ions were smoothly deposited on the Zn metal surface, preventing lamellar Zn dendrite growth. Additionally, the additive improved the wettability of the $LiFePO_4$ electrode, increasing the lithium ion diffusion coefficient from 1.78×10^{-11} to 8.22×10^{-11} cm^2 s^{-1}, thus enhancing the cell's performance at high rates. This suggests that the main mechanism of the additive is to facilitate ion diffusion at the interface through its surface-active properties. Both Zn^{2+} and Li^+ ions play crucial roles at the anode and cathode, respectively. Therefore, in optimizing battery performance, it is important to consider both the electrolyte and its additives.

In addition to the factors mentioned above, structural decomposition reactions occurring in the electrolyte during the cycling process also influence ion diffusion within the cell, which in turn affects the electrochemical performance [46]. Unlike the Zn-$Na_3V_2(PO_4)_3$ cell structure and reaction mechanism discussed earlier, materials in a 1 M $Zn(CF_3SO_3)_2$ aqueous solution were found to undergo unexpected structural decomposition reactions during prolonged cycling. Specifically, $Na_3V_2(PO_4)_3$ decomposes into vanadium oxides such as $Zn_3V_2O_8$, V_2O_5, and VO_2. This decomposition leads to significant changes in the charge/discharge plateau, reversible capacity, kinetics, and structural stability. Notably, cycling stability, which is a primary concern, is also greatly impacted. As shown in Figure 3f, when $Na_3V_2(PO_4)_3$@C is cycled further at 500 $mA \cdot g^{-1}$ within the range of 0.4 to 2.0 V, the reversible capacity initially increases to 145 $mAh \cdot g^{-1}$ and stabilizes at 160 $mAh \cdot g^{-1}$ after 450 cycles. Subsequent studies revealed that the structure and morphology of zinc remain stable post-cycling, indicating that $Na_3V_2(PO_4)_3$@C undergoes phase changes due to the cumulative effects of repeated cycling. Thus, structural decomposition reactions in the electrolyte can significantly affect the cycling stability of the battery.

The charge relationship inside the battery also has a profound impact on the mechanism of the battery, which in turn affects the performance of the battery. The phase evolution of LFP during charge and discharge of mixed Zn/$LiFePO_4$ cells was studied by XRD of the atom synchrotron. From the charge–discharge curve (Figure 3g), only one discharge platform located at ≈1.1 V can be observed, indicating a single-phase transition. Acyclic $LiFePO_4$ has distinct peaks at 7.7°, 9.2°, 11.4°, and 13.2° and can be found in the (020), (011), (021), and (121) planes, respectively. During charging, these peaks gradually disappeared, while new reflections of ≈8.0°, 9.2°, 11.5°, and 13.8° appeared, which can be used for 200, 101, 201, and 211 reflections of the $FePO_4$ phase, indicating a complete transformation of the LFP phase into a heterogeneous phase. After discharge, all $LiFePO_4$ peaks reappeared completely, while the crystalline phase of $FePO_4$ disappeared, indicating good phase reversibility. A more pronounced change can be observed in the contour plot (Figure 3h), which shows that only Li ions and not Zn^{2+} ions are inserted into $FePO_4$ during discharge, although the size of Li ions is slightly larger than that of Zn^{2+} ions. The main reason can be attributed to the properties of Zn^{2+} and Li ions: compared to Li ions, Zn^{2+} ions have a higher charge density (double charge divided by a small radius of 0.74 A), resulting in reduced diffusivity within the body of ordinary polar crystals due to strong coulomb interactions and inhibition problems related to electrolyte chemistry, affecting the implantation/stripping solvation/desolvation energy balance.

3.2. Dual Ionization Properties

Dual-ion insertion is also widely used in batteries, and its effects on performance merit exploration. Unlike multiple-ion insertion, the impact of H^+ in dual-ion insertion cannot be ignored, leading to different effects on battery performance [47]. Consequently, research in this area has different focuses compared to multiple-ion insertion. The primary challenge for this mechanism is addressing the effects of H^+. Many researchers have proposed solutions to this issue.

Compared to multi-ion action, the properties of dual-ion action are different due to the ions. As shown in Figure 4a, the Zn/MnO_2 charge–discharge curve shows @ carbon fiber paper (CFP) cells at different rates in the first cycle. When the charge and discharge rate is increased from 0.3 C to 6.5 C, about 60% of the capacity can be maintained at 0.3 C, showing excellent magnifying capacity. Interestingly, with an increase of the charge and discharge rate, the voltage and capacity of the first voltage platform (region I) decreased very little, while the voltage and capacity of the second voltage platform (region II) decreased significantly, indicating that the reaction kinetics of the first (high) platform were much faster than those of the second (low) platform. At a high rate of 6.5 °C, the reaction of the second platform accounts for less than 20% of the total capacity. This significant difference in kinetics between the two reaction regions can also be observed by cyclic voltammetry (CV) scanning at different rates.

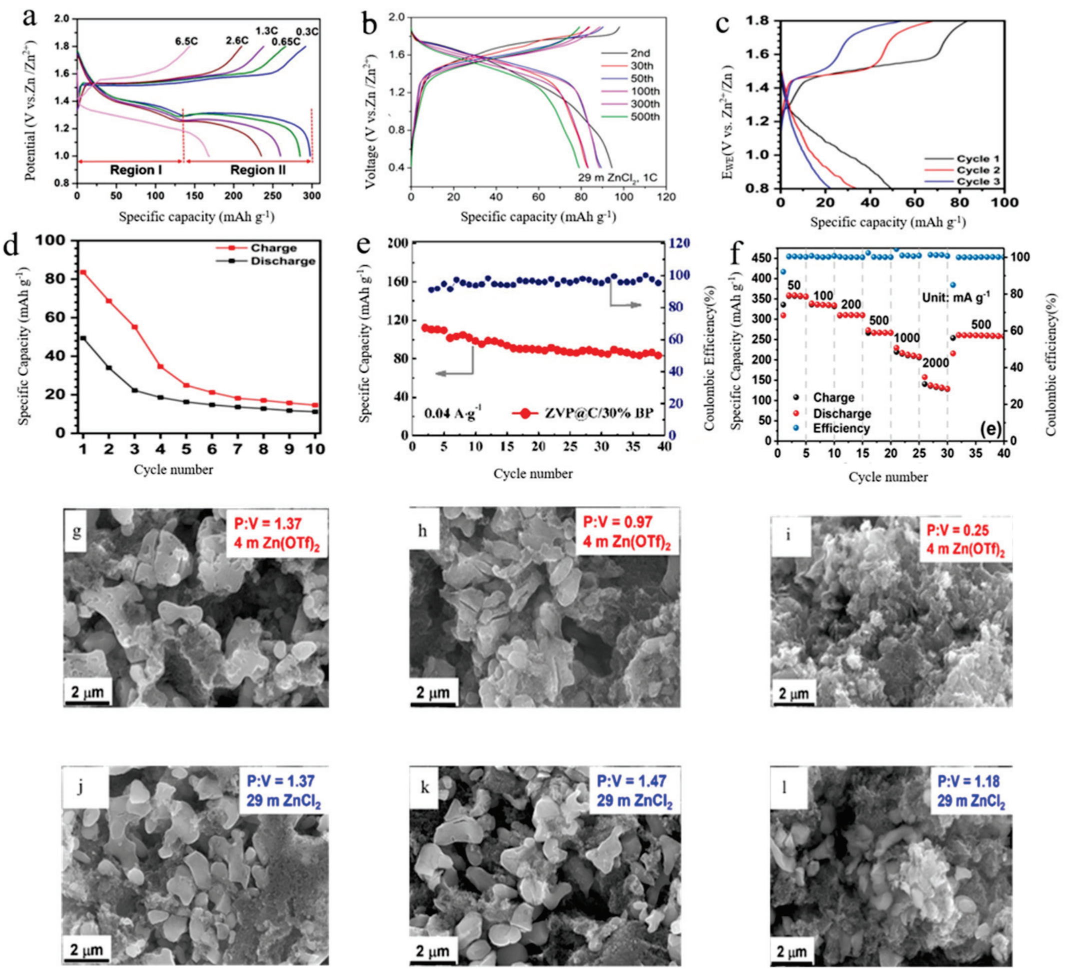

Figure 4. (**a**) Charge/discharge curves at different rates in the first cycle; Copyright© 2017, American Chemical Society, American (**b**) Charge/discharge curves of $Li_3V_2(PO_4)_3$ during different cycles; Copyright© 2022, American Chemical Society, American (**c**) Charge/discharge curves of $Zn/Na_3V_2(PO_4)_2F_3$ at 0.3 C; Copyright© 2020, American Chemical Society, American (**d**) Cycling performance of $Na_3V_2(PO_4)_2F_3/C$ in non-aqueous zinc-ion batteries at 0.3 C; Copyright© 2020, American Chemical Society. (**e**) Cycling stability of $Zn_3V_4(PO_4)_6$ starting from the second cycle at 0.04 Ag^{-1} @C/30%BP cycle stability [48]; Copyright© 2022, American Chemical Society, American (**f**) Specific capacity and coulombic efficiency obtained at different specific currents [49]. Copyright © 2020 American Chemical Society, American (**g**–**l**) Corresponding SEM images and P:V ratios collected by EDX at the 2nd (**g**,**j**), 5th (**h**,**k**), and 20th (**i**,**l**) cycle; Copyright© 2022, American Chemical Society, American.

Li et al. [34] demonstrated that engineering the solvated structure of aqueous Zn electrolytes (AZEs) is an effective method to inhibit H^+ intercalation and promote dominant Zn^{2+} intercalation. To validate this concept, they selected $Li_3V_2(PO_4)_3$ as the cathode and compared its electrochemical performance using two previously reported electrolytes: 4 M Zn $(OTf)_2$ and 29 M $ZnCl_2$. They also evaluated a newly designed hybrid electrolyte comprising poly (ethylene glycol) 400 (Polyethylene glycol (PEG) 400) and water as co-solvents, with $Zn(OTf)_2$ as the salt. As shown in Figure 4b, $ZnCl_2$ did not exhibit a low-voltage plateau but only a smaller activation-like process. In contrast to the maximum discharge capacity of 200 $mAh{\cdot}g^{-1}$ observed with 4 M $Zn(OTf)_2$, $ZnCl_2$ achieved a discharge capacity of approximately $mAh{\cdot}g^{-1}$ at the 60th cycle after the initial activation process. Figure 4g–l shows that the morphology and P:V ratio of $Li_3V_2(PO_4)_3$ electrodes only change slightly in $ZnCl_2$ WiSE, in which clear and distinguishable crystalline particles are preserved upon cycling. The presence of H^+ in the cell, due to the electrolyte's role in charge transfer and storage, necessitates the suppression of H^+ to ensure safety and prevent potential fire hazards.

To address the issue of H^+ intercalation, the use of non-aqueous electrolytes can be considered. As shown in Figure 4c, the $Na_3V_2(PO_4)_2F_3/C$ cathode exhibits poor reversibility in non-aqueous Zn-ion batteries. Constant current cycling at a lower rate of 0.3 C reveals that the initial discharge capacity of the cell is only 49 $mAh \cdot g^{-1}$. Furthermore, Figure 4d shows that this capacity decreases sharply during the first three cycles and gradually stabilizes at 11 $mAh \cdot g^{-1}$ by the end of 10 cycles. The non-aqueous Zn-ion battery with $Na_3V_2(PO_4)_2F_3/C$ exhibits a significantly shorter cycle life (10 cycles) compared to the aqueous cell (30 cycles). These results indicate notable differences in electrochemical behavior between aqueous and non-aqueous systems. While non-aqueous systems have some drawbacks in terms of recyclability, aqueous batteries offer unique advantages.

In contrast, Zhao et al. [48] synthesized a novel rocking-chair AZIB cathode material, $Zn_3V_4(PO_4)_6$@C (ZVP@C), and evaluated its electronic conductivity with a composite carbon coating. According to Figure 4e, ZVP@C/30% BP provides good stability even at current densities as low as 40 $mA \cdot g^{-1}$. This stability is attributed to the two-electron reaction of vanadium and the co-intercalation of Zn^{2+}/H^+. The capacity retention of Zn^{2+}/H^+ reached 80% after 400 cycles at 1 $A \cdot g^{-1}$, which was due to the stabilization of the crystal structure and the co-intercalation reaction of Zn^{2+}/H^+.

The electrochemical performance of high-performance δ-calcium vanadium oxide bronze/reduced graphene oxide (CVO/rGO) as an AZMB cathode material was evaluated using Zn foil as the negative electrode, 3 M $Zn(OTf)_2$ as the electrolyte, and an aqueous solution in a button cell [49]. The specific capacities at various current densities measured by GCPL are shown in Figure 4f. Specific capacities of 267 and 215 $mAh \cdot g^{-1}$ were achieved at current densities of 500 and 1000 $mA \cdot g^{-1}$, respectively. This figure demonstrates the good cyclability of the cell. The CVO/rGO composite exhibits satisfactory performance as a cathode material and is suitable for studying the insertion mechanism.

Summarizing the performance of bi-ionic insertion, it can be observed that co-intercalation is an effective method to mitigate the impact of H^+ on battery performance. Although a simpler approach is to inhibit or even eliminate H^+ by changing the electrolyte, this will subsequently alter the battery's performance.

3.3. Single-Ion Performance

In general, the main difference between single-ion action and multi-ion action is that to avoid the presence of H^+, a non-aqueous electrolyte is preferred, often a high-concentration electrolyte using the "water-in-salt" concept. This inhibits H^+ activity, reduces multi-ionic interactions, and establishes a foundation for further optimization of the ion insertion mechanism [50]. Therefore, single-ion interactions also possess distinct characteristics affecting battery performance.

In the 21 M LiTFSI/1 M $Zn(Tr)_2$ (aqueous salt) electrolyte, the O_2 precipitation reaction occurs even when charged to 2.10 V (Figure 5a). Additionally, the high concentration of the 21 M LiTFSI/1 M $Zn(Tr)_2$ electrolyte inhibits the dissolution of $VOPO_4$ and the corrosion of the Zn anode by reducing water activity. While the high electrolyte concentration can limit excessive ion reactions, it also affects cell performance.

Under 5 $A \cdot g^{-1}$ conditions, the capacity retention after 1000 cycles was as high as 93% when the voltage window was 0.8~2.1 V (Figure 5b). In contrast, when the voltage window was 0.8~1.8 V, the corresponding capacity of the $Zn/VOPO_4$ cell was only 20 $mAh \cdot g^{-1}$, and the capacity retention after 1000 cycles was only 49%. This indicates that the high concentration of electrolyte imposes certain requirements on the operating conditions of the battery.

By evaluating the Ti | | Zn asymmetric cell, a Coulombic efficiency of about 99.7% can be achieved by 70 PEG at a current density of 1 mA cm^{-2}, as shown in Figure 5c. In contrast, 0 PEG cells form extensive dendrites under the same operating conditions and fail after three cycles. The Coulombic efficiency of the cell can be improved to some extent by additives.

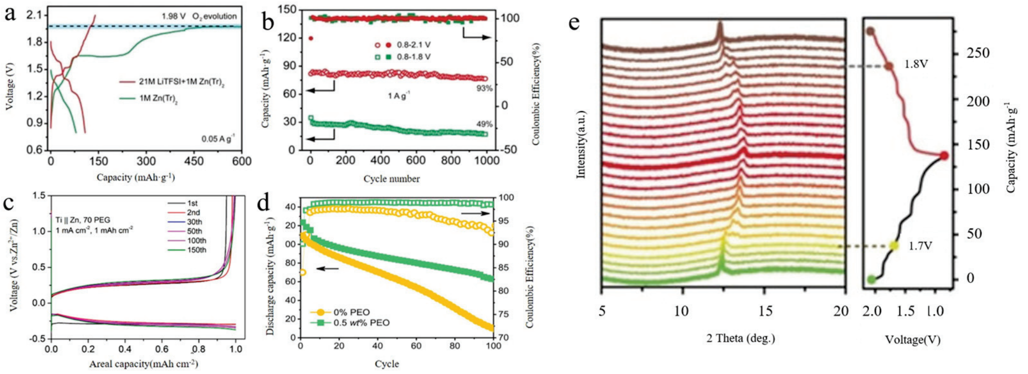

Figure 5. (**a**) First charge/discharge curves of Zn/$VOPO_4$-based batteries with different electrolytes; Copyright© 2019 Wiley-VCH Verlag GmbH & Co. KGaA, Weinheim, Germany. (**b**) Cycling performance of batteries employing the electrolyte in different voltage windows of 21 M LiTFSI/1 m Zn(Tr)$_2$; Copyright© 2019 Wiley-VCH Verlag GmbH & Co. KGaA, Weinheim, Germany. (**c**) Charge/discharge curves of Zn asymmetric cells with Ti | | 1 mA^{-2} at 70 PEG [34]; Copyright© 2022, American Chemical Society, Washington, WA, USA. (**d**) Cycling stability and Coulombic efficiency of a full cell with electrolyte with or without PEO additive, 1 M $ZnSO_4$ in 0.5 C [51]; Copyright© 2020 Wiley-VCH GmbH. (**e**) In situ XRD patterns of VOPO4/SWCNT electrodes; Copyright© 2019 Wiley-VCH Verlag GmbH & Co. KGaA, Weinheim, Germany.

In situ XRD was performed during a typical charge/discharge cycle to further understand the crystal structure evolution of $VOPO_4$ (Figure 5e). During the discharge process from 1.7 to 0.8 V (vanadium reduction), three lattice distortions occurred, as suggested by the successive appearance of three new peaks, in accordance with the three discharge plateaus in the low-voltage region. However, the crystal structure of $VOPO_4$ at the charged state of 1.8 V did not recover fully to the corresponding discharged state of 1.7 V, thus demonstrating that the crystal structure evolution was not completely reversible in the voltage window of 0.8–1.8 V. Therefore, the Zn/$VOPO_4$ batteries display unsatisfactory cycling performance from 0.8 to 1.8 V. Impressively, when the batteries were charged to 2.1 V, the crystal structure of $VOPO_4$ recovered to the initial state. Thus, when the voltage window was 0.8–2.1, the Zn/$VOPO_4$ batteries displayed excellent cycling performance.

With the addition of 0.5 wt% Polyethylene oxide (PEO), the battery can be safely charged to a higher voltage of 2.05 V, while Zn achieved a higher capacity of 125 mAh·g^{-1}. (Note: The higher oxidative settling voltage of the PEO-containing electrolyte is partly due to the increase in polarization on the Zn anode (≈<50 mV). The use of Zn/$LiMn_2O_4$ cells with PEO additives shows significantly improved capacity retention (Figure 5d). Additionally, the Coulombic efficiency (CE) degraded rapidly to 92% in the PEO-free electrolyte over 100 cycles, whereas it remained as high as 99% in the Zn/$LiMn_2O_4$ cells with a 0.5 wt% PEO electrolyte additive. This improvement can be attributed to the stabilized Zn anode and suppression of gas generation in the PEO-containing electrolyte. Mono-ion batteries enhance safety by addressing the issue of the H^+ presence through the use of high-concentration electrolytes.

From the above discussion, it can be seen that single-ion batteries differ from other types of batteries in terms of performance. The electrochemical performance is inferior to other batteries, but it has safety and stability. It is clear that numerous factors influence the electrochemical performance of the battery, ranging from characteristics to mechanisms. Therefore, in further discussions, it is essential to consider these various factors to achieve a clearer understanding of the battery's energy storage mechanism.

4. Opportunities and Challenges

During the exploration of different batteries, it was found that rechargeable batteries utilizing multivalent ions can theoretically offer higher storage capacities due to multiple electron transfers. Aqueous zinc-ion batteries (ZIBs) based on Zn^{2+} intercalation chemistry have gained significant attention due to their zinc anodes, which provide high capacity, high abundance, low cost, and low redox potentials [52]. However, due to the nature of the electrolyte in aqueous zinc-ion batteries, H^+ is inevitably present and affects the storage and transfer of electrons [53]. According to the comparison of the charge and discharge curve and the cyclic stability curve above, we can try to summarize the influence of H^+ on the electrochemical performance of the battery and the methods for avoiding or reducing such influence. On the one hand, the presence of H^+ can enhance ion conductivity, balance the insertion and removal process of Zn^{2+} ions, reduce the formation of zinc dendrites and electrode polarization, and improve cycle stability and battery life. Therefore, in the past development process of batteries, aqueous electrolytes have been favored by many researchers. On the other hand, although people are increasingly concerned about water-based zinc-ion batteries, there are also some problems. First, H^+ ion embedding changes the structure of the electrode material, causing volume expansion and contraction, which may lead to fracture and deactivation of the material. Second, the side reaction of water decomposition will produce gas, increasing the internal gas pressure. Finally, H^+ may have certain safety risks under high temperature conditions, which will cause great risks in the industrial production process, so it should be avoided as much as possible. Therefore, methods to inhibit the action of H^+ have garnered interest, leading to the development of batteries with single-ion insertion [54]. Summarizing the conclusions of the above literature, we can find strategies to solve or avoid the above problems. H^+ insertion can be inhibited by engineering the solvation structure of aqueous zinc electrolytes (AZEs). Co-insertion is an effective method to alleviate the effect of hydrogen ions on battery performance. In order to avoid the presence of H^+, a non-aqueous electrolyte is preferred, usually a high-concentration electrolyte that uses the concept of "water in salt". This inhibits H^+ activity and reduces multi-ion interactions, laying a foundation for further optimization of ion insertion mechanisms.

In fact, before the widespread use of non-aqueous solvents began in the 1950s, water was the most readily available and almost the only solvent used in all areas of pure and applied chemistry [55]. However, as batteries continue to evolve, their application scenarios are expanding, leading to the continuous development of various battery types. Consequently, non-aqueous zinc batteries are advancing. To address issues such as dendrite formation and simultaneous water splitting during the charge–discharge process, and to improve Coulombic efficiency and cycling stability, water-in-salt electrolytes have been developed and are increasingly used in batteries [56]. These electrolytes not only solve the aforementioned problems but also inhibit the production of H^+. As a result, water-in-salt electrolytes have gained significant attention due to their advantageous properties [57]. They not only mitigate the effects of H^+ but also enhance the reversibility of crystal structure transformation during the charge/discharge cycle, thereby improving the cycle life of the battery. The large resistances at the interface between electrolytes and the cathode/anode are the major bottlenecks for delivering desirable electrochemical performances of batteries. The electrolyte/anode interface also suffers from metallic dendrite formation, leading to rapid performance degradation. The use of a solid electrolyte can improve the above problems to a certain extent, with specific methods as follows: (1) surface modification of a solid electrolyte; (2) the application of artificial interlayers; and (3) incorporating multifunctional additives into the electrode material. These methods improve the cycle stability of the battery to a certain extent [58].

With further research, similar limitations of aqueous electrolytes containing salt become apparent. The higher salt concentration increases the viscosity in the cell, limiting transport properties, charge/discharge rates, and performance in advanced zinc batteries. Currently, each electrolyte composition has its advantages and limitations. Selecting the right electrolyte can maximize benefits and result in a battery that meets specific needs across various environments. Therefore, significant progress is still needed in battery research, presenting both opportunities and challenges for future development.

5. Conclusions and Outlook

Different types of batteries possess distinct advantages and disadvantages. Multi-ion batteries demonstrate exceptional performance, increased capacity, and extended cycle life; however, they are susceptible to interference from H^+ ions. Single-ion batteries effectively mitigate the H^+ issue but may not match the multi-ion batteries in certain aspects. Aqueous battery electrolytes are straightforward to produce, readily available, and widely utilized; nonetheless, they pose specific safety risks. Non-aqueous batteries can bypass these challenges but encounter limitations related to electrolyte composition and cost.

Above, we discussed the effects of different types and a number of roles of ions on battery performance, but in practice, we find that the ionic species in the battery will exceed our expectations for various reasons, and then we need to control the anionic species.

Achieving precise control of phosphate-based polyanion cathodes can be carried out through material synthesis, doping modifications, morphology control, process optimization, and so on. For example, fine synthesis methods such as solvothermal and solid phase sintering are used to ensure the homogeneity and purity of the materials. Precise control of reaction temperature and time can be used to optimize the crystal structure. Doping with other metal ions (e.g., Mg, Al) can be used to improve conductivity and stability. Surface coating of conductive carbon materials can improve electron conduction. Precise control of nanoparticles can be achieved by adjusting reaction conditions (e.g., pH). Optimizing preparation process parameters can improve the specific capacity and cycling stability. Ensuring that the choice of electrolytes is compatible with the cathode material can minimize side reactions.

All our discussions are still relatively biased towards qualitative analysis, and our main subsequent work is to shift the focus of our research towards quantitative analysis, which will be used to determine the optimum composition of phosphate-based polyanion cathodes for practical applications, which can be achieved through design of compositional variables, material characterization, electrochemical testing, and data modeling and analysis. The design of experiments (DOE) method is used to systematically vary the ratio and conditions of different compositions and to evaluate the effect of different doping elements and concentrations on battery properties. X-ray diffraction (XRD) and scanning electron microscopy (SEM) are used to analyze the crystal structure and morphology of the materials, and energy spectrum analysis (EDS) is used to determine the elemental distribution. Cyclic voltammetry (CV) constant current charge/discharge tests are performed to assess specific capacity and cycling stability. Electrochemical impedance spectroscopy (EIS) is used to study the conductivity and charge transfer impedance of materials. The relationship between composition and performance can be modeled using multiple regression analysis or machine learning methods. Key factors affecting performance are identified and optimal composition combinations are predicted. With this systematic approach, the optimal composition of phosphate-based polyanion cathodes can be quantitatively determined to realize their efficient performance in practical applications.

From the above discussion, it is clear that different batteries have their own strengths and limitations, and no single type can meet all usage conditions. The goal now is to enhance existing batteries to better fit various conditions and achieve superior performance. Development and research of aqueous batteries are currently more advanced than those of non-aqueous batteries, both in scale and timeline. Additionally, publications on aqueous batteries have increased at a higher rate compared to non-aqueous batteries. Aqueous batteries, due to their advantages, are likely to remain the dominant choice for the foreseeable future. Therefore, it is crucial to continue analyzing the characteristics of different batteries and determine appropriate research directions moving forward.

As a conduit for energy from production to consumption, batteries play a crucial role in optimizing the allocation of time and space in modern society and have a wide range of applications [59]. Large-scale battery storage systems can be used for grid peaking, improving the utilization of renewable energy, and playing an increasingly important role in the energy sector. Battery energy storage power stations represent an untapped blue ocean. From the perspective of battery structure and power converters, the scalability and modularity of power storage through batteries—coupled with their ability to act as both energy suppliers and consumers—provide significant operational flexibility [60]. Battery energy storage has advantages in scalability, service life, and flexibility. However, current battery energy storage is mainly dominated by technologies such as lithium-ion batteries, liquid flow batteries, lead-acid batteries, and sodium-based batteries. Large-scale applications of battery systems with zinc ions as the anode have yet to be realized. However, low-cost, high-security aqueous zinc-ion batteries have promising prospects for large-scale energy storage [61]. Due to their different working principles and application scenarios, each energy storage technology has its own advantages and limitations. Therefore, physical and chemical energy storage will remain mainstream for quite some time. However, compared with other energy storage methods, electrochemical energy storage has unique advantages. Although zinc-ion energy storage cannot replace higher-power batteries, it still has significant research value. It can be used as a substitute for other batteries in some special circumstances. Under the right conditions, zinc battery energy storage will excel in some aspects compared to other energy storage methods. A simple flowchart illustrating the process from a battery to an energy storage plant is shown in Figure 6. Zinc batteries can be combined to form a battery bank, which, like solar and wind energy, can be converted from direct current (DC) to alternating current (AC) through an integrated off-grid control system. The power can then be utilized comprehensively through an energy storage plant using unidirectional and bidirectional meters in an AC distribution box. This illustrates the simple process from a battery to an energy storage power station, highlighting the potential for large-scale industrial use of zinc battery energy storage, which is a key focus of our future efforts. Therefore, our current focus is to enhance the application scenarios of zinc batteries as conditions allow.

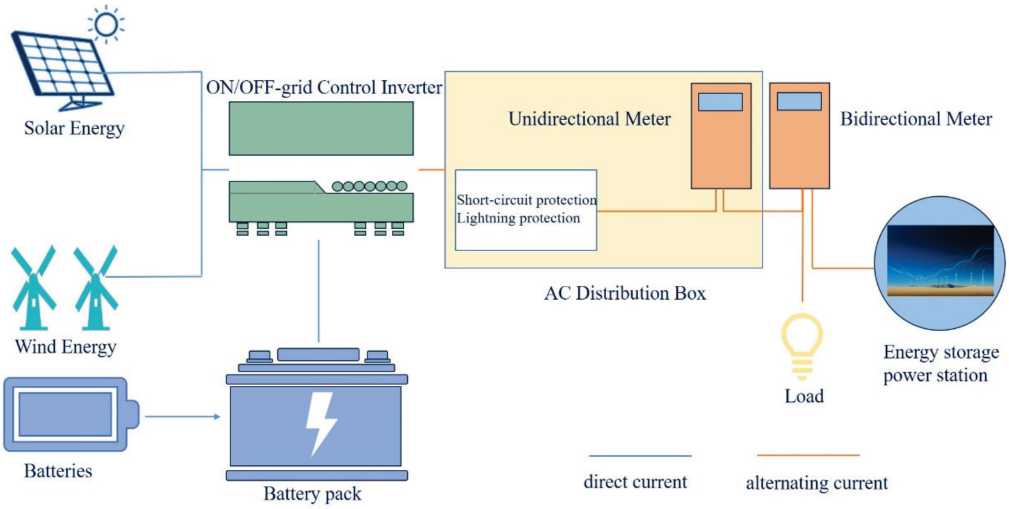

Figure 6. Flow chart of zinc battery to energy storage power station.

At the same time, we should always pay attention to the application of new technologies in batteries. The future of batteries depends not only on the iterative optimization of existing technologies, but also focuses on the intersection of other disciplines with battery energy storage. Machine learning (ML) and artificial intelligence (AI) are two key areas of computer science. AI and ML have a wide range of applications across a variety of industries, driving automation, personalized service, and efficiency, with tremendous potential for innovation. Optimizing material composition and structure through model predictions to improve conductivity and stability in ML models, including artificial neural networks (ANNs), support-vector machines (SVMs), random forest (RF), partial least squares regression (PLS), and logistic regression (LR), have successfully predicted the properties of battery materials [62]. We can quickly screen a large number of phosphate battery material combinations through these technologies, find high-performance positive and negative electrode and electrolyte materials, and guide the experimental design of phosphate cathode materials. Discovering and exploring untried chemical spaces will help develop new materials with potential applications, and integrate chemistry, physics, and data science to foster multidisciplinary collaboration and improve material quality. These technologies will drive innovation in battery technology and provide more efficient energy storage solutions.

Author Contributions: Conceptualization, L.C. and L.-F.Z.; methodology, L.C., H.W. and Z.-Y.C.; software, H.W., Z.-Y.C. and Y.-S.W.; validation, H.W., Z.-Y.C. and Y.-S.W.; formal analysis, L.C.; investigation, L.C.; resources L.C.; data curation, L.C.; writing—original draft preparation, L.C.; writing—review and editing, L.C.; visualization, L.C.; supervision, L.-F.Z. and T.D.; project administration, L.-F.Z. and T.D.; funding acquisition, L.-F.Z. and T.D. All authors have read and agreed to the published version of the manuscript.

Funding: This research was funded by the National Natural Science Foundation of China (No. 52270177), the Natural Science Foundation of Shenyang (No. 22-315-6-13), Liaoning Province Science and Technology Plan Joint Program (Key Research and Development Program Project) (2023JH2/101800058) and the Fundamental Research Funds for the Central Universities (No. N2425035).

Institutional Review Board Statement: Not applicable.

Informed Consent Statement: Not applicable.

Conflicts of Interest: The authors declare no conflicts of interest.

References

1. Pan, X.; Shao, T.; Zheng, X.; Zhang, Y.; Ma, X.; Zhang, Q. Energy and Sustainable Development Nexus: A Review. *Energy Strategy Rev.* **2023**, *47*, 101078. [CrossRef]
2. Ding, K.; Jiang, T.; Peng, J.; Wang, P.; Gou, W.; Xu, Q.; Fan, Q.; Wang, W.; Sun, Y. Recent Advances of $Na_3V_2(PO_4)_3$ as Cathode for Rechargeable Zinc-Based Batteries. *Carbon Lett.* **2023**, *33*, 989–1012. [CrossRef]
3. Zhang, H.; Wu, X.; Yang, T.; Liang, S.; Yang, X. Cooperation Behavior between Heterogeneous Cations in Hybrid Batteries. *Chem. Commun.* **2013**, *49*, 9977–9979. [CrossRef] [PubMed]
4. Wei, Y.; Dai, S.; Yu, J.; Wu, S.; Wang, J. Research on Status and Prospects of Battery Energy Storage Stations on Energy Internet. In Proceedings of the 2019 IEEE 3rd Information Technology, Networking, Electronic and Automation Control Conference (ITNEC), Chengdu, China, 15–17 March 2019. [CrossRef]
5. Olabi, A.G.; Abbas, Q.; Shinde, P.A.; Abdelkareem, M.A. Rechargeable Batteries: Technological Advancement, Challenges, Current and Emerging Applications. *Energy* **2023**, *266*, 126408. [CrossRef]
6. Zhang, W.; Yin, J.; Wang, W.; Bayhan, Z.; Alshareef, H.N. Status of Rechargeable Potassium Batteries. *Nano Energy* **2021**, *83*, 105792. [CrossRef]
7. He, J.; Tao, T.; Yang, F.; Sun, Z. Unravelling Li^+ Intercalation Mechanism and Cathode Electrolyte Interphase of $Na_3V_2(PO_4)_3$ and $Na_3(VOPO_4)_2F$ Cathode as Robust Framework Towards High-Performance Lithium-Ion Batteries. *ChemSusChem* **2022**, *15*, e202200817. [CrossRef]
8. Sun, W.; Wang, F.; Hou, S.; Yang, C.; Fan, X.; Ma, Z.; Gao, T.; Han, F.; Hu, R.; Zhu, M.; et al. Zn/MnO_2 Battery Chemistry With H^+ and Zn^{2+} Coinsertion. *J. Am. Chem. Soc.* **2017**, *139*, 9775–9778. [CrossRef]
9. Bin, D.; Du, Y.; Yang, B.; Lu, H.; Liu, Y.; Xia, Y. Progress of Phosphate-Based Polyanion Cathodes for Aqueous Rechargeable Zinc Batteries. *Adv. Funct. Mater.* **2023**, *33*, 2211765. [CrossRef]
10. Yi, X.; Feng, Y.; Rao, A.M.; Zhou, J.; Wang, C.; Lu, B. Quasi-Solid Aqueous Electrolytes for Low-Cost Sustainable Alkali-Metal Batteries. *Adv. Mater.* **2023**, *35*, 2302280. [CrossRef]
11. Tian, X.; Zhao, Q.; Zhou, M.; Huang, X.; Sun, Y.; Duan, X.; Zhang, L.; Li, H.; Su, D.; Jia, B.; et al. Synergy of Dendrites-Impeded Atomic Clusters Dissociation and Side Reactions Suppressed Inert Interface Protection for Ultrastable Zn Anode. *Adv. Mater.* **2024**, *36*, 2400237. [CrossRef]
12. Kundu, D.; Vajargah, S.H.; Wan, L.; Adams, B.; Prendergast, D.; Nazar, L.F. Aqueous *vs.* Nonaqueous Zn-Ion Batteries: Consequences of the Desolvation Penalty at the Interface. *Energy Environ. Sci.* **2018**, *11*, 881–892. [CrossRef]

13. Gao, Y.; Li, G.; Wang, F.; Chu, J.; Yu, P.; Wang, B.; Zhan, H.; Song, Z. A High-Performance Aqueous Rechargeable Zinc Battery Based on Organic Cathode Integrating Quinone and Pyrazine. *Energy Storage Mater.* **2021**, *40*, 31–40. [CrossRef]
14. Zhao, L.N.; Zhang, T.; Zhao, H.L.; Hou, Y.L. Polyanion-Type Electrode Materials for Advanced Sodium-Ion Batteries. *Mater. Today Nano* **2020**, *10*, 100072. [CrossRef]
15. Lv, Z.; Ling, M.; Yue, M.; Li, X.; Song, M.; Zheng, Q.; Zhang, H. Vanadium-Based Polyanionic Compounds as Cathode Materials for Sodium-Ion Batteries: Toward High-Energy and High-Power Applications. *J. Energy Chem.* **2021**, *55*, 361–390. [CrossRef]
16. Guo, J.-Z.; Gu, Z.-Y.; Du, M.; Zhao, X.-X.; Wang, X.-T.; Wu, X.-L. Emerging Characterization Techniques for Delving Polyanion-Type Cathode Materials of Sodium-Ion Batteries. *Mater. Today* **2023**, *66*, 221–244. [CrossRef]
17. Li, W.; Jing, X.; Jiang, K.; Wang, D. Observation of Structural Decomposition of $Na_3V_2(PO_4)_3$ and $Na_3V_2(PO_4)_2F_3$ as Cathodes for Aqueous Zn-Ion Batteries. *ACS Appl. Energy Mater.* **2021**, *4*, 2797–2807. [CrossRef]
18. Wu, Z.; Lu, C.; Ye, F.; Zhang, L.; Jiang, L.; Liu, Q.; Dong, H.; Sun, Z.; Hu, L. Bilayered $VOPO_4{\cdot}2H_2O$ Nanosheets with High-Concentration Oxygen Vacancies for High-Performance Aqueous Zinc-Ion Batteries. *Adv. Funct. Mater.* **2021**, *31*, 2106816. [CrossRef]
19. Liu, Q.; Wang, H.; Jiang, C.; Tang, Y. Multi-Ion Strategies towards Emerging Rechargeable Batteries with High Performance. *Energy Storage Mater.* **2019**, *23*, 566–586. [CrossRef]
20. Liu, T.; Peng, N.; Zhang, X.; Zheng, R.; Xia, M.; Zhang, J.; Yu, H.; Zhang, L.; Shu, J. Insight into Anion Storage Batteries: Materials, Properties and Challenges. *Energy Storage Mater.* **2021**, *42*, 42–67. [CrossRef]
21. Hao, J.; Long, J.; Li, B.; Li, X.; Zhang, S.; Yang, F.; Zeng, X.; Yang, Z.; Pang, W.K.; Guo, Z. Toward High-Performance Hybrid Zn-Based Batteries via Deeply Understanding Their Mechanism and Using Electrolyte Additive. *Adv. Funct. Mater.* **2019**, *29*, 1903605. [CrossRef]
22. Olbasa, B.W.; Huang, C.-J.; Fenta, F.W.; Jiang, S.-K.; Chala, S.A.; Tao, H.-C.; Nikodimos, Y.; Wang, C.-C.; Sheu, H.-S.; Yang, Y.-W.; et al. Highly Reversible Zn Metal Anode Stabilized by Dense and Anion-Derived Passivation Layer Obtained from Concentrated Hybrid Aqueous Electrolyte. *Adv. Funct. Mater.* **2022**, *32*, 2103959. [CrossRef]
23. Zhao, H.B.; Hu, C.J.; Cheng, H.W.; Fang, J.H.; Xie, Y.P.; Fang, W.Y.; Doan, T.N.L.; Hoang, T.K.A.; Xu, J.Q.; Chen, P. Novel Rechargeable $M_3V_2(PO_4)_3$//Zinc (M = Li, Na) Hybrid Aqueous Batteries with Excellent Cycling Performance. *Sci. Rep.* **2016**, *6*, 25809. [CrossRef] [PubMed]
24. Li, G.; Yang, Z.; Jiang, Y.; Jin, C.; Huang, W.; Ding, X.; Huang, Y. Towards Polyvalent Ion Batteries: A Zinc-Ion Battery Based on NASICON Structured $Na_3V_2(PO_4)_3$. *Nano Energy* **2016**, *25*, 211–217. [CrossRef]
25. Hu, P.; Zhu, T.; Wang, X.; Zhou, X.; Wei, X.; Yao, X.; Luo, W.; Shi, C.; Owusu, K.A.; Zhou, L.; et al. Aqueous $Zn//Zn(CF_3SO_3)_2//Na_3V_2(PO_4)_3$ Batteries with Simultaneous Zn^{2+}/Na^+ Intercalation/de-Intercalation. *Nano Energy* **2019**, *58*, 492–498. [CrossRef]
26. Li, W.; Wang, K.; Cheng, S.; Jiang, K. A Long-Life Aqueous Zn-Ion Battery Based on $Na_3V_2(PO_4)_2F_3$ Cathode. *Energy Storage Mater.* **2018**, *15*, 14–21. [CrossRef]
27. Bi, X.; Peng, Y.; Liu, S.; Liu, Y.; Yang, X.; Feng, K.; Hu, J. $Na_3(VO)_2(PO_4)_2F$ Coated Carbon Nanotubes: A Cathode Material with High-Specific Capacity for Aqueous Zinc-Ion Batteries. *Electrochim. Acta* **2024**, *475*, 143657. [CrossRef]
28. Wan, F.; Zhang, Y.; Zhang, L.; Liu, D.; Wang, C.; Song, L.; Niu, Z.; Chen, J. Reversible Oxygen Redox Chemistry in Aqueous Zinc-Ion Batteries. *Angew. Chem. Int. Edit.* **2019**, *58*, 7062–7067. [CrossRef]
29. Shi, H.-Y.; Song, Y.; Qin, Z.; Li, C.; Guo, D.; Liu, X.-X.; Sun, X. Inhibiting $VOPO_4{\cdot}x\ H_2O$ Decomposition and Dissolution in Rechargeable Aqueous Zinc Batteries to Promote Voltage and Capacity Stabilities. *Angew. Chem. Int. Edit.* **2019**, *58*, 16057–16061. [CrossRef]
30. Cao, L.; Li, D.; Pollard, T.; Deng, T.; Zhang, B.; Yang, C.; Chen, L.; Vatamanu, J.; Hu, E.; Hourwitz, M.J.; et al. Fluorinated Interphase Enables Reversible Aqueous Zinc Battery Chemistries. *Nat. Nanotechnol.* **2021**, *16*, 902–910. [CrossRef]
31. Wang, X.; Zhang, Z.; Xiong, S.; Tian, F.; Feng, Z.; Jia, Y.; Feng, J.; Xi, B. A High-Rate and Ultrastable Aqueous Zinc-Ion Battery with a Novel $MgV_2O_6{\cdot}1.7H2O$ Nanobelt Cathode. *Small* **2021**, *17*, 2100318. [CrossRef]
32. Oberholzer, P.; Tervoort, E.; Bouzid, A.; Pasquarello, A.; Kundu, D. Oxide versus Nonoxide Cathode Materials for Aqueous Zn Batteries: An Insight into the Charge Storage Mechanism and Consequences Thereof. *ACS Appl. Mater. Interfaces* **2019**, *11*, 674–682. [CrossRef] [PubMed]
33. Li, C.; Kingsbury, R.; Zhou, L.; Shyamsunder, A.; Persson, K.A.; Nazar, L.F. Tuning the Solvation Structure in Aqueous Zinc Batteries to Maximize Zn-Ion Intercalation and Optimize Dendrite-Free Zinc Plating. *ACS Energy Lett.* **2022**, *7*, 533–540. [CrossRef]
34. Wang, F.; Blanc, L.E.; Li, Q.; Faraone, A.; Ji, X.; Chen-Mayer, H.H.; Paul, R.L.; Dura, J.A.; Hu, E.; Xu, K.; et al. Quantifying and Suppressing Proton Intercalation to Enable High-Voltage Zn-Ion Batteries. *Adv. Energy Mater.* **2021**, *11*, 2102016. [CrossRef]
35. Park, M.J.; Manthiram, A. Unveiling the Charge Storage Mechanism in Nonaqueous and Aqueous $Zn/Na_3V_2(PO_4)_2F_3$ Batteries. *ACS Appl. Energ. Mater.* **2020**, *3*, 5015–5023. [CrossRef]
36. Chen, X.; Zhang, H.; Liu, J.-H.; Gao, Y.; Cao, X.; Zhan, C.; Wang, Y.; Wang, S.; Chou, S.-L.; Dou, S.-X.; et al. Vanadium-Based Cathodes for Aqueous Zinc-Ion Batteries: Mechanism, Design Strategies and Challenges. *Energy Storage Mater.* **2022**, *50*, 21–46. [CrossRef]
37. Blanc, L.E.; Kundu, D.; Nazar, L.F. Scientific Challenges for the Implementation of Zn-Ion Batteries. *Joule* **2020**, *4*, 771–799. [CrossRef]
38. Tao, Y.; Huang, D.; Chen, H.; Luo, Y. Electrochemical Generation of Hydrated Zinc Vanadium Oxide with Boosted Intercalation Pseudocapacitive Storage for a High-Rate Flexible Zinc-Ion Battery. *ACS Appl. Mater. Interfaces* **2021**, *13*, 16576–16584. [CrossRef]

39. Kadam, N.; Sarkar, A. A System for Recharging Zn-Air Battery with High Reversibility Using a Water-in-Salt Electrolyte. *J. Energy Storage* **2022**, *54*, 105265. [CrossRef]
40. Wang, Z.; Diao, J.; Burrow, J.N.; Brotherton, Z.W.; Lynd, N.A.; Henkelman, G.; Mullins, C.B. Chaotropic Salt-Aided "Water-In-Organic" Electrolyte for Highly Reversible Zinc-Ion Batteries Across a Wide Temperature Range. *Adv. Funct. Mater.* **2024**, *34*, 2311271. [CrossRef]
41. Nie, C.; Wang, G.; Wang, D.; Wang, M.; Gao, X.; Bai, Z.; Wang, N.; Yang, J.; Xing, Z.; Dou, S. Recent Progress on Zn Anodes for Advanced Aqueous Zinc-Ion Batteries. *Adv. Energy Mater.* **2023**, *13*, 2300606. [CrossRef]
42. Jiang, Y.; Xiang, Y.; Zou, Q.; Liu, B.; Liu, S.; Zeng, H.; Chen, L.; Li, J.; Wu, X.; Xiong, L. Improving $Li_3V_2(PO_4)_3$ Cathode Performance by Mn^{2+} Doping for High-Rate Aqueous Zinc Ion Hybrid Batteries. *Ionics* **2022**, *28*, 3855–3864. [CrossRef]
43. Li, C.; Yuan, W.; Li, C.; Wang, H.; Wang, L.; Liu, Y.; Zhang, N. Boosting $Li_3V_2(PO_4)_3$ Cathode Stability Using a Concentrated Aqueous Electrolyte for High-Voltage Zinc Batteries. *Chem. Commun.* **2021**, *57*, 4319–4322. [CrossRef] [PubMed]
44. Kainat, S.; Anwer, J.; Hamid, A.; Gull, N.; Khan, S.M. Electrolytes in Lithium-Ion Batteries: Advancements in the Era of Twenties (2020's). *Mater. Chem. Phys.* **2024**, *313*, 128796. [CrossRef]
45. Zhang, C.-Z.; Jiang, J.-C.; Huang, A.-C.; Tang, Y.; Xie, L.-J.; Zhai, J.; Xing, Z.-X. A Novel Multifunctional Additive Strategy Improves the Cycling Stability and Thermal Stability of SiO/C Anode Li-Ion Batteries. *Process Saf. Environ. Prot.* **2022**, *164*, 555–565. [CrossRef]
46. Fang, C.; Tran, T.-N.; Zhao, Y.; Liu, G. Electrolyte Decomposition and Solid Electrolyte Interphase Revealed by Mass Spectrometry. *Electrochim. Acta* **2021**, *399*, 139362. [CrossRef]
47. Wang, K.; Wang, Y.; Wang, C.; Xia, Y. Graphene Oxide Assisted Solvothermal Synthesis of $LiMnPO_4$ Naonplates Cathode Materials for Lithium Ion Batteries. *Electrochim. Acta* **2014**, *146*, 8–14. [CrossRef]
48. Zhao, Q.; Zhu, Y.; Liu, S.; Liu, Y.; He, T.; Jiang, X.; Yang, X.; Feng, K.; Hu, J. $Zn_3V_4(PO_4)_6$: A New Rocking-Chair-Type Cathode Material with High Specific Capacity Derived from Zn^{2+}/H^+ Cointercalation for Aqueous Zn-Ion Batteries. *ACS Appl. Mater. Interfaces* **2022**, *14*, 32066–32074. [CrossRef]
49. Liu, X.; Euchner, H.; Zarrabeitia, M.; Gao, X.; Elia, G.A.; Gross, A.; Passerini, S. Operando pH Measurements Decipher H^+/Zn^{2+} Intercalation Chemistry in High-Performance Aqueous Zn/δ-V_2O_5 Batteries. *ACS Energy Lett.* **2020**, *5*, 2979–2986. [CrossRef]
50. Suo, L.; Borodin, O.; Wang, Y.; Rong, X.; Sun, W.; Fan, X.; Xu, S.; Schroeder, M.A.; Cresce, A.V.; Wang, F.; et al. "Water-in-Salt" Electrolyte Makes Aqueous Sodium-Ion Battery Safe, Green, and Long-Lasting. *Adv. Energy Mater.* **2017**, *7*, 1701189. [CrossRef]
51. Jin, Y.; Han, K.S.; Shao, Y.; Sushko, M.L.; Xiao, J.; Pan, H.; Liu, J. Stabilizing Zinc Anode Reactions by Polyethylene Oxide Polymer in Mild Aqueous Electrolytes. *Adv. Funct. Mater.* **2020**, *30*, 2003932. [CrossRef]
52. Xia, C.; Guo, J.; Li, P.; Zhang, X.; Alshareef, H.N. Highly Stable Aqueous Zinc-Ion Storage Using a Layered Calcium Vanadium Oxide Bronze Cathode. *Angew. Chem. Int. Edit.* **2018**, *57*, 3943–3948. [CrossRef] [PubMed]
53. Zhang, A.; Yin, X.; Saadoune, I.; Wei, Y.; Wang, Y. Zwitterion Intercalated Manganese Dioxide Nanosheets as High-Performance Cathode Materials for Aqueous Zinc Ion Batteries. *Small* **2024**, 2402811. [CrossRef] [PubMed]
54. Shan, C.; Wang, Y.; Liang, M.; Lu, K.; Xiong, C.; Hu, W.; Liu, B. A Comprehensive Review of Single Ion-Conducting Polymer Electrolytes as a Key Component of Lithium Metal Batteries: From Structural Design to Applications. *Energy Storage Mater.* **2023**, *63*, 102955. [CrossRef]
55. Demir-Cakan, R.; Rosa Palacin, M.; Croguennec, L. Rechargeable Aqueous Electrolyte Batteries: From Univalent to Multivalent Cation Chemistry. *J. Mater. Chem. A* **2019**, *7*, 20519–20539. [CrossRef]
56. Vazquez, D.G.; Pollard, T.P.; Mars, J.; Yoo, J.M.; Steinrück, H.-G.; Bone, S.E.; Safonova, O.V.; Toney, M.F.; Borodin, O.; Lukatskaya, M.R. Creating Water-in-Salt-like Environment Using Coordinating Anions in Non-Concentrated Aqueous Electrolytes for Efficient Zn Batteries. *Energy Environ. Sci.* **2023**, *16*, 1982–1991. [CrossRef]
57. Jumare, I.A. Energy Storage with Salt Water Battery: A Preliminary Design and Economic Assessment. *J. Energy Storage* **2020**, *27*, 101130. [CrossRef]
58. Feng, J.; Gao, Z.; Sheng, L.; Hao, Z.; Wang, F.R. Progress and Perspective of Interface Design in Garnet Electrolyte-based All-solid-state Batteries. *Carbon Energy* **2021**, *3*, 385–409. [CrossRef]
59. Yao, W.; Zheng, Z.; Zhou, J.; Liu, D.; Song, J.; Zhu, Y. A Minireview of the Solid-State Electrolytes for Zinc Batteries. *Polymers* **2023**, *15*, 4047. [CrossRef]
60. Duggal, I.; Venkatesh, B. Short-Term Scheduling of Thermal Generators and Battery Storage with Depth of Discharge-Based Cost Model. *IEEE Trans. Power Syst.* **2015**, *30*, 2110–2118. [CrossRef]
61. Zhang, F.; Huang, F.; Huang, R.; Dong, N.; Jiao, S.; Cao, R.; Pan, H. Hierarchical Porous Separator with Excellent Isotropic Modulus Enabling Homogeneous Zn^{2+} Flux for Stable Aqueous Zn Battery. *Sci. China Mater.* **2023**, *66*, 982–991. [CrossRef]
62. Lv, C.; Zhou, X.; Zhong, L.; Yan, C.; Srinivasan, M.; Seh, Z.W.; Liu, C.; Pan, H.; Li, S.; Wen, Y.; et al. Machine Learning: An Advanced Platform for Materials Development and State Prediction in Lithium-Ion Batteries. *Adv. Mater.* **2022**, *34*, 2101474. [CrossRef] [PubMed]

Disclaimer/Publisher's Note: The statements, opinions and data contained in all publications are solely those of the individual author(s) and contributor(s) and not of MDPI and/or the editor(s). MDPI and/or the editor(s) disclaim responsibility for any injury to people or property resulting from any ideas, methods, instructions or products referred to in the content.

molecules

MDPI

Review

Constructing Three-Dimensional Architectures to Design Advanced Copper-Based Current Collector Materials for Alkali Metal Batteries: From Nanoscale to Microscale

Chunyang Kong [1], Fei Wang [2], Yong Liu [1,*], Zhongxiu Liu [1], Jing Liu [1], Kaijia Feng [1], Yifei Pei [1], Yize Wu [1] and Guangxin Wang [1,3,*]

[1] Provincial and Ministerial Co-Construction of Collaborative Innovation Center for Non-Ferrous Metal New Materials and Advanced Processing Technology, School of Materials Science and Engineering, Henan University of Science and Technology, Luoyang 471023, China; kcy00312@163.com (C.K.); liuzhongxiu2020@163.com (Z.L.); liuliu158600@163.com (J.L.); fengkaijia2021@163.com (K.F.); 15738595833@163.com (Y.P.); 221402010224@stu.haust.edu.cn (Y.W.)
[2] Faculty of Engineering, Huanghe Science & Technology University, Zhengzhou 450063, China; wangf157@hhstu.edu.cn
[3] Research Center for High Purity Materials, Henan University of Science and Technology, Luoyang 471023, China
* Correspondence: liuyong209@haust.edu.cn (Y.L.); wanggx2016@126.com (G.W.)

Abstract: Alkali metals (Li, Na, and K) are deemed as the ideal anode materials for next-generation high-energy-density batteries because of their high theoretical specific capacity and low redox potentials. However, alkali metal anodes (AMAs) still face some challenges hindering their further applications, including uncontrollable dendrite growth and unstable solid electrolyte interphase during cycling, resulting in low Coulombic efficiency and inferior cycling performance. In this regard, designing 3D current collectors as hosts for AMAs is one of the most effective ways to address the above-mentioned problems, because their sufficient space could accommodate AMAs' volume expansion, and their high specific surface area could lower the local current density, leading to the uniform deposition of alkali metals. Herein, we review recent progress on the application of 3D Cu-based current collectors in stable and dendrite-free AMAs. The most widely used modification methods of 3D Cu-based current collectors are summarized. Furthermore, the relationships among methods of modification, structure and composition, and the electrochemical properties of AMAs using Cu-based current collectors, are systematically discussed. Finally, the challenges and prospects for future study and applications of Cu-based current collectors in high-performance alkali metal batteries are proposed.

Keywords: alkali metal anode; 3D Cu-based current collector; dendrite free; electrochemical performance

1. Introduction

With the development of society, people's demand for energy is gradually increasing. Meanwhile, the environmental problems caused by the massive use of fossil fuels have gradually attracted people's attention [1,2]. To overcome the above problems, new energy systems are being vigorously promoted, such as wind energy, solar energy and so on [3–5]. Nevertheless, such new energy sources have the characteristics of intermittence and fluctuation, which make it difficult to ensure the stability of energy transmission. This requires stable and reliable energy storage devices, such as rechargeable batteries, including lead-acid batteries, Li-ion batteries, Na-ion batteries, Zn-ion batteries and so on [6–10]. Among the many types of energy storage batteries, Li-ion batteries (LIBs) are widely commercialized in mobile phones, laptops, electric vehicles and other electronic devices because of their long lifespan and low self-discharge rate [11–14]. However, the practical specific energy of LIBs containing traditional graphite anodes is close to the theoretical value [15,16], and even though many efforts have been made to improve the specific energy of Li-ion batteries [17–20], they are still unable to meet people's gradually increasing requirements [21,22]. Therefore, it is critical to develop new high-energy-density batteries [23].

Alkali metals (Li, Na and K) are deemed as the ideal anode materials for next-generation high-energy-density batteries because of their high theoretical energy densities (Li, 3860 mAh g^{-1}; Na, 1166 mAh g^{-1}; K, 685 mAh g^{-1}) and low redox potentials (Li, -3.04 V; Na, -2.71 V; K, -2.93 V versus SHE) [16,23–26]. Nevertheless, the further application of alkali metal anodes (AMAs) is hindered by some issues with alkali metals, such as uncontrolled dendrite growth, infinite volume expansion during cycling, and the high reactivity between alkali metal anodes and electrolytes, dead alkali metals, and fragile solid electrolyte interphases (SEIs), which lead to low Coulombic efficiency (CE) and unsatisfactory cycling performance, as well as even safety hazards [16,27–32]. To date, considerable efforts have been made to address these problems, including electrolyte optimization, the construction of artificial SEIs on alkali metal anodes, introducing solid-state electrolytes, the modification of separators, host design and so on [29,33–40].

In recent years, it has been demonstrated that constructing three-dimensional (3D) current collectors can alleviate volume expansion and suppress dendrite growth, because they have sufficient space to accommodate AMAs' volume expansion, and high specific surface areas, which could lower the local current density [30,41–44]. Through functional modification, current collectors can also provide multiple functions, which include reducing nucleation overpotential and local current density [34,45]. To date, Cu has been widely studied as a current collector due to its good conductivity and processability, and 3D Cu-based current collectors (3D Cu-based CCs) have received extensive attention for use as AMAs [45–49]. For example, An et al. prepared the 3D porous Cu CCs from CuZn alloy foil by the vacuum distillation method, and the electrochemical performances of lithium metal anodes (LMAs) with these 3D Cu CCs were greatly enhanced [46]. Furthermore, Li and co-workers used chemically treated Cu foam as the Na host, which achieved a stable Na cycling behavior and suppressed volume expansion upon cycling [47]. Moreover, an anode substrate obtained by chemically loading a thin layer of gold particles onto 3D Cu foam was reported by Zhang's group [48]. This design can reduce K dendrite growth by forming stable SEI. In addition, Guo et al. summarized the application of 3D Cu-based CCs in lithium metal batteries (LMBs) [49]. Zhou et al. summarized the modification strategies of Cu CCs for LMBs [50]. Hence, developing 3D Cu-based CCs is a practical and feasible way to solve the problems encountered in the application of AMAs. Although some previous reviews on LMAs have mentioned 3D Cu-based CCs [49,50], to the best of our knowledge, critical reviews exclusively focusing on 3D Cu-based CCs for alkali metal anodes have rarely been reported.

Herein, we summarize recent progress on the application of 3D Cu-based current collectors in stable and dendrite-free alkali metal batteries (AMBs). The modification strategies of 3D Cu-based current collectors and corresponding electrochemical performances in LMBs are first reviewed. The preparation or modification methods, nano- or microstructures, and electrochemical properties of 3D Cu-based CCs based on different designs are systematically summarized and discussed in this section. Furthermore, the recent progress in relation to modified 3D Cu-based CCs in sodium metal batteries (SMBs) and potassium metal batteries (PMBs) is also summarized. Finally, we put forward the prospect of using 3D Cu-based CCs for high-performance AMBs.

2. 3D Cu-Based CCs for LMBs

Lithium metal batteries are considered promising candidates for use in the next generation of high-energy-density batteries. However, as mentioned above, lithium metal anodes face serious problems of dendrite growth and volume change, which hinder the practical application of LMBs. To tackle these problems, the researchers proposed using 3D CCs as lithium hosts. Meanwhile, a reasonable electrode structure can also promote the rapid transport and uniform deposition of lithium ions [51]. Due to their good electrical conductivity and processability [52], Cu-based materials have been widely studied for use in the construction and modification of 3D current collectors. To date, most of the researches on three-dimensional Cu-based CCs have focused on the three-dimensional structure design (or structural modification) and surface chemical modification of the current collectors. In this chapter, we will systematically introduce the modification strategies commonly used in three-dimensional Cu-based CCs and the corresponding electrochemical properties of Cu-based CCs in LMBs.

2.1. Structural Modification

Structural modification is a strategy to promote the uniform deposition of lithium ions, mitigate volume changes in lithium metal anodes, and enhance the stability of LMAs by designing or adjusting the structure of the current collector [53,54]. To date, several methods have been widely used in the preparation of three-dimensional copper-based current collectors, including the template method [55], the dealloying method [56], the electrodeposition method [57], etc.

2.1.1. Template Method

The template method is an important technique used to fabricate micro- and nanostructured materials [52], especially in the preparation of porous materials. Materials with different structures can be prepared by using different templates. This method has been widely used in the preparation of 3D Cu-based CCs. Besides this, according to the types of templates, template method could be roughly divided into the inorganic template method and the organic template method.

The inorganic template method uses inorganic materials as templates to prepare other materials with different 3D structures. For example, He and co-workers reported 3D Cu-based CCs prepared by using NaCl as the template [43]. After the NaCl template is removed, the copper powder is successfully converted into a 3D Cu skeleton with abundant micropores. The open micrometer-sized pores and high surface area of the 3D CCs can promote the uniform distribution of Li^+ flux and homogeneous Li plating. Consequently, the CE of Li deposition on the 3D CCs was maintained above 95% at 400 cycles at 1 mA cm^{-2}. In addition, Chen et al. prepared a lithiophilic hyperbranched Cu nanostructure on Cu foil using an anodic oxide aluminum (AAO) membrane as the template [58]. Figure 1a shows the process of fabricating the CCs and the anodes. With the assistance of the AAO membrane, the vertically aligned Cu (VA-Cu) pillars were deposited on the Cu foil. After that, as shown in Figure 1b, the hyperbranched oxides were grown in-situ on the Cu pillars. The numerous lithiophilic Cu_xO hyperbranches can act as nucleation sites, thus promoting homogeneous Li deposition. Compared with copper foil (99.2 mV), Cu@Cu_xO exhibits a lower nucleation overpotential (44.3 mV) at 1 mA cm^{-2} and 1 mAh cm^{-2}. Therefore, the Li/Cu@Cu_xO electrodes exhibited a low and stable overpotential of 20 mV, and could maintain this over 600 cycles at 1 mA cm^{-2} and 1 mAh cm^{-2}, as presented in Figure 1c. Moreover, the Li/Cu@Cu_xO||$LiFePO_4$ full cell exhibited a high specific capacity and a high-capacity retention rate of 87.6% after 300 cycles, as shown in Figure 1d. The outstanding electrochemical performances can be ascribed to the improved lithiophilicity and sufficient nucleation sites, which promote uniform Li deposition. Meanwhile, the 3D structure also contributes to cycling performance due to the effect of mitigating the electrode volume change.

In addition, some organic compounds can also be used as templates to prepare or modify 3D Cu-based CCs. For example, Stan and coworkers reported an open-porous 3D Cu-based current collector by using polylactic acid (PLA) nanoparticles as the template [59]. These 3D structures with large specific surface areas can effectively reduce local current density and nucleation overpotential. Moreover, the dendrite growth and volume change are also alleviated due to the abundance of internal space. As a result, the performance of a full battery with zero-excess lithium assembled from this current collector has been significantly improved. Similarly, Ke et al. successfully prepared highly porous copper structures on copper foam (HPC/CF) using polystyrene (PS) microspheres as the template [60]. Figure 1e shows the fabrication process of the 3D HPC/CF composite. The 3D hierarchically bicontinuous porous skeleton has numerous highly curved submicron-sized copper ligaments, which can be used as the preferred Li deposition sites, as presented in Figure 1f. The HPC/CF have a larger pore area (0.05 m^2 g^{-1}) than pristine Cu foam (0.023 m^2 g^{-1}), and the pore volume of the HPC/CF can reach 0.5216 cm^3 g^{-1}, which provides abundant internal space to accommodate the deposited lithium, relieving the volume change of the electrode. The 3D HPC/CF current collectors can effectively suppress the Li dendrites' growth and improve the Li plating/stripping behavior. As a result, the LMAs derived from the 3D HPC/CF skeleton exhibited a high capacity for retention of 71.1% at 2 C for 500 cycles, which shows a good application prospect, as displayed in Figure 1g. The outstanding cycling performances can be ascribed to the inhibition of dendrite growth owing to the superior Li dendrite growth inhibition achieved through the novel structural design.

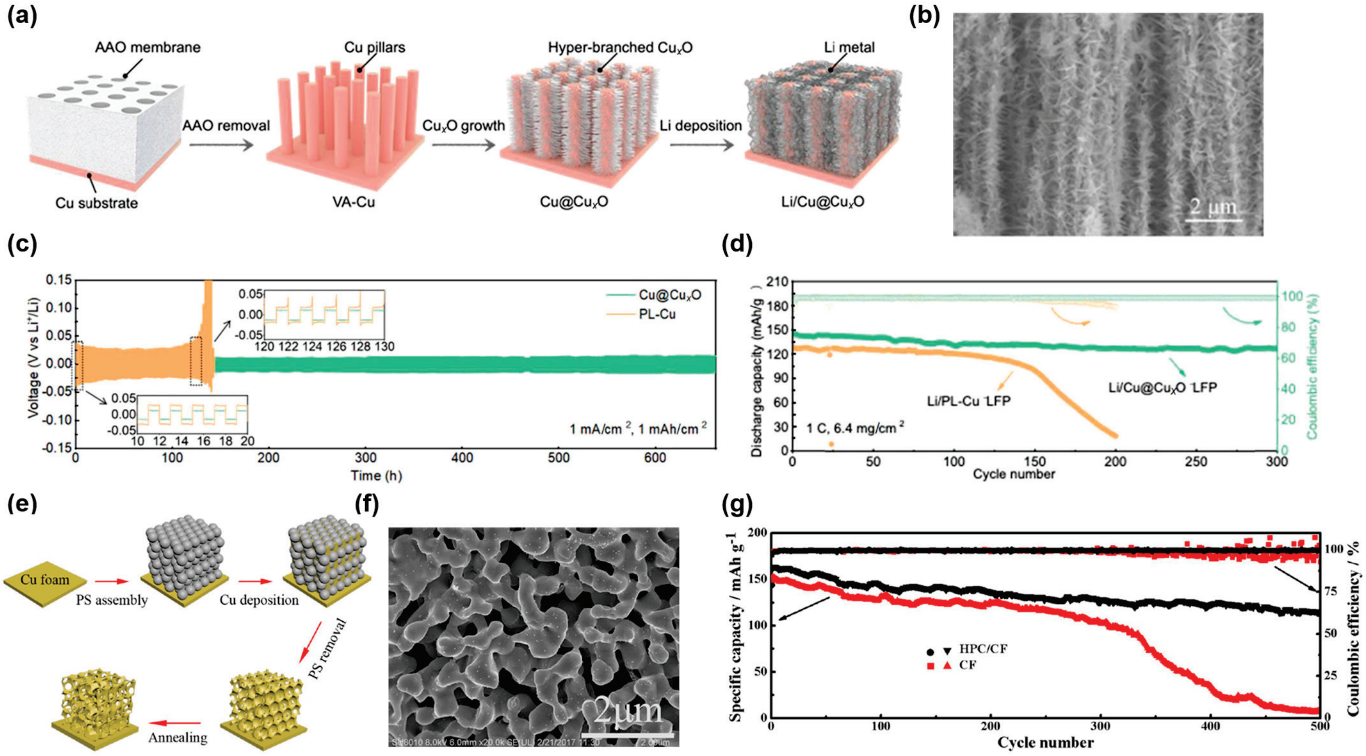

Figure 1. (**a**) Synthesis procedure of Cu@Cu_xO current collector and Li/Cu@Cu_xO electrode. (**b**) Side-view scanning electron microscopy (SEM) images of Cu@Cu_xO. (**c**) Galvanostatic voltage profiles of Li/Cu@Cu_xO and Li/PL–Cu symmetric cells. (**d**) Cycling performance of Li/Cu@Cu_xO | LFP and Li/PL–Cu | LFP at 1 C. Reprinted with permission [58]. Copyright 2023, Wiley-VCH. (**e**) Schematic illustration of the synthetic procedure of the 3D HPC/CF. (**f**) SEM images of the 3D HPC/CF. (**g**) Cyclic stability of Li@3D HPC/CF | LFP and Li@CF | LFP full cell at 2 C. Reprinted with permission [60]. Copyright 2018, American Chemical Society.

In summary, the 3D Cu-based CCs prepared by the inorganic template method or the organic template method have shown a good application prospect in improving the stability of LMAs. However, the reusability of templates and their suitability for large-scale preparation need to be further considered and improved.

2.1.2. Dealloying Method

The dealloying method is a technique that removes some specific components from an alloy to construct 3D skeletons with interconnected channels and nanopores [61]. The dealloying method is widely used to construct 3D copper current collectors due to the adjustable porosity and ease of operation it offers [62]. At present, the main technological routes of dealloying can be divided into three categories: chemical etching [63,64], vapor dealloying [65] and electrochemical etching [66].

Chemical etching is a facile, low-cost, and controllable preparation technique. For example, Li et al. used sulfuric acid (H_2SO_4) and zinc sulfate ($ZnSO_4$) solution to etch brass foils (Cu–Zn alloy) and prepared Cu-based CCs with 3D structures [67]. The prepared porous Cu could promote uniform Li deposition and suppress the growth of Li dendrites. The porous Cu CC showed a high and stable CE and low overpotential. Compared to planar Cu foil, the porous Cu can significantly improve the cyclic stability of LMBs.

Furthermore, based on the differences in the melting and boiling points and saturated vapor pressures of different alloy components, one or several alloy components in precursor alloy can be evaporated to construct a three-dimensional skeleton structure, which is called the vapor dealloying method [68]. For example, Qian and coworkers prepared the 3D porous Cu-based CCs via a facile vacuum distillation method from brass foils [46]. Cu CCs with different pore structures can be prepared by adjusting distillation time and temperature. The 3D porous Cu can suppress Li dendrite growth and mitigate the volume change during the Li stripping/plating process. The as-prepared Cu CCs exhibited stable CE and low overpotential, thus improving the performance of LMAs. Similarly, Wang's group reported a lithiophilic 3D Cu–CuSn porous framework, produced via a vapor phase dealloying method [69]. Figure 2a shows the procedures of fabricating 3D Cu–CuSn and the composite anode (3D Cu–LiSn–Li). Due to the sublimation of Zn and the diffusion of Cu and Sn, many irregular holes (diameters of 2–5 μm) are produced on the surface of the 3D Cu–CuSn, as shown in Figure 2b. The corresponding elemental EDS mapping images also show that copper and tin are uniformly distributed. The 3D Cu–CuSn displays a lower nucleation overpotential of 66.7 mV than the Cu foil (96.3 mV) at 1 mA cm^{-2} and 1 mAh cm^{-2} due to the improvement of the lithiophilicity. After the infusion of molten lithium, an alloying reaction occurs, the principle of which is shown in Equation (1).

$$2Cu_{41}Sn_{11} + 55Li \rightarrow 11Li_5Sn_2 + 82Cu \tag{1}$$

The resulting LiSn alloy can promote uniform Li deposition and the rapid migration of Li-ions. The 3D porous skeleton can suppress dendrite growth and alleviate the volumetric expansion of the electrode. As a result, the 3D Cu–LiSn–Li||LFP full cell exhibited a superior cycling performance at 5 C, as presented in Figure 2c. Moreover, the 3D Cu–LiSn–Li||LFP full cell showed a better rate performance than the Bare Li||LFP full cell at various rates (Figure 2d).

In addition to chemical etching and vapor dealloying, electrochemical etching is also investigated for use in the preparation of 3D Cu CCs. For instance, Zhao et al. fabricated a 3D porous Cu CC as a Li host via the electrochemical etching of copper–zinc alloy [70]. The as-prepared uniform and compact 3D porous structure not only has high electrical conductivity and mechanical properties, but also helps to form a smooth and stable SEI. The excellent properties and suitable porous structure of the 3D Cu can effectively inhibit lithium dendrites and dead lithium from arising. Consequently, the Li@3D Cu||$LiFePO_4$ full cells exhibited superior cycling and rate performance. Similarly, Li and coworkers reported a three-dimensional hierarchical porous copper (3DHP Cu) CC produced via an electrochemical dealloying method [71]. The preparation process of 3DHP Cu is shown in Figure 2e. After dealloying, a homogeneous and compact porous structure can be observed on the Cu surface, as presented in Figure 2f. The hierarchical distribution of micropores and nanopores (500–800 nm) can promote the migration of Li-ions, make the current distribution uniform, and alleviate the volume change. The symmetric cells based on 3DHP Cu could stably cycle for more than 250 h at 3 mA cm^{-2} and 1 mAh cm^{-2} with a low overpotential (Figure 2g). Moreover, the Li@3DHP Cu||LiFePO$_4$ full cell exhibited superior rate capability, as shown in Figure 2h. The outstanding electrochemical performances can be attributed to enhanced electrode reaction kinetics and uniform Li plating, because the hierarchical distribution of micropores and nanopores provides rich lithium-ion rapid transport channels.

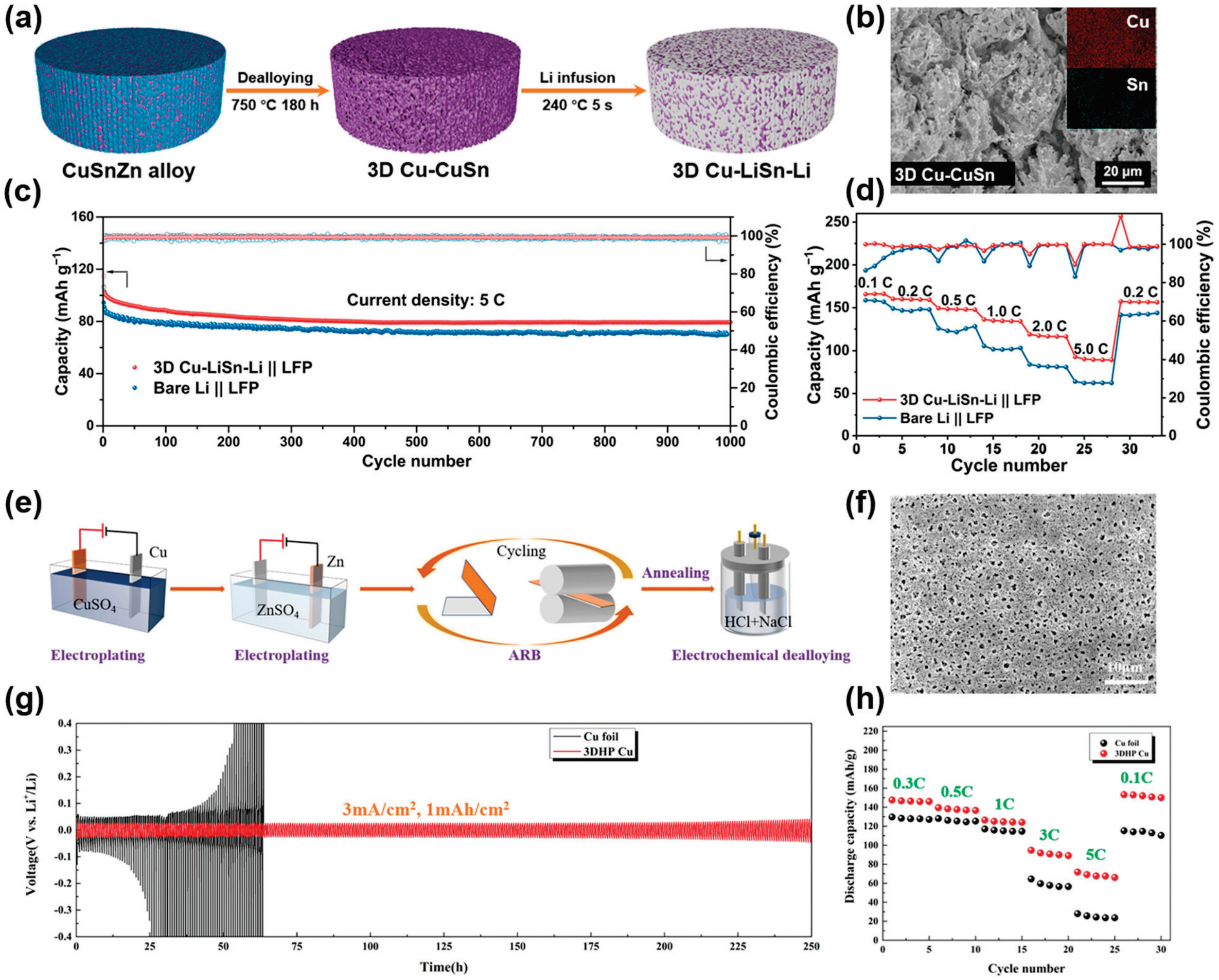

Figure 2. (**a**) Progress of synthesizing the 3D Cu–CuSn and 3D Cu–LiSn–Li electrodes. (**b**) Cross-sectional SEM images with the corresponding EDS elemental mapping of the 3D Cu–CuSn. (**c**) Cycling stability of the 3D Cu–LiSn–Li||LFP and Li||LFP batteries at 5 C. (**d**) Rate capabilities of 3D Cu–LiSn–Li||LFP and Li||LFP full cells. Reprinted with permission [69]. Copyright 2023, American Chemical Society. (**e**) Schematic diagram of the preparation of 3DHP Cu. (**f**) SEM image of the 3DHP Cu from the top view. (**g**) Galvanostatic cycling performance of Li@3DHP Cu electrode. (**h**) Rate capabilities of Li@Cu||LFP and Li@3DHP Cu||LFP cells. Reprinted with permission [71]. Copyright 2021, American Chemical Society.

In summary, dealloying is a facile method for preparing 3D Cu-based CCs. Various dealloying techniques have their own characteristics. Chemical dealloying often uses acid and alkali solutions as etching solutions, which is not friendly to the environment. Hence, it is necessary to study green etchants as part of the development of chemical dealloying technology. In contrast, electrochemical dealloying usually uses salt solutions and has less impact on the environment. However, the effect of electrochemical dealloying is affected by many factors, including voltage, current, time, temperature, etc. Therefore, it is important to explore the interaction between different factors. The vapor dealloying process is simple and friendly, but it is limited by the melting and boiling points of the alloy components, and the energy consumption is high in some cases.

2.1.3. Electrodeposition

Electrodeposition involves the formation of a coating through the transfer of positive and negative ions within an electrolyte solution, induced by an external electric field. This process involves oxidation-reduction reactions on the electrode, resulting in the gain and loss of electrons. Electrodeposition is also widely used in the preparation of 3D CCs.

One of the more commonly used methods for preparing 3D copper structures is to electroplate copper on the planar Cu substrate. However, the deposited copper is easily fractured from the substrate due to its brittleness. In view of this, Volder and coworkers fabricated 3D Cu–CNT composites with mechanically resilient structures via co-plating carbon nanotubes (CNTs) with Cu on the copper substrate [72]. The 3D Cu–CNT CC with an open porous structure and suitable specific surface area can accommodate the plating of Li and avoid the excessive consumption of electrolytes caused by the introduction of CNTs. Moreover, the 3D Cu–CNT composites can also be calendered without damaging the structure, which has great potential in relation to improving the specific energy of LMBs. In addition, to inhibit the growth of lithium dendrites and unstable surface reactions, Kim et al. proposed an “Li dendrite cage” strategy and prepared a 3D interconnected porous Cu foam CC for LMA via a simple electrodeposition method [73]. Figure 3a shows the procedure of fabricating the 3D interconnected porous Cu foam. The surface morphology of the 3D Cu foam is presented in the SEM image (Figure 3b). With the assistance of a dynamic hydrogen bubbles template, three-dimensional porous structures with an average pore diameter of 12 μm were successfully fabricated on copper foil. The thickness of the 3D Cu foam is ~17 μm, as presented in the cross-sectional SEM (Figure 3c). Figure 3d shows the CE performance of 3D Cu foam and Cu foil at 0.5 mA cm^{-2}, which exhibits that the CE of 3D Cu foam is more stable than the Cu foil. This can be ascribed to the advantage of the “cage effect”, that is, the dendrite’s growth is restricted within the abundant inner pores, inhibiting its growth to the outside, as shown in Figure 3e. Meanwhile, volume changes during the cycles are also mitigated due to the sufficient space within 3D structures. In addition, Zhang et al. prepared an ultrathin 3D array-structured Cu current collector via electrodeposition [74]. Firstly, the patterned design is established, and then the copper is electrodeposited to obtain the 3D current collector, as presented in Figure 3f. The surface morphology of the Cu CC can be observed in Figure 3g, h. This current collector (referred to as CMMC) has a low areal density, making it ultra-thin and lightweight, which helps in the construction of high-energy-density LMBs. Figure 3i shows the cycling performance of symmetrical cells at 0.2 mA cm^{-2} and 0.2 mAh cm^{-2}. The Li–CMMC electrode exhibited a stable cycling over 2000 h at a low polarization voltage of 12 mV. Due to the synergistic effect of lithiophilic Cu_xO and its appropriate structural design, the full cells with CMMC exhibited good cycling performance. Furthermore, as shown in Figure 3j, the capacity retention rate of the CMMC–Li | | $LiFePO_4$ full cell can reach 71% after 100 cycles.

2.1.4. Others

Apart from the several methods mentioned above, some other works have been reported. For example, Zhang et al. obtained an ultrathin hierarchical porous Cu CC through the anodic oxidation method [75]. The uniform 3D micro/nanopores could effectively homogenize the local electric field and induce uniform Li deposition, thereby suppressing the Li dendrites’ growth and forming a stable SEI layer. As a result, the full cell’s performance with this current collector is improved. As a material preparation technology that has developed rapidly in recent years, the application of 3D printing in the field of energy storage, especially in rechargeable batteries, has been widely investigated. For example, Lei and coworkers reported a 3D Cu mesh produced by 3D printing [76]. Unlike the uneven electric field on the surface of the traditional Cu CC, the 3D-printed structures can effectively modulate the electric field distribution and provide sufficient internal space for Li deposition. The subsequent electrochemical properties also indicate that the 3D Cu mesh could suppress Li dendrite growth, improve CE, and mitigate volume changes, which shows the great potential of using 3D printing in the preparation of a 3D current collector.

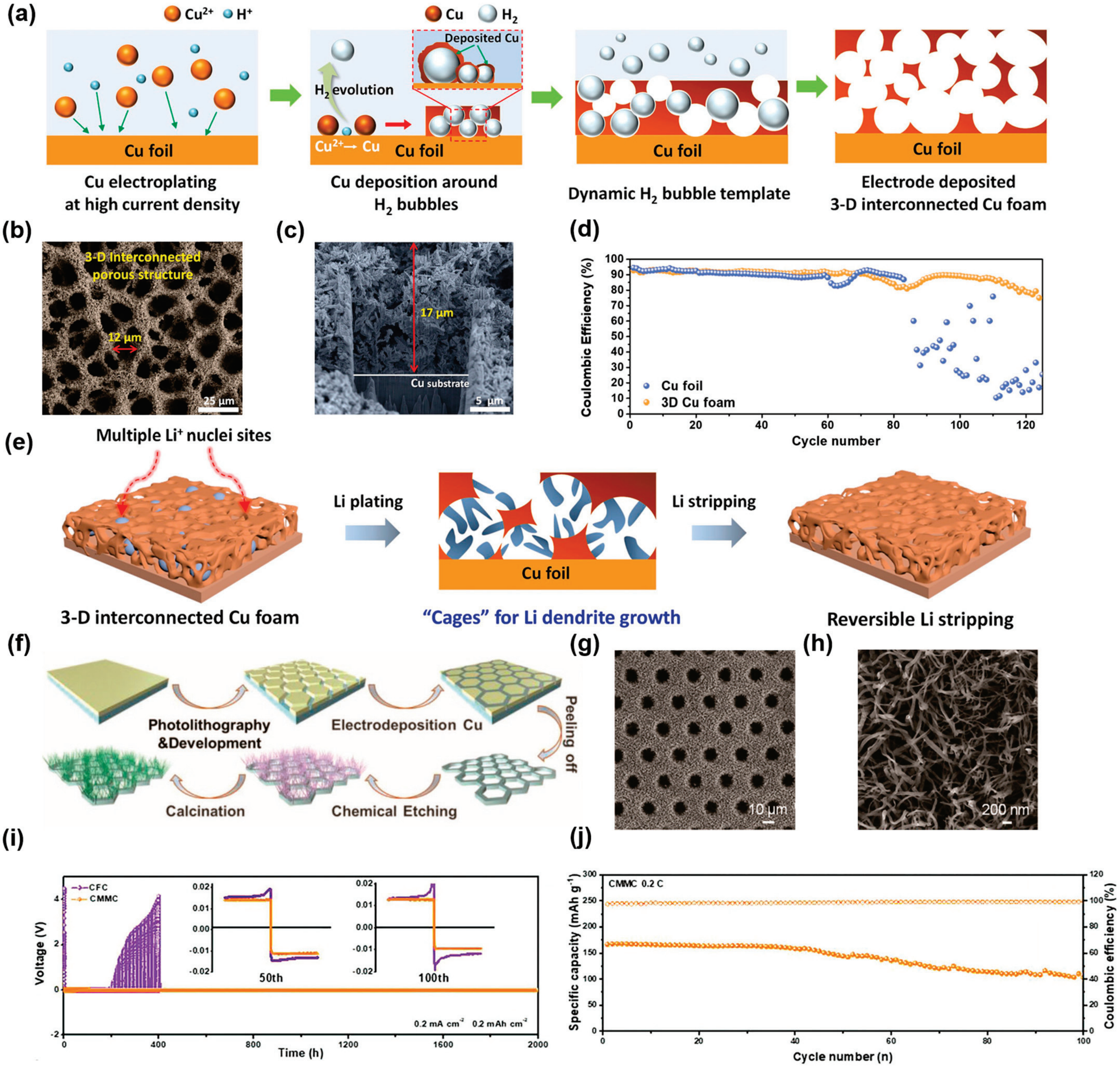

Figure 3. (**a**) Schematic illustration of the method of synthesizing 3D interconnected porous Cu foam. (**b**) SEM image of 3D Cu foam. (**c**) FIB–SEM image of 3D interconnected porous Cu foam. (**d**) Cycling performance of 3D Cu foam. (**e**) Li nucleation and plating/stripping behavior on 3D Cu foam electrode. Reprinted with permission [73]. Copyright 2023, Elsevier. (**f**) Process of synthesizing CMMC. (**g**) SEM images of CMMC. (**h**) SEM images of CMMC. (**i**) Cycling performances of Li–CMMC and Li–CFC electrodes. (**j**) Cycling stability of CMMC–Li | | LFP battery at 0.2 C. Reprinted with permission [74]. Copyright 2023, Wiley-VCH.

2.2. Chemical Modification

In addition to designing or adjusting the structure of the current collector, other materials can also be introduced to improve the surface properties of the Cu CCs. This class of methods can be classified as chemical modifications, which include functional spot modification [77,78], oxidation modification [79,80], protective layer modification [81] and so on.

2.2.1. Functional Spot Modification

Previous studies have shown that lithium has a large nucleation overpotential on a copper substrate, which indicates that copper's surface is lithiophobic [82]. Therefore, improving the surface properties of Cu CC and enhancing its lithium affinity can promote uniform Li deposition and improve the cyclic stability of LMBs.

Cui and coworkers found that some metals (such as Au, Ag, Zn and Mg) can form alloys with lithium to reduce nucleation overpotential and induce uniform Li deposition [82]. For instance, Han and coworkers introduced lithiophlic Ag nanoparticles (Ag NPs) onto graphene sheets as lithium hosts, achieving the uniform deposition of lithium [83]. Similarly, these metals can be employed to modify the copper current collectors, thereby augmenting the lithiophilicity of the Cu-based current collectors. For example, Chen et al. prepared silver-modified copper mesh as a current collector via the magnetron sputtering method [84]. The process of fabricating Cu mesh with Ag layer (CuM/Ag) is shown in Figure 4a. The lithiophilic Ag layer is uniformly distributed on the Cu framework (Figure 4b). Figure 4c shows the structure of the Cu/Ag/Li composite anode (Li@CuM/Ag) under an optimal microscope. As shown in Figure 4d, CuM/Ag exhibited negligible nucleation overpotential due to the excellent lithiophilicity of CuM/Ag. The silver layer could effectively reduce nucleation overpotential and induce uniform lithium deposition at the nucleation sites. The Li-Ag alloy produced by the reaction of the silver layer with lithium shows better reversibility during the process of Li deposition/stripping and interfacial reaction kinetics. Hence, Li@CuM/Ag symmetric cells can stably cycle over 1000 h at 0.5 mA cm^{-2} and 1 mAh cm^{-2}, and the overpotential is only 25 mV, as shown in Figure 4e. Figure 4f shows the cyclic stability of full cells. At the rate of 2 C, the initial specific capacity (146 mAh g^{-1}) and the capacity retention rate (86.39% after 150 cycles) of the Li@CuM/Ag||$LiCoO_2$ full cells are higher than those of Li@Cu mesh||$LiCoO_2$ and Li||$LiCoO_2$ full cells. The excellent cycling performances can be attributed to the enhanced lithiophilicity and uniform Li deposition because of the introduction of a silver layer onto the Cu mesh. In addition to some commonly used lithiophilic metals, such as zinc, silver, etc., the application of some metals (such as bismuth, tungsten, gallium, germanium, vanadium, etc.) and their compound materials in the field of energy storage is gradually being explored [85–90]. For instance, Geaney and coworkers reported a novel Germanium (Ge) nanowires (NWs)-modified 3D Cu-based current collector [91]. The synthesis procedure is shown in Figure 4g. The thermal decomposition of diphenyl germane (DPG) stimulates the growth of Ge NWs from a copper germinide (Cu_3Ge) seed. Such Ge NWs grows directly on the surface of copper without binders or conducting agents, helping to improve the energy density of LMBs. Figure 4h shows the morphology of the Cu–Ge surface. Ge NWs can be observed to grow densely on the surface of copper. Densely grown Ge NWs have high lithiophilicity and can provide abundant lithiophilic anchoring sites, which is conducive to regulating lithium-ion flux, lowering the local current density, and facilitating homogeneous Li plating. As a consequence, the Cu–Ge CC exhibited stable cycling (>400 cycles) and a high average CE (99.2%) at 0.5 mA cm^{-2} and 1 mAh cm^{-2}, as shown in Figure 4i. Moreover, the Cu–Ge@Li–NMC full cell with a high-voltage NMC811cathode can cycle steadily for 150 cycles at 0.5 C with almost no capacity loss, as presented in Figure 4j. The superior electrochemical properties can be ascribed to the novel 3D structure and excellent lithiophilicity due to the introduction of Ge NWs.

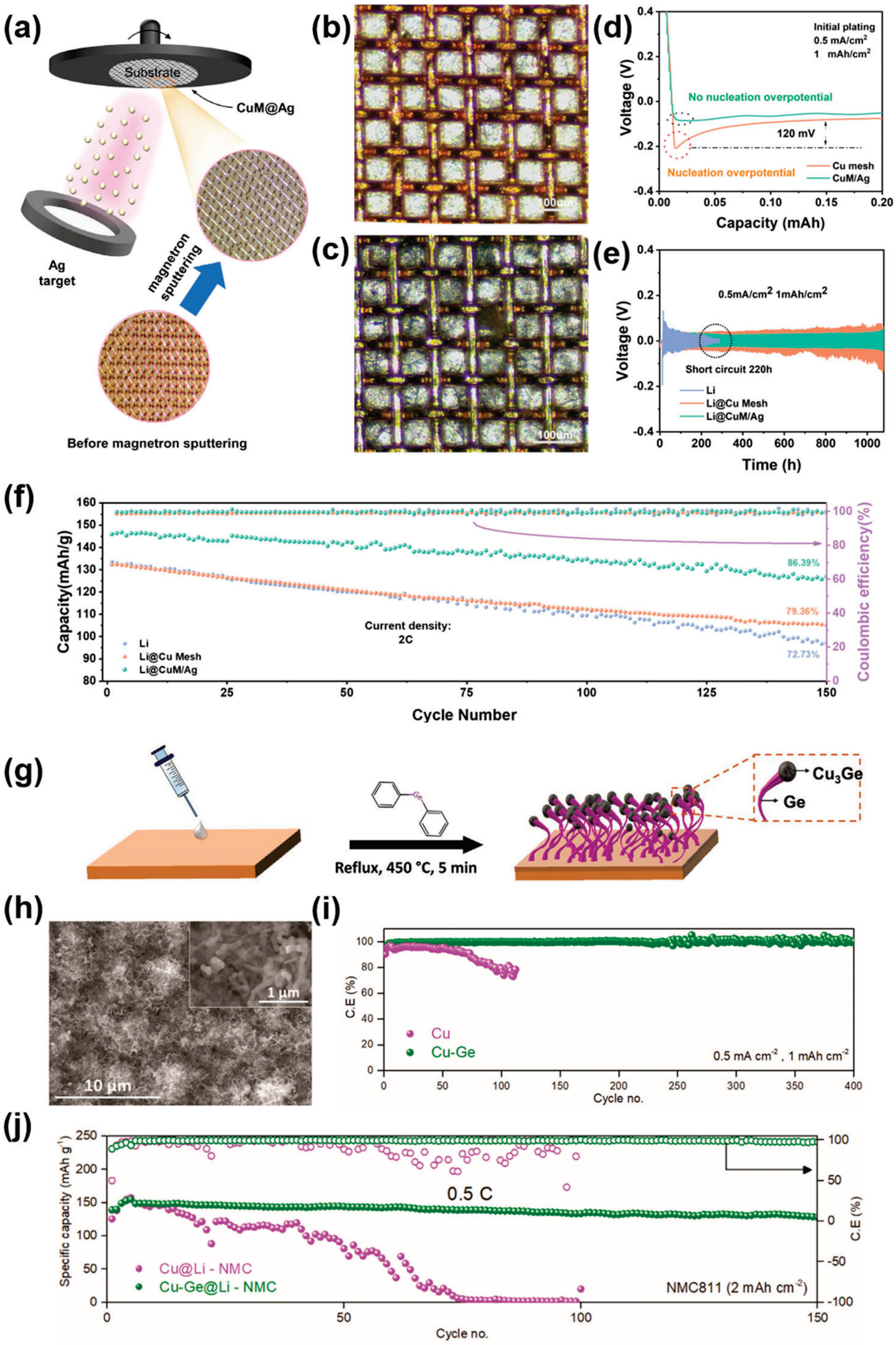

Figure 4. (**a**) Schematic diagram of method of synthesizing CuM/Ag. (**b**) Digital photos of CuM/Ag under optical microscopy. (**c**) Digital photographs of Li@CuM/Ag. (**d**) Voltage curves of Li plating on Cu mesh and CuM/Ag. (**e**) Cycling performance of Li, Li@Cu mesh, and Li@CuM/Ag electrodes. (**f**) Cyclic stability of Li@CuM/Ag||LCO cell at 2 C. Reprinted with permission [84]. Copyright 2023, Wiley-VCH. (**g**) Schematic diagram of Ge NWs synthesis on Cu foil. (**h**) SEM image of Cu-Ge. (**i**) Electrochemical performance of the Gu–Ge. (**j**) Cycling stability of Cu–Ge@Li–NMC811 battery at 0.5 C. Reprinted with permission [91]. Copyright 2023, Wiley-VCH.

2.2.2. Oxidation Modification

In addition to introducing lithiophilic sites, copper oxides (CuO and Cu_2O) have been demonstrated to be beneficial in promoting the uniform deposition of lithium. This is because copper oxides can improve the lithiophilicity of Cu-based CCs, promote the transport of Li-ions and enhance the stability of SEI by the in-situ formation of Li_2O with Li. This method of oxidizing copper to obtain copper oxides, thereby improving the lithiophilicity of the CCs and facilitating homogeneous Li deposition, is called the oxidation modification. The most commonly used oxidation methods include electrochemical anodizing [92], chemical oxidation [79], thermal oxidation [93], etc.

The oxidation treatment of copper foil is a facile method used to construct three-dimensional current collectors based on planar copper. At the same time, copper oxides can also enhance the lithiophilicity of the Cu substrate. For instance, Liu et al. fabricated a 3D integrated gradient Cu-based CC via electrochemically anodizing [92]. The 3D structure is achieved by growing copper oxide (CuO) nanowire arrays on the copper foil, and the synthesis procedure is shown in Figure 5a. The morphology of CuO nanowire arrays is shown in Figure 5b. The density of the CuO nanowire arrays has a great influence on the Li deposition behavior, which depends on the anodizing time. According to the different anodizing times, the prepared current collectors can be divided into S–CuO@Cu (anodizing for 100 s), M–CuO@Cu (anodizing for 500 s), and D–CuO@Cu (anodizing for 1000 s). Sparse nanowire arrays (S–CuO@Cu) expose a considerable amount of the lithiophobic surface and cannot inhibit Li dendrite growth. Excessively dense nanowire arrays (D–CuO@Cu) hinder the downward deposition of lithium ions due to the blockage of channels during Li nucleation, causing the top deposition of lithium. Only the uniform nanowire arrays (M–CuO@Cu) can induce the bottom-up deposition of lithium and inhibit the generation of Li dendrites. Therefore, as shown in Figure 5c, M–CuO@Cu–Li exhibited excellent cyclic stability with a low voltage hysteresis for more than 1200 h at 1 mA cm^{-2} and 1 mAh cm^{-2}. Moreover, the LFP||M–CuO@Cu–Li full cell displayed excellent cyclic performance, with a capacity retention rate of approximately 88% after 300 cycles at 1 C, and the full cell maintained high and stable Coulombic efficiency simultaneously (as shown by red stars), as presented in Figure 5d. The excellent cycling performances can be attributed to the reasonable nanowire arrays structures and enhanced lithiophilicity. It is also proven that a reasonable three-dimensional structure is of significance for uniform lithium deposition.

In addition to copper foil, the 3D Cu (such as copper foam, copper mesh) can also be modified by oxidation. For example, Qian and coworkers reported the production of pressure-tuned and surface-oxidized copper foams (RCOFs) via chemical oxidation and mechanical compression [94]. The preparation procedure is shown in Figure 5e. After mechanical rolling, RCOFs still maintained their 3D structure, and the morphology is shown in Figure 5f. Cu_xO improves the lithiophilicity of copper foam, and the pore structure of copper foam is regulated by mechanical roller pressing. The synergistic effects of surface modification and structural regulation give RCOFs good electrochemical properties. The symmetric cells-based RCOFs can cycle for 2000 h with a low and stable polarization at 5 mA cm^{-2} and 1 mAh cm^{-2}, as presented in Figure 5g. The Li–RCOFs//LFP full cell exhibited a high capacity for retention of 99% after 500 cycles at 1.2 C (Figure 5h), which shows the obvious superiority of this joint modification strategy. The outstanding electrochemical performances can be ascribed to the reasonable adjustment of the porosity and lithiophilicity of Cu foam by mechanical rolling and oxidation treatment.

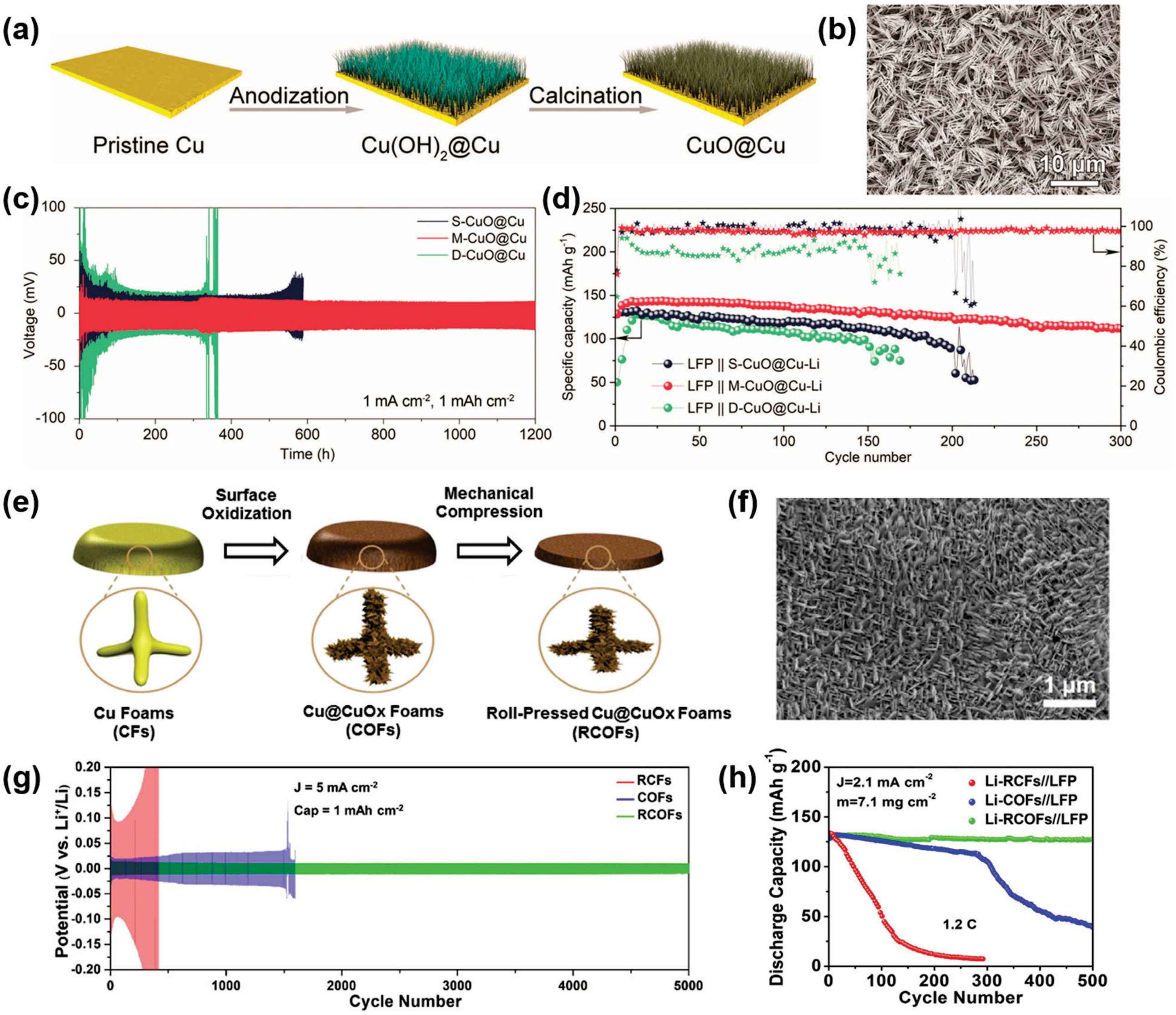

Figure 5. (**a**) Process of synthesizing CuO@Cu nanowire arrays. (**b**) SEM image of the surface view of M–CuO@Cu nanowire arrays. (**c**) Cycling stability of CuO@Cu–Li anodes in symmetric cells. (**d**) Cycling performance of LFP | | CuO@Cu–Li full-cells at 1 C. Reprinted with permission [92]. Copyright 2023, Wiley-VCH. (**e**) The fabrication of roll-pressed Cu@CuO$_x$ foams (RCOFs). (**f**) SEM image of RCOFs. (**g**) Cycling performances of Li–RCOFs electrode. (**h**) Cycling performances of Li–RCOFs//LFP cell. Reprinted with permission [94]. Copyright 2020, Elsevier.

2.2.3. Protective Layer Modification

A major obstacle in the application of LMA is its high reactivity. The reaction of lithium with the electrolyte causes the consumption of the electrolyte and the loss of active Li, and the generated weak SEI is also not conducive to uniform Li deposition. To solve this problem, the strategy of constructing an artificial protective layer (or artificial SEI) on Cu-based CCs has been proposed and studied extensively.

Organic materials have been widely studied for their use as modification layers on Cu-based CCs due to their good structural flexibility and interfacial compatibility with lithium metal. Furthermore, organic materials contain abundant polar functional groups. On the one hand, these functional groups can be adsorbed on the surface of the copper current collector through bonding or other interactions, avoiding the “tip effect”; on the other hand, polar functional groups can absorb Li-ions and improve the chemical affinity between Li-ions and the electrolyte, thus homogenizing lithium-ion flux and promoting uniform Li deposition. For example, Jiang et al. fabricated a 3D Cu-based

CC modified with polydopamine (PDA) by laser processing and chemical treatment [95]. The preparation process is illustrated in Figure 6a. Laser processing provides a planar Cu-rich internal space and large specific surface area. Moreover, the PDA thin layer with abundant lithiophilic functional groups (such as –OH and $–NH_2$) can effectively decrease the nucleation overpotential and facilitate uniform Li nucleation and deposition, as displayed in Figure 6b. Furthermore, the PDA layer can act as a strong artificial SEI layer to inhibit the growth of lithium dendrites and relieve volume expansion due to its excellent mechanical strength and toughness. Hence, the PDA@3D Cu electrode can cycle steadily for more than 1000 h with a low voltage hysteresis (~24 mV) at 0.5 mA cm^{-2} (Figure 6c).

Apart from organic protective layers, many inorganic materials have been investigated as protective layers of Cu-based CCs. For example, Liao and coworkers fabricated a Cu-based current collector modified with a Zn_3N_2 protective layer using filtered cathode vacuum arc (FCVA) technology [96]. When lithium ions are first deposited, the Zn_3N_2 protective layer reacts with lithium to generate LiZn alloy and lithium nitride (Li_3N). The LiZn alloy enhances the lithiophilicity of the Cu CC and acts as the nucleating seed to induce uniform Li nucleation and deposition. Meanwhile, Li_3N with high ion conductivity can be used as the artificial SEI layer to promote the transport of lithium ions and isolate the electrolyte and LMA. Therefore, the Zn_3N_2@Cu||LFP anode-free full cell exhibited a high-capacity retention rate of 63.1% after 100 cycles, which is significantly better than that of the Cu||LFP full cell (14.9% after 100 cycles). In addition, Piao and coworkers constructed a Cu-based 3D host modified with a multifunctional solid electrolyte interphase [97]. The procedure of synthesizing the modified 3D host (MSEI@Cu) is shown in Figure 6d. MSEI@Cu is prepared via a novel double-coating strategy. Specifically, Cu nanowires grown on a copper foam surface are covered by a double coating, which includes a compact surface carbon layer and an internal carbon matrix containing $CuSO_4$ and In_2S_3. After the reaction with lithium, an artificial SEI layer rich in Li_2S and Li_xIn is formed on the surface of MSEI@Cu. At the same time, the content of LiF is increased by facilitating the decomposition of $TFSI^-$ anions. The rich inorganic components significantly improved the mechanical properties and stability of SEI, and enhanced the transport kinetics of Li-ions. The amorphous carbon layer on the surface can accommodate the volume change of the electrode and isolate the contact between the electrolyte and the inner layer, inhibiting the excessive decomposition of the electrolyte. Hence, the electrochemical properties of the Li–MSEI@Cu were significantly improved. The symmetric cell with a Li–MSEI@Cu electrode can stably cycle for 1400 h, with a low overpotential of 15 mV at 1 mA cm^{-2} and 1 mAh cm^{-2} (Figure 6e). Accordingly, the Li–MSEI@Cu||LFP full cell exhibited excellent cyclic stability for 500 cycles with 80% capacity retention at 1 C, as shown in Figure 6f. The excellent cycling performances can be attributed to enhanced lithium-ion transport kinetics and the inhibition of the excessive decomposition of the electrolyte due to the ingenious design of multifunctional SEI. It is worth noting that the novel modification method provides a new idea for constructing a multi-functional artificial SEI.

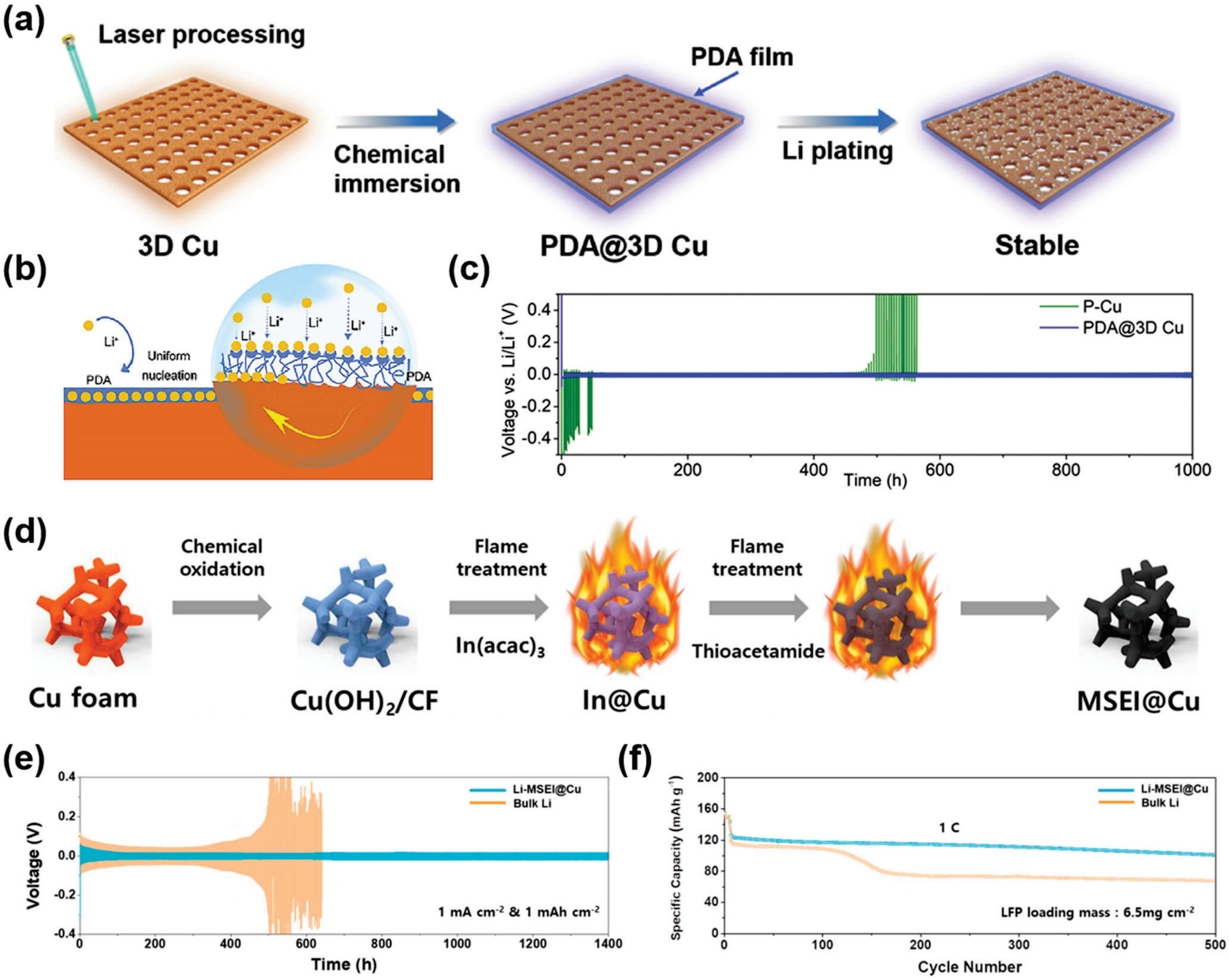

Figure 6. (**a**) Schematic diagram of the fabrication and lithiation process of PDA@3D Cu. (**b**) Schematic illustration of Li deposition through PDA layer. (**c**) Cycling performance of Li@PDA@3D Cu electrodes. Reprinted with permission [95]. Copyright 2020, Elsevier. (**d**) Process of synthesizing MSEI@Cu. (**e**) Cycling performances of Li–MSEI@Cu electrode. (**f**) Cycling stability of Li–MSEI@Cu | | LFP cell at 1 C (1C = 170 mAh g^{-1}). Reprinted with permission [97]. Copyright 2024, The Royal Society of Chemistry.

3. 3D Cu-Based CCs for SMBs and PMBs

Sodium metal anodes (SMAs) and potassium metal anodes (PMAs) are considered ideal alternatives to Li for use in next-generation high-performance batteries due to their high theoretical specific capacity and low cost. Similarly, as alkali metal anodes, they encounter the same problems and challenges as lithium metal anodes, such as dendrite growth, volume expansion, fragile SEI and so on [98–101]. Many research results have shown that 3D Cu-based current collectors can also be used in sodium metal batteries (SMBs) and potassium metal batteries (PMBs) to improve their performance.

To date, 3D Cu-based current collectors have been explored for use in sodium metal anodes [102,103]. For example, Chen et al. prepared a Cu_6Sn_5 alloy layer on Cu foils (Cu_6Sn_5@Cu) and applied it to sodium metal anodes [104]. The sodiophilic Cu_6Sn_5 can significantly reduce the nucleation overpotential of Na. Besides this, Cu substrates can alleviate the volume and stress changes during alloying and maintain the structural stability of the current collectors. As a result, the Cu_6Sn_5@Cu CC showed high average CE (over 99.84%) during 2000 cycles at 5 mA cm^{-2} and 1 mAh cm^{-2}. In addition, Huang's group reported a facile approach to stabilizing the SMAs by constructing Sn nanoparticles-anchored graphene on planar Cu (Sn@LIG@Cu) [105]. Figure 7a illustrates the process of preparing the Sn@LIG@Cu CC. The Sn nanoparticles can improve the sodiophilicity of Cu current collectors and reduce the Na nucleation overpotential, as shown in Figure 7b. The low overpotential (~5.2 mV) is conducive to Na nucleation and dendrite-free sodium deposition. Based on this, the Sn@LIG@Cu showed a high average CE after a long cycle. Moreover, the flexible polyimide (PI) columns can act as the binder and buffer layer, which can effectively mitigate the volume change of SMAs during cycling. The unique patterned structure design provides continuous channels for rapid ion transportation, thus promoting the Na-ions' transport kinetics. In view of this, the Na@Sn@LIG@Cu||NVP full cell exhibited superior cycling stability over 600 cycles with 90% retention capacity at 1 C (Figure 7c). The excellent electrochemical performances can be ascribed to enhanced Na^+ transport kinetics and dendrite-free sodium deposition due to their unique patterned structure and the introduction of sodiophilic Sn nanoparticles. Moreover, this unique structure design and advanced preparation method provide a feasible approach to the application of 3D Cu-based CCs on SMAs. When applied to alkali metal batteries, the Cu-based current collector has the problem of poor affinity with alkali metals. Therefore, the surface modification of Cu-based CCs has been widely investigated. For instance, Yu and coworkers fabricated a porous Cu skeleton modified with cuprous selenide nanosheets (Cu_2Se/Cu foam) via the selenization treatment of Cu foam [106]. The composite SMA (Na_2Se/Cu@Na) is prepared by infusing molten Na into a Cu_2Se/Cu foam, as shown in Figure 7d. The Cu_2Se nanosheets vertically grown on the surface of copper foam play crucial roles in improving the Na metal anode's performance (Figure 7e). On the one hand, the uniform distribution of Cu_2Se nanosheets can improve the sodiophilicity of Cu CC and promote the infusion of molten sodium, thus forming a composite anode, whereas the bare copper foam cannot be wetted by molten sodium to form a composite SMA. On the other hand, the Na_2Se nanosheet clusters formed after molten sodium infusion can promote the rapid transport of sodium ions and enhance the electrode reaction kinetics. Meanwhile, the 3D composite structure can homogenize the distribution of Na-ion flux, inhibit the volume change, and facilitate uniform Na deposition. As a result, the Na_2Se/Cu@Na||NVP ($Na_3V_2(PO_4)_3$) full cell delivered an initial charge capacity of 102 mAh g^{-1} with 95.1% capacity retention after 800 cycles, even at 10 C, as presented in Figure 7f. Moreover, as shown in Figure 7g, compared with bare Na||NVP full cells, the Na_2Se/Cu@Na||NVP full cells exhibit a higher discharge capacity, especially at high rates. Such excellent performances can be attributed to the fast sodium-ion transport and the stable three-dimensional structure. It is worth noting that the current collector is also applicable to potassium metal batteries, which indicates the excellent performance and great application potential of the 3D Cu-based CCs.

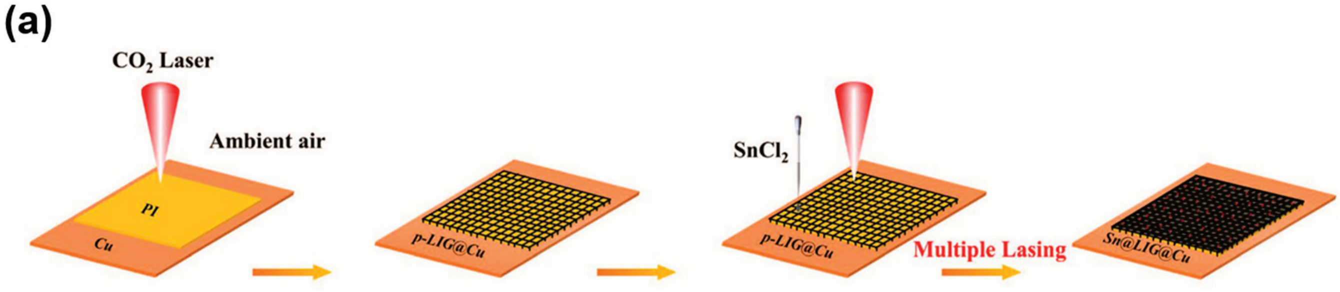

Figure 7. *Cont.*

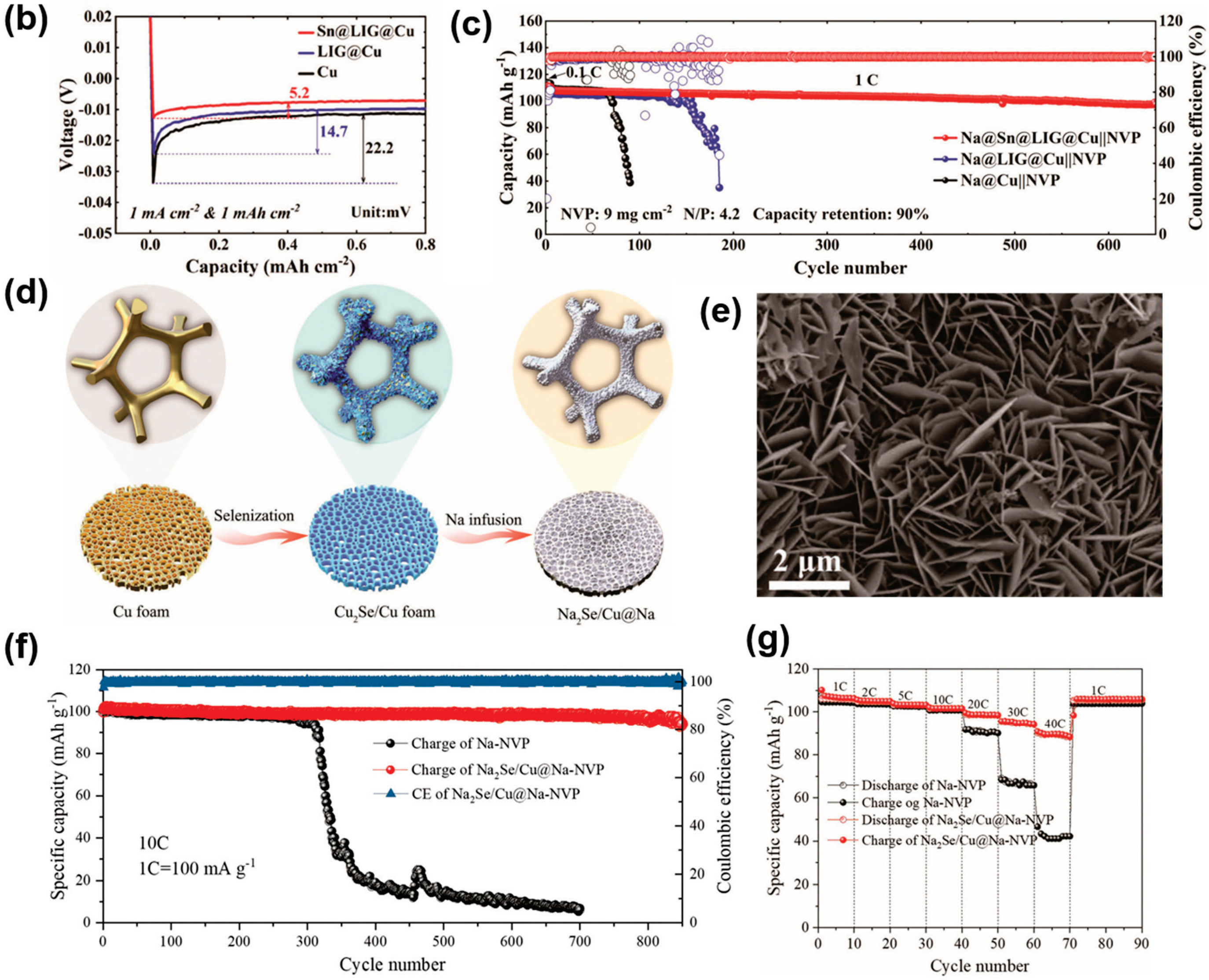

Figure 7. (**a**) Process of synthesizing Sn@LIG@Cu. (**b**) Voltage curves of Na deposition on different substrates. (**c**) The cycle performance of Na@Sn@LIG@Cu||NVP at 1 C. Reprinted with permission [105]. Copyright 2023, Wiley-VCH. (**d**) Synthesis procedure of Na_2Se/Cu@Na composite anode. (**e**) SEM image of CF/Cu_2Se. (**f**) The cycling performances of Na||NVP and Na_2Se/Cu@Na||NVP full batteries at 10 C. (**g**) The rate capacity of Na_2Se/Cu@Na||NVP full batteries. Reprinted with permission [106]. Copyright 2022, Wiley-VCH.

Apart from SMAs, 3D Cu-based CCs have also been investigated for PMAs [107,108]. For instance, Wang et al. designed a Cu_3Pt alloy-modified Cu mesh and applied it as the CC in PMBs [108]. The Cu_3Pt-Cu mesh has a coarse surface with massive nanoparticles, which can provide a large specific area and homogenize the distribution of electrical field and ion flux. Moreover, Cu_3Pt has excellent affinity for K, which can lower the nucleation overpotential and induce uniform K deposition. Accordingly, the full cell (Prussian blue (PB) as the cathode material, Cu_3Pt-Cu mesh as the anode CC) exhibited an ultralong lifespan over 250 cycles. Similarly, Zhang's group prepared a highly potassiophilic Pd/Cu CC, and investigated the application in a low-temperature K metal battery [109]. Figure 8a shows the fabrication process of the Pd/Cu current collector, K/Pd/Cu anode and the cell configuration. The coated Pd layer enhances the potassiophilicity of the CC, and the Cu foam with large specific surface area could lower the local current density, which enables the Pd/Cu current collector to exhibit excellent electrochemical performance. The Pd/Cu shows a more stable CE than bare Cu foam over 450 cycles at 0.5 mA cm^{-2} and 0.5 mAh cm^{-2} (Figure 8b). Moreover, the K/Pd/Cu||PB full cell can stably cycle over 60 cycles even at −20 °C due to its excellent dendrite inhibition ability, as displayed in Figure 8c. Due to the huge differences in the transport speeds of electrons and ions on the three-dimensional current collector, electrons are prone to accumulate at the top of the current collector and form current hot spots, which makes the growth of dendrites inevitable. Hence, surface modification has been shown to regulate the electron and ion transport of the current collector [110]. For example, Zhao and coworkers demonstrated an up-and-down "simultaneous" deposition model in low-temperature and dendrite-free PMBs [111]. They introduced copper selenide (CuSe) to the surface of the Cu foam through vacuum evaporation (Figure 8d). Afterward, a K_2Se/Cu (KSEC) conductive layer was obtained by reacting with potassiuam. The KSEC layer has low electron conductivity and can form an electric field gradient, thereby avoiding the accumulation of electrons and the formation of current hot spots. Meanwhile, the KSEC layer has excellent potassium ion transport kinetics, which could promote the rapid transfer of potassium ions from the top to the bottom for nucleation and deposition at the bottom. This strategy of simultaneously regulating the electronic and ionic conductivity of the 3D anode promotes uniform potassium deposition. Figure 8e shows the functional mechanism of KSEC. However, K_2S/Cu (KSC) prepared by the same method follows a top-down deposition model owing to the slow diffusion of potassium ions in the K_2S layer and the short diffusion distance, as presented in Figure 8f. Due to the reasonable structural and functional design, the KSEC electrode exhibited a long cycle lifespan over 1000 h with a low overpotential of 80 mV at 1 mA cm^{-2} and 1 mAh cm^{-2}, as shown in Figure 8g. Moreover, the KSEC–K|PTCDA full cell exhibited an excellent cycling stability over 500 cycles with a high-capacity retention at 2 C (Figure 8h). The superior cycling performances can be ascribed to the reasonable adjustment of the electronic and ionic conductivity via the formation of the KSEC layer. And more details about the electrochemical performances of 3D Cu-based CCs in AMBs can be found in Table 1.

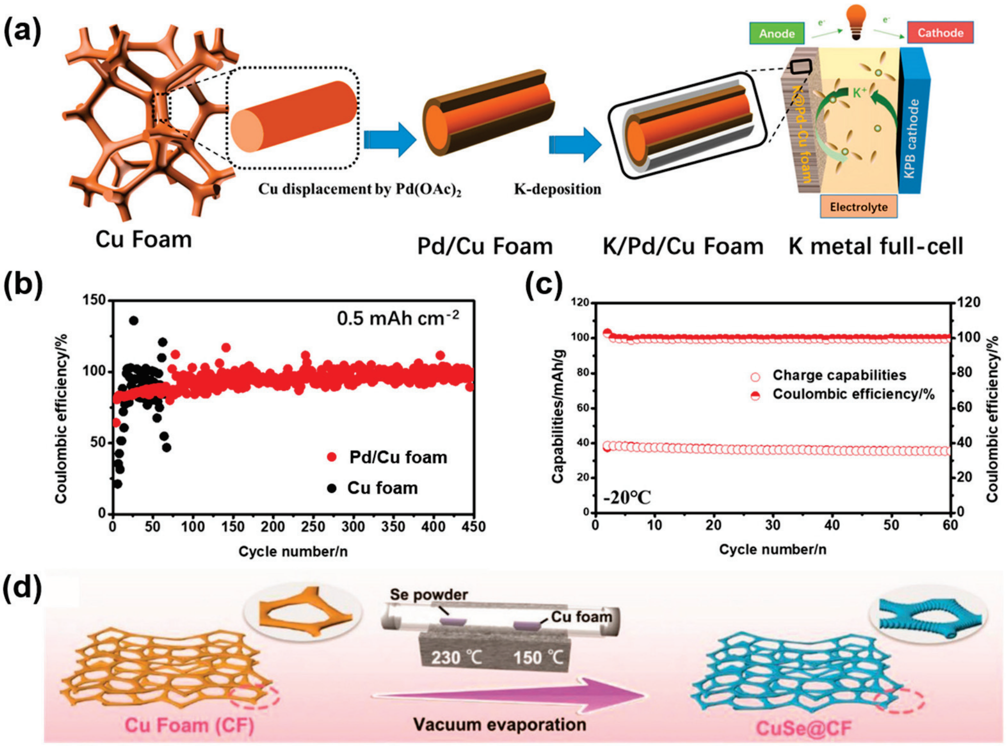

Figure 8. *Cont.*

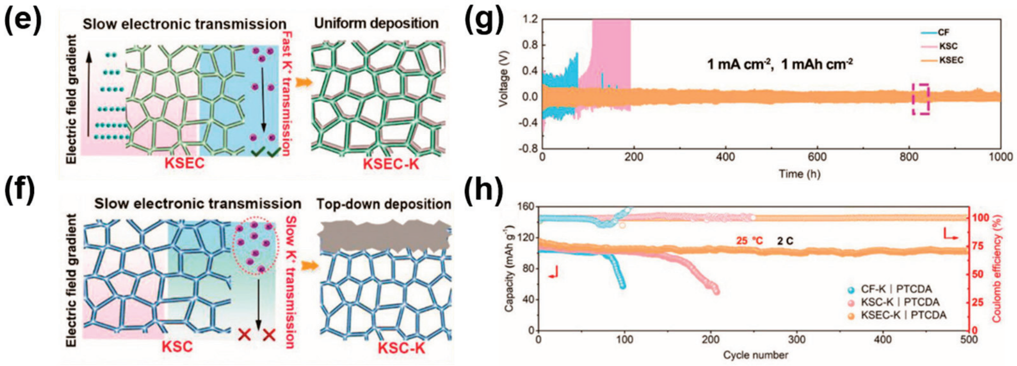

Figure 8. (**a**) Process of synthesizing Pd/Cu foam and K/Pd/Cu foam. (**b**) Electrochemical performance of the Pd/Cu foam. (**c**) Cycling stability of K/Pd/Cu | | PB cell at −20 °C. Reprinted with permission [109]. Copyright 2022, Elsevier. (**d**) Schematic diagram of the synthesis procedure of CuSe@CF. (**e**) K deposition behavior on KSEC anode, "synchronized" deposition. (**f**) K deposition behavior on KSC anode, "top-down" depositional. (**g**) Galvanostatic voltage profiles of KSC and KSEC electrodes. (**h**) Cycling performance of KSEC–K | PTCDA cell at 2 C. Reprinted with permission [111]. Copyright 2023, Wiley-VCH.

Table 1. Cycling performance of symmetrical cells under different 3D Cu-based current collector modification strategies.

Substrate	Current Collectors	Method	Cycle Performance V ^{a} (mV), T ^{b} (h) C_1 ^{c} (mA cm^{-2}), C_2 ^{c} (mAh cm^{-2})	Ref.
		Lithium metal anodes		
		Modification strategy: Structrual modification		
/	3D Cu skeleton	Template method	40, 500 (1, 1)	[43]
Cu foil	Cu@Cu$_x$O	Template method	20, 600 (1, 1)	[58]
Cu foam	HPC/CF	Template method	/, 620 (0.5, 1)	[60]
Cu-Zn alloy foil	3D Cu	Dealloying	/, 800 (0.52, 0.26)	[46]
Cu-Zn alloy foil	3D Cu	Dealloying	20, 400 (1, 1)	[70]
Cu-Zn alloy foil	2h-3D CuZn	Dealloying	25, 450 (1, 1)	[63]
Cu-Zn alloy foil	Porous Cu	Dealloying	20, 440 (1, 1)	[67]
Cu-Zn alloy mesh	HP-Cu@Sn	Dealloying Electroless plating	/, 800 (1, 1)	[112]
Cu foil	3DHP Cu	Electrodeposition Dealloying	33, 850 (1, 1)	[71]
Cu foil	3D P-CuZn	Electrodeposition Dealloying	/, 560 (1, 1)	[64]
Cu foil	3DOM Cu-450	Electrodeposition	25, 700 (0.2, 0.5)	[57]
Cu foil	Cu@Sn nanocones	Electrodeposition	10, 600 (1, 1)	[113]
Cu foil	3D Cu-CNT	Electrodeposition	/, 550 (0.5, 1)	[72]
/	3DP-Cu	3D printing	/, 250 (1, 1)	[114]
/	3D Cu mesh	3D printing	20, 500 (1, 1)	[76]
		Modification strategy: Chemical modification		
Cu foam	Ag@CF	Chemical reaction	30, 1600 (1, 1)	[77]
Cu foil	Cu-Ge	Chemical reaction	/, 1000 (0.5, 1)	[91]
Cu mesh	CuM/Ag	Magnetron sputtering	25, 1000 (0.5, 1)	[84]
Cu foam	ISG-CuO-2mM	Chemical oxidation	/, 1150 (1, 1)	[79]
Cu foam	RCOFs	Chemical oxidation Mechanical rolling	/, 5000 (5, 1)	[94]
Cu foam	Cu-Cu$_x$O	Chemical oxidation	15, 1800 (1, 1)	[115]
Cu foam	ZnO NFs/CuF	solvothermal	10, 1600 (1, 1)	[116]
Cu foil	CuO@Cu	Electrochemical anodizing	10, 1200 (1, 1)	[92]

Table 1. *Cont.*

Substrate	Current Collectors	Method	Cycle Performance V ^{a} (mV), T ^{b} (h) C_1 ^{c} (mA cm^{-2}), C_2 ^{c} (mAh cm^{-2})	Ref.
Cu foam	GN@Cu foam	Chemical immersion	10, 2000 (0.5, 1)	[117]
Cu foil	PDA@3D Cu	Chemical immersion	24, 1000 (0.5, 0.5)	[95]
Cu foil	γ-APS-Cu	Drop casting	12, 1400 (0.5, 1)	[81]
Cu foil	GO-Zn/Cu	Electrodeposition Spin-coating	20, 600 (1, 1)	[118]
		Sodium metal anodes		
Cu foam	CuNW-Cu	Electrochemical anodizing	25, 1400 (1, 2)	[102]
Cu-Zn alloy	3D porous Cu	Dealloying	/, 1000 (1, 1)	[103]
Cu foil	Cu/Zn/SnO_2	Magnetron sputtering	25, 820 (1, 1)	[119]
Cu mesh	Pt-Cu/Cu mesh	Chemical reaction	/, 400 (1, 1)	[120]
Cu foam	SF-Cu-3.6	Chemical oxidation	19, 400 (1, 1)	[121]
Cu foam	Cu_2Se/Cu foam	Solution selenization	70, 500 (1, 1)	[106]
Cu foil	Sn@LIG@Cu	Laser process	19.7, 1000 (10, 10)	[105]
		Potassium metal anodes		
Cu foam	rGO@3D-Cu	Chemical immersion	/, 200 (0.5, 0.5)	[107]
Cu mesh	Cu_3Pt-Cu mesh	Chemical reaction	1000, 300 (0.5, 1)	[108]
Cu foam	CuSe@CF	Vacuum evaporation	80, 1000 (1, 1)	[111]

^{a} Voltage hysteresis (mV); ^{b} time (h); ^{c} C_1: current density (mA cm^{-2}); C_2: specific area capacity (mAh cm^{-2}).

4. Conclusions and Outlook

In conclusion, this review summarizes the commonly used methods for the modification of Cu-based CCs and recent progress on the applications of 3D Cu-based CCs for AMBs. The ideal three-dimensional Cu-based current collector would provide multiple advantages, which include (1) alleviating electrode volume changes; (2) reducing local current density and delaying dendrite growth; (3) reducing nucleation energy barriers; (4) changing SEI composition and promoting uniform deposition; (5) inducing the preferential deposition of alkali metal ions at the bottom. However, most of the existing current collector modification strategies struggle to take these points into account. As a result, appropriate modification strategies should be combined with the characteristics of structural modification and chemical modification to improve the performance of AMBs. In recent years, significant progress has been made in research into the application of 3D Cu-based CCs in AMBs. Nonetheless, there are still many challenges and problems that need to be solved. To better improve the performance of AMAs, further investigations should focus on the following points (Figure 9).

1. The mechanisms of the nucleation and growth of alkali metal ions and dendrite formation should be further investigated. For alkali metal batteries, the nucleation and growth behaviors of alkali metal ions determine the performance of the battery to a certain extent. Meanwhile, the dendrite problem, as a critical factor affecting the stability and safety of alkali metal batteries, has received much attention and research. Many current collector modifications are also aimed at inhibiting dendrite growth. At present, many works have been reported on promoting the uniform deposition of alkali metal ions and inhibiting dendritic growth. However, the explanation of the mechanism remains relatively singular, mainly regarding the reduction of local current density and the increases in nucleation sites. The existing modifications generally increase the specific surface area by constructing three-dimensional porous structures, thus reducing the local current density. These modification strategies can only delay the growth of dendrites to a certain extent, and cannot truly address the problem of dendrites. Therefore, the further exploration of more core mechanisms is essential to more effectively guide the development of Cu-based CCs and alkali metal batteries.

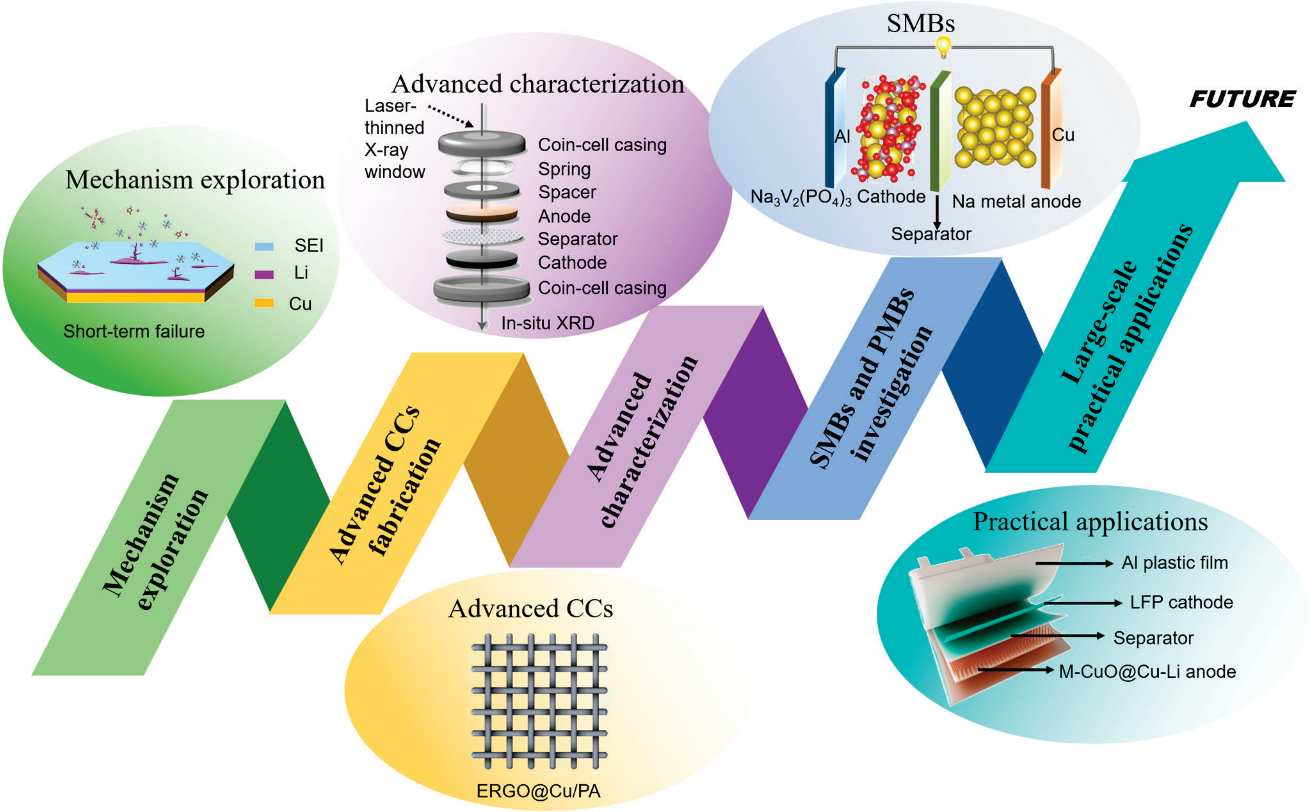

Figure 9. Outlook and prospective research directions relating to advanced 3D Cu-based current collectors for AMBs. Top left: reprinted with permission from [122] Copyright 2021, American Chemical Society. Top middle: reprinted with permission from [19] Copyright 2021, Nature Portfolio. The Royal Society of Chemistry. Top right: reprinted with permission from [123] Copyright 2024, The Royal Society of Chemistry. Bottom left: reprinted with permission from [124] Copyright 2023, American Chemical Society. Bottom right: reprinted with permission from [92] Copyright 2023, Wiley-VCH.

2. More advanced 3D Cu-based current collectors should be explored and investigated. Pure metal (pure Cu and Cu alloys)-based current collectors play a positive role in optimizing the performance of AMAs. However, these current collectors still face the problems of dendrite growth and volume change during long-term cycling, meaning they struggle to meet the actual application needs of alkali metal batteries. It is worth noting that some materials also play a huge role in the construction and modification of 3D Cu-based current collectors, including carbon materials, polymer materials and so on. Carbon materials (including graphite, graphene, etc.) have high electrical conductivity, excellent mechanical strength, light weight and so on [125]. It has been confirmed that constructing composite materials with carbon materials is a common method to improve the performance of electrode materials [126]. Polymer materials with polar functional groups have good flexibility and play a significant role in inducing lithium deposition and mitigating volume changes. In order to maximize the specific energy of AMBs, lightness of weight is the future development direction of current collectors. In view of the abundant reserves, low price and good electrical properties of copper materials, the study of lightweight three-dimensional copper composite current collectors (with carbon materials, polymer materials, etc.) is still of positive significance for the practical application of AMAs.

3. More advanced characterization techniques should be further explored and applied in alkali metal batteries. Compared with traditional characterization techniques (such as X-ray diffraction (XRD), scanning electron microscopy (SEM), transmission electron microscopy (TEM) and so on), advanced characterization techniques can more accurately

measure the changes in various components and parameters in the battery system, thereby helping to clarify the relationship between various parameters. Undoubtedly, this helps to clarify the mechanisms by which battery performance improvement or battery failure occur. For example, in situ characterization techniques, including in situ XRD, in situ X-ray photoelectron spectroscopy (XPS), in situ Raman spectroscopy and in situ atomic force microscopy (AFM), etc., have developed rapidly in recent years, and have been widely used in the characterization of solid-state electrolytes. These characterizations can also be further explored and introduced into the study of current collectors.

4. The study of SMBs and PMBs should be further developed. As a topic of great interest, there are a lot of studies on lithium metal anodes, whereas there is little research on sodium metal anodes and potassium metal anodes. Although sodium, potassium and lithium encounter dendrite growth, volume change and other problems, there are some differences in their practical applications, including as cathode materials, electrolytes and so on. Besides this, in recent years, the lithium resource reserves have decreased and their price has risen, resulting in the high cost of lithium batteries. As a result, more attention and investigations should be directed towards SMBs and PMBs, which may replace lithium metal batteries in some applications in order to meet people’s demand for energy density.

5. The practical and large-scale application of 3D Cu-based current collectors in AMBs should be further investigated. At present, some studies on the application of 3D Cu-based CCs in alkali metal batteries have made great progress. However, their preparation methods or modified materials are not suitable for use in practical application. For example, some studies use magnetron sputtering, laser etching or other processes, and the equipment is expensive and not suitable for large-scale preparation. Besides this, some studies have used gold, silver or their compounds to improve the surface properties of Cu-based current collectors and regulate the nucleation and growth of alkali metals. Obviously, these expensive materials are not suitable for use in practical preparation and applications. In addition, most of the 3D Cu-based current collectors are assembled in coin cells to test their performance, which is different from the actual application environment. Hence, in this context, developing proper preparation methods and corresponding equipment is critical for preparing large-area 3D Cu-based CCs for use in practical AMBs.

Overall, this review summarizes some recent advances in the development of 3D Cu-based CCs for use in high performance AMBs. We hope this review will further promote the practical application of 3D Cu-based current collectors in AMBs and other fields.

Author Contributions: Conceptualization, Y.L. and G.W.; data curation, C.K., Z.L., K.F. and J.L.; writing—original draft preparation, C.K., Z.L., F.W. and K.F.; writing—review and editing, Y.L., Y.P., Y.W. and G.W.; supervision, Y.L. and G.W.; funding acquisition, Y.L. and G.W. All authors have read and agreed to the published version of the manuscript.

Funding: This work was financially supported by the Natural Science Foundation of Henan Province (No. 242300420021), the Major Science and Technology Projects of Henan Province (No. 221100230200), the Open Fund of State Key Laboratory of Advanced Refractories (No. SKLAR202210), the Student Research Training Plan of Henan University of Science and Technology (No. 2024054), and the Undergraduate Innovation and Entrepreneurship Training Program of Henan Province (No. S202310464012).

Institutional Review Board Statement: Not applicable.

Informed Consent Statement: Not applicable.

Data Availability Statement: The data are contained within this article.

Conflicts of Interest: The authors declare that they have no conflicts of interest.

References

1. Degen, F.; Winter, M.; Bendig, D.; Tuebke, J. Energy consumption of current and future production of lithium-ion and post lithium-ion battery cells. *Nat. Energy* **2023**, *8*, 1284–1295. [CrossRef]
2. Harper, G.; Sommerville, R.; Kendrick, E.; Driscoll, L.; Slater, P.; Stolkin, R.; Walton, A.; Christensen, P.; Heidrich, O.; Lambert, S.; et al. Recycling lithium-ion batteries from electric vehicles. *Nature* **2019**, *575*, 75–86. [CrossRef]

3. Zhang, X.; Wang, X.-G.; Xie, Z.; Zhou, Z. Recent progress in rechargeable alkali metal-air batteries. *Green Energy Environ.* **2016**, *1*, 4–17. [CrossRef]
4. Wang, A.; Hong, W.; Yang, L.; Tian, Y.; Qiu, X.; Zou, G.; Hou, H.; Ji, X. Bi-Based Electrode Materials for Alkali Metal-Ion Batteries. *Small* **2020**, *16*, 2004022. [CrossRef]
5. Gao, Y.-M.; Liu, Y.; Feng, K.-J.; Ma, J.-Q.; Miao, Y.-J.; Xu, B.-R.; Pan, K.-M.; Akiyoshi, O.; Wang, G.-X.; Zhang, K.-K.; et al. Emerging WS_2/WSe_2@graphene nanocomposites: Synthesis and electrochemical energy storage applications. *Rare Met.* **2024**, *43*, 1–19. [CrossRef]
6. Xu, B.-R.; Li, Q.-A.; Liu, Y.; Wang, G.-B.; Zhang, Z.-H.; Ren, F.-Z. Urea-induced interfacial engineering enabling highly reversible aqueous zinc-ion battery. *Rare Met.* **2024**, *43*, 1599–1609. [CrossRef]
7. Liu, Y.; Feng, K.; Han, J.; Wang, F.; Xing, Y.; Tao, F.; Li, H.; Xu, B.; Ji, J.; Li, H. Regulation of Zn^{2+} solvation shell by a novel N-methylacetamide based eutectic electrolyte toward high-performance zinc-ion batteries. *J. Mater. Sci. Technol.* **2025**, *211*, 53–61. [CrossRef]
8. Liu, Y.; Tao, F.; Xing, Y.; Pei, Y.; Ren, F. Melamine Foam-Derived Carbon Scaffold for Dendrite-Free and Stable Zinc Metal Anode. *Molecules* **2023**, *28*, 1742. [CrossRef]
9. Xu, B.; Wang, G.; Liu, Y.; Li, Q.; Ren, F.; Ma, J. Co-regulation effect of solvation and interface of pyridine derivative enabling highly reversible zinc anode. *J. Mater. Sci. Technol.* **2025**, *204*, 1–9. [CrossRef]
10. Wu, N.; Zhao, Z.; Hua, R.; Wang, X.; Zhang, Y.; Li, J.; Liu, G.; Guo, D.; Sun, G.; Liu, X.; et al. Pre-Doping of Dual-Functional Sodium to Weaken Fe–S Bond and Stabilize Interfacial Chemistry for High-Rate Reversible Sodium Storage. *Adv. Energy Mater.* **2024**, *28*, 2400371. [CrossRef]
11. Guo, Y.-D.; Zhao, E.-Q.; Zhao, X.-F.; Liu, S.-L. One dimensional CeO_2 nanorods/poly(ethylene oxide) solid composite electrolyte for all-solid-state lithium-ion batteries. *J. Rare Earths* **2024**, *42*, 570–577. [CrossRef]
12. Ahsan, Z.; Cai, Z.-F.; Wang, S.; Wang, H.-C.; Ma, Y.-Z.; Song, G.-S.; Zhang, S.-H.; Yang, W.-D.; Imran, M.; Wen, C. Enhanced stability and electrochemical properties of lanthanum and cerium co-modified $LiVOPO_4$ cathode materials for Li-ion batteries. *J. Rare Earths* **2023**, *41*, 1590–1596. [CrossRef]
13. Lu, L.-L.; Lu, Y.-Y.; Zhu, Z.-X.; Shao, J.-X.; Yao, H.-B.; Wang, S.; Zhang, T.-W.; Ni, Y.; Wang, X.-X.; Yu, S.-H. Extremely fast-charging lithium ion battery enabled by dual-gradient structure design. *Sci. Adv.* **2022**, *8*, eabm6624. [CrossRef] [PubMed]
14. Hao, X.; Zhao, Q.; Su, S.; Zhang, S.; Ma, J.; Shen, L.; Yu, Q.; Zhao, L.; Liu, Y.; Kang, F.; et al. Constructing Multifunctional Interphase between $Li_{1\cdot4}Al_{0\cdot4}Ti_{1\cdot6}(PO_4)_3$ and Li Metal by Magnetron Sputtering for Highly Stable Solid-State Lithium Metal Batteries. *Adv. Energy Mater.* **2019**, *9*, 1901604. [CrossRef]
15. Sullivan, M.; Tang, P.; Meng, X. Atomic and Molecular Layer Deposition as Surface Engineering Techniques for Emerging Alkali Metal Rechargeable Batteries. *Molecules* **2022**, *27*, 6170. [CrossRef] [PubMed]
16. Xiang, J.; Yang, L.; Yuan, L.; Yuan, K.; Zhang, Y.; Huang, Y.; Lin, J.; Pan, F.; Huang, Y. Alkali-Metal Anodes: From Lab to Market. *Joule* **2019**, *3*, 2334–2363. [CrossRef]
17. Tang, Z.; Zhou, S.; Huang, Y.; Wang, H.; Zhang, R.; Wang, Q.; Sun, D.; Tang, Y.; Wang, H. Improving the Initial Coulombic Efficiency of Carbonaceous Materials for Li/Na-Ion Batteries: Origins, Solutions, and Perspectives. *Electrochem. Energy Rev.* **2023**, *6*, 8. [CrossRef]
18. Song, J.; Wang, H.; Zuo, Y.; Zhang, K.; Yang, T.; Yang, Y.; Gao, C.; Chen, T.; Feng, G.; Jiang, Z.; et al. Building Better Full Manganese-Based Cathode Materials for Next-Generation Lithium-Ion Batteries. *Electrochem. Energy Rev.* **2023**, *6*, 20. [CrossRef]
19. Xu, C.; Märker, K.; Lee, J.; Mahadevegowda, A.; Reeves, P.J.; Day, S.J.; Groh, M.F.; Emge, S.P.; Ducati, C.; Layla Mehdi, B.; et al. Bulk fatigue induced by surface reconstruction in layered Ni-rich cathodes for Li-ion batteries. *Nat. Mater.* **2021**, *20*, 84–92. [CrossRef]
20. Yang, K.; Tian, R.-Z.; Wang, Z.-Y.; Zhang, H.-Z.; Ma, Y.; Shi, X.-X.; Song, D.-W.; Zhang, L.-Q.; Zhu, L.-Y. Regulating surface base of $LiCoO_2$ to inhibit side reactions between $LiCoO_2$ and sulfide electrolyte. *Rare Met.* **2023**, *42*, 4128–4141. [CrossRef]
21. Chen, J.; Xu, X.; He, Q.; Ma, Y. Advanced Current Collectors for Alkali Metal Anodes. *Chem. Res. Chin. Univ.* **2020**, *36*, 386–401. [CrossRef]
22. Liu, Z.; Ha, S.; Liu, Y.; Wang, F.; Tao, F.; Xu, B.; Yu, R.; Wang, G.; Ren, F.; Li, H. Application of Ag-based materials in high-performance lithium metal anode: A review. *J. Mater. Sci. Technol.* **2023**, *133*, 165–182. [CrossRef]
23. Chen, J.; Wang, Y.; Li, S.; Chen, H.; Qiao, X.; Zhao, J.; Ma, Y.; Alshareef, H.N. Porous Metal Current Collectors for Alkali Metal Batteries. *Adv. Sci.* **2022**, *10*, 2205695. [CrossRef]
24. Wang, H.; Yu, D.; Kuang, C.; Cheng, L.; Li, W.; Feng, X.; Zhang, Z.; Zhang, X.; Zhang, Y. Alkali Metal Anodes for Rechargeable Batteries. *Chem* **2019**, *5*, 313–338. [CrossRef]
25. Ma, C.; Xu, T.; Wang, Y. Advanced carbon nanostructures for future high performance sodium metal anodes. *Energy Storage Mater.* **2020**, *25*, 811–826. [CrossRef]
26. Bao, W.; Wang, R.; Li, B.; Qian, C.; Zhang, Z.; Li, J.; Liu, F. Stable alkali metal anodes enabled by crystallographic optimization—A review. *J. Mater. Chem. A* **2021**, *9*, 20957–20984. [CrossRef]
27. Ma, L.; Wu, J.; Zhu, G.; Lv, Y.; Zhang, Y.; Pang, H. Recent advances in two-dimensional materials for alkali metal anodes. *J. Mater. Chem. A* **2021**, *9*, 5232–5257. [CrossRef]
28. Zhou, C.; Lu, K.; Zhou, S.; Liu, Y.; Fang, W.; Hou, Y.; Ye, J.; Fu, L.; Chen, Y.; Liu, L.; et al. Strategies toward anode stabilization in nonaqueous alkali metal-oxygen batteries. *Chem. Commun.* **2022**, *58*, 8014–8024. [CrossRef]

29. Hu, L.; Deng, J.; Liang, Q.; Wu, J.; Ge, B.; Liu, Q.; Chen, G.; Yu, X. Engineering current collectors for advanced alkali metal anodes: A review and perspective. *Ecomat* **2023**, *5*, e12269. [CrossRef]
30. Wang, G.; Song, C.; Huang, J.-Q.; Park, H.S. Recent Advances in Carbon-Based Current Collectors/Hosts for Alkali Metal Anodes. *Energy Environ. Mater.* **2023**, *6*, e12460. [CrossRef]
31. Miao, Y.; Zheng, Y.; Tao, F.; Chen, Z.; Xiong, Y.; Ren, F.; Liu, Y. Synthesis and application of single-atom catalysts in sulfur cathode for high-performance lithium-sulfur batteries. *Chin. Chem. Lett.* **2023**, *34*, 107121. [CrossRef]
32. Chu, Z.; Zhuang, S.; Lu, J.; Li, J.; Wang, C.; Wang, T. In-situ electro-polymerization of L -tyrosine enables ultrafast, long cycle life for lithium metal battery. *Chin. Chem. Lett.* **2023**, *34*, 107563. [CrossRef]
33. Liu, Z.; Liu, Y.; Miao, Y.; Liu, G.; Yu, R.; Pan, K.; Wang, G.; Pang, X.; Ma, J. Emerging Carbon Nanotube-Based Nanomaterials for Stable and Dendrite-Free Alkali Metal Anodes: Challenges, Strategies, and Perspectives. *Energy Environ. Mater.* **2023**, *6*, e12525. [CrossRef]
34. Jeong, H.; Jang, J.; Jo, C. A review on current collector coating methods for next-generation batteries. *Chem. Eng. J.* **2022**, *446*, 136860. [CrossRef]
35. Jia, Z.; Liu, Y.; Li, H.; Xiong, Y.; Miao, Y.; Liu, Z.; Ren, F. In-situ polymerized PEO-based solid electrolytes contribute better Li metal batteries: Challenges, strategies, and perspectives. *J. Energy Chem.* **2024**, *92*, 548–571. [CrossRef]
36. Wang, F.; Gao, J.; Liu, Y.; Ren, F. An amorphous ZnO and oxygen vacancy modified nitrogen-doped carbon skeleton with lithiophilicity and ionic conductivity for stable lithium metal anodes. *J. Mater. Chem. A* **2022**, *10*, 17395–17405. [CrossRef]
37. Tan, L.; Chen, P.; Chen, Q.-Y.; Huang, X.; Zou, K.-Y.; Nie, Y.-M.; Li, L.-J. A Li_3Bi/LiF interfacial layer enabling highly stable lithium metal anode. *Rare Met.* **2023**, *42*, 4081–4090. [CrossRef]
38. Wang, M.; Li, Y.; Li, S.-Y.; Jia, X.-X.; Nie, B.; Sun, H.-T.; Wang, Y.-Y.; Zhu, J. Lithiophilic montmorillonite as a robust substrate toward high-stable lithium metal anodes. *Rare Met.* **2023**, *42*, 2157–2165. [CrossRef]
39. Wang, H.; Wang, F.; Liu, Y.; Liu, Z.; Miao, Y.; Zhang, W.; Wang, G.; Ji, J.; Zhang, Q. Emerging natural clay-based materials for stable and dendrite-free lithium metal anodes: A review. *Chin. Chem. Lett.* **2024**, 109589. [CrossRef]
40. Su, H.; Zhang, H.; Chen, Z.; Li, M.; Zhao, J.; Xun, H.; Sun, J.; Xu, Y. Electrolyte and interphase engineering through solvation structure regulation for stable lithium metal batteries. *Chin. Chem. Lett.* **2023**, *34*, 108640. [CrossRef]
41. Yang, Y.; Yuan, W.; Zhang, X.; Ke, Y.; Qiu, Z.; Luo, J.; Tang, Y.; Wang, C.; Yuan, Y.; Huang, Y. A review on structuralized current collectors for high-performance lithium-ion battery anodes. *Appl. Energy* **2020**, *276*, 115464. [CrossRef]
42. Cui, Y.; Ye, Y. Porous current collector for fast-charging lithium-ion batteries. *Nat. Energy* **2024**, *9*, 639–640.
43. Wang, Y.; Wang, Z.; Lei, D.; Lv, W.; Zhao, Q.; Ni, B.; Liu, Y.; Li, B.; Kang, F.; He, Y.-B. Spherical Li Deposited inside 3D Cu Skeleton as Anode with Ultrastable Performance. *ACS Appl. Mater. Interfaces* **2018**, *10*, 20244–20249. [CrossRef]
44. Wei, C.; Yao, Z.; Ruan, J.; Song, Z.; Zhou, A.; Song, Y.; Wang, D.; Jiang, J.; Wang, X.; Li, J. Double-layered skeleton of Li alloy anchored on 3D metal foam enabling ultralong lifespan of Li anode under high rate. *Chin. Chem. Lett.* **2024**, *35*, 109330. [CrossRef]
45. Huang, C.; Zhang, Z.; Zhou, Y.; Chen, Y.; Wen, S.; Wang, F.; Liu, Y. Stannic oxide quantum dots constructed evenly alloyable layer stabilizing lithium metal batteries. *J. Alloys Compd.* **2023**, *955*, 170230. [CrossRef]
46. An, Y.L.; Fei, H.F.; Zeng, G.F.; Xu, X.Y.; Ci, L.J.; Xi, B.J.; Xiong, S.L.; Feng, J.K.; Qian, Y.T. Vacuum distillation derived 3D porous current collector for stable lithium-metal batteries. *Nano Energy* **2018**, *47*, 503–511. [CrossRef]
47. Wang, C.; Wang, H.; Matios, E.; Hu, X.; Li, W. A Chemically Engineered Porous Copper Matrix with Cylindrical Core-Shell Skeleton as a Stable Host for Metallic Sodium Anodes. *Adv. Funct. Mater.* **2018**, *28*, 1802282. [CrossRef]
48. Li, H.; Liu, Y.; Wang, J.; Yan, W.; Zhang, J. Robust 3D Copper Foam Functionalized with Gold Nanoparticles as Anode for High-Performance Potassium Metal Batteries. *Chem.-Asian J.* **2022**, *17*, e202200430. [CrossRef]
49. Guo, C.; Zhang, W.; Tu, J.; Chen, S.; Liang, J.; Guo, X. Construction of 3D Copper-Based Collector and Its Application in Lithium Metal Batteries. *Prog. Chem.* **2022**, *34*, 370–383.
50. Zhou, B.; Bonakdarpour, A.; Stosevski, I.; Fang, B.; Wilkinson, D.P. Modification of Cu current collectors for lithium metal batteries—A review. *Prog. Mater. Sci.* **2022**, *130*, 100996. [CrossRef]
51. Zhang, Z.; Xiao, X.; Zhu, X.; Tan, P. Addressing Transport Issues in Non-Aqueous Li–air Batteries to Achieving High Electrochemical Performance. *Electrochem. Energy Rev.* **2023**, *6*, 18. [CrossRef]
52. Kurniawan, M.; Ivanov, S. Electrochemically Structured Copper Current Collectors for Application in Energy Conversion and Storage: A Review. *Energies* **2023**, *16*, 4933. [CrossRef]
53. Han, X.; Wu, T.; Gu, L.; Chen, M.; Song, J.; Tian, D.; Chen, J. Li-MOF-based ions regulator enabling fast-charging and dendrite-free lithium metal anode. *Chin. Chem. Lett.* **2023**, *34*, 107594. [CrossRef]
54. Ke, Q.; Xu, Q.; Lai, X.; Yang, X.; Gao, H.; Wang, Z.; Qiu, Y. Ultralong-life lithium metal batteries enabled by decorating robust hybrid interphases on 3D layered framworks. *Chin. Chem. Lett.* **2023**, *34*, 107602. [CrossRef]
55. Zhu, R.; Sheng, N.; Rao, Z.; Zhu, C.; Aoki, Y.; Habazaki, H. Employing a T-shirt template and variant of Schweizer's reagent for constructing a low-weight, flexible, hierarchically porous and textile-structured copper current collector for dendrite-suppressed Li metal. *J. Mater. Chem. A* **2019**, *7*, 27066–27073. [CrossRef]
56. Shi, Y.; Wang, Z.; Gao, H.; Niu, J.; Ma, W.; Qin, J.; Peng, Z.; Zhang, Z. A self-supported, three-dimensional porous copper film as a current collector for advanced lithium metal batteries. *J. Mater. Chem. A* **2019**, *7*, 1092–1098. [CrossRef]

57. Tang, Y.P.; Shen, K.; Lv, Z.Y.; Xu, X.; Hou, G.Y.; Cao, H.Z.; Wu, L.K.; Zheng, G.Q.; Deng, Y.D. Three-dimensional ordered macroporous Cu current collector for lithium metal anode: Uniform nucleation by seed crystal. *J. Power Sources* **2018**, *403*, 82–89. [CrossRef]
58. Chen, J.; Qiao, X.; Fu, W.; Han, X.; Wu, Q.; Wang, Y.; Zhang, Y.; Shi, L.; Zhao, J.; Ma, Y. Lithiophilic hyperbranched Cu nanostructure for stable Li metal anodes. *Smartmat* **2023**, *4*, e1174. [CrossRef]
59. Ingber, T.T.K.; Bela, M.M.; Puettmann, F.; Dohmann, J.F.; Bieker, P.; Boerner, M.; Winter, M.; Stan, M.C. Elucidating the lithium deposition behavior in open-porous copper micro-foam negative electrodes for zero-excess lithium metal batteries. *J. Mater. Chem. A* **2023**, *11*, 17828–17840. [CrossRef]
60. Ke, X.; Cheng, Y.; Liu, J.; Liu, L.; Wang, N.; Liu, J.; Zhi, C.; Shi, Z.; Guo, Z. Hierarchically Bicontinuous Porous Copper as Advanced 3D Skeleton for Stable Lithium Storage. *ACS Appl. Mater. Interfaces* **2018**, *10*, 13552–13561. [CrossRef]
61. Kunduraci, M. Dealloying technique in the synthesis of lithium-ion battery anode materials. *J. Solid State Electrochem.* **2016**, *20*, 2105–2111. [CrossRef]
62. Wu, X.; He, G.; Ding, Y. Dealloyed nanoporous materials for rechargeable lithium batteries. *Electrochem. Energy Rev.* **2020**, *3*, 541–580. [CrossRef]
63. Zhang, D.; Dai, A.; Wu, M.; Shen, K.; Xiao, T.; Hou, G.; Lu, J.; Tang, Y. Lithiophilic 3D Porous CuZn Current Collector for Stable Lithium Metal Batteries. *ACS Energy Lett.* **2020**, *5*, 180–186. [CrossRef]
64. Zhang, S.; Zhao, Y.; Qian, Y.; Wang, X.; Huang, J.; Ma, Y.; Suo, L.; Li, W.; Zhang, B. Stable Li deposition of 3D highstrength-lithiophilicity-porous CuZn current collector with gradient structure. *J. Alloys Compd.* **2023**, *951*, 169953. [CrossRef]
65. Sun, C.; Yang, Y.; Bian, X.; Guan, R.; Wang, C.; Lu, D.; Gao, L.; Zhang, D. Uniform Deposition of Li-Metal Anodes Guided by 3D Current Collectors with In Situ Modification of the Lithiophilic Matrix. *ACS Appl. Mater. Interfaces* **2021**, *13*, 48691–48699. [CrossRef] [PubMed]
66. Ma, Y.; Ma, X.; Bai, J.; Xu, W.; Zhong, H.; Liu, Z.; Xiong, S.; Yang, L.; Chen, H. Electrochemically Dealloyed 3D Porous Copper Nanostructure as Anode Current Collector of Li-Metal Batteries. *Small* **2023**, *19*, 2301731. [CrossRef] [PubMed]
67. Li, L.; Zhong, K.; Dang, Y.; Li, J.; Ruan, M.; Fang, Z. Chemical dealloying pore structure control of porous copper current collector for dendrite-free lithium anode. *J. Porous Mater.* **2021**, *28*, 1813–1822. [CrossRef]
68. An, Y.; Tian, Y.; Wei, C.; Tao, Y.; Xi, B.; Xiong, S.; Feng, J.; Qian, Y. Dealloying: An effective method for scalable fabrication of 0D, 1D, 2D, 3D materials and its application in energy storage. *Nano Today* **2021**, *37*, 101094. [CrossRef]
69. Li, W.; Zheng, S.; Gao, Y.; Feng, D.; Ru, Y.; Zuo, T.; Chen, B.; Zhang, Z.; Gao, Z.; Geng, H.; et al. High Rate and Low-Temperature Stable Lithium Metal Batteries Enabled by Lithiophilic 3D Cu-CuSn Porous Framework. *Nano Lett.* **2023**, *23*, 7805–7814. [CrossRef]
70. Zhao, H.; Lei, D.; He, Y.-B.; Yuan, Y.; Yun, Q.; Ni, B.; Lv, W.; Li, B.; Yang, Q.-H.; Kang, F.; et al. Compact 3D Copper with Uniform Porous Structure Derived by Electrochemical Dealloying as Dendrite-Free Lithium Metal Anode Current Collector. *Adv. Energy Mater.* **2018**, *8*, 1800266. [CrossRef]
71. Luan, C.; Chen, L.; Li, B.; Zhu, L.; Li, W. Electrochemical Dealloying-Enabled 3D Hierarchical Porous Cu Current Collector of Lithium Metal Anodes for Dendrite Growth Inhibition. *ACS Appl. Energy Mater.* **2021**, *4*, 13903–13911. [CrossRef]
72. Park, S.K.; Copic, D.; Zhao, T.Z.; Rutkowska, A.; Wen, B.; Sanders, K.; He, R.; Kim, H.-K.; De Volder, M. 3D Porous Cu-Composites for Stable Li-Metal Battery Anodes. *ACS Nano* **2023**, *17*, 14658–14666. [CrossRef] [PubMed]
73. Kim, S.; Lee, M.; Oh, S.; Ryu, W.-H. Li-Dendrite cage electrode with 3-D interconnected pores for Anode-Free Lithium-Metal batteries. *Chem. Eng. J.* **2023**, *474*, 145447. [CrossRef]
74. Zhang, G.; Yu, H.; Li, D.; Yan, Y.; Wei, D.; Ye, J.; Zhao, Y.; Zeng, W.; Duan, H. Ultrathin Lithiophilic 3D Arrayed Skeleton Enabling Spatial-Selection Deposition for Dendrite-Free Lithium Anodes. *Small* **2023**, *19*, 2300734. [CrossRef] [PubMed]
75. Zhang, S.; Zeng, J.; Ma, Y.; Zhao, Y.; Qian, Y.; Suo, L.; Huang, J.; Wang, X.; Li, W.; Zhang, B. Ultrathin hierarchical porous Cu current collector fabricated by anodic oxidation in complexing agent system for stable anode-free Lithium metal batteries. *Electrochim. Acta* **2023**, *442*, 141895. [CrossRef]
76. Chen, C.; Li, S.; Notten, P.H.L.; Zhang, Y.; Hao, Q.; Zhang, X.; Lei, W. 3D Printed Lithium-Metal Full Batteries Based on a High-Performance Three-Dimensional Anode Current Collector. *ACS Appl. Mater. Interfaces* **2021**, *13*, 24785–24794. [CrossRef] [PubMed]
77. Zhao, Q.; Li, J.; Chen, X.; Zhang, Y. Facile Lithiophilic 3D Copper Current Collector for Stable Li Metal Anode. *J. Electron. Mater.* **2022**, *51*, 4248–4256. [CrossRef]
78. Kim, E.; Choi, W.; Ryu, S.; Yun, Y.; Jo, S.; Yoo, J. Effect of 3D lithiophilic current collector for anode-free Li ion batteries. *J. Alloys Compd.* **2023**, *966*, 171393. [CrossRef]
79. Jiang, Y.; Wang, B.; Liu, A.; Song, R.; Bao, C.; Ning, Y.; Wang, F.; Ruan, T.; Wang, D.; Zhou, Y. In situ growth of CuO submicro-sheets on optimized Cu foam to induce uniform Li deposition and stripping for stable Li metal batteries. *Electrochim. Acta* **2020**, *339*, 135941. [CrossRef]
80. Liu, X.-F.; Xie, D.; Tao, F.-Y.; Diao, W.-Y.; Yang, J.-L.; Luo, X.-X.; Li, W.-L.; Wu, X.-L. Regulating the Li Nucleation/Growth Behavior via Cu_2O Nanowire Array and Artificial Solid Electrolyte Interphase toward Highly Stable Li Metal Anode. *ACS Appl. Mater. Interfaces* **2022**, *14*, 23588–23596. [CrossRef]
81. Chen, L.; Chen, G.; Lin, X.H.; Zheng, Z.C.; Wen, Z.X.; Wu, D.; Weng, Z.; Zhang, N.; Liu, X.H.; Ma, R.Z. Lithiophilic and Anticorrosive Cu Current Collector via Dual-Bonded Porous Polymer Coating for Stable Lithium-Metal Batteries. *ACS Appl. Mater. Interfaces* **2023**, *15*, 10273–10282. [CrossRef] [PubMed]

82. Yan, K.; Lu, Z.D.; Lee, H.W.; Xiong, F.; Hsu, P.C.; Li, Y.Z.; Zhao, J.; Chu, S.; Cui, Y. Selective deposition and stable encapsulation of lithium through heterogeneous seeded growth. *Nat. Energy* **2016**, *1*, 16010. [CrossRef]
83. Gao, Y.; Cui, B.-F.; Wang, J.-J.; Sun, Z.-Y.; Chen, Q.; Deng, Y.-D.; Han, X.-P.; Hu, W.-B. Improving Li reversibility in Li metal batteries through uniform dispersion of Ag nanoparticles on graphene. *Rare Met.* **2022**, *41*, 3391–3400. [CrossRef]
84. Chen, W.; Li, S.; Wang, C.; Dou, H.; Zhang, X. Targeted Deposition in a Lithiophilic Silver-Modified 3D Cu Host for Lithium-Metal Anodes. *Energy Environ. Mater.* **2023**, *6*, e12412. [CrossRef]
85. Feng, K.; Sun, Z.; Liu, Y.; Tao, F.; Ma, J.; Qian, H.; Yu, R.; Pan, K.; Wang, G.; Wei, S.; et al. Shining light on transition metal tungstate-based nanomaterials for electrochemical applications: Structures, progress, and perspectives. *Nano Res.* **2022**, *15*, 6924–6960.
86. Yan, N.-F.; Cui, H.-M.; Shi, J.-S.; You, S.-Y.; Liu, S. Recent progress of $W_{18}O_{49}$ nanowires for energy conversion and storage. *Tungsten* **2023**, *5*, 371–390. [CrossRef]
87. Miao, S.-C.; Jia, Y.; Deng, Z.-W.; Deng, Y.; Chen, R.-X.; Zhang, X.-M.; Xu, C.-H.; Yao, M.; Cai, W.-L. Transition metals for stabilizing lithium metal anode: Advances and perspectives. *Tungsten* **2024**, *6*, 212–229. [CrossRef]
88. Lin, J.-H.; Yan, Y.-T.; Qi, J.-L.; Zha, C.-Y. Atomic tailoring-induced deficiency in tungsten oxides for high-performance energy-related devices. *Tungsten* **2024**, *6*, 269–277.
89. Zhu, R.-J.; Liu, J.; Hua, C.; Pan, H.-Y.; Cao, Y.-J.; Li, M. Preparation of vanadium-based electrode materials and their research progress in solid-state flexible supercapacitors. *Rare Met.* **2024**, *43*, 431–454. [CrossRef]
90. Qian, H.; Liu, Y.; Chen, H.; Feng, K.; Jia, K.; Pan, K.; Wang, G.; Huang, T.; Pang, X.; Zhang, Q. Emerging bismuth-based materials: From fundamentals to electrochemical energy storage applications. *Energy Storage Mater.* **2023**, *58*, 232–270. [CrossRef]
91. Ahad, S.A.; Adegoke, T.E.; Ryan, K.M.; Geaney, H. Cu Current Collector with Binder-Free Lithiophilic Nanowire Coating for High Energy Density Lithium Metal Batteries. *Small* **2023**, *19*, 2207902. [CrossRef] [PubMed]
92. Liu, Y.; Li, Y.; Du, Z.; He, C.; Bi, J.; Li, S.; Guan, W.; Du, H.; Ai, W. Integrated Gradient Cu Current Collector Enables Bottom-Up Li Growth for Li Metal Anodes: Role of Interfacial Structure. *Adv. Sci.* **2023**, *10*, 2301288. [CrossRef] [PubMed]
93. Wu, S.; Jiao, T.; Yang, S.; Liu, B.; Zhang, W.; Zhang, K. Lithiophilicity conversion of the Cu surface through facile thermal oxidation: Boosting a stable Li-Cu composite anode through melt infusion. *J. Mater. Chem. A* **2019**, *7*, 5726–5732. [CrossRef]
94. Li, R.; Wang, J.; Lin, L.; Wang, H.; Wang, C.; Zhang, C.; Song, C.; Tian, F.; Yang, J.; Qian, Y. Pressure-tuned and surface-oxidized copper foams for dendrite-free Li metal anodes. *Mater. Today Energy* **2020**, *15*, 100367. [CrossRef]
95. Jiang, J.M.; Pan, Z.H.; Kou, Z.K.; Nie, P.; Chen, C.L.; Li, Z.W.; Li, S.P.; Zhu, Q.; Dou, H.; Zhang, X.G.; et al. Lithiophilic polymer interphase anchored on laser-punched 3D holey Cu matrix enables uniform lithium nucleation leading to super-stable lithium metal anodes. *Energy Storage Mater.* **2020**, *29*, 84–91. [CrossRef]
96. Zhu, Y.; Wu, S.; Zhang, L.; Zhang, B.; Liao, B. Lithiophilic Zn_3N_2-Modified Cu Current Collectors by a Novel FCVA Technology for Stable Anode-Free Lithium Metal Batteries. *ACS Appl. Mater. Interfaces* **2023**, *15*, 43145–43158. [CrossRef] [PubMed]
97. Maeng, J.Y.; Bae, M.; Kim, Y.; Kim, D.; Chang, Y.; Park, S.; Choi, J.; Lee, E.; Lee, J.; Piao, Y. Establishing a multifunctional solid electrolyte interphase on a 3D host by an ultra-fast double coating strategy for stable lithium metal batteries. *J. Mater. Chem. A* **2024**, *12*, 1058–1071. [CrossRef]
98. Xiong, J.-Z.; Yang, Z.-C.; Guo, X.-L.; Wang, X.-Y.; Geng, C.; Sun, Z.-F.; Xiao, A.-Y.; Zhuang, Q.-C.; Chen, Y.-X.; Ju, Z.-C. Review on recent advances of inorganic electrode materials for potassium-ion batteries. *Tungsten* **2024**, *6*, 174–195. [CrossRef]
99. Gong, H.-Q.; Wang, X.-Y.; Ye, L.; Zhang, B.; Ou, X. Recycling of spent lithium-ion batteries to resynthesize high-performance cathode materials for sodium-ion storage. *Tungsten* **2024**, *6*, 574–584. [CrossRef]
100. Cu, Q.; Shang, C.-Q.; Zhou, G.-F.; Wang, X. Freestanding $MoSe_2$ nanoflowers for superior Li/Na storage properties. *Tungsten* **2024**, *6*, 238–247. [CrossRef]
101. Zou, H.-Y.; Fang, L.; Yu, G.; Wang, D. Nanocrystalline WSe_2 excels at high-performance anode for Na storage via a facile one-pot hydrothermal method. *Tungsten* **2024**, *6*, 248–258. [CrossRef]
102. Wang, T.-S.; Liu, Y.; Lu, Y.-X.; Hu, Y.-S.; Fan, L.-Z. Dendrite-free Na metal plating/stripping onto 3D porous Cu hosts. *Energy Storage Mater.* **2018**, *15*, 274–281. [CrossRef]
103. Sun, J.; Guo, C.; Cai, Y.; Li, J.; Sun, X.; Shi, W.; Ai, S.; Chen, C.; Jiang, F. Dendrite-free and long-life Na metal anode achieved by 3D porous Cu. *Electrochim. Acta* **2019**, *309*, 18–24. [CrossRef]
104. Chen, Q.; Zhang, T.; Hou, Z.; Zhuang, W.; Sun, Z.; Jiang, Y.; Huang, L. Large-scale sodiophilic/buffered alloy architecture enables deeply cyclable Na metal anodes. *Chem. Eng. J.* **2022**, *433*, 133270. [CrossRef]
105. Xiao, H.; Li, Y.; Chen, W.; Xie, T.; Zhu, H.; Zheng, W.; He, J.; Huang, S. Stabilize Sodium Metal Anode by Integrated Patterning of Laser-Induced Graphene with Regulated Na Deposition Behavior. *Small* **2023**, *19*, 2303959. [CrossRef] [PubMed]
106. Liu, F.; Wang, L.; Ling, F.; Zhou, X.; Jiang, Y.; Yao, Y.; Yang, H.; Shao, Y.; Wu, X.; Rui, X.; et al. Homogeneous Metallic Deposition Regulated by Porous Framework and Selenization Interphase Toward Stable Sodium/Potassium Anodes. *Adv. Funct. Mater.* **2022**, *32*, 2210166. [CrossRef]
107. Liu, P.; Wang, Y.; Gu, Q.; Nanda, J.; Watt, J.; Mitlin, D. Dendrite-Free Potassium Metal Anodes in a Carbonate Electrolyte. *Adv. Mater.* **2020**, *32*, 1906735. [CrossRef]
108. Wang, J.; Yuan, J.; Chen, C.; Wang, L.; Zhai, Z.; Fu, Q.; Liu, Y.; Dong, L.; Yan, W.; Li, A.; et al. Cu3Pt alloy-functionalized Cu mesh as current collector for dendritic-free anodes of potassium metal batteries. *Nano Energy* **2020**, *75*, 104914. [CrossRef]

109. Wang, J.; Yan, W.; Zhang, J. High area capacity and dendrite-free anode constructed by highly potassiophilic Pd/Cu current collector for low-temperature potassium metal battery. *Nano Energy* **2022**, *96*, 107131. [CrossRef]
110. Li, L.; Ji, P.; Huang, M.; Zhang, Z.; Wang, H.; Verpoort, F.; Yang, J.; He, D. Hybrid ionic/electronic interphase enabling uniform nucleation and fast diffusion kinetics for stable lithium metal anode. *Chin. Chem. Lett.* **2024**, *35*, 109144. [CrossRef]
111. Jiang, J.; Liu, Y.; Liao, Y.; Li, W.; Xu, Y.; Liu, X.; Jiang, Y.; Zhang, J.; Zhao, B. Construction of Synchronous-Deposition K Metal Anodes Via Modulation of Ion/Electron Transport Kinetics for High-Rate and Low-Temperature K Metal Batteries. *Small* **2023**, *19*, 2300854. [CrossRef]
112. Luo, Z.; Liu, C.; Tian, Y.; Zhang, Y.; Jiang, Y.; Hu, J.; Hou, H.; Zou, G.; Ji, X. Dendrite-free lithium metal anode with lithiophilic interphase from hierarchical frameworks by tuned nucleation. *Energy Storage Mater.* **2020**, *27*, 124–132. [CrossRef]
113. Wang, R.; Shi, F.; He, X.; Shi, J.; Ma, T.; Jin, S.; Tao, Z. Three-dimensional lithiophilic Cu@Sn nanocones for dendrite-free lithium metal anodes. *Sci. China-Mater.* **2021**, *64*, 1087–1094. [CrossRef]
114. Lim, G.J.H.; Lyu, Z.; Zhang, X.; Koh, J.J.; Zhang, Y.; He, C.; Adams, S.; Wang, J.; Ding, J. Robust pure copper framework by extrusion 3D printing for advanced lithium metal anodes. *J. Mater. Chem. A* **2020**, *8*, 9058–9067. [CrossRef]
115. Lu, R.; Zhang, B.; Cheng, Y.; Amin, K.; Yang, C.; Zhou, Q.; Mao, L.; Wei, Z. Dual-regulation of ions/electrons in a 3D Cu-CuxO host to guide uniform lithium growth for high-performance lithium metal anodes. *J. Mater. Chem. A* **2021**, *9*, 10393–10403. [CrossRef]
116. Liao, J.-L.; Zhang, S.; Bai, T.-S.; Ji, F.-J.; Li, D.-P.; Cheng, J.; Zhang, H.-Q.; Lu, J.-Y.; Gao, Q.; Ci, L.-J. A ZnO decorated 3D copper foam as a lithiophilic host to construct composite lithium metal anodes for Li–O_2 batteries. *Rare Met.* **2023**, *42*, 1969–1982. [CrossRef]
117. Yang, G.; Chen, J.; Xiao, P.; Agboola, P.O.; Shakir, I.; Xu, Y. Graphene anchored on Cu foam as a lithiophilic 3D current collector for a stable and dendrite-free lithium metal anode. *J. Mater. Chem. A* **2018**, *6*, 9899–9905. [CrossRef]
118. Ma, J.; Yang, J.; Wu, C.; Huang, M.; Zhu, J.; Zeng, W.; Li, L.; Li, P.; Zhao, X.; Qiao, F.; et al. Stabilizing nucleation seeds in Li metal anode via ion-selective graphene oxide interfaces. *Energy Storage Mater.* **2023**, *56*, 572–581. [CrossRef]
119. Chen, Q.; Liu, B.; Zhang, L.; Xie, Q.; Zhang, Y.; Lin, J.; Qu, B.; Wang, L.; Sa, B.; Peng, D.-L. Sodiophilic Zn/SnO_2 porous scaffold to stabilize sodium deposition for sodium metal batteries. *Chem. Eng. J.* **2021**, *404*, 126469. [CrossRef]
120. Wang, J.; Kang, Q.; Yuan, J.; Fu, Q.; Chen, C.; Zhai, Z.; Liu, Y.; Yan, W.; Li, A.; Zhang, J. Dendrite-free lithium and sodium metal anodes with deep plating/stripping properties for lithium and sodium batteries. *Carbon Energy* **2021**, *3*, 153–166. [CrossRef]
121. Xia, J.; Zhang, F.; Liang, J.; Fang, K.; Wu, W.; Wu, X. In-situ constructing a supersodiophilic fluffy surface layer on a Cu foam host for stable Na metal anodes. *J. Alloys Compd.* **2021**, *853*, 157371. [CrossRef]
122. Wang, L.; Luo, G. Atomistic Mechanism and Long-Term Stability of Using Chlorinated Graphdiyne Film to Reduce Lithium Dendrites in Rechargeable Lithium Metal Batteries. *Nano Lett.* **2021**, *21*, 7284–7290. [CrossRef] [PubMed]
123. Pirayesh, P.; Jin, E.; Wang, Y.; Zhao, Y. Na metal anodes for liquid and solid-state Na batteries. *Energy Environ. Sci.* **2024**, *17*, 442–496. [CrossRef]
124. Zhang, S.; Ma, Y.; Zhao, Y.; Qian, Y.; Suo, L.; Wang, X.; Huang, J.; Li, W.; Zhang, B. Lightweight and Flexible 3D ERGO@Cu/PA Mesh Current Collector of Li Metal Battery for Dendrite Suppression. *ACS Appl. Polym. Mater.* **2023**, *5*, 3289–3297. [CrossRef]
125. Zhao, Q.; Hao, X.; Su, S.; Ma, J.; Hu, Y.; Liu, Y.; Kang, F.; He, Y.-B. Expanded-graphite embedded in lithium metal as dendrite-free anode of lithium metal batteries. *J. Mater. Chem. A* **2019**, *7*, 15871–15879. [CrossRef]
126. Guo, Y.-M.; Zhang, L.-J. Research Progress in Synthesis and Electrochemical Performance of Cobalt Sulfide as Anode Material for Secondary Batteries. *Chin. J. Rare Met.* **2022**, *46*, 227–237.

Disclaimer/Publisher's Note: The statements, opinions and data contained in all publications are solely those of the individual author(s) and contributor(s) and not of MDPI and/or the editor(s). MDPI and/or the editor(s) disclaim responsibility for any injury to people or property resulting from any ideas, methods, instructions or products referred to in the content.

molecules

MDPI

Review

Advancing Metallic Lithium Anodes: A Review of Interface Design, Electrolyte Innovation, and Performance Enhancement Strategies

Junwei Shi [1], Kailin Jiang [1], Yameng Fan [2], Lingfei Zhao [2], Zhenxiang Cheng [2], Peng Yu [3,*], Jian Peng [2,4,*] and Min Wan [1,*]

[1] School of Chemical and Environmental Engineering, Wuhan Polytechnic University, Wuhan 430048, China; junweishi0319@163.com (J.S.); jkl6868@163.com (K.J.)
[2] Institute for Superconducting and Electronic Materials, Australian Institute for Innovative Materials, University of Wollongong, Innovation Campus, Squires Way, Wollongong, NSW 2522, Australia; yfan@uow.edu.au (Y.F.); lingfeiz@uow.edu.au (L.Z.); cheng@uow.edu.au (Z.C.)
[3] State Key Laboratory of Material Processing and Die & Mold Technology, School of Materials Science and Engineering, Huazhong University of Science and Technology, Wuhan 430074, China
[4] Department of Mechanical and Materials Engineering, University of Western Ontario, London, ON N6A 5B9, Canada
* Correspondence: 2022511012@hust.edu.cn (P.Y.); jpeng256@uwo.ca (J.P.); wanm@whpu.edu.cn (M.W.)

Abstract: Lithium (Li) metal is one of the most promising anode materials for next-generation, high-energy, Li-based batteries due to its exceptionally high specific capacity and low reduction potential. Nonetheless, intrinsic challenges such as detrimental interfacial reactions, significant volume expansion, and dendritic growth present considerable obstacles to its practical application. This review comprehensively summarizes various recent strategies for the modification and protection of metallic lithium anodes, offering insight into the latest advancements in electrode enhancement, electrolyte innovation, and interfacial design, as well as theoretical simulations related to the above. One notable trend is the optimization of electrolytes to suppress dendrite formation and enhance the stability of the electrode–electrolyte interface. This has been achieved through the development of new electrolytes with higher ionic conductivity and better compatibility with Li metal. Furthermore, significant progress has been made in the design and synthesis of novel Li metal composite anodes. These composite anodes, incorporating various additives such as polymers, ceramic particles, and carbon nanotubes, exhibit improved cycling stability and safety compared to pure Li metal. Research has used simulation computing, machine learning, and other methods to achieve electrochemical mechanics modeling and multi-field simulation in order to analyze and predict non-uniform lithium deposition processes and control factors. In-depth investigations into the electrochemical reactions, interfacial chemistry, and physical properties of these electrodes have provided valuable insights into their design and optimization. It systematically encapsulates the state-of-the-art developments in anode protection and delineates prospective trajectories for the technology's industrial evolution. This review aims to provide a detailed overview of the latest strategies for enhancing metallic lithium anodes in lithium-ion batteries, addressing the primary challenges and suggesting future directions for industrial advancement.

Keywords: metallic lithium anodes; electrochemical properties; interface design modification; lithium dendrites; high energy density

1. Introduction

In response to global warming and extreme weather events, the worldwide demand for energy continues to grow, while the outlook for traditional energy systems appearing bleak [1–4]. The development of clean energy, such as low carbon, environmentally friendly, high-performance energy conversion, and storage systems, is essential for enhancing the current energy structure and reducing the use of fossil energy [5–7]. As a typical clean energy, lithium batteries offer significant advantages, including high energy density, high discharge power, long cycle life, no memory effect, and environmental sustainability in facilitating the widespread use of portable electronic devices and electric vehicles [8,9]. The unique configuration of lithium pouch cells can lead to differences in pressure distribution, electrode material distribution, and electrolyte distribution, which can affect their failure characteristics [10]. Through innovations in the field of electroplating chemistry, researchers have learned about the deposition and exfoliation behavior of lithium ions and have optimized electrolyte composition and operating conditions, thereby minimizing dendrite growth and improving cycling performance, providing important insights for the study of lithium-ion plating processes in non-aqueous liquid electrolytes to improve the stability of lithium metal anodes [11,12]. Strategies such as the use of composite anodes, the introduction of protective coatings, the optimization of electrolytes, and the integration of lithium metal anodes with advanced cathode materials and separators have shown promising results [13]. Among various advancements, the lithium metal anode is regarded as the most promising candidate for the next-generation of high-energy-density lithium batteries, owning to its mass specific capacity of 3860 mAh g^{-1} and a volume specific capacity of 2065 mAh cm^{-3} [14–16]. Additionally, the electrochemical redox potential (-3.040 V vs. standard hydrogen electrode) of the metallic lithium anode is significantly lower than those of other metal anodes [17]. These unique advantages also position metallic Li as one of the most important anode materials in the era of all-solid-state batteries, potentially facilitating a significant leap in the safe and energy density of lithium batteries.

Despite the above-mentioned advantages, with the deepening of the research on lithium metal anode, there are still challenges that need to be overcome before lithium metal anode batteries can be commercialized. Firstly, due to the high diffusion barrier and weak interaction energy, lithium atoms tend to form one-dimensional long tubular or filamentary lithium dendrites [18–20]. The constantly growing lithium dendrites can penetrate the separator and reach the cathode, causing internal electrical contact and short circuits in the battery, which may lead to thermal runaway and explosion risks [19,21–23]. Secondly, metallic lithium shows thermodynamic instability and is prone to react with solvents or additives in the electrolyte to form a solid electrolyte interphase (SEI) [24]. The typically formed SEIs are brittle and inhomogeneous, resulting in poor anode interface stability [25]. The rupture of the SEI during cycling results in the constant depletion of electrolyte and Li. Furthermore, the electrical insulation of the SEI layer makes it possible for lithium dendrites to detach from the anode and become electrochemically inert, known as “dead lithium”, resulting in low Coulombic efficiency and lithium utilization [26,27]. Lastly, the infinite volume change of the lithium metal anode during deposition/stripping can easily destroy the naturally formed SEI with poor mechanical properties, thus exposing the highly reactive lithium metal to the electrolyte and forming a new interface [28,29]. The continuous destruction and regeneration of SEI not only leads to the ongoing consumption of active lithium and electrolyte but also increases the battery’s impedance, ultimately leading to a rapid decline in the electrochemical performance of the battery [30].

In summary, studies on metal lithium anodes have identified three major challenges: lithium dendrite growth, uncontrolled interfacial reactions, and significant volume expansion, as shown in Figure 1 [31]. Generally, there are three types of solutions: electrode design, electrolyte modification, and interface engineering. However, with the increasing popularity of research on metal lithium anodes, new discoveries, and modification strategies continue to emerge in recent years. And previous generalizations cannot keep up with the latest progress, especially in novel, convenient, low-cost, and multi new strategies, or provide clear explanations for some issues. A prefatory review article focusing on the modification and protection of anodes can greatly benefit researchers by quickly orienting them towards the current developmental direction of the field [32]. Therefore, this review aims to summarize recent research from a broad perspective, including comprehensive fundamental knowledge and the latest work on metallic Li anodes. Moreover, this work, grounded in a vast array of published studies, offers detailed discussions on specific mechanisms not thoroughly explained in other comments.

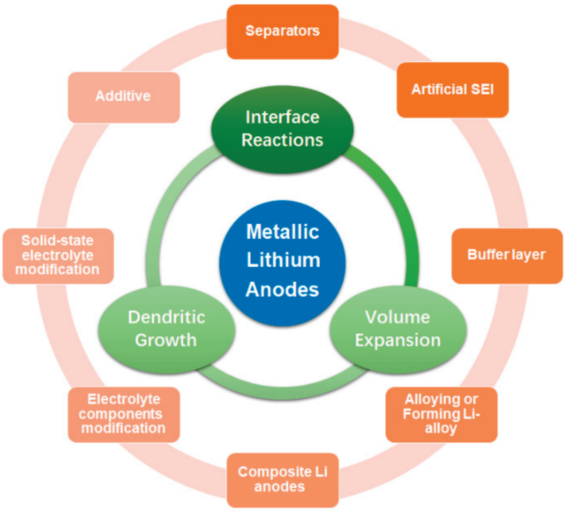

Figure 1. Challenges and improvement strategies for lithium metal anodes.

2. Strategies for Designing Advanced Li Metal Anode

Beginning from the lithium anode itself, modification strategies and protection measures primarily follows two directions: alloying/forming Li-alloy and designing composite Li anodes. These approaches are essentially effective in guiding nucleation deposition and constraining volume expansion.

2.1. Alloying or Forming Li-Alloy

To address issues such as reaction between electrodes and electrolytes, electrode alloying is commonly employed to improve safety, achieve dendrite-free anode, high Coulombic efficiency, and extend cycle lifespan [33]. Significant advancement has been achieved with the development of various Li alloy anodes, including various forms of lithium-carbon alloys (such as graphite-Li hybrid anodes), Li-Al alloys, lithium-zinc alloys, lithium-indium alloys, etc. [34–36]. However, challenges related to interface contact, as well as problems arising from stress due to volume expansion and the conduction rate of ions and electrons inside the electrode, have not been adequately addressed.

The mechanical properties of alloys play a crucial role in controlling dendrite formation on the anode. Compared to lithium-carbon alloys, a slightly higher voltage of lithium-metal alloy anodes contributes to enhancing the interfacial stability with SEs, as shown in Figure 2. Huang demonstrated the importance of the mechanical properties of the alloy in terms of dendrite suppression. Compared to other Li-alloys, the high compressive strength and high Young's modulus of Li-Al alloy enabled it to effectively maintain the integrity of the electrode during repeated loading and unloading. It was shown that Li-Al alloy anodes exhibited the highest ability to inhibit dendrite formation, and no soft shorts were observed in symmetrical cells under high current densities of 40 mA cm^{-2} and a capacity of 3 mAh cm^{-2}, with excellent cycling performance and electrochemical performance. It is expected to be a promising anode for high-rate and high-area capacity solid-state battery (SSBs) [37]. Peng used a one-step phase change alloying reaction to construct a lithium alloy/ionic conductor composite anode. In this process, the original $LiMgPO_4$ (LMP) was converted into ionically conductive Li_3PO_4 and Mg, and Mg reacts with Li to form Li-Mg alloys to form Li-LMP composites. On the one hand, the alloying of nanoscale Li_3PO_4 improved the mechanical strength of Li-LMP, enabling it to withstand the local stresses that would occur during cycling, and on the other hand, it enhanced the ion transfer inside Li-LMP and accelerated the dynamic mass transfer process. Li-

LMP exhibited higher rate performance and cycling stability in both ether and carbonate electrolytes [38]. Guo constructed a solid solution-based Li-Mg alloy framework through mechanical rolling, which acted as an electron/ionic double conductive lithium host, inhibiting lithium dendrites and volume changes to stabilize the metal lithium anode. The lithophilic Li-Mg solid solution alloy promoted uniform Li deposition and promoted Li extraction during the peeling process, which inhibited the parasitic reaction and dendrites on the surface of the Li metal anode [39]. Zheng chose 3D carbon cloth (CC) as the substrate to cover the entire zinc oxide quantum dots to inhibit Li dendrite growth. The spontaneous reaction between ZnO QDs and molten Li formed LiZn alloy and covered the CC surface, so the substrate had a high Li adsorption affinity and appropriate Li diffusion barrier energy. The three-dimensional structure of CC provided a higher specific surface area and reduced the effective current density of the electrode, and the surface of the formed LiZn alloy had a high adsorption energy (−1.89 eV) and a diffusion barrier suitable for Li atoms (0.68 eV), which was conducive to the uniform dense nucleation and deposition of Li. Due to the dendrite-free Li deposits, the Li/LiZn/CC anode worked for 2700 h at 1 and 10 mA cm^{-2} for 2700 and 1900 h, respectively, showing remarkable stability in symmetrical cells [40].

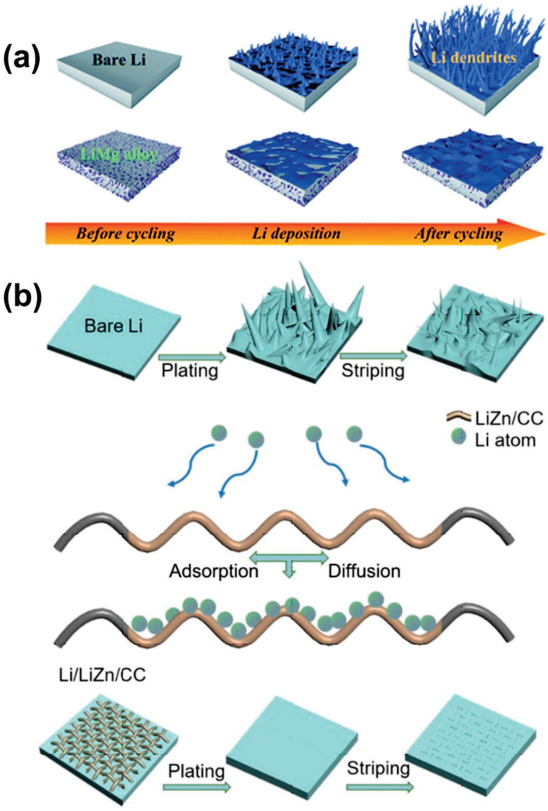

Figure 2. Schematics of (**a**) the inhibition of lithium growth by Li-Mg alloy [39]. (**b**) Li deposition on bare Li or Li/LiZn/CC substrates [40].

2.2. Composite Li Anodes

Composite lithium anodes employing 3D host materials with pre-stored lithium properties, or 3D current collectors featuring lithophilic properties, have been demonstrated as effective methods to facilitate the uniform deposition of lithium and prevent the formation of dendrites. This approach can effectively mitigates issues such as irregular lithium deposition, serious volume changes, and safety hazards, as shown in Figure 3 [14]. And the specific data are shown in Table 1.

Qutaish calculated the influence of different heteroatoms (pyridinic N, pyrrolic N, quaternary N, and Co−N$_4$) on the growth mechanism of Li clusters using density functional theory: Li grew axially on the surface of the carbon skeleton, while other heteroatoms, such as nitrogen defects, led to the vertical growth of Li [41].

Zhang prepared a 3D $Ti_3C_2T_x$@Cu current collector where the 3D structure not only effectively reduced the average current density but also alleviated volume expansion. $Ti_3C_2T_x$ nanosheets as a Li affinity agent facilitated uniform deposition and dendrite-free structure, resulting in a reduction in nucleation overpotential and an increase in Li nucleation sites. After prolonged plating/stripping, the Li-$Ti_3C_2T_x$@Cu anode's surface could still maintain uniformity. Under the condition of 1 mA cm^{-2} current density and 1 mAh cm^{-2} surface capacity, the super-stable cycling time of the Li-$Ti_3C_2T_x$@Cu symmetric cell was about 950 h [42]. Yang electroplated a 3D micro-porous structure of a lithium-friendly nickel scaffold on a flat copper with nano-scale surface roughness to serve as a metal lithium anode collector. The high specific surface area and nanoscale rough surface allowed for low local current density and uniform electric field distribution, which facilitated the uniform deposition of lithium metal at high current densities. The $Ni(OH)_2$ thin layer formed in situ during electrodeposition exhibited high lithium affinity, inducing uniform nucleation of lithium. This 3D lithiophilic Ni micro-porous (3D NMV) matrix endowed the Li metal anode with long cycle performance exceeding 830 cycles under an ultra-high current density of 10 mA cm^{-2} [43]. Using low-cost bamboo as a raw material, a nickel-embedded porous graphite carbon fiber (PGCF@Ni) advanced anode was constructed by Wang. Due to its excellent conductivity and high specific surface area, lithium could be uniformly deposited/stripped on the prepared SEI@Li/PGCF@Ni anode without lithium dendrites. In a symmetrical battery, under the conditions of 1 mA cm^{-2}/1 mAh cm^{-2}, the overpotential after 2000 h was only about 10 mV. The Li-S full battery assembled through collaborative design (SEI@Li/PGCF@Ni||PGCF@Ni/S) exhibited excellent stability, with a capacity retention rate as high as 77.9% after 600 cycles at 1 C [44]. Chen effectively guided uniform Li deposition in the 3D subject by applying magnetron sputtering to uniformly anchor the liphyphilic silver layer on the copper net (Li@/Ag) and realized the spatial control of Li nucleation. The symmetrical battery could maintain a low overpotential (230 mV) and long cycle life (90 h) at a high current of 10 mA cm^2 with a plating amount of 3 mAh cm^2. Also, Li@/Ag||$LiCoO_2$ cells exhibited high capacity retention (86.39%) after 150 cycles at 2 C [45]. Liu devised a 3D ZIF-8@RGO scaffold material that could function both as a current collector and a host for the metal lithium anode. The preferential deposition of Li was achieved through the synergistic effect of the lithiophilic N/Zn nucleation sites and the independently conductive RGO. The Li/ZIF-8@RGO anode was able to operate for 600 h (pre-loaded with 5 mAh cm^{-2}), without short-circuiting, and demonstrated high Coulombic efficiency of up to 98.48% over 350 cycles. The full battery also exhibited excellent cycle stability and rate capability [46].

The use of blockchain technology as a tool for process management can enhance the safety of the manufacturing and transporting lithium-ion batteries, as shown in Figure 4. As reported by Ma, who reported the utilization of a conductive polymer-filled metal-organic framework (MOF) as the host for lithium ions, polypyrrole (PPy) acted as a 'link' to connect stored lithium 'blocks' in the MOF pores. When highly conductive PPy guided fast Li$^+$ penetration/extrusion and acted as nucleation sites for isotropic Li growth, the MOF pores separated block-shaped Li deposits into regions for 3D matrix Li storage. This resulted in excellent Coulombic efficiency with low overpotential and dendrite-free growth during Li plating/stripping [47]. A host integrating Co-Fe binary metal selenide quantum dots into a 3D inverse opal nitrogen-doped carbon framework (3DIO FCSe-QDs@NC) was designed for application to sulfur cathodes and metal lithium anodes. The highly dispersed FCSe-QDs had good adsorption and catalytic properties, which effectively immobilized soluble LiPSs, improved diffusion conversion, and alleviated the shuttle behavior of polysulfides. At the same time, the abundant lithophilic sites of the three-dimensional ordered porous network could achieve uniform lithium deposition and uniform lithium-ion melting, thereby inhibiting dendrite growth. Taking advantage of these features, the lithium-ion battery assembled with 3DIO FCSe-QDs@NC as the main body exhibited excellent rate performance and stable cycling ability (with a decay rate as low as 0.014% over 2000 cycles under the 2 C condition). It is worth noting that under ultra-low conditions with a sulfur loading of 8.50 mg cm^{-2} and an electrolyte/sulfur ratio of 4.1 µL mg^{-1}, the areal capacity of the electrode reached 8.41 mAh cm^{-2} [48]. Xu designed a novel yolk-shell nitrogen doped carbon frameworks embedded with heterostructures ZnSe-CoSe$_2$ (ZnSe-CoSe$_2$@NC) for both anode and cathode protection in Li-S batteries, among which the in situ formed Li$_2$Se phase contributed to the Li$^+$ transfer. Co and Zn guided the uniform growth of Li within the 3D framework, effectively suppressing Li dendrite growth. This design provided outstanding conductivity and stability, with a long cycle life over 1000 cycles at 2 C and a high areal capacity of 4.16 mAh cm^{-2} after 100 cycles at 0.2 C with high sulfur loading (6.08 mg cm^{-2}) and lean electrolyte (4.1 µL mg^{-1}) [49]. The 3D main structure has become a promising strategy to address the critical issues of the metal lithium anode, including severe volume changes and dendrite growth during battery cycling. Zhang constructed a 3D CNT framework with MnO$_x$ coating using a simple hydrothermal method. Using it as the main body for the injection of molten Li, the thickness of the ultra-thin Li metal anode could be controlled to form a self-supported 10 µm ultra-thin Li metal anode, increasing the utilization of Li and limiting volume expansion. The abundant MnO$_x$ nanoparticles acted as Li affinity sites, reducing the Li nucleation barrier and optimizing the electrochemical kinetics of the anode/electrolyte interface. It showed excellent lifetime extended to 2000 cycles in the symmetric cell, as well as better capacity and rate performance than the naked Li anode in the full cell [50]. Shin demonstrated through electrochemical simulations that carbon activity (lithophilic) and intergranular porosity could modulate lithium plating behavior by controlling the competitive kinetics of charge transfer and Li$^+$ transport. It was shown that the lithophilicity at the bottom of the electrode was enhanced, the porosity between the particles at the top increased, and Li preferentially nucleated and then grew from the bottom upwards. The high-capacity, long-cycle main structure heterostructure prepared by two-step electrophoretic deposition spatially limit the volume change of a large number of lithium metal (6 mAh cm^{-2}) with a cycle life of more than 900 cycles, which proved that the controllable heterogeneity of interfacial activity and porous structure could limit the storage behavior of lithium metal in the MOF-derived carbon host structure [51].

Wang developed a compact TiO$_2$@VN (vanadium nitride) heterojunction structure with high true density (5.01 g cm^{-3}), made by clever selective nitro enation, as a dual host for sulfur and Li without carbon. TiO$_2$@VN exhibied special Li affinity and could serve as a Li matrix, uniformly adjusting Li nucleation and inhibiting dendrite growth, resulting in a high electrode-level volume/weight energy density for the assembled full cell [52]. Wang also designed an advanced nitrogen-doped carbon microreactor embedded with a rich Co$_3$O$_4$/ZnO heterojunction (CZO/HNC) as the host for the collaborative optimization of the S cathode and Li metal anode. The optimized band structure of CZO/HNC effectively promoted ion diffusion, which, in turn, promoted the bidirectional conversion of LiPSs. The lithophilic nitrogen dopant and the Co$_3$O$_4$/ZnO site jointly regulated the deposition of dendritic lithium. The above synergistic effect resulted in the S@CZO/HNC cathode exhibiting excellent cycling stability at 2 C, with a capacity decay of only 0.039% per cycle over 1400 cycles, while the symmetrical Li@CZO/HNC cell achieved stable lithium plating/stripping behavior over 400 h. The Li-S full cell exhibited an astonishing cycle life of over 1000 cycles [53]. Zhu designed a porous flexible self-supporting membrane composed of single-walled carbon nanotubes (SWCNTs), and the intertwined conductive network of single-walled carbon nanotubes could effectively reduce the huge volume expansion and local current density during cycling. The main body of the lithium metal anode was designed as a highly lithium-loving heterostructure (Mn$_3$O$_4$/ZnO@SWCNT), and the constructed p-n-type heterojunction generated a built-in electric field to promote electron transfer and Li$^+$ migration. As a pre-implanted nucleation site, the strong binding of lithium-philic Mn$_3$O$_4$/ZnO particles to lithium atoms significantly reduce the lithium nucleation barrier. As a result of the above-mentioned synergistic effects, symmetrical cells composed of Mn_3O_4/ZnO@SWCNT-Li can stably remained low for more than 2500 h at 1 mA cm^{-2} and 1 mAh cm^{-2} [54].

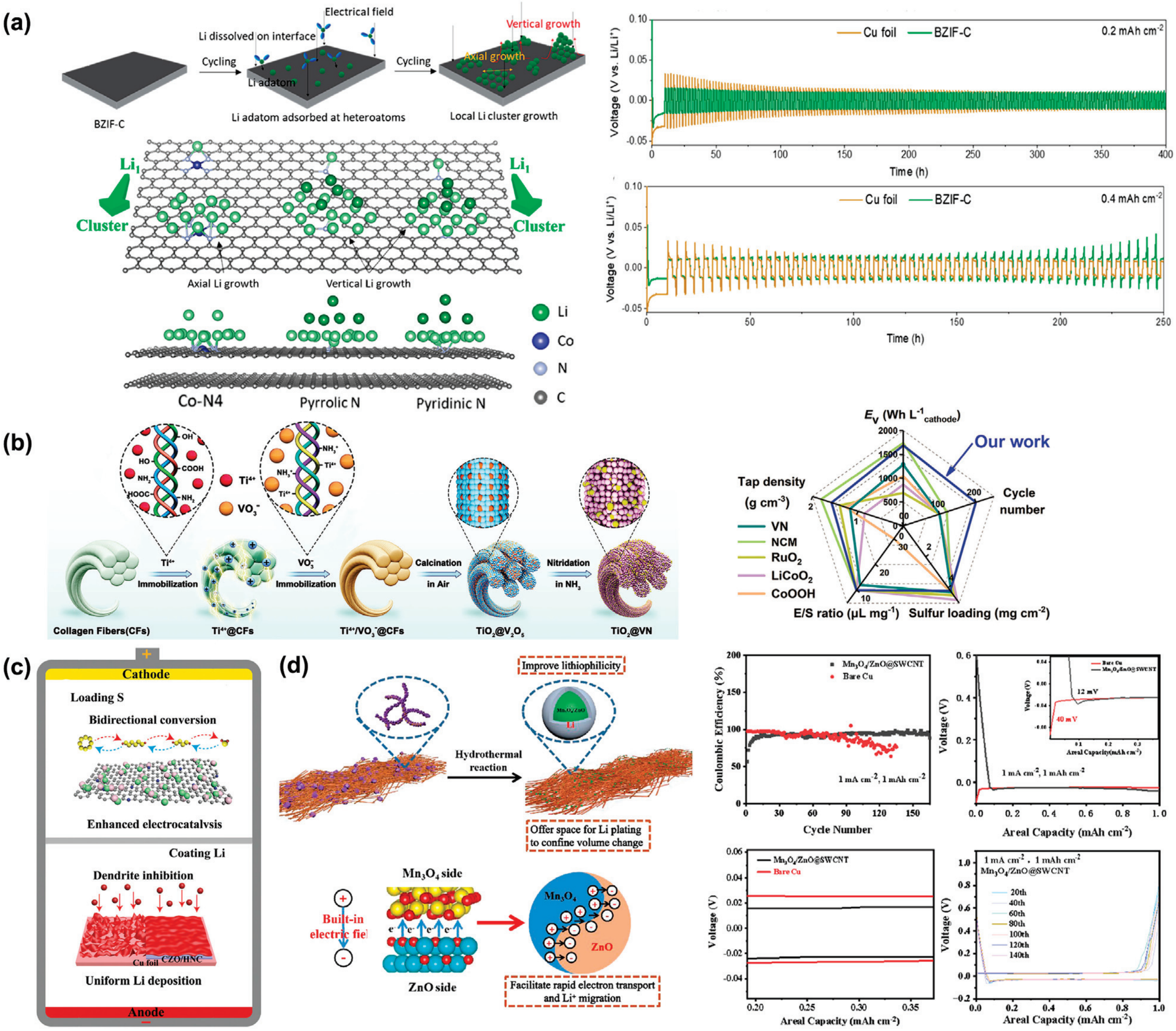

Figure 3. Schematic representation of (**a**) the deposition and growth during the Li plating process with its electrochemical performance [41]. (**b**) The synthesis procedure of fibrous TiO_2@VN heterostructure with its electrochemical performance [52]. (**c**) The role played by CZO/HNC in the Li-S full cell [53]. (**d**) The synthesis of Mn_3O_4/ZnO@SWCNT with its electrochemical\performance [54].

Table 1. The progress and electrochemical performance of LMBs in Section 2.2.

Modification	Current Density (mA cm^{-2})	Cycle Life (h)	Number of Cycles	Sulfur Loading (mg cm^{-2})	Lean Electrolyte (μL mg^{-1})	Ref.
3D $Ti_3C_2T_x$@Cu current collector	1	950				[42]
3D NMV	10		830			[43]
Li@/Ag||$LiCoO_2$	10	90	150			[45]
Li/ZIF-8@RGO		600	350			[46]
3DIO FCSe-QDs@NC			2000	8.5	4.1	[48]
ZnSe-$CoSe_2$@NC			1000	6.08	4.1	[49]
3D CNT with MnO_x coating			2000			[50]
MOF-derived carbon heterostructure (EPD)			900			[51]
Li@CZO/HNC		400	1400			[53]
Mn_3O_4/ZnO @SWCNT-Li	1	2500				[54]

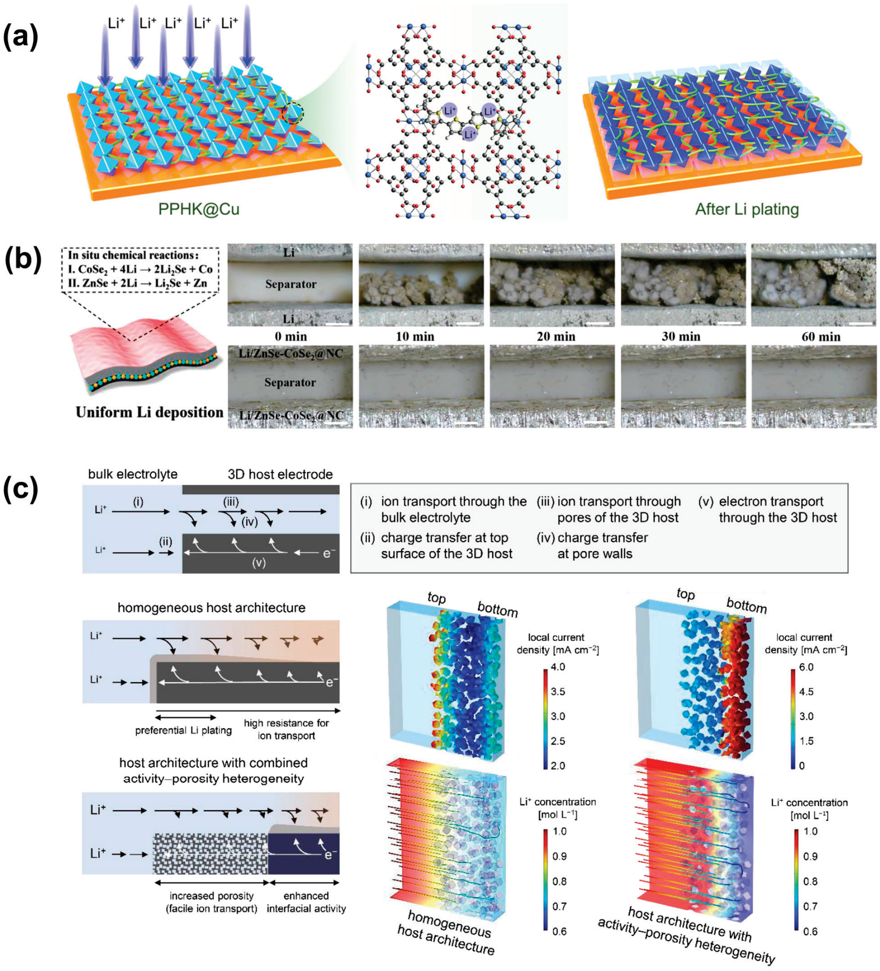

Figure 4. Schematic diagram of (**a**) a strategy to promote homogeneous Li deposition through the "blockchain" synergy via PPy-filled HKUST-1 [47]. (**b**) The structure of two-in-one ZnSe-CoSe$_2$@NC host on anode and in situ observations of symmetric cells with pure Li and Li/ZnSe-CoSe$_2$@NC electrode cycling at a current density of 3 mA cm^{-2} [49]. (**c**) The multiple reaction steps involved in Li plating in a 3D host architecture [51].

3. Electrolyte Modification

3.1. Liquid Electrolyte

Liquid electrolytes have been a focal point in lithium-ion battery research for many years. The nature of the solid electrolyte interphase layer is primarily influenced by the properties of the organic electrolyte, making the optimization of salt-solvent combinations an effective strategy for generating uniform and robust SEI layers. In recent years, some novel electrolyte materials and additive have emerged [55]. Currently, mainstream modified electrolytes are mainly divided into two categories: the in situ construction of lithium-rich SEI by adding an appropriate amount of fluorinated compounds as electrolyte additives to commercial electrolytes, and the addition of sacrificial additives.

Based on the influence of solvent polarity and donor number on Li$^+$ solvation, solvent design with functional structure can increase the number of Li$^+$-anion coordination and thus form inorganic species-rich SEI on the Li anode, as shown in Figure 5. Kim proposed a design strategy for suspended electrolytes to achieve the above objectives: a mixture of inorganic nanoparticles (Li$_2$O) and liquid electrolytes was used as the electrolytes. The electrolytes were suspended carbonate electrolyte (SCE), suspended fluoride electrolyte (SFE), and suspended LHCE (SLHCE) and were compared. The interfacial interaction between the Li$_2$O surface and the surrounding Li$^+$ solvated shell achieved the interaction between Li_2O and the surrounding liquid electrolyte. This decreased the Li^+-solvent coordination and increased the Li^+-anion coordination, thereby changing the Li^+ solvation environment, forming a weak solvation environment, promoting lithium-ion mobility, and stabilizing the formation of SEI [56].

In recent years, there have been innovative modification ideas for traditional additives such as $LiNO_3$. Hou amplified the positive effects of -NO_3 by modifying it to enhance its reducibility. -NO_3 was linked in isosorbide mononitrate to ether groups to break its resonant structure in nitrate esters, thereby significantly improving its reducibility. The decomposition of -NO_3 resulted in SEI enriched with abundant LiN_xO_y and induced even deposition of Li, which have potential commercial application prospects [57]. Zhao confirmed that $LiNO_3$ could serve as an effective salt additive for carbonate electrolyte solvents and ether electrolytes. Previous efforts on high solubility of $LiNO_3$ could not be achieved in carbonate ester solvents. This may have been caused by the use of mixtures of cyclic/linear carbonate ester solvents (which contained other additives) as battery electrolytes. Cyclic carbonate ester solvents (such as ethylene carbonate) could dissolve up to 0.7 M $LiNO_3$ without any additives, significantly improving the reversibility of the anode and demonstrating that $LiNO_3$-rich carbonate ester electrolytes could significantly enhance the stability of LMBs [58].

Pal developed an ether-assisted ionic liquid electrolyte to provide superior lithium metal deposition, high voltage (5 V) stability, and ultra-safety: ether solvent 1,2,2 dimethoxyethane (DME) was added to the electrolyte with a high lithium salt concentration of N-methylNpropylpyrrolidine bis(fluorosulfonyl)imide (C3mpyrFSI). This provided the better possible improvements in ionic conductivity, lithium diffusivity, and lithium plating/stripping kinetics, resulting in stable, high-speed cycling for lithium-metal/LFP (3.5 V) batteries. In the batteries with $LiNi_{0.8}Mn_{0.1}Co_{0.1}O_2$ (4.4 V) and $LiNi_{0.6}Mn_{0.2}Co_{0.2}O_2$ (4.3 V) as the cathode and Li as the anode, high Coulombic efficiency was achieved at both room temperature and high temperature. The ether ionic liquid chemistry enabled the ideal lithium plating morphology with high pile-up density, leading to minimal formation of "dead" or non-active lithium and dendrite-free long-term cycling [59].

In the non-flammable triethyl phosphate (TEP)-based electrolyte with tris(hexafluoroisopropyl) phosphate (THFP) as an additive, the polarity of the C-F bond and the abundant CF_3 group in THFP reduced the highest occupancy molecular orbital (LUMO) and lowest unoccupied molecular orbital (HOMO) energy levels in THFP. The reduction of THFP contributed to the formation of a stable and lithium-rich SEI layer, which improved the binding capacity of PF_6^- anions, significantly inhibited the growth of lithium dendrites, and reduced the decomposition of electrolytes. At the same time, THFP is also involved in the formation of a thin, CF-containing electrolyte interface layer (CEI), allowing it to provide stable cycling of the cathode at high pressures. Li | | Li and THFP-added full-Li/NCM622 cells exhibited low polarization and long cycle life [60]. Another approach is to slow down Li dendrite growth by protecting the electrolyte from trace amounts of H_2O. Hexafluoropropylene oxide (HFPO) was proposed as an additive to the electrolyte to induce a hydrophobic Li^+-solvent coordination structure. The hydrophobicity of HFPO, as well as the olefin groups and non-polar perfluorocarbon chains (-$CF_2CF_2CF_3$), protected symmetrical cells from a slight attack by H_2O and avoided the formation of ionic insulation decomposition products on the lithium anode and cathode. The LUMO and HOMO corresponding to HFPO made it reduce/oxidize on both the lithium anode and cathode, forming a rich organic SEI film and cathode electrolyte interface layer (CEI), which could adapt to the evolution of the anode/cathode structure [61]. Metal ions and organic polymers were used as electrolyte additives to effectively control lithium-ion deposition and alleviate lithium dendrite problems, thereby improving the coulombic efficiency and stability of lithium-ion batteries. When lithium nitrate additives and small amounts of tetramethylurea (TMU) were introduced into commercial carbonate electrolytes as multifunctional co-solvents, normally insoluble NO^{3-} ions can be incorporated into the solvation structure of Li^+ ions to form conductive and stable SEIs. The solvation structure was controlled, and the scavenging effect could be used to inhibit the production of HF [62]. Fluorinated aromatic diluent was introduced into the high-concentration electrolyte, where the diluent was paired with anions to facilitate the formation of a uniform and robust SEI. Their synergistic effect on the SEI endowed Li metal with extraordinarily high coulombic efficiency as high as 99.8% [63].

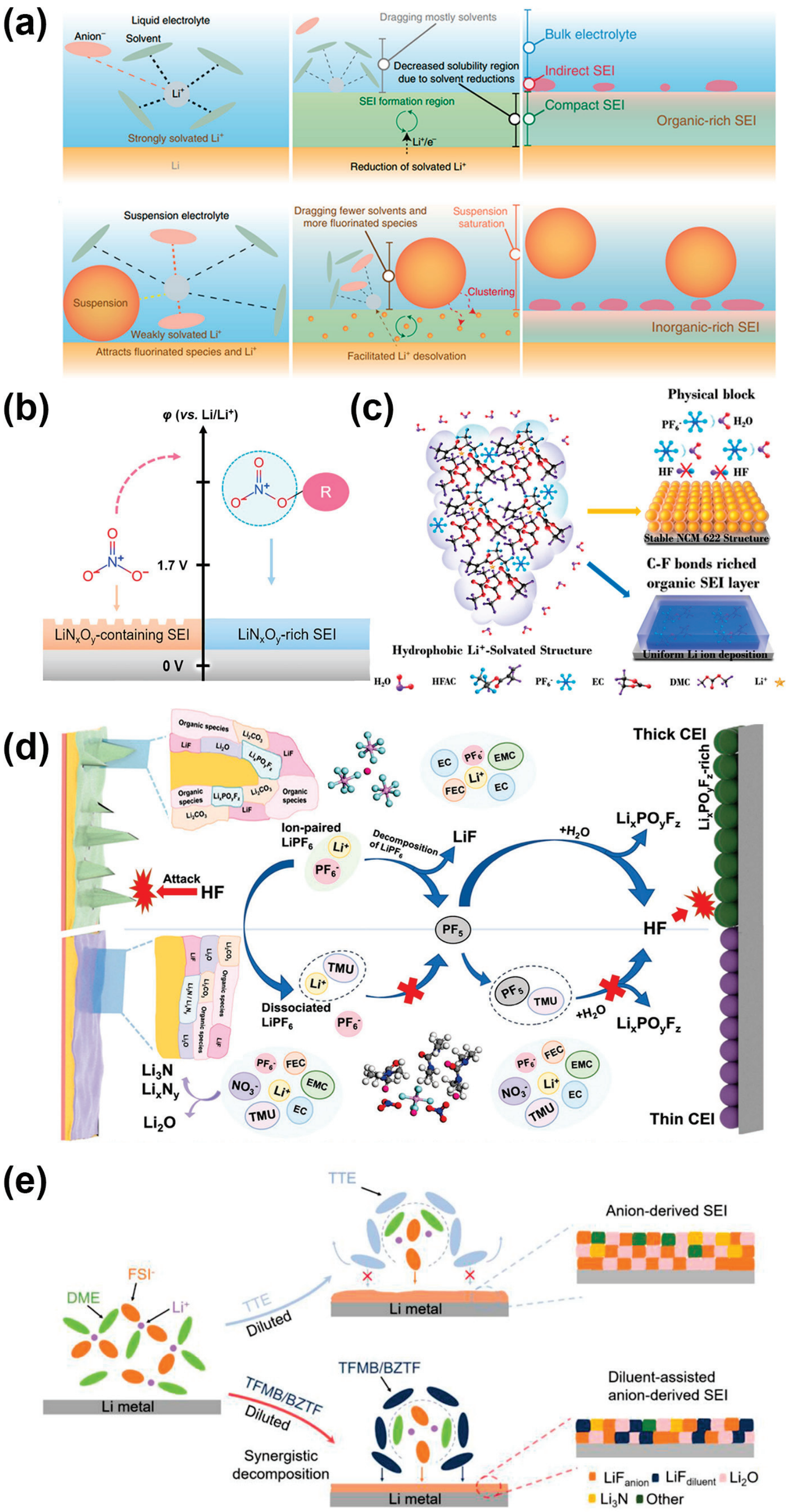

Figure 5. Schematic illustration of (**a**) comparison of the effects of a conventional liquid electrolyte and a suspension electrolyte on the evolution process on the Li anode [56]. (**b**) Strategy of NO_3^-

stabilization of SEI: reduction of NO_3 with resonance structure to form SEI containing LiN_xO_y. Then, NO_3 was modified to improve the reducibility and form LiN_xO_y-rich SEI [57]. (**c**) Mechanism of HFAC on the formation of organic-rich SEI layer and inhibition of $LiPF_6$ decomposition [61]. (**d**) Interaction of SEI composition, solvation structure, morphology of lithium deposit, HF attack, CEI thickness, and electrochemical performance in CCE and CCE-TMU/$LiNO_3$ electrolytes [62]. (**e**) The electrolyte structure and the correspondingly formed SEI in TTE-diluted and TFMB/BZTF-diluted HCEs [63].

3.2. Solid-State Electrolyte

SSBs can increase energy density and eliminate the safety risks associated with flammable liquid electrolytes found in traditional lithium-ion batteries. Companies in the automotive and battery industries are already planning research and development in the field of SSBs [64,65]. Yi coated a non-flammable gel layer on the surface of CPE and designed a multilayered hybrid electrolyte (MHE) to eliminate the safety hazards of solid-state lithium-ion batteries. The hydrogen bonding interaction between F and H atoms allowed the solvent to easily anchor the $TFSI^-$ anion in the liquid electrolyte. The gel layer was therefore well compatible with the lithium metal anode. Coupled with the good mechanical properties of CPE, the prepared MHE had a wide electrochemical window, a high ion mobility number, and ionic conductivity [66]. Zhang discovered that the blending of different polymers significantly enhanced the high-temperature deformation resistance of materials, and the use of dual-salt could strengthen the migration of lithium in solid substrate. As a result, a solid polymer electrolyte composed of a blend of polymers with polyethylene oxide (PEO) and polyvinylidene difluoride (PVDF) was developed, which is suitable for large-scale production and an ideal choice for high-temperature solid polymer batteries. In the PEO/PVDF blend matrix, the battery performance is excellent, and the presence of PVDF can maintain the shape of the membrane, avoid short circuits, and improve the safety of battery operation at high temperatures [67]. Ma designed a novel scalable, ultra-thin, high-temperature-resistant solid electrolyte (SPE) to provide a stable SSE/lithium-containing LiF and Li_3N interface. The SPE included an electro spun polyacrylonitrile (PAN) matrix and a polyethylene oxide (PEO)/lithium salt-ion conductor with excellent mechanical strength, which effectively inhibited lithium dendrites, prevented short circuits, and improved the performance of symmetrical lithium-ion batteries [68].

Kang produced SE with high ionic conductivity from a high dielectric constant polymer that could strongly interact with lithium salts. This polymer had a significant dipole moment that directed the transport of lithium ions (Li^+) along the chain, facilitating their continuous jumping in the solid polymer electrolyte (SPE) system [69]. In the solid electrolyte layer, the low porosity of oxide-based SE requires very high sintering temperatures to achieve, accompanied by poor interfacial contact. However, the most typical MOF-based SEs have high production costs, redundant preparation processes, and poor thermal stability, which is the most critical issue. Additionally, the relatively low ionic conductivity of both oxide-based SE and MOF-based SE at room temperature greatly limits the critical current density and high-rate performance of the battery, which is one of the great challenges in battery performance optimization. At present, most of the strategies using liquid alkali metal anode/interface layer have achieved some success in inhibiting alkali metal dendrite growth and improving the cycling stability of the battery. The highly conductive liquid anode has a strong ability to dissolve alkali metals even after nucleation is completed, and it is an effective strategy to fundamentally inhibit dendrite growth. However, attention needs to be paid to the safety performance of SEs and liquid alkali metal anodes/interface layers to prevent short circuits caused by liquid flow. Considering the above, Peng proposed a new system that combines a sulfide-based solid electrolyte with a liquid metal lithium anode (Li-Bp-DME), which further improved battery performance while retaining the inherent advantage of Li-Bp-DME in suppressing lithium dendrite nucleation and growth. Compared with other SEs, these sulfide-based SEs had superior ionic conductivity at room temperature and better high-rate charge-discharge performance, which could almost completely block the penetration of Li-Bp-DME, and greatly improved the cycling stability and lifetime. The addition of a polymer interface layer in the system further improved the compatibility and stability of Li-Bp-DME with sulfide-based solid electrolytes at the interface. The new battery structure using sulfide-based SEs, liquid metal lithium anodes (Li-BpDME), and interface optimization achieved long cycle life and record-breaking high critical current density up to 17.78 mA cm^{-2} [70]. $Li_{7-x}PS_{6-x}Cl_x$ (x = 0.6, 1.0, 1.3, 1.45, and 1.6) electrolytes were characterized physically in situ and in situ, chemical, and electrochemical studies. During the synthesis process of the SE, the distribution of Cl and the cooling process have a significant influence on the microstructure, interface composition, and morphology evolution of the Li|SE interface. For SEs with an appropriate amount of Cl, Cl atoms form interconnected LiCl nanoparticles on the surface of the SE grains, which can extend into a LiCl framework. This is beneficial for Cl ions to migrate to the interface during electrochemical cycling, thereby improving the cycling performance of the battery [71].

4. Interface Design Modification

4.1. Separators

Regarding the growth of anode metal dendrites, functional separators and interlayers are also an innovative method for defect remediation. Common methods include introducing a protective layer as an artificial SEI (anode) and comprehensive improvement of the wetting of the electrolyte and the uniformization of ion flux (anode and cathode) [72]. Separators are widely studied as a better alternative that involves the preparation of a special functional membrane and the use of its interaction with free solvent molecules to filter out the free molecules and obtain a high concentration of electrolyte after dissolution. The absence of expensive and toxic additives to the electrolyte is the biggest advantage of the separator. Lithium metal batteries assembled with functional separators can generally operate efficiently at room temperature, improving battery safety, as shown in Figures 6 and 7. Figure 6 summarizes the schematic diagram of Separators, and Figure 7 summarizes the schematic diagram of Artificial SEI.

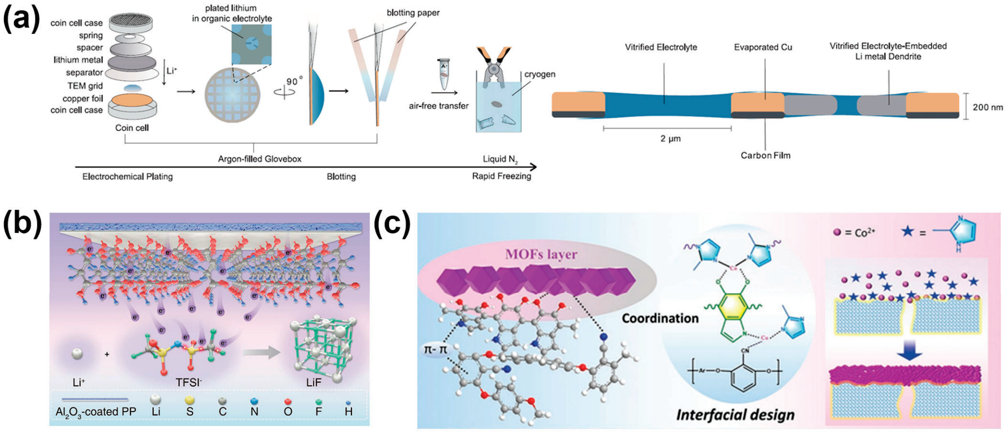

Figure 6. Separators: Schematic of (**a**) preparation process and schematic cross-section of vitrified specimens [73]. (**b**) Synthesis of LiF-rich SEIs: SAMs with carboxy-terminal groups accelerate the reduction process of LiTFSI by dipole moment directed electron provision [74]. (**c**) Internal construction of sandwich-structured MOFs/NA/MOFs hybrid separators [75].

Zhang used thin-film vitrification to retain the cell's electrode-electrolyte interface in its native organic liquid electrolyte environment. Using cryogenic scanning transmission electron microscopy characterization, the complete structure and chemical properties of the metal lithium battery interface were studied, and it was found that SEI expansion could be effectively alleviated by increasing the electrode/electrolyte interface area and changing the composition and thickness of SEI. Since the presence of solvents in SEI reduces the distance required for electron tunneling during electrolyte decomposition, solvent diffusion may play a more important role in the ongoing formation of SEI than other factors [73]. Liu designed self-assembled monolayers (SAMs) with high-density and long-range ordered polar carboxyl groups connected to alumina-coated separators. They could provide a strong dipole moment while providing excess electrons to accelerate the degradation kinetics of carbon-fluorine bonds in Li bis (oxalato) borate. The resulting SEI rich in LiF nanocrystals promoted rapid transfer of Li^+ and inhibited dendrite growth. In particular, the SAMs significantly enhanced the cycling performance of the whole cell under high-cathode loading, limited lithium excess, and poor electrolyte conditions [74]. A sandwich MOF/PEN@PDA/MOF multifunctional membrane was fabricated through the in situ growth of ordered anionic MOF layers on both sides of a pre-modified polyether nitrile (PEN) porous super engineering film by polydopamine pre-treatment. The optimized membrane completed the task of guiding the migration of lithium ions, limiting the free migration of anions, balancing the internal electric field, and prolonging the nucleation time of lithium dendrites, resulting in a high Li-ion transfer number of 0.81. Moreover, the multifunctional membrane showed better thermal stability than traditional polypropylene membranes. With reduced interfacial side reactions, the optimized battery exhibited highly stable cycles over 500 h. The assembled LFP/Li battery with the optimized membrane even showed steady cycling performance and a coulombic efficiency as high as 98% even at 90 °C [75]. The unique characteristics of covalent organic frameworks (COFs) make it a potential separator to address the issues mentioned above. COFs have a strong affinity with Li+, but the relationship with solvent molecules in electrolyte is exclusive. According to the above principle, Yang synthesized a self-loading COF membrane (TPB-BD$(OH)_2$-COF) as a separator for lithium metal batteries, which realized the aggregation of electrolyte and reduced the side effects of free solvent and lithium metal. The separator worked well even under extreme conditions (60 °C) [76]. Wang used MoP@NC composites modified with N-doped thin carbon layer (MoP@NC) and porous carbon nanofibers (PCNF) to coat the surface of the Celgard separator in an attempt to solve the problem of low sulfur utilization rate and short cycle life of lithium-sulfur batteries. The MoP@NC materials extracted from molybdenum-based MOFs (Mo-MOFs) had abundant pore volumes and multiple catalytic sites, and they presented rod-like morphologies with uniform structure and stable properties. PCNFs and N-doped thin carbon layers could effectively alleviate volume expansion, buffer electrolytes, and capture LiPS. When used as a modified layer on a separator, MoP@NC/PCNFs-based cells had optimized lithium and sulfur affinities, achieving ideal sulfur electrochemistry, and could be applied to high-performance Li-S batteries [77].

4.2. Artificial SEI

The Li deposition process is primarily controlled by the SEI on the metal surface, making the design of artificial SEI a crucial approach for regulating lithium electrodeposition. The main objective of designing an SEI layer on the metal lithium anode is to enhance the ionic conductivity of the SEI, thereby reducing the loss of lithium ions from the metal surface. Additionally, the construction of artificial SEI with improved mechanical properties can also suppress mechanical failures (fracture/cracking) caused by dendrite growth or interfacial displacement [78].

Ju developed a versatile artificial SEI that uses commercially produced soy protein fibers (SPF) to stabilize the metal lithium anode. The abundance of polar functional groups in its protein molecules could promote consistent lithium-ion flux and induce uniform lithium deposition. Lithium-philic and porous SPF could significantly alleviate the ion concentration gradient between electrodes, contributing to the deposition of biomimetic lithium along the fiber structure. The introduced SPF promoted the formation of SEI structures rich in LiF nanocrystals after cycling, thereby achieving low interfacial impedance and fast charge transfer kinetics, greatly reducing the concentration gradient of lithium ions, and achieving uniform distribution of lithium ions [79].

It is generally accepted that dendrite growth is thought to be related to the average stress during plating/stripping and the elastoplastic deformation of lithium metal and SEI. Theories such as the Butler–Volmer reaction kinetics of local current distribution, the space charge layer, and the mass transfer limit near the electrode surface have been proposed to explain the mechanisms of electrochemical and mechanical processes. Liu developed an electrochemical-mechanical model involving electrochemical kinetics and mechanics to simulate the performance manipulation of artificial SEI to achieve uniform lithium electrodeposition, mainly developed from a modified version of the Butler–Volmer equation. The model included an electric field, a stress field, and a lithium-ion concentration field, and the author described the process of electrodeposition at the interface between SEI and lithium metal. The results showed that the ionic conductivity and Young's modulus of SEI played an important role in the deposition behavior of lithium battery. If the ionic conductivity of SEI was increased above the critical level, the stress concentration was significantly reduced, and Li was preferentially deposited. When the SEI had sufficient mechanical strength (Young's modulus of about 4.0 GPa), the inhomogeneous deposition was reduced. On top of this, increasing the ionic conductivity could further improve the performance of the battery [80]. Zhang used an electrochemical phase field (PF) model to simulate inhomogeneous lithium deposition in porous lithium metal anodes. In the four factors studied: the porosity of the lithium metal anode, the diffusion coefficient of lithium ions, the reaction constant of lithium deposition, and the structural electrode with porosity gradient, it can be found that the lithium deposition in the pores can be improved by increasing the diffusion coefficient of lithium ions and designing lithium metal anodes with reaction constant gradient and porosity gradient [81]. On carbon fiber cloth ($CoSe_2$-NC@CFC), a layered 3D structure using $CoSe_2$ nanoparticles to anchor nitrogen-doped carbon nanosheet arrays was established to regulate lithium nucleation/plating processes and stabilize the electrolyte anode interface. Due to the enhanced lithium affinity of $CoSe_2$-NC, Li_2Se and Co nanoparticles formed in situ during the initial nucleation process, as well as the large pore space, could induce uniform Li nucleation/plating, optimize the SEI, and reduce volume changes [82].

Zhang selected 1-butyl-1-methylpyrrolidine bis (trifluoromethanesulfonyl) imide (BMI-TFSI) as the initiator to promote the formation of an artificial SEI protective layer between PIA-SPE and the metal lithium anode, providing it with more TFSI-anionic groups. A stable SEI layer (consisting of LiF, Li_2S_x, and Li_3N) was formed in situ on the electrolyte/Li surface, which promoted uniform deposition of lithium [83]. Li achieved an ideal lithium metal anode by the reaction of porous polymer backbone macromolecular brush (polyethylene glycol) methyl methacrylate, super-cross-linked polystyrene nanospheres (representing xPCMS-g-PEGMA) and single-ion conductive lithiation Nafion. The porous xPCMS core with a rigid hyper-crosslinked framework significantly improved the mechanical strength, providing sufficient channels for rapid ion conduction. Flexible PEGMA and lithiated Nafion polymers formed a structurally stable artificial protective layer that provided uniform Li diffusion and high Li migration number. The structure enabled ultra-high current density, unprecedented reversible lithium plating/stripping, and ultra-long-term stable cycling [84].

4.3. Buffer Layer

Aiming at the problems of poor physical contact and serious interface reaction at the negative electrode interface, the construction of a buffer layer on the surface of the solid electrolyte can improve the contact between the negative electrode interface and alleviate the interface chemical reaction [85]. Shen developed reduced Graphite oxide (RGO) coupled porous MoO_2-Mo_3N_2 heterojunction nanoribbons decorated copper collector (GMM@Cu) used for high-performance LMBs. The composite collector with functional interface had rich nucleation sites. Electroplating Li_2O and Li_3N, which are lipophilic to lithium, effectively accelerated the Self-diffusion of lithium ions in BIEF and promoted the uniform electrodeposition of lithium. The synergistic effect of the built-in electric field formed by good interface contact and the dense, lithium-rich SEI layer promoted charge transfer and ion diffusion and improved the uneven lithium-ion flux to suppress the growth of dendrites. In addition, the introduction of flexible Graphene layer improved the structural integrity and electron transport dynamics [86].

Zhang constructed a value-gradient iron-based protective layer on the Li anode and applied it to various batteries, which proved the superiority of the protective layer in the protection of lithium anode. The protective layer consisted of an outer layer containing Fe^{3+}/Fe^{2+} and an inner layer containing Fe^0, which not only isolated the lower layer of lithium metal from the corrosive carbonate electrolyte, but also stored lithium evenly during the plating process to inhibit lithium dendrite growth, exhibiting dendrite-free lithium plating/stripping behavior. The Li symmetrical battery ran stably for 1000 h at 1 mA cm^{-2} and 1 mAh cm^{-2}, and it even survived for 380 h at 30 mAh cm^{-2} ultra-high capacity. The lithium anode achieved high performance in $LiFePO_4$ batteries with 1600 and 1000 cycles of stable operation at 5 °C, respectively. Its high-load $LiCoO_2$ cells also exhibited excellent cycling stability and rate capability [87].

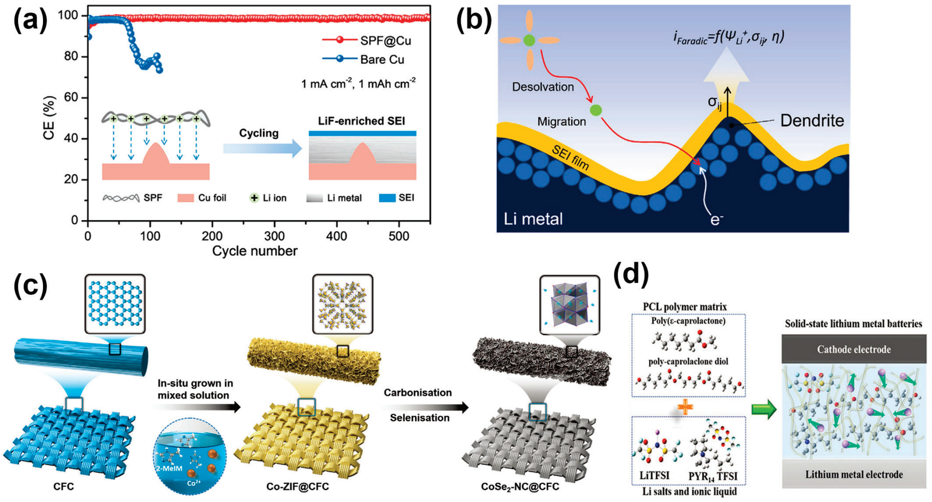

Figure 7. Artificial SEI: schematic diagram of (**a**) the SPF-mediated Li metal anode before and after cycling [79]. (**b**) Electrodeposition of Li at the interface between the bulk metal electrode and SEI (electrochemical kinetics and mechanical stresses) [80]. (**c**) Preparation route for $CoSe_2$-NC@CFC [82]. (**d**) The PIA-SPE [83].

5. Conclusions and Prospects

Lithium anode protection is a critical aspect of ensuring the stability and safety of lithium-ion batteries. Advances in SEI engineering, composite solid electrolytes, and electrode architectures have shown great potential in overcoming the challenges associated with lithium metal anodes. Continued research efforts to address the remaining challenges will pave the way for the widespread application of high-energy-density lithium-metal-based batteries in various industries. Advanced Li metal anode, electrolyte modification, and interface design modification collaboratively operate to solve the technical problems faced by the Li metal anode. These strategies not only solve the single problem but can usually solve several problems at the same time. Even so, there are still some challenges to improving the performance of lithium anodes in lithium batteries. First of all, the performance of the protective material itself needs to be further improved, and it is necessary to develop the composite properties of new materials or materials, exploring new combinations and new functions, such as the combination of special films and bonds. Secondly, although a modification strategy with high comprehensive performance has been developed, the problem of dendrite growth has not been completely solved, and its nucleation and growth mechanism lack sufficient understanding, so further theoretical research is needed using machine learning, artificial intelligence, and theoretical calculation. For example, electrochemical mechanical modeling, multi-field simulation, electrochemical phase field, and other means are used to analyze and predict the inhomogeneous lithium deposition process and control the factors, so as to guide the actual deposition behavior and create better performance. Finally, due to the fact that most of the dendrite growth processes are not observed in time, there is a lack of research on the in situ evolution mechanism of the lithium metal anode interface, and more appropriate in situ analysis techniques need to be developed to analyze and understand the evolution behavior of the interface. Under the development trend of button cell battery to pouch battery, how to better contact with other components in the all-solid-state battery without affecting the interaction is a problem that lithium metal anode still needs to face. Researchers are needed to create more novel SEIs or electrolytes. Regarding the performance improvement strategy of lithium anode in lithium batteries, it can be developed in theoretical calculation and comprehensive regulation in the future.

Author Contributions: Conceptualization, M.W.; methodology, J.P.; software, Z.C.; formal analysis, L.Z.; investigation, Y.F.; resources, J.P.; data curation, J.S.; writing—original draft preparation, J.S.; writing—review and editing, J.S.; visualization, K.J.; project administration, P.Y.; funding acquisition, J.S. All authors have read and agreed to the published version of the manuscript.

Funding: This work was supported by the Research Funding of Wuhan Polytechnic University NO. 53210052436 and NO. 5321005225.

Conflicts of Interest: The authors declare no conflict of interest.

References

1. Liu, W.; Placke, T.; Chau, K.T. Overview of batteries and battery management for electric vehicles. *Energy Rep.* **2022**, *8*, 4058–4084. [CrossRef]
2. Chen, S.; Zhang, M.; Zou, P.; Sun, B.; Tao, S. Historical development and novel concepts on electrolytes for aqueous rechargeable batteries. *Energy Environ. Sci.* **2022**, *15*, 1805–1839. [CrossRef]
3. Ruan, P.; Liang, S.; Lu, B.; Fan, H.J.; Zhou, J. Design strategies for high-energy-density aqueous zinc batteries. *Angew. Chem. Int. Ed.* **2022**, *61*, e202200598. [CrossRef] [PubMed]
4. Bates, A.M.; Preger, Y.; Torres-Castro, L.; Harrison, K.L.; Harris, S.J.; Hewson, J. Are solid-state batteries safer than lithium-ion batteries? *Joule* **2022**, *6*, 742–755. [CrossRef]
5. Lombardo, T.; Duquesnoy, M.; El-Bouysidy, H.; Aren, F.; Gallo-Bueno, A.; Jorgensen, P.B.; Bhowmik, A.; Demortiere, A.; Ayerbe, E.; Alcaide, F.; et al. Artificial intelligence applied to battery research: Hype or reality? *Chem. Rev.* **2022**, *122*, 10899–10969. [CrossRef] [PubMed]
6. Yuan, D.; Dou, Y.; Wu, Z.; Tian, Y.; Ye, K.-H.; Lin, Z.; Dou, S.X.; Zhang, S. Atomically thin materials for next-generation rechargeable batteries. *Chem. Rev.* **2022**, *122*, 957–999. [CrossRef] [PubMed]
7. Rana, M.; Alghamdi, N.; Peng, X.; Huang, Y.; Wang, B.; Wang, L.; Gentle, I.R.; Hickey, S.; Luo, B. Scientific issues of zinc-bromine flow batteries and mitigation strategies. *Explor* **2023**, *3*, 20220073. [CrossRef]
8. Neumann, J.; Petranikova, M.; Meeus, M.; Gamarra, J.D.; Younesi, R.; Winter, M.; Nowak, S. Recycling of Lithium-Ion Batteries-Current State of the Art, Circular Economy, and Next Generation Recycling. *Adv. Energy Mater.* **2022**, *12*, 2102917. [CrossRef]
9. Rohland, P.; Schroeter, E.; Nolte, O.; Newkome, G.R.; Hager, M.D.; Schubert, U.S. Redox-active polymers: The magic key towards energy storage—A polymer design guideline progress in polymer science. *Prog. Polym. Sci.* **2022**, *125*, 101474. [CrossRef]
10. Editorial Office of Nature Energy. Battery revolution to evolution. *Nat. Energy* **2019**, *4*, 893. [CrossRef]
11. Liu, H.; Sun, X.; Cheng, X.B.; Guo, C.; Yu, F.; Bao, W.Z.; Wang, T.; Li, J.F.; Zhang, Q. Working principles of lithium metal anode in pouch cells. *Adv. Energy Mater.* **2022**, *12*, 2202518. [CrossRef]
12. Wang, Q.; Lu, T.T.; Xiao, Y.B.; Wu, J.Y.; Guan, L.X.; Hou, L.F.; Du, H.Y.; Wei, H.; Liu, X.D.; Yang, C.K.; et al. Leap of Li metal anodes from coin cells to pouch cells: Challenges and progress. *Electrochem. Energy Rev.* **2023**, *6*, 22. [CrossRef]
13. Liang, H.M.; Wang, L.; Sheng, L.; Xu, H.; Song, Y.Z.; He, X.M. Focus on the electroplating chemistry of li ions in nonaqueous liquid electrolytes: Toward stable lithium metal batteries. *Electrochem. Energy Rev.* **2022**, *5*, 23. [CrossRef]
14. Deng, R.; Wang, M.; Yu, H.; Luo, S.; Li, J.; Chu, F.; Liu, B.; Wu, F. Recent advances and applications toward emerging lithium-sulfur batteries: Working principles and opportunities. *Energy Environ. Mater.* **2022**, *5*, 777–799. [CrossRef]
15. Liang, Z.; Shen, J.; Xu, X.; Li, F.; Liu, J.; Yuan, B.; Yu, Y.; Zhu, M. Advances in the development of single-atom catalysts for high-energy-density lithium-sulfur batteries. *Adv. Mater.* **2022**, *34*, 2200102. [CrossRef] [PubMed]
16. Liang, Y.; Liu, H.; Wang, G.; Wang, C.; Ni, Y.; Nan, C.-W.; Fan, L.-Z. Challenges, interface engineering, and processing strategies toward practical sulfide-based all-solid-state lithium batteries. *InfoMat* **2022**, *4*, e12292. [CrossRef]
17. Lu, Y.; Zhao, C.-Z.; Huang, J.-Q.; Zhang, Q. The timescale identification decoupling complicated kinetic processes in lithium batteries. *Joule* **2022**, *6*, 1172–1198. [CrossRef]

18. Zhang, R.; Shen, X.; Zhang, Y.-T.; Zhong, X.-L.; Ju, H.-T.; Huang, T.-X.; Chen, X.; Zhang, J.-D.; Huang, J.-Q. Dead lithium formation in lithium metal batteries: A phase field model. *J. Energy Chem.* **2022**, *71*, 29–35. [CrossRef]
19. Ko, C.J.; Chen, C.H.; Chen, K.C. Influence of inhomogeneity of lithium-ion transport within the anode/electrolyte interface on mossy lithium formation. *J. Power Sources* **2023**, *563*, 232779. [CrossRef]
20. Chen, Y.L.; Yuan, X.P.; He, C.P.; Gou, Q.Y.; Yang, N.; Xie, G.; Zhang, K.Y.; Yao, Y.C.; Hou, Y.Q. Mechanistic exploration of dendrite growth and inhibition for lithium metal batteries. *Energies* **2023**, *16*, 3745. [CrossRef]
21. Zhang, Y.; Li, Y.; Shen, W.; Li, K.; Lin, Y. Important role of atom diffusion in dendrite growth and the thermal self-healing mechanism. *ACS Appl. Energy Mater.* **2023**, *6*, 1933–1945. [CrossRef]
22. Cao, X.L.; Lu, Y.J.; Song, X.; Yuan, Z.; Wang, F.H. Perspective of unstable solid electrolyte interphase induced lithium dendrite growth: Role of thermal effect. *Electrochim. Acta* **2023**, *439*, 141722. [CrossRef]
23. Li, B.R.; Chao, Y.; Li, M.C.; Xiao, Y.B.; Li, R.; Yang, K.; Cui, X.C.; Xu, G.; Li, L.Y.; Yang, C.K.; et al. A review of solid electrolyte interphase (SEI) and dendrite formation in lithium batteries. *Electrochem. Energy Rev.* **2023**, *6*, 7. [CrossRef]
24. Li, C.; Liang, Z.; Li, Z.; Cao, D.; Zuo, D.; Chang, J.; Wang, J.; Deng, Y.; Liu, K.; Kong, X.; et al. Self-Assembly monolayer inspired stable artificial solid electrolyte interphase design for next-generation lithium metal batteries. *Nano Lett.* **2023**, *23*, 4014–4022. [CrossRef] [PubMed]
25. Zhang, D.; Li, B.; Wang, S.; Yang, S.B. Simultaneous Formation of Artificial SEI Film and 3D Host for Stable Metallic Sodium Anodes. *ACS Appl. Mater. Interfaces* **2017**, *9*, 40265–40272. [CrossRef] [PubMed]
26. Gross, S.J.; Hsieh, M.T.; Mumm, D.R.; Valdevit, L.; Mohraz, A. Alleviating expansion-induced mechanical degradation in lithium-ion battery silicon anodes via morphological design. *Extrem. Mech. Lett.* **2022**, *54*, 101746. [CrossRef]
27. She, Z.; Uceda, M.; Pope, M.A. Encapsulating a responsive hydrogel core for void space modulation in high-stability graphene-wrapped silicon anodes. *ACS Appl. Mater. Interfaces* **2022**, *14*, 10363–10372. [CrossRef] [PubMed]
28. Zhu, M.Q.; Li, B.; Li, S.M.; Du, Z.G.; Gong, Y.J.; Yang, S.B. Dendrite-free metallic lithium in lithiophilic carbonized metal-organic frameworks. *Adv. Energy Mater.* **2018**, *8*, 1703505. [CrossRef]
29. Fan, H.L.; Dong, Q.Y.; Gao, C.H.; Hong, B.; Zhang, Z.A.; Zhang, K.; Lai, Y.Q. Encapsulating Metallic Lithium into Carbon Nanocages Which Enables a Low-Volume Effect and a Dendrite-Free Lithium Metal Anode. *ACS Appl. Mater. Interfaces* **2019**, *11*, 30902–30910. [CrossRef]
30. Zhu, W.H.; Deng, W.; Zhao, F.; Liang, S.S.; Zhou, X.F.; Liu, Z.P. Graphene network nested Cu foam for reducing size of lithium metal towards stable metallic lithium anode. *Energy Storage Mater.* **2019**, *21*, 107–114. [CrossRef]
31. Park, C.; Kim, J.; Lim, W.; Lee, J. Toward maximum energy density enabled by anode-free lithium metal batteries: Recent progress and perspective. *Explor* **2023**, *4*, 20210255. [CrossRef]
32. Yang, J.Z.; Yin, B.S.; Sun, Y.; Pan, H.G.; Sun, W.P.; Jia, B.H.; Zhang, S.W.; Ma, T.Y. Zinc anode for mild aqueous zinc-ion batteries: Challenges, strategies, and perspectives. *Nano-Micro Lett.* **2022**, *14*, 47. [CrossRef] [PubMed]
33. Liu, G.; Wang, N.; Qi, F.; Lu, X.; Liang, Y.; Sun, Z. Novel Ni-Ge-P anodes for lithium-ion batteries with enhanced reversibility and reduced redox potential. *Inorg. Chem. Front.* **2023**, *10*, 699–711. [CrossRef]
34. Liu, Y.; Li, Y.; Chen, L.; Yan, F.; Lin, Z.; Wang, J.; Qiu, J.; Cao, G.; Wang, B.; Zhang, H. Expanding the reversibility of graphite-Li metal hybrid anodes by interface and inner-structure modifications. *Energy Storage Mater.* **2022**, *53*, 621–628. [CrossRef]
35. Chen, C.; Yang, Y.F.; Shao, H.X. Enhancement of the lithium cycling capability using Li-Zn alloy substrate for lithium metal batteries. *Electrochim. Acta* **2014**, *137*, 476–483. [CrossRef]
36. Yanev, S.; Heubner, C.; Nikolowski, K.; Partsch, M.; Auer, H.; Michaelis, A. Editors' Choice-alleviating the kinetic limitations of the Li-In alloy anode in all-solid-state batteries. *J. Electrochem. Soc.* **2024**, *171*, 020512. [CrossRef]
37. Huang, Y.; Shao, B.; Han, F. Li alloy anodes for high-rate and high-areal-capacity solid-state batteries. *J. Mater. Chem. A* **2022**, *10*, 12350–12358. [CrossRef]
38. Peng, K.; Chen, Z.; Zhao, X.; Shi, K.; Zhu, C.; Yan, X. Dual-Conductive Li alloy composite anode constructed by a synergetic Conversion-Alloying reaction with $LiMgPO_4$. *Chem. Eng. J.* **2022**, *439*, 135705. [CrossRef]
39. Guo, B.; Guo, P.; Zhao, G.; Liu, S.; Shi, J.; Huang, M.; Shi, Z.; Wang, H.; Yan, Z. A solid-solution-based Li-Mg alloy for highly stable lithium metal anodes. *Sustain. Energy Fuels* **2022**, *6*, 4137–4145. [CrossRef]
40. Zheng, H.; Cheng, X.; Zheng, Q.; Zhang, J.; Li, T.; Xie, E.; Xu, Y. The thermodynamically directed dendrite-free lithium metal batteries on LiZn alloy surface. *Nano Res.* **2022**, *16*, 8354–8359. [CrossRef]
41. Qutaish, H.; Chang, H.; Suh, J.H.; Han, S.A.; Yum, H.-Y.; Park, M.-S.; Moon, J.; Kim, J.H. Growth mechanism of lithium clusters on the surface of porous carbon framework for lithium metal batteries. *ACS Mater. Lett.* **2023**, *5*, 1593–1600. [CrossRef]
42. Zhang, L.Y.; Jin, Q.; Zhao, K.X.; Zhang, X.T.; Wu, L.L. Lithiophilic $Ti_3C_2T_x$-modified Cu foam by electrophoretic deposition for dendrite-free lithium metal anodes. *Acs Appl. Energy Mater.* **2022**, *5*, 2514–2521. [CrossRef]
43. Yang, Y.; Huang, X.; Hu, W.; Rao, Y.; Wu, Y.; Ju, S. Electrodeposited 3D lithiophilic Ni microvia host for long cycling Li metal anode at high current density. *Electrochim. Acta* **2023**, *441*, 141797. [CrossRef]
44. Wang, C.H.; Li, Y.H.; Cao, F.; Zhang, Y.Q.; Xia, X.H.; Zhang, L.J. Employing Ni-embedded porous graphitic carbon fibers for high-efficiency lithium-sulfur batteries. *ACS Appl. Mater. Interfaces* **2022**, *14*, 10457–10466. [CrossRef]
45. Chen, W.; Li, S.; Wang, C.; Dou, H.; Zhang, X. Targeted deposition in a lithiophilic silver-modified 3D Cu host for lithium-metal anodes. *Energy Environ. Mater.* **2023**, *6*, e12412. [CrossRef]

46. Liu, Q.; Wang, R.L.; Liu, Z.F.; Wang, X.S.; Han, C.P.; Liu, H.B.; Li, B.H. A 3D lithiophilic ZIF-8@RGO free-standing scaffold with dendrite-free behavior enabling high-performance Li metal batteries. *J. Mater. Chem. A* **2023**, *11*, 12910–12917. [CrossRef]
47. Ma, Y.; Wei, L.; He, Y.; Yuan, X.Z.; Su, Y.H.; Gu, Y.T.; Li, X.J.; Zhao, X.H.; Qin, Y.Z.; Mu, Q.Q.; et al. A "blockchain" synergy in conductive polymer-filled metal-organic frameworks for dendrite-free Li plating/stripping with high coulombic efficiency. *Angew. Chem.-Int. Ed.* **2022**, *61*, 10. [CrossRef]
48. Huang, Y.; Lin, L.; Zhang, Y.; Liu, L.; Sa, B.; Lin, J.; Wang, L.; Peng, D.-L.; Xie, Q. Dual-functional lithiophilic/sulfiphilic binary-metal selenide quantum dots toward high-performance Li-S full batteries. *Nano-Micro Lett.* **2023**, *15*, 67. [CrossRef] [PubMed]
49. Xu, J.; Xu, L.L.; Zhang, Z.L.; Sun, B.; Jin, Y.; Jin, Q.Z.; Liu, H.; Wang, G.X. Heterostructure ZnSe-CoSe$_2$ embedded with yolk-shell conductive dodecahedral as two-in-one hosts for cathode and anode protection of lithium-sulfur full batteries. *Energy Storage Mater.* **2022**, *47*, 223–234. [CrossRef]
50. Zhang, G.; Wang, K.; Xu, Y.; Zhang, X.; Peng, Q.; Ma, Y.; Li, S.; Zhang, X.; Sun, X.; Ma, Y. A 10-μm ultrathin lithium metal composite anodes with superior electrochemical kinetics and cycling stability. *Energy Environ. Mater.* **2023**, *6*, e12598. [CrossRef]
51. Shin, H.R.; Kim, S.; Park, J.; Kim, J.H.; Park, M.S.; Lee, W. Electrode-level strategies enabling kinetics-controlled metallic Li confinement by the heterogeneity of interfacial activity and porosity. *Energy Storage Mater.* **2023**, *56*, 515–523. [CrossRef]
52. Wang, H.; Wei, Y.; Wang, G.; Pu, Y.; Yuan, L.; Liu, C.; Wang, Q.; Zhang, Y.; Wu, H. Selective nitridation crafted a high-density, carbon-free heterostructure host with built-in electric field for enhanced energy density Li-S batteries. *Adv. Sci.* **2022**, *9*, 2201823. [CrossRef]
53. Wang, B.; Ren, Y.; Zhu, Y.; Chen, S.; Chang, S.; Zhoua, X.; Wanga, P.; Sun, H.; Menga, X.; Tanga, S. Construction of Co$_3$O$_4$/ZnO heterojunctions in hollow n-doped carbon nanocages as microreactors for lithium-sulfur full batteries. *Adv. Sci.* **2023**, *10*, 2300860. [CrossRef]
54. Zhu, Y.; Yang, Y.; Zhang, H.; Liu, S.; Wu, Z.; Wu, C.; Gao, X.; Hu, E.; Chen, Z. A Highly-Lithiophilic Mn$_3$O$_4$/ZnO-Modified Carbon Nanotube Film for Dendrite-Free Lithium Metal Anodes. *J. Colloid Interface Sci.* **2023**, *648*, 299–307. [CrossRef] [PubMed]
55. Wang, H.S.; Yu, Z.; Kong, X.; Kim, S.C.; Boyle, D.T.; Qin, J.; Bao, Z.N.; Cui, Y. Liquid electrolyte: The nexus of practical lithium metal batteries. *Joule* **2022**, *6*, 588–616. [CrossRef]
56. Kim, M.S.; Zhang, Z.W.; Rudnicki, P.E.; Yu, Z.A.; Wang, J.Y.; Wang, H.S.; Oyakhire, S.T.; Chen, Y.L.; Kim, S.C.; Zhang, W.B.; et al. Suspension electrolyte with modified Li$^+$ solvation environment for lithium metal batteries. *Nat. Mater.* **2022**, *21*, 445. [CrossRef]
57. Hou, L.P.; Yao, N.; Xie, J.; Shi, P.; Sun, S.Y.; Jin, C.B.; Chen, C.M.; Liu, Q.B.; Li, B.Q.; Zhang, X.Q.; et al. Modification of nitrate ion enables stable solid electrolyte interphase in lithium metal batteries. *Angew. Chem.-Int. Ed.* **2022**, *61*, 6. [CrossRef] [PubMed]
58. Zhao, Q.; Utomo, N.W.; Kocen, A.L.; Jin, S.; Deng, Y.; Zhu, V.X.; Moganty, S.; Coates, G.W.; Archer, L.A. Upgrading carbonate electrolytes for ultra-stable practical lithium metal batteries. *Angew. Chem.-Int. Ed.* **2022**, *61*, 8. [CrossRef]
59. Pal, U.; Rakov, D.; Lu, B.Y.; Sayahpour, B.; Chen, F.F.; Roy, B.; MacFarlane, D.R.; Armand, M.; Howlett, P.C.; Meng, Y.S.; et al. Interphase control for high performance lithium metal batteries using ether aided ionic liquid electrolyte. *Energy Environ. Sci.* **2022**, *15*, 1907–1919. [CrossRef]
60. Sun, H.H.; Liu, J.D.; He, J.; Wang, H.P.; Jiang, G.X.; Qi, S.H.; Ma, J.M. Stabilizing the cycling stability of rechargeable lithium metal batteries with tris(hexafluoroisopropyl)phosphate additive. *Sci. Bull.* **2022**, *67*, 725–732. [CrossRef]
61. Li, F.; Liu, J.D.; He, J.; Hou, Y.Y.; Wang, H.P.; Wu, D.X.; Huang, J.D.; Ma, J.M. Additive-assisted hydrophobic Li$^+$-solvated structure for stabilizing dual electrode electrolyte interphases through suppressing LiPF$_6$ hydrolysis. *Angew. Chem.-Int. Ed.* **2022**, *61*, 6. [CrossRef]
62. Piao, Z.H.; Xiao, P.T.; Luo, R.P.; Ma, J.B.; Gao, R.H.; Li, C.; Tan, J.Y.; Yu, K.; Zhou, G.M.; Cheng, H.M. Constructing a stable interface layer by tailoring solvation chemistry in carbonate electrolytes for high-performance lithium-metal batteries. *Adv. Mater.* **2022**, *34*, 10. [CrossRef]
63. Zhu, C.N.; Sun, C.C.; Li, R.H.; Weng, S.T.; Fan, L.W.; Wang, X.F.; Chen, L.X.; Noked, M.; Fan, X.L. Anion-diluent pairing for stable high-energy Li metal batteries. *ACS Energy Lett.* **2022**, *7*, 1338–1347. [CrossRef]
64. Cao, Y.Y.; Zhang, G.Q.; Zou, J.C.; Dai, H.C.; Wang, C.L. Natural pyranosyl materials: Potential applications in solid-state batteries. *Chemsuschem* **2023**, *16*, e202202216. [CrossRef] [PubMed]
65. Wang, C.H.; Kim, J.T.; Wang, C.S.; Sun, X.L. Progress and prospects of inorganic solid-state electrolyte-based all-solid-state pouch cells. *Adv. Mater.* **2023**, *35*, 2209074. [CrossRef] [PubMed]
66. Yi, Q.; Zhang, W.Q.; Wang, T.Y.; Han, J.X.; Sun, C.W. A high-performance lithium metal battery with a multilayer hybrid electrolyte. *Energy Environ. Mater.* **2023**, *6*, 8. [CrossRef]
67. Zhang, Y.H.; Lu, M.N.; Li, Q.; Shi, F.N. Hybrid lithium salts regulated solid polymer electrolyte for high-temperature lithium metal battery. *J. Solid State Chem.* **2022**, *310*, 8. [CrossRef]
68. Ma, Y.X.; Wan, J.Y.; Yang, Y.F.; Ye, Y.S.; Xiao, X.; Boyle, D.T.; Burke, W.; Huang, Z.J.; Chen, H.; Cui, Y.; et al. Scalable, ultrathin, and high-temperature-resistant solid polymer electrolytes for energy-dense lithium metal batteries. *Adv. Energy Mater.* **2022**, *12*, 9. [CrossRef]
69. Kang, Q.; Li, Y.; Zhuang, Z.C.; Wang, D.S.; Zhi, C.Y.; Jiang, P.K.; Huang, X.Y. Dielectric polymer based electrolytes for high-performance all-solid-state lithium metal batteries. *J. Energy Chem.* **2022**, *69*, 194–204. [CrossRef]
70. Peng, J.; Wu, D.X.; Song, F.M.; Wang, S.; Niu, Q.H.; Xu, J.R.; Lu, P.S.; Li, H.; Chen, L.Q.; Wu, F. High current density and long cycle life enabled by sulfide solid electrolyte and dendrite-free liquid lithium anode. *Adv. Funct. Mater.* **2022**, *32*, 14. [CrossRef]

71. Zeng, D.W.; Yao, J.M.; Zhang, L.; Xu, R.N.; Wang, S.J.; Yan, X.L.; Yu, C.; Wang, L. Promoting favorable interfacial properties in lithium-based batteries using chlorine-rich sulfide inorganic solid-state electrolytes. *Nat. Commun.* **2022**, *13*, 13. [CrossRef] [PubMed]
72. Hao, H.C.; Hutter, T.; Boyce, B.L.; Watt, J.; Liu, P.C.; Mitlin, D. Review of multifunctional separators: Stabilizing the cathode and the anode for alkali (Li, Na, and K) metal-sulfur and selenium batteries. *Chem. Rev.* **2022**, *122*, 8053–8125. [CrossRef] [PubMed]
73. Zhang, Z.W.; Li, Y.Z.; Xu, R.; Zhou, W.J.; Li, Y.B.; Oyakhire, S.T.; Wu, Y.C.; Xu, J.W.; Wang, H.S.; Yu, Z.A.; et al. Capturing the swelling of solid-electrolyte interphase in lithium metal batteries. *Science* **2022**, *375*, 66. [CrossRef]
74. Liu, Y.J.; Tao, X.Y.; Wang, Y.; Jiang, C.; Ma, C.; Sheng, O.W.; Lu, G.X.; Lou, X.W. Self-assembled monolayers direct a LiF-rich interphase toward long-life lithium metal batteries. *Science* **2022**, *375*, 739. [CrossRef]
75. Lin, G.; Jia, K.; Bai, Z.; Liu, C.; Liu, S.; Huang, Y.; Liu, X. Metal-organic framework sandwiching porous super-engineering polymeric membranes as anionphilic separators for dendrite-free lithium metal batteries. *Adv. Funct. Mater.* **2022**, *32*, 2207969. [CrossRef]
76. Yang, Y.; Yao, S.Y.; Liang, Z.W.; Wen, Y.C.; Liu, Z.B.; Wu, Y.W.; Liu, J.; Zhu, M. A self-supporting covalent organic framework separator with desolvation effect for high energy density lithium metal batteries. *ACS Energy Lett.* **2022**, *7*, 885–896. [CrossRef]
77. Wang, X.; Meng, L.; Liu, X.; Deng, N.; Yan, Z.; Wang, G.; Wei, L.; Zhang, L.; Cheng, B.; Kang, W. MOF-derived MoP nanorods decorated with a N-doped thin carbon layer as a robust lithiophilic and sulfiphilic nanoreactor for high-performance Li-S batteries. *Sustain. Energy Fuels* **2022**, *6*, 3989–4000. [CrossRef]
78. He, Y.; Wang, L.; Wang, A.; Zhang, B.; Pham, H.; Park, J.; He, X. Insight into uniform filming of LiF-rich interphase via synergistic adsorption for high-performance lithium metal anode. *Explor* **2023**, *4*, 20230114. [CrossRef] [PubMed]
79. Ju, Z.J.; Lu, G.X.; Sheng, O.W.; Yuan, H.D.; Zhou, S.Q.; Liu, T.F.; Liu, Y.J.; Wang, Y.; Nai, J.W.; Zhang, W.K.; et al. Soybean protein fiber enabled controllable Li deposition and a Lif-nanocrystal-enriched interface for stable Li metal batteries. *Nano Lett.* **2022**, *22*, 1374–1381. [CrossRef]
80. Liu, Y.Y.; Xu, X.Y.; Kapitanova, O.O.; Evdokimov, P.V.; Song, Z.X.; Matic, A.; Xiong, S.Z. Electro-chemo-mechanical modeling of artificial solid electrolyte interphase to enable uniform electrodeposition of lithium metal anodes. *Adv. Energy Mater.* **2022**, *12*, 8. [CrossRef]
81. Zhang, C.; Zhu, S.W.; Wang, D.; Lei, C.; Zhao, Y. Phase field modeling of lithium deposition in porous lithium metal anodes. *J. Energy Storage* **2023**, *73*, 109279. [CrossRef]
82. Cao, J.Q.; Xie, Y.H.; Yang, Y.; Wang, X.H.; Li, W.Y.; Zhang, Q.L.; Ma, S.; Cheng, S.Y.; Lu, B.A. Achieving uniform Li plating/stripping at ultrahigh currents and capacities by optimizing 3D nucleation sites and Li_2Se-Enriched SEI. *Adv. Sci.* **2022**, *9*, 10. [CrossRef] [PubMed]
83. Zhang, D.C.; Liu, Z.B.; Wu, Y.W.; Ji, S.M.; Yuan, Z.X.; Liu, J.; Zhu, M. In situ construction a stable protective layer in polymer electrolyte for ultralong lifespan solid-state lithium metal batteries. *Adv. Sci.* **2022**, *9*, 11. [CrossRef] [PubMed]
84. Li, S.; Huang, J.; Cui, Y.; Liu, S.; Chen, Z.; Huang, W.; Li, C.; Liu, R.; Fu, R.; Wu, D. A robust all-organic protective layer towards ultrahigh-rate and large-capacity li metal anodes. *Nat. Nanotechnol.* **2022**, *17*, 613. [CrossRef] [PubMed]
85. Hu, F.; Li, Y.; Wei, Y.; Yang, J.; Hu, P.; Rao, Z.; Chen, X.; Yuan, L.; Li, Z. Construct an ultrathin bismuth buffer for stable solid-state lithium metal batteries. *ACS Appl. Mater. Interfaces* **2020**, *12*, 12793–12800. [CrossRef] [PubMed]
86. Shen, X.; Shi, S.; Li, B.; Li, S.; Zhang, H.; Chen, S.; Deng, H.; Zhang, Q.; Zhu, J.; Duan, X. Lithiophilic interphase porous buffer layer toward uniform nucleation in lithium metal anodes. *Adv. Funct. Mater.* **2022**, *32*, 2206388. [CrossRef]
87. Zhang, Z.; Guan, S.; Liu, S.; Hu, B.; Xue, C.; Wu, X.; Wen, K.; Nan, C.-W.; Li, L. A valence gradient protective layer for dendrite-free and highly stable lithium metal anodes. *Adv. Energy Mater.* **2022**, *12*, 2103332. [CrossRef]

Disclaimer/Publisher's Note: The statements, opinions and data contained in all publications are solely those of the individual author(s) and contributor(s) and not of MDPI and/or the editor(s). MDPI and/or the editor(s) disclaim responsibility for any injury to people or property resulting from any ideas, methods, instructions or products referred to in the content.

MDPI AG
Grosspeteranlage 5
4052 Basel
Switzerland
Tel.: +41 61 683 77 34

Molecules Editorial Office
E-mail: molecules@mdpi.com
www.mdpi.com/journal/molecules

Disclaimer/Publisher's Note: The title and front matter of this reprint are at the discretion of the Guest Editors. The publisher is not responsible for their content or any associated concerns. The statements, opinions and data contained in all individual articles are solely those of the individual Editors and contributors and not of MDPI. MDPI disclaims responsibility for any injury to people or property resulting from any ideas, methods, instructions or products referred to in the content.

MDPI

Academic Open
Access Publishing

mdpi.com

ISBN 978-3-7258-6421-8